CARBON NANOTUBE COMPOSITES PREPARED BY ULTRASONICALLY ASSISTED TWIN SCREW EXTRUSION

A Dissertation

Presented to

The Graduate Faculty of The University of Akron

In Partial Fulfillment

of the Requirements for the Degree

Doctor of Philosophy

Todd Lewis

August, 2014

CARBON NANOTUBE COMPOSITES PREPARED BY ULTRASONICALLY ASSISTED TWIN SCREW EXTRUSION

Todd Lewis

Dissertation

Approved:

_____
Advisor
Dr. Avraam I. Isayev

_____
Committee Member
Dr. Alamgir Karim

_____
Committee Member
Dr. Sadhan C. Jana

_____
Committee Member
Dr. Shing-Chung "Josh" Wong

_____
Committee Member
Dr. Wieslaw K. Binienda

Accepted:

_____
Department Chair
Dr. Robert A. Weiss

_____
Dean of the College
Dr. Stephen Z. D. Cheng

_____
Dean of the Graduate School
Dr. George R. Newkome

_____
Date

ABSTRACT

Two ultrasonic twin screw extrusion systems were designed and manufactured for the ultrasonic dispersion of multi-walled carbon nanotubes in viscous polymer matrices at residence times of the order of seconds in the ultrasonic treatment zones. The first design consisted of an ultrasonic slit die attachment in which nanocomposites were treated. A second design incorporated an ultrasonic treatment section into the barrel of the extruder to utilize the shearing of the polymer during extrusion while simultaneously applying treatment. High performance, high temperature thermoset phenylethynyl terminate imide oligomer (PETI-330) and two different polyetherether ketones (PEEK) were evaluated at CNT loadings up to 10 wt%. The effects of CNT loading and ultrasonic amplitude on the processing characteristics and rheological, mechanical, electrical, thermal and morphological properties of nanocomposites were investigated. PETI and PEEK nanocomposites showed a decrease in resistivity, an increase in modulus and strength and a decrease in strain at break and toughness with increased CNT loading. Ultrasonically treated samples showed a decrease in die pressure and extruder torque with increasing ultrasonic treatment and an increase in complex viscosity and storage modulus at certain ultrasonic treatment levels. Optical microscopy showed enhanced dispersion of the CNT bundles in ultrasonically treated samples. However, no significant improvement of

mechanical properties was observed with ultrasonic treatment due to lack of adhesion between the CNT and matrix in the solid state.

A curing model for PETI-330 was proposed that includes the induction and curing stages to predict the degree of cure of PETI-330 under non-isothermal conditions. Induction time parameters, rate constant and reaction order of the model were obtained based on differential scanning calorimetry (DSC) data. The model correctly predicted experimentally measured degrees of cure of compression molded plaques cured to various degrees.

An apparatus for high temperature resin transfer molding (HT-RTM) was designed and built to produce PETI-8 and PETI-330/carbon fabric composite panels. Performance of the panels was tested at various temperatures. The produced panels exhibited low void content in wetted areas and had higher short beam shear properties in comparison with vacuum assisted resin transfer moldings.

To investigate the environmental aspects of nanomaterials, a testing apparatus was designed and manufactured to study the effectiveness of particulate respirators at filtering CNTs. Three different grades of respirators were evaluated for their effectiveness to prevent the inhalation of CNTs. Dust masks, commonly used in a processing environment, were found to be highly ineffective at preventing the inhalation of CNTs. However, respirators with a National Institute for Occupational Safety and Health (NIOSH) rating of P95 or greater were shown to prevent the inhalation of CNTs under normal breathing conditions.

ACKNOWLEDGEMENTS

I would like to thank my advisor, Dr. Avraam I. Isayev for his patience, encouragement, and understanding. His effort, forethought and guidance was instrumental in the completion of this research. I would also like to express my sincere gratitude to my committee members for their patience, direction and comments during this study.

This work could not have been completed without the support of my wife, Angela, or my close friend and colleague, Dr. Antonio Carrillo. Additionally, this research would not have been possible without the help and contributions from Dr. Sayata Ghose, Dr. Jaesun Choi and Ryan Schmidt.

This research was funded by the National Science Foundation (NSF) under Grants CMMI-0654326 and CMMI-1131342, NASA Headquarters and NASA Langley.

TABLE OF CONTENTS

Page

LIST OF TABLES

LIST OF FIGURES

CHAPTER I

INTRODUCTION

For the past two decades nanostructures have dominated the science world. Nano materials have been used for more than a century in the form of carbon black but with the advancement of microscopy and their increased resolution many new materials have been discovered and more applications have been developed. Nano-clays, nano-printing, nano-lithography, nano-polymer, nano-fibers and nano-tubes are all thoroughly researched areas. One of the largest areas of interest was started by Iijima with micrographs of carbon nanotubes (CNTs). Although Iijima was not the first person to publish pictures of CNTs it was his work that started the carbon nanotube hysteria [1]. CNTs can be and have been used to incorporate enhanced mechanical, thermal, and electrical properties into composite materials.

High temperature, high performance resins have significant industrial importance and industrial and academic research continues to improve their properties. The following is not intended to be comprehensive but is an overview on the advancement of high temperature and high performance materials composites. Information on the following materials including but not limited to their development, use and properties can be found in very detailed books that have been published on the subject [2-8].

Kapton, Vespel and Pyre-ML by Dupont, Skybond by Monsanto, and Astrel 360 by 3M were the start of high temperature, high performance materials produced from heterocyclic polymers. While Kapton became an industrial success and Vespel has had success in areas where tribological properties are important the remaining never found a niche in the market place and were all phased out. The development of aromatic polyamide Kevlar, by Dupont, the polyetherimide Ultem, by General Electric and the polyarylene ethers such as polyetherketone (PEK) and polyetheretherketone (PEEK) [3] soon followed. With the development of Ultem, a moldable high temperature thermoplastic with good mechanical properties had materialized. Further work led to the development of Torlon by Amoco, a polyamide imide, and PMR-15, a thermoset, imide oligomer discovered at the NASA Glenn Research Center. PMR-15 had the processability of a low viscosity oligomer with high temperature and mechanical performance.

Upilex R and S, both polyimides, were introduced by Ube Industries, Ltd. Upilex S was the first truly high performance as well as high temperature polymer. It had unprecedented tensile strength and modulus along with a low coefficient of thermal expansion and quickly found industrial significance [2]. Continued research using phenylethynyl groups in polyimides to functionalize heterocyclic oligomers led to the development of a new line of high performance materials. PETI-5, a phenylethynyl terminated imide was first in the line of development. However, while its use was limited the phenylethynyl terminated imides chemistry was established. Continued research led to the development of other phenylethynyl terminated imides such as PETI-

298 and PETI-330, also developed by NASA Langley Research Center (LaRC). Arising from this work, aromatic polyimides are currently the leading candidates due to their high performance and range of processability [8]. These polyimides are known for their high temperature stability and retention of properties but pose problems in processing and curing and have low impact strengths.

Often, an individual material does not possess all of the required characteristics sought after or required. Composite materials use the advantageous features of two or more materials to create a more optimal material. CNTs are known for their unusually high mechanical and electrical properties as well as their tendency to aggregate in the form of bundles during their manufacturing due to strong van der Waals forces at their nano size scale. The finding and commercialization of these nanostructures in multi- and single-walled forms with a range of L/D ratios was a primary focus of the 90's. However, their properties have yet to be fully utilized due to the lack of a suitable processing method for dispersion.

The primary focus of this research is the incorporation of CNTs into two different polymer matrices for enhanced mechanical and electrical properties. The first matrix studied is phenylethynyl terminated imide (PETI-330), a high temperature thermoset, whose cure behavior and composite properties were studied. The second matrix is polyetheretherketone (PEEK), a high temperature thermoplastic material, whose composite properties were investigated. Two novel ultrasonic extrusion processes have been investigated for the dispersion of carbon nanotubes through the evaluation of the rheological, mechanical, thermal, electrical and morphological properties.

Sonication has long been used as a method of dispersion for materials in a solution. By putting aggregated materials in an ultrasonic bath and sonicating for an extended period of time, dispersion of the aggregates is enhanced and homogenous dispersion at prolonged periods can be fully achieved. The focus of this study is the in situ implementation of ultrasound in the melt mixing of CNTs and the study and characterization of these composites for the dispersion of CNT bundles and the resultant properties. This continuous extrusion process is environmentally friendly and can readily be scaled up for the commercial production of nanocomposites.

This dissertation consists of nine chapters. Chapter II presents a background of the materials being used and a literature survey of the current methods being utilized for the dispersion of carbon nanotubes in polymer nanocomposites. Chapter III describes the experimental materials, procedures and processes used for the production and characterization of carbon nanotube nanocomposites, the methods used to evaluate the cure kinetics of PETI-330 and the experimental materials, and the procedures and processes for the environmental testing of respirators. Chapter IV presents the proposed cure kinetics model for PETI-330. The model has been tested experimentally to verify its accuracy in predicting the degree of cure in molding applications. Chapter V describes the processing, characterization and results of PETI-330/CNT nanocomposites processed using a twin screw extruder with an ultrasonic slit die attachment. Chapter VI presents research on high temperature resin transfer moldings of PETI-330 infused carbon nanofiber mats. Chapter VII describes the processing, characterization and results of PEEK 380P/CNT nanocomposites processed using a twin screw extruder with an

ultrasonic slit die attachment. Chapter VIII describes the processing, characterization and results of PEEK 450PF/CNT nanocomposites processed using a modified twin screw extruder that incorporates ultrasonic treatment into the extruder. Chapter IX presents method, analysis and results for testing respirators in a CNT rich environment. Finally, a summary of this research and path forward are presented in Chapter X.

CHAPTER II

LITERATURE REVIEW

High temperature, high performance polymers and their composites are sought for the most demanding application. The theoretical synergy of nanomaterials in high performance matrices has led to heightened research interest. The primary objectives of this chapter are 1:to summarize research in the area of high temperature thermoset polyimides pertaining to PETI-330 and its nanocomposites; 2: to summarize research focused on PEEK and its nanocomposites; 3: to review theories of cure kinetics, focusing on work that was the precursor for this research; and 4: to summarize the background for the environmental impact study of nanomaterials as they pertain to inhalation.

2.1 High Temperature Materials

High performance, high temperature materials are defined according to the end use. This research studied materials that have high temperature longevity (longer than 10,000 hours at 177^{o}C), high heat deflection temperature (10 % deflection at a temperature greater than 177^{o}C under a stress of 1.52 MPa in three point bending, thermal decomposition temperatures greater than 450^{o}C (weight loss of less than 5% measured by TGA) with high glass transition temperatures. This follows the criteria laid out by NASA

for research in this area [8]. Below is a brief outline of factors influencing the performance of polymers at elevated temperatures.

It is known that polymers with high molecular weights and narrow weight distributions exhibit high performance properties. Low molecular weight chains provide increased chain mobility resulting in lower mechanical properties and leads to lower glass transition temperatures. Characteristics that significantly affect the thermal stability and properties are primary bond strength, secondary bonding forces, molecular weight, molecular weight distribution, molecular symmetry, rigidity of intrachain structure, crosslinking, purity, mechanism of bond cleavage, additives and reinforcements [8]. Bond energy is the most significant factor of those listed above and therefore, the backbones of the majority of high temperature, high performance polymers are composed mainly of aromatic groups or cyclic rings. Secondary bonding forces such as hydrogen bonding and van der Waals forces add to the stability of the material while contaminants that are metallic can initiate degradation. The method of degradation is also significant. Polymers that degrade at the end caps of the chains first and then rapidly propagate inward have less thermal stability than polymers that degrade by random chain scission.

Thermoset (cross-linked) materials are more thermally stable and have higher mechanical properties due to their three dimensional structure. There are more bonds to break in the three dimensional network to create the low molecular weight species than there are in non-crosslinked thermoplastic polymers. The regularity of the structure and the crystallinity have a significant effect on the mechanical, thermal and chemical properties of the polymer.

2.2 Polyimides

Aromatic polyimides are known for their outstanding mechanical properties that are sustainable at high temperatures. They are used for thin films in electronic applications, structural adhesives and sealants, high temperature insulators, aircraft wire coatings and as membranes for gas separation [8-18]. However, their poor processability limits their incorporation into commercial composites. Polyimides are known to have poor solubility in common solvents, evolution of volatiles during curing and high processing temperatures. Several methods have been used to attempt to circumvent these problems such as resin transfer molding (RTM) and vacuum assisted resin transfer molding (VARTM) for processing and the use of fillers or prepegs to improve their mechanical properties.

2.2.1 Polyimide Synthesis

Common approaches are the polymerization of monomeric reactants (PMR) and insitu imidization. PMR is the process of dissolving a dialkyl ester of an aromatic tetracarboxylic, an aromatic diamine and a monoalkyl ester of 5-norbornene-2,3-dicarboxylic acid (nadicester (NE)) in a low-boiling alkyl alcohol, methyl or ethyl alcohol. The monomers undergo in situ cyclo-dehydration to form a norbornene end-capped, low molecular weight imide pre-polymer. PMR-15 is the most widely recognized composite material that is formed through the in situ imidization process using the combination of NE, 4,4-methylene dianiline (MDA), and dimethyl ester of 3,3,4,4-benzo-phenonetetracarboxylic acid (BTDE) with a calculated average molecular weight of 1500

g/mol and the chemistry was developed by NASA [19] and others such as Parker *et al.* [20]. While it is easily processable, has high mechanical properties with high temperature retention for extended periods of time, it does not exhibit the low viscosity needed for processing, commonly forms micro cracks and does not have the required long term thermo-oxidative stability at temperatures above 300^{o}C. The classification of 4,4'-diamino diphenyl methane (DDM), a curing agent used in PMR-15, as a carcinogen is also a deterrent to its use. Poor toughness and the formation of micro-cracks under cyclic stress and temperature exposure also pose end use troubles.

Another approach centered around a series of phenylethynyl-terminated polyimide oligomers (PETI) [21-24]. The imide oligomers were chosen because of the availability of monomers and their excellent mechanical and thermal properties. Previous research had shown that the phenylethynyl groups could be placed in the backbone and then thermally reacted to provide crosslinks. These materials had the benefits of chemical and temperature stability along with the option of a variety of oligomers that they could be processed with [8-11]. These cured materials have several advantages: (1) no volatiles are formed during the curing reaction; (2) the phenylethynyl group exhibits greater process control over the ethynyl group with a larger processing window; (3) superior thermal and thermo-oxidative stability; and (4) a long shelf life [12, 13, 17]. Many of these materials were developed at NASA Langley Research Center using technology that was developed by the National Starch and Chemical Company. This technology uses 4-phenylethynylphthalic anhydride (4-PEPA) [25] for end capping and chain addition polymerization. They have high thermal and mechanical properties, chemical resistance

and the required viscosity to be used in prepreg applications where melt stability and controlled curing are required. PETI-5 was a standout and showed good mechanical properties and better processability [11, 26]. However, it lacks the viscosity required for infusing a melt into a prepeg. The desire for enhanced processability and higher thermo-mechanical properties led to the development and formulation of PETI-330. PETI-330 was developed at NASA Langley Research Center [27].

Phenylethynyl terminated imide (PETI-330) oligomeris based on 2,3,3',4' –biphenyl tetracarboxylic dianhydride, an asymmetric isomer (a-BPDA), by Ube Industries, and phenylethynylpthalic anhydride (PEPA) as end capping groups. Imide oligomers are created with reactive end groups. For phenylethynylphthalic anhydride (PEPA) terminated oligomers these end groups are thermally reactive but don't rapidly react up to temperatures of 300^{o}C. A brief scheme of synthesis is displayed in Figure 2.1 and a brief synopsis of the steps is listed below [27], [28]. An amine solution is created by combining equal parts of 1,3-bis (4-aminophenoxy) benzene (1,3,4-APB) and 1,3-diaminobenzene (1,3 PDA) in their common solvent N methyl-2-pyrrolidinone (NMP). A slurry of 2,3,3',4'-biphenyltetracarboxylic dianhydride (a-BPDA) and 4-phenylethynylphthalic anhydride (PEPA) is added to the amine solution and the reaction is kept at a temperature of 75^{o}C for 4 hours. The mixture is then heated to reflux in a Dean Stark trap using toluene at 185^{o}C for 12 hours. Then it is subsequently cooled to 75^{o}C and filtered and washed multiple times in warm water. After being washed the resultant material is dried in an oven at 135^{o}C for 24 hours or until the weight becomes constant. The technology was licensed to Ube Industries and is produced under the trade

name PETI-330. It comes in a yellowish powder that is in oligomer form and has a calculated number average molecular weight of 750 g/mole and a cured T_g of 330^{o}C. It is also important to note that there is very light crosslinking between the polymer chains but more branching, rigid entanglements and chain extension or addition polymerization that give PETI its high strength and corresponding brittle properties.

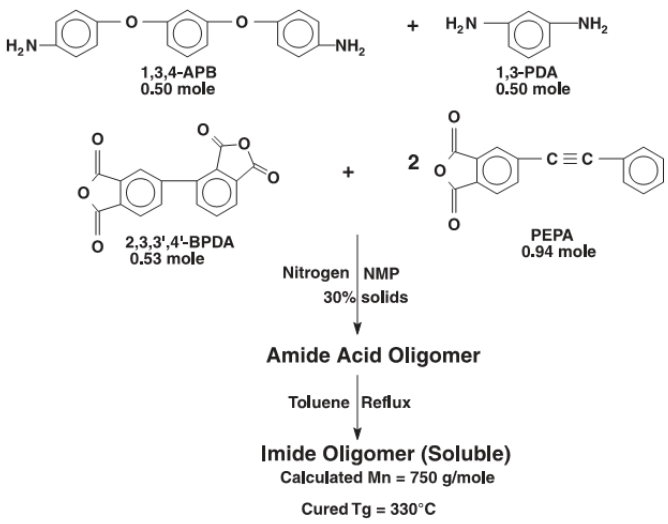

Figure 2.1: Reaction Scheme for PETI-330 [29]

2.2.2 Cure Kinetics

It is common knowledge that the curing of thermoset materials does not follow, nor can it be predicted, by a common rate equation. There are two distinct steps in the curing of a thermoset material. First, there exists a period during the curing process in which no reaction takes place. This period varies with the time-temperature history that each cured specimen progresses through. This stage is then followed by a period of curing which goes to full or partial completion. It is important to know the entire time-temperature cure

curve in order to obtain the optimum processing conditions for different parts and to be able to predict the completion of cure for any time-temperature history that the specimen experiences.

It is noted that PETI is undergoing an imidization reaction. However, as it is has already been established in literature as a curing reaction the same nomenclature has been used in this work. The properties of PETI-330 RTM composites and laminates cured under fixed and varied cure/post cure cycles [29-32] before and after thermal aging have been investigated. Connell *et al.* [29] studied the mechanical properties of PETI-330/AS-4 and T-65-35 8 harness satin carbon fiber fabric laminates under fixed curing conditions and found PETI-330 to be a thermally stable high temperature material. PETI-330 laminates were found to have a ~74% retention of open hole compression strength (OHC) and up to 62% retention of short beam shear strength when tested at 288°C versus room temperature. After aging for 1000 hours at 288°C, PETI-330 laminates were found to retain ~78% of its room temperature OHC strength and ~92% of its OHC modulus. Research investigating the different cure/post cure cycles in PETI-330 RTM laminates was also carried out. RTM laminates were cured at 371°Cand then subsequently went through post cure cycles over a range of temperatures from 316-371°C for periods of 6 and 12 hours. Samples were then evaluated before and after aging for 100 hours at elevated temperatures. Evaluation of T_g and weight loss after aging showed significant differences with variation in cure/post cure cycle. The cured Tg in corresponding sets of data was found to vary from 343°C to 360°C, evaluated by DMTA, and weight loss

differences as great as 3.3% to 8.0% after isothermal aging between samples of different curing cycles.

Another study focused on optimizing the liquid molding cycle for PETI-330 [28]. This work was very detailed and gave a broad understanding of this material. The authors showed that PETI-330 has a very large processing window, has melt stability for more than 2 hours at 280^{o}C with a viscosity of less than 1 Pa-s and that curing only rapidly occurs above 350^{o}C. They also showed that at 370^{o}C the cure time should be more than 30 min and more than 1 hour at 360^{o}C. Studies on other phenylethynyl terminated imides have also focused on curing. Studies on PETI-5 have looked at microwave and thermal curing [26, 33, 34]. These works led to the conclusion that a first order rate equation predicted curing only up to approximately 90% of cure and then it followed a 1.5 order rate. They postulated this to be due to reactions that are occurring at the end of curing such as polyene crosslinking. To the author's knowledge, no curing model has been published for PETI-330.

All thermosets are cured under non-isothermal conditions and therefore have a complicated time dependent thermal history. Many curing models are based on isothermal rate equations and do not account for heating ramps that are unavoidable during actual processing conditions. To be able to optimize the complicated cure cycle of these polymers an accurate model is needed that accounts for the entire time-temperature trace. In 1970 an article by MacCullum and Tanner [35] started the discussion on what equation could be used to describe a non-isothermal system by questioning whether an

isothermal kinetic rate equation, as shown in equation 2.1, could be used to describe non-isothermal behavior.

$$\left(\frac{\partial \alpha}{\partial t}\right)_T = K(T) f(\alpha) \tag{2.1}$$

where α is the fractional conversion, T is the temperature, t is the time, and K is the rate constant which is a function of temperature. Previous work had been based on the idea that the dynamic, nonisothermal, rate is equal to the isothermal rate but MacCallum and Tanner proposed that in nonisothermal process the fractional conversion is a function of both time and temperature as seen in equation 2.2.

$$d\alpha = \left(\frac{\partial \alpha}{\partial t}\right)_T dt + \left(\frac{\partial \alpha}{\partial T}\right)_t dT \tag{2.2}$$

While many theories have been proposed to date there is still no consensus on the exact solution to this problem. Isayev and Deng [36, 37] proposed a model based on a reduced time approach to be able to predict the degree of cure in nonisothermal curing in rubber. This model was adopted and modified for the present research. Their model is described below for both isothermal and nonisothermal curing.

2.2.3 Isothermal Model

Isayev and Deng [37] used the following kinetics model to describe rubber vulcanization kinetics and the progression is directly from their work and is repeated below from Isayev, Chan, and Shyu [38] as the same theory was adapted for the current cure model. The isothermal model assumes that there is an induction period during which

no reaction takes place. During isothermal conditions it is assumed that this induction period has an Arrhenius-type dependence on temperature as shown in equation 2.3.

$$t_i = t_0 \exp\left(\frac{T_b}{T}\right) \tag{2.3}$$

where T is the temperature, t_o and T_b are the material constants independent of temperature. Based on the work of Kamal and Sourour [39] a model for isothermal curing kinetics was used, as shown in Equation 2.4:

$$\alpha = \frac{kt^n}{1+kt^n} \tag{2.4}$$

where *t* is the actual time minus the induction time and k is the rate constant with an Arrhenius-type dependence on temperature as such:

$$k = k_o \exp\left(-\frac{E}{RT}\right) \tag{2.5}$$

where k_o is the pre-exponential factor, *E* is the activation energy and *R* is the universal gas constant. The derivative of equation 2.4 with respect to time yields:

$$\frac{d\alpha}{dt} = \frac{nkt^{n-1}}{\left(1+kt^n\right)^2} \tag{2.6}$$

By expressing t in terms of α and k in equation 2.4, equation 2.6 becomes:

$$\frac{d\alpha}{dt} = k_o e^{-E/RT} \alpha^{(n-1)/n} (1-\alpha)^{n+1/n} \tag{2.7}$$

where α, n, k, t, E, R and T are the degree of curing, order of reaction, a rate constant, time, activation energy, gas constant and temperature, respectively.

2.2.4 Non-Isothermal Model

The nonisothermal induction time is derived from the isothermal induction time using the concept of induction time index:

$$\bar{t} = \int_0^{t_I} \frac{dt}{t_i(T)} = 1 \tag{2.8}$$

where t_I is the nonisothermal induction time, $t_i(T)$ is the isothermal induction time. As soon as the value of $\bar{t}$ attains unity, 1, the upper limit of the integral in Equation 2.8 becomes the induction time for the nonisothermal process. In this theory it is assumed that the nonisothermal induction time is made up of many minute isothermal steps. This non-isothermal induction time can be determined from DSC thermograms as a function of heating rate and is defined as the point at which the heat flow diverges from the base line.

2.3 Polyetheretherketone (PEEK)

PEEK is a high temperature, high performance thermoplastic. The tensile strength, modulus and T_g are lower than those of most polyimides due to the ether groups in the backbone providing flexibility and the fact that they do not have the strong intermolecular forces. However, due to these same properties it has better toughness, easily processable and lower in cost than polyimides. The repeat structure of PEEK is shown in Figure 2.2.

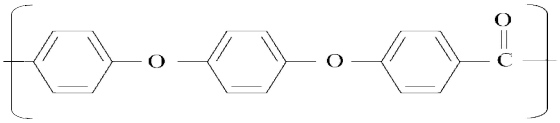

Figure 2.2 Structure of poly ether-ether-ketone

2.3.1 Synthesis

Many different reaction routes have been used to synthesize PEEK. Several of the common reaction mechanisms used are aromatic nucleophilic displacement [40], aromatic electrophilic reaction [41, 42], oxidative coupling [43], Scholl reaction [44], nickel catalyzed coupling of aromatic chlorides [45] and ring opening of cyclic oligomers [46]. The most common of these methods is aromatic nucleophilic displacement due to the availability of aromatic dihydroxy compounds and activated aromatic dihalo or dinitro compounds and the simplicity of the polymerization. A typical FTIR scan is shown in Figure 2.3 with all of the prominent peaks labeled with their appropriate groups.

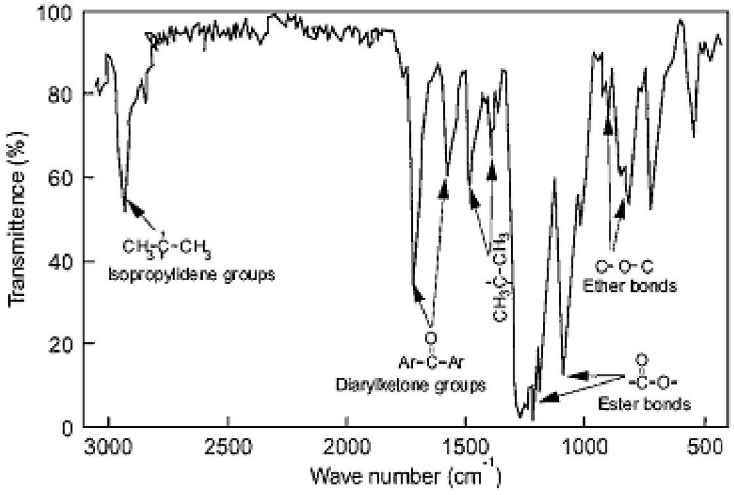

Figure 2.3: IR spectrum for PEEK [47]

2.3.2 Thermal and Mechanical Properties

PEEK is a semi-crystalline thermoplastic that is highly aromatic. It has excellent thermal and dimensional stability, flame retardance, high mechanical properties, minimal creep and good chemical resistance. It has a high continuous use and distortion temperatures. Its thermal properties have been thoroughly studied using DSC and are displayed in Table 2. Heating and cooling traces are displayed in Figure 2.4 [48, 49]. From these traces it can be noticed in the cooling scan that there exists a shoulder on the crystallization peak. It has been suggested that PEEK may undergo a two stage crystallization process depending upon the crystallization temperature. PEEK's mechanical properties are summarized in Table 2.2. PEEK and its composites are heavily utilized in aerospace, textile, food, automotive, electronic, medical and military applications.

Table 2.1: Thermal Properties of Victrex PEEK [50]

Victrex PEEK Thermal Properties	
T_g	143°C (289°F)
T_m	343°C (649°F)
Continuous Use Temperature	260°C (500°F)
Distortion Temperature	315°C (599°F)
Heat Transfer Coefficient	0.25 W/(m*K)
Coefficient of Linear Expansion	$1.7 \times 10^{-7} K^{-1}$

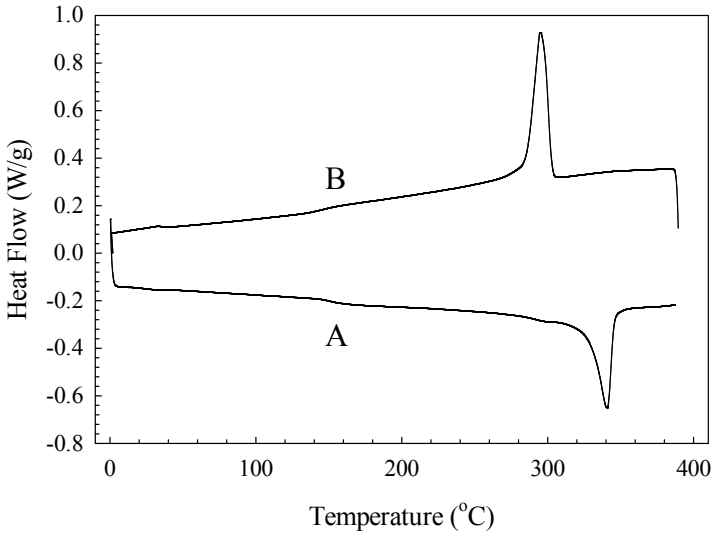

Figure 2.4: DSC thermograms of amorphous PEEK during heating (A) and cooling (B) at 10°C/min

Table 2.2: Mechanical Properties of neat Victrex PEEK [50]

PEEK Mechanical Properties	
Density	1300 kg/m^3
Young's Modulus	3700 MPa
Tensile Strength	90 MPa
Elongation at Break	50 %
Notch Impact Test	55 kJ/m^2

2.3.3 Crystallization and Morphology

The crystalline structure and strong backbone of PEEK give it high mechanical properties. X-ray diffraction patterns of unoriented films [51, 52], compression molded plaques [53, 54], oriented and annealed sheets [53], drawn fibers [54, 55], show that the

unit cell is orthorhombic and consists of two thirds of a repeat unit. A representation of the spherulitic growth is depicted in Figure 2.5. The dimensions of the unit cell are a = 0.775 to 0.788 nm, b = 0.586 to 0.594 nm and c = 0.988 to 1.007 nm.

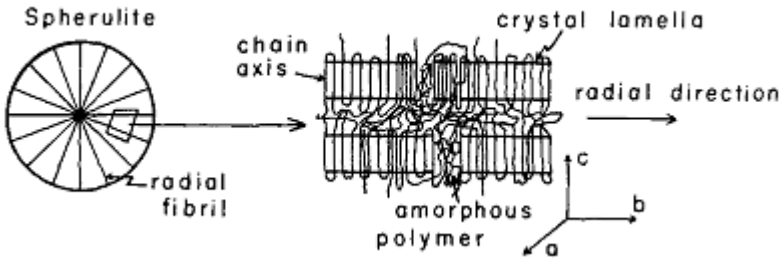

Figure 2.5: Representation of a spherulite [56]

The relation between mechanical properties of semi-crystalline polymers and their composites with crystalline structure and percent crystallinity has been extensively studied. Reviews by Cogswell [57] and others [56, 58] establish the connection of mechanical properties to crystalline morphology of PEEK. The addition of carbon fibers into the matrix stimulates nucleation and growth of crystallites perpendicular to the surfaces of the fibers and significantly affects the mechanical properties. These trans-crystallites improve the adhesion between the fiber and the matrix and significantly effects mechanical properties [59, 60]. The crystallinity of moldings is also a function of numerous other factors such as mold temperature, cooling rate, holding time and temperature and annealing [61-70].

2.4 Carbon Nanotubes (CNTs)

Carbon is known as one of the most versatile elements on the periodic table and readily shares its valence electrons to form stable compounds. It has six electrons surrounding its nucleus and four valence electrons in its outer shell. Diamond and graphite are commonly known crystalline forms of carbon that are created through different hybridization mechanisms. Diamond is formed through sp^3 hybridization into a tetrahedral structure with all valence electrons bonding leaving a structure that is extremely hard, thermally conductive, electrically insulative and clear. Graphite forms through sp^2 hybridization into a hexagonal network where only three valence electrons are bonded and the fourth forms π bonds with neighboring orbitals, giving graphite its conductive nature. While diamond and graphite were once considered the only two allotropic forms of solid state carbon, the discovery of fullerenes by Smalley and his coworkers [71] added another form to the list. Fullerenes, like graphite, form through sp^2 hybridization but form into spherical shapes, which are reminiscent of Buckminster Fullerene's architectural shapes or that of a soccer ball in their spherical form.

It was Iijimia's [1] discovery of the tubular form, nanotubes, that really excited the scientific world. Since then, the scale up of their production in the purest form possible and their incorporation into thousands of different composites has left industry searching for a way to fully incorporate their properties into composites as only minor improvements have been observed. While carbon nanotubes have been around for decades their complete utilization has not been achieved. The physical characteristics of

carbon nanotubes makes them attractive for many different applications from field emitters to biological probes. However, their agglomeration still limits their effectiveness in composites and heavy mixing has shown to breakdown the carbon nanotubes and decrease its properties.

CNTs are sheets of graphene rolled up and have extraordinary mechanical, electrical and thermal properties due to their physical structure and large aspect ratios (100-1000). While graphite is semi-metallic, CNT's can be either metallic or semi-conducting due to the topological defects from the fullerene end caps (pentagons in a hexagonal lattice) and the chirality or helicity [72]. The chirality or helicity of their structure depends on the orientation of the graphene, the relation of the benzene rings to the axis of the tube. CNTs whose benzene rings have a flat side perpendicular to the axis of the tube are designated as armchair and are metallic in nature. Those whose benzene rings have flat sides that are parallel to the axis are semi-metallic and all others have varying degrees of chirality and metallic properties. Armchair nanotubes have high electrical conductivity while zigzag nanotubes are only semi-conductors.

While carbon nanotubes are quite stable they are not chemically inert. Nanotubes can be oxidized [73, 74] and the tube can be opened by attacking the ends where the pentagonal defects are present. Table 2.3 is a summary of theoretical and experimental results for the physical properties of CNTs. There are numerous prototype procedures to produce CNTs, the ones that was very briefly discussed herein are those that have already been implemented commercially and whose products are currently being used in research.

The CNT synthesis methods that was briefly discussed herein are arc discharge, laser ablation, and chemical vapor deposition.

Table 2.3: Theoretical and experimental properties of carbon nanotubes [72, 75]

Property	**Value**	**Type**
Specific Gravity	0.8 g/cm3 1.8 g/cm3	SWNT MWNT
Elastic Modulus	1 Tpa 0.3-1 Tpa	SWNT MWNT
Strength	50-500 Gpa 10-60 Gpa	SWNT MWNT
Resistivity	5-50 μΩ cm	
Specific Surface Area	10-20 m2/g	

Arc discharge is literally the discharge of an arc between two carbon electrodes. The anode is brought to approximately 1mm away from the cathode and a current is then passed through the electrodes with temperatures reaching up to 4000 K [76]. CNTs form on the negative electrode but are contaminated with bucky balls and fullerenes. Arc discharge can be used to produce CNTs with or without catalysts to produce CNTs or SWNTs, respectively [77]. Research has shown that by varying the atmosphere contents and pressure, voltage and current that high yield, high purity nanotubes can be produced [78]. A consistency in the nanotubes is maintained by keeping constant power and varying the distance between the electrodes as the anode is consumed.

Laser ablation utilizes a metal catalyst (~ 1 wt%) in conjunction with a graphite composite and vaporizes graphite with a laser in an inert atmosphere and was first used

by Guo *et al.* [79]. As the target is vaporized a cloud of C_3, C_2 and C is formed. The vaporized material is then collected via condensation on a water cooled target with the low molecular weight carbon species combining to form larger molecules and almost always produces SWNTs. It has been documented that MWNTs are favored by pure graphite while a mixture of graphite and metal catalysts favor the synthesis of SWNTs [80]. The yield is approximately 70%, CNTs are entangled and the laser ablation process can be done at room temperature.

Thermal synthesis is a catalytic method and consists of chemical vapor deposition. Chemical vapor deposition is the use of a metal catalyst substrate and a carbon rich atmosphere that is constantly flowing over the substrate at specified pressure and temperature. Commonly used hydrocarbons are acetylene or ethylene and are decomposed in a reactor at temperatures from 550^{o}C to 750^{o}C and common catalysts are iron, nickel or cobalt [80]. Both MWNTs and SWNTs can be synthesized in this manner [81, 82].

2.5 Composite Processing of CNTs

Almost two decades after the discovery of CNTs and almost three decades after the discovery of CNFs their potential as a low loading filler has not been achieved. Due to their diameter and length they have a theoretically low percolation loading, which is inversely proportional to their aspect ratio [83]. Theoretical predictions [84, 85] and the increased mechanical performance of nanotube composites [86, 87] are promising. However, they form bundles and ropes that are difficult to break [88]. The ropes,

composed of bundles, are further intertwined and entangled with each other to form "spaghetti" or "rats nest" structures that are very difficult to disperse even under high shear. Since nanotubes are a rigid, high molecular weight material with strong attractive forces the entropy of mixing is low. While their dispersion is key to their success as a filler, care has to be taken to ensure that the structure of the tubes and fibers is retained during processing. Defects or breakages of the structures weaken their potential.

The attraction between CNTs is due to the highly polarizable, extended π electron system that gives rise to large van der Waals forces. When CNTs are incorporated into a polymer attractive forces between the CNTs also arise due to entropic factors [89, 90]. A lack of polymer in the colloids causes an osmotic pressure difference forcing the particles together. These attractive forces are further enhanced due to the geometry of the CNTs. Their lengths give them a long line of attraction when they are next to each other making their dispersion even more difficult.

A method to incorporate CNTs into a polymer matrix that completely disperses the agglomerated CNTs without producing any defects into the tubes and fibers has yet to be discovered. Three methods of incorporation have been heavily studied and they include solution processing, in-situ polymerization and melt processing. These are discussed in the following section and several good review papers on the topics exist [72, 91, 92]

2.5.1 Dispersion in Solvents, Surfactants and Functionalization

Solution processing from a scientific standpoint is very effective. Solvents such as amides, DMF and NMP [93, 94] and Lewis bases [95] have been shown to be effective in solvating CNTs but their reagglomeration on a time frame of days is still a problem. Mixing can be enhanced through some form of mechanical means such as stirring, sonication, shear mixing or even electro-spinning.

With the use of surfactants CNTs have been made soluble in water. The surfactants attach to the surface of the CNTs and allow them to form semi-stable, dispersed colloids [96-98]**.** The purpose of the surfactants is to create a steric repulsive force between the individual tubes and in turn disperse the bundles. While work with MWNTs [99] using a polyelectrolyte-surfactant dissolved the CNTs in organic solvents forming lamellar structures, the surfactant was not removable afterwards. Gong *et al.* used surfactants as wetting agents in an attempt to improve the thermomechanical properties of CNT/epoxy composites [100]. However, a homogeneous composite was not obtained.

Strong acid treatment has been shown to be effective in dispersing nanotubes but has also been shown to produce defects in the CNTs as well. Concentric, sulfuric and nitric acids can be used to cause chemical oxidation on the surface of the nanotube producing functional groups on the surface [101, 102]and intercalates between the nanotube bundles. During the process the ends of the CNTs are opened up and defects can form on the walls of the tubes. The oxidizing groups promote the attachment of organic and inorganic molecules to the surface to make the nanotubes soluble in the polymer matrix. After acid

treatment the nanotubes are dispersed in another fluid such as diluted ethanol [103]. Unfortunately, the tubes acquire defects during treatment that weakens their physical properties.

Surface functionalization of nanotubes is done in the hopes to overcome the intrinsic polarity of the graphitic structures by disrupting the π bonding system through defects. If the π bonding is decreased, the polarity and resulting van der Waals forces are reduced. Chen *et al.* [104] used thioylchlroride and octadecylamine to functionalize SWNTs and used solution phase near infrared spectroscopy to investigate them. Wong *et al.* [105] used amines to modify MWNTs by attaching them to the carboxyl group on the open ends of the nanotubes. Others have used poly(propionylethylenimine-co-ethylenimine) via amide linkages and poly(vinyl acetate-co-vinyl alcohol) via ester linkages making the functionalized nanotubes soluble in organic solvents [106, 107]. PMMA/nanotube composites have been processed where the nanotube π bonds were opened using AIBN [108]. The open π bonds allow the PMMA to attach to the tubes but the growth of the PMMA was restricted from the C-C bond it formed with the tube. Tang and Xu [109] synthesized poly(phenylacetylene) wrapped CNTs. These tubes were then soluble in several organic solvents and had improved photo-stabilization.

Glasglow *et al.*[110] noted that treatments such as etching in air near 400^{o}C, sulfuric, nitric and peracetic acid treatments can be used to make up to 25% of the fibers surface to be oxygen. While surface oxidatations of up to 4% showed an increase in tensile strength, further increases showed a decrease in tensile strength. Work by Lakshminarayanan *et al.*[111] used nitric acid to create micropores and allow the CNFs to be dispersed in water.

Lafdi *et al.*[112] showed an increase in tensile strength of 35% and an increase in modulus of 140% using highly oxidized tubes in epoxy composites at only a 4 wt% loading. Baek *et al.*[113] grafted aromatic ether-ketone to VGCFs through polycondensation. This was shown to increase dispersion and improve compatibility with aliphatic and aromatic matrices.

Unfortunately, solution processing is not a commercially viable method due to the heavy use of chemicals and the fact that it is a batch process. The required use of large amounts of solvents is environmentally unfriendly and it is difficult to find an efficient way to separate the mixture from the solvent after dispersion and mixing has taken place. Batch processes are very time consuming and therefore costly. The nanotubes are often the victim of defects after treatment and have lost a portion of their physical properties. Also, all of the above treatments are detrimental to the conductivity of the CNTs and are not used when high conductivity is warranted.

2.5.2 In-Situ Polymerization

This method also has great scientific merit and has seen substantial use in the compatibilization of different polymers or the preparation of polymers which are insoluble or thermally prohibitive of conventional processing methods. The CNTs and CNFs can be dispersed in the matrix mixture or solvent prior to polymerization allowing the polymerization to prohibit their re-agglomeration. This also chemically starts at the molecular level which gives the matrix a better chance of wetting or adhering to the walls of the CNTs and CNFs. Poly(phenylacetylene) (PPA) has been shown to make short

nanotubes soluble by helically wrapping around the tube during polymerization [109, 114]. Park *et al.* [115] and Wise *et al.* [116] used this method to disperse SWNTs in DMF and DMA to process polyamic acid by chemical and thermal imidization of thin films. The solution was found to be very stable and was unchanged for up to two years with refrigeration. Cochet *et al.* [117] synthesized polyaniline/MWNT composites. The site-selective interaction between the polymer and the nanotubes promoted charge transfer and improved the electrical properties. CNT composites of PMMA/MWNTs by Jia*et al.* [108], polyimide (PI)/SWNTs by Park *et al.* [118], PMMA/MWNTs by Velasco-Santos *et al.* [119] and liquid crystalline epoxy (LCE)/MWNT by in situ polymerization by Jang *et al.* [120] have all been done. PI/SWNT films were found to have over a 10 order of magnitude increase in conductivity at a 0.1 vol. % SWNT loading. PMMA/MWNT composites had an increase in the Young's modulus of 1135% at 1 wt% loading and the Tg was increased over 40^{o}C. For LCE/MWNT composites with a 1 wt% loading showed a decrease in the nematic phase transition temperature. This is due to the decrease in mobility with the incorporation of CNTs. Uchida *et al.*[121] studied poly(p-phenelyenebenzobisthiazole) (PBZT)/VGCNF in polyphosphoric acid and spun fibers by dry-jet wet spinning and dispersion. High orientation was achieved as seen through TEM. They also noted that the CNFs retained their length during processing. Unfortunately, this method is not commercially viable for the same reasons as solution processing. It is environmentally unfriendly and it is a batch process.

2.5.3 Melt Processing

Melt processing is the industry preferred method of compounding polymers. It has been around for an extended period of time and a wealth of knowledge and experimental data exists. It is a continuous, environmentally friendly and already exists. Melt mixing uses heat and shear to melt and then mix the composite. Screw designs can be tailored to individual applications to allow for varying degrees of mixing and to accommodate different matrix/filler combinations. Many studies have been conducted on the dispersion of CNTs and CNFs into commercial resins. CNT/polymer composites were initially reported by Ajayan *et al.* with their work on MWNT/epoxy systems [122]. Further work by Sadler *et al.* [123] showed a decrease in the electrical percolation and an increase in conductivity at 0.4 wt% loading but did not achieve complete dispersion and could even find agglomerates on the mm size scale. Many research projects have focused on PC/CNT composites [124-128]. Twin screw extruders were used in all of these studies and a moderate level of dispersion was found to occur. It has been coarsely estimated [129] that the van der Waals force when the CNTs contact each other is 10^4 J/m^3.The shear stress energy delivered to the agglomerates must be greater than this to overcome their mutual attraction. Work by Zeng *et al.*[130] used melt blending at concentrations of 5 and 10 wt% with two different grades of CNFs. Recent studies of PEEK composites with carbon nanofibers [131] were done at loadings up to 15wt%.

2.5.4 Mechanical Properties

In fiber reinforced systems the fiber provides the strength and stiffness while the matrix acts as linkages to transfer the load between the discrete fibers to create an enhanced network and also provides elastic energy absorption to protect the fibers from mechanical damage. The behavior of these composites is directly related to the loading level, surface to volume ratio of the filler, orientation of the filler, uniform dispersion of the filler within the matrix and is extremely dependent upon adhesion of the matrix to the filler. Extensive work on composites containing glass fibers and nanofibers has been done. Nanofibers and more specifically CNFs are interesting from a scientific point of view in that their mechanical properties are progressively more size dependant at their small dimensions. Other advantages of nanofibers are their limited degradation due to shear during processing that longer fibers, such as glass fibers, succumb to during conventional processing techniques, their increased surface area to volume ratio and excellent part surface finish.

Work by Sandler *et al.* [131] using a co-rotating twin screw extruder with a L/D ratio of 33 on PEEK nanocomposites prepared showed a 40 % increase in modulus, a 50 % increase in strength and no loss in yield strain but more than 75 % decrease in strain at break at a loading of 15 wt% CNF. However, it was noted that only a minimal decrease in strain at break was observed at loadings up to 10 wt% CNF. Work on HDPE/SWNT [132] nanotubes were dispersed in solution and then sprayed on HDPE and then dried and processed through a co-rotating twin screw extruder. The strength showed an increase of 65% and modulus increased 50% at a 2.6 wt% SWNT loading. Work on PET/MWNT

[133] found that the strength increased by 11 % and the modulus increased by 19% at a 2 wt% loading of MWNT. Work on Nylon/MWNTs showed a 300 % increase in the modulus and a 160 % increase in strength upon the addition of 2 wt% MWNT [134, 135]. PS/MWNT composite films synthesized by solution-evaporation method have shown a 25% increase in tensile modulus and break stress at a 1 wt% loading [136]. PVA/MWNT composites showed an 1.8 times increase in modulus and a 1.6 times increase in hardness [137]. Work by Zeng *et al.* [130] used melt blending of PMMA with two different grades of CNFs at concentrations of 5 and 10 wt%. With both fibers similar results were seen with an increase in modulus of more than 50% and an increase in compressive strength of more than 100% at the 5 wt% loading with no additional gains upon increased filler loadings. Work by Kruiger *et al.* [138] showed a 2.3 times increase in tensile strength at a 17 vol. % loading of CNFs in polypropylene nanocomposites. Further information can be found in reviews on CNT and CNF nanocomposites [72, 92, 139, 140]

2.5.5 Electrical Properties

Composite materials that have good electrical properties are highly sought after. Polymers are naturally insulating materials and a surface resistivity of $10^6 – 10^{10}\Omega$/square is required for electrostatic charge dissipation to occur [141]. Highly conductive materials can be used for electromagnetic shielding (EMI) and have conductivities above 10 S/m [142]. Carbon black and graphite have been used in the past to increase the electrical conductivity of the naturally insulative polymers. However, the volume fraction of filler needed to gain even moderate conductivity yields a very brittle material. CNTs and CNFs

with metallic or semi-metallic properties are sought after for their electrical conductivity that they can add to a composite at low loadings.

Studies on the electrical percolation threshold of nanotube fillers have found limits to be as low as a fraction of a percent and up to above 10 wt%. Studies done on PC/MWNT [126, 143] composites show the percolation from 1-2 wt% while studies on PC/SWNT [124] showed a percolation of less than 1 wt%. Other studies show PC/MWNT [144] percolation thresholds of up to 5 wt%. GE plastics [145] has used MWNTs in poly(phenylene oxide) (PPO) and polyamide blends (PPO/PA/MWNT) to replace micron sized fillers in order to decrease the loading for increased electrical conductivity without decreasing the mechanical properties that the 15 wt% loading of traditional fillers does. Coleman *et al.* [146] found a increase of 10 orders of magnitude in conductivity upon the addition of 8 wt% loading of WWNTs in poly(p-phenylenevinylene-co-dioctoxy-phenylenevinylene) composites. Work by Ghose *et al.* [147] showed that PETI-330 went from insulating, as a neat material, to electrically conductive with a 10 wt% loading of MWNT's. A further increase in CNTs showed minimal improvement in electrical conductivity. As can be seen there is a wide array of percolation thresholds throughout literature for the same composites. The complete dispersion of nanotubes would create a discontinuous network or conductive path and therefore the percolation would rise with dispersion [72, 148, 149] thus rendering a percolation due to levels of dispersion.

2.5.6 Thermal Properties

The addition of CNTs has been shown to increase the glass transition temperature, melting and thermal decomposition temperatures. These increased thermal properties are theorized to arise from two different mechanisms [137]. One reason is that the CNTs limit and constrain the motion of the molecules and chains of the matrix. Secondly, the CNTs act as nucleation sites and enhance polymer crystallization. Epoxy/MWNT composites have shown an increase in the T_g of 25^{o}C with a 1 wt% MWNT loading [100] while PMMA/MWNT composites have shown an increase of 40^{o}C with a 1wt% of SWNT loading [119]. Kashiwagi *et al.* [150] showed that PP/MWNT composites had an increase of 12^{o}C in the thermal decomposition temperature and that the MWNTs significantly reduced the heat release rate of PP at a 2 wt% loading, providing improved flame retardance. Biercuk *et al.*[151] found that the incorporation of 1 wt% SWNTs into an epoxy matrix increased the thermal conductivity by 70% at room temperature while Choi *et al.* [148] found an increase of 300% at a 3 wt%.

In studies on PEEK, Goyal *et al.*[152] showed a 500% increase in the storage modulus at 250^{o}C and an increase in T_g by 19^{o}C by incorporating aluminum nitride at loadings up to 70 wt%. These increased thermal properties are thought to be caused by the effect of increased and improved crystallinity due to the interactions between PEEK and the aluminum nitride. Sadler *et al.* [131] found that CNF's do not affect the T_g of composites even up to loadings of 15 wt%. An increase in the tan δ peak with increased filler content was observed but there was no shift in the peak. Work by Zeng *et al.*[130] used melt blending at concentrations of 5 and 10 wt% with two different grades of CNFs. A rise in

the onset of degradation temperature of almost 50^{o}C and an increase in Tg of 5^{o}C was observed.

2.5.7 Rheological Properties

While the dispersion of CNTs the desired goal of many researchers there are no reliable direct techniques to quantify dispersion. Electron microscopy only gives a narrow picture or field of view of a cut or fractured surface and is not sufficient in itself to verify complete dispersion. Reciprocal and global space techniques can be used to characterize dispersion but the results are very difficult to interpret [153]. What is important to note is that the rheology depends not only heavily on concentration but also on dispersion, behaving one way below its mechanical percolation and another way above its percolation [154]. This difference can be clearly seen in Figures 2.6 and 2.7. It has been shown that at low concentrations, homogeneously dispersed nanotubes in a polymer matrix are very stable and do not re-agglomerate (the matrix viscosity has to be sufficiently high enough to suppress Brownian motion). If these conditions are met the rheology remains like that of a viscous liquid with a steady-state viscosity and is a linear function of concentration.

The increase in the storage modulus with increasing filler content and dispersion is well documented in literature. At concentrations above the mechanical percolation an elastic gel of entangled tubes is seen in the dispersed state. This gives a rubber like G' at the lower frequencies for high concentrations. These behaviors can be seen in Figure 2.12.

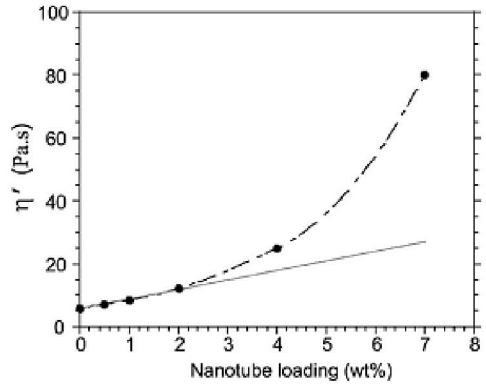

Figure 2.6: Dynamic viscosity versus CNT loading in a PDMS matrix measured at 50 Hz The solid line depicts the non-interacting system and dashed line represents the entangled system [154].

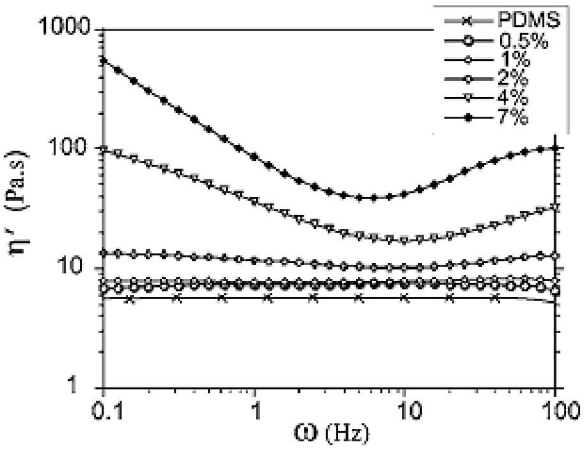

Figure 2.7: Dynamic viscosity versus frequency for well-dispersed samples of different concentrations [154].

The rheological data is also an indication of how a material behaves during melt processing operations such as injection molding. Since the rheological parameters are sensitive to filler size, shape and dispersion, it can be used as a method to elucidate the degree of dispersion for most fillers. It has been shown that the non-linear response and

viscoelasticity of materials is highly sensitive to changes in chemistry and filler and provides distinguishable differences at the mesoscopic level.

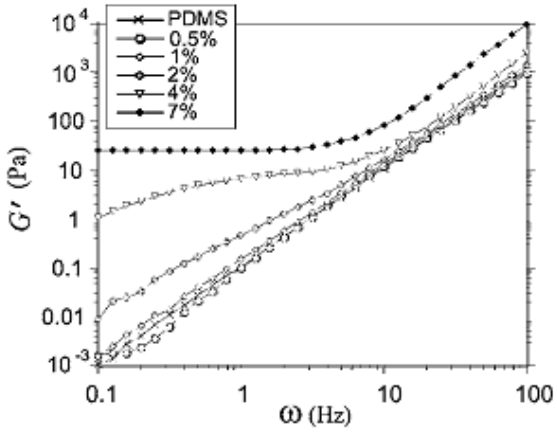

Figure 2.8: Storage modulus versus frequency for well dispersed CNT composites at different loadings [154]

2.6 Ultrasound

The term "ultrasound" denotes a range of frequencies that are above the scope of human hearing which is at frequencies above 18 kHz [155]. These waves are characterized by the frequency and amplitude at which they propagate. When applied to a medium a wave propagates through the material as an acoustical wave that is a series of longitudinal compressions and refractions, that produce corresponding contraction-extension stresses that cause localized pressure variances throughout the medium. These alternating positive and negative pressure variations have a significant effect on the extensive and intensive properties of the system. Energy is absorbed into the system

through vibrations of the molecular structure. Ultrasound is commonly used in ultrasonic welding of plastics, ultrasonic cleaning and mixing baths, medical imaging and chemical analysis.

Cavitation has been used to describe the phenomena of bubble dynamics and is commonly used to refer to their growth and collapse. In the broad sense of the word it is defined as, “the formation and activity of bubbles or cavities in a liquid," [156]. Cavitation is caused by a reduction in pressure which allows a bubble grow by bringing in low molecular weight fluid, gas or vapor. This low molecular weight fluid provides the substance within the bubble or cavity that allows for its existence. While the presence of bubbles facilitates cavitation it is possible for cavitation to occur in gas-free liquids. The formation of new bubbles can occur when the imposed acoustic pressure amplitude exceeds that hydrostatic pressure in the liquid causing a break in the cohesive forces between molecules and the creation of a void. These voids are likely to be induced at interfaces between mediums, at defect sites and density fluctuations within the medium. Bubbles in all of the aforementioned cases can reach a critical size such that the low molecular weight fluid within the cavity can no longer support the pressure of the forces of the fluid in which it exists and the bubble violently collapses upon itself instantaneously releasing a comparatively large amount of energy. This intense shock wave has the ability to cause scission of macromolecules and degradation.

Common causes of cavitation are hydrodynamic, acoustic, optic and particle cavitation. These are pressure variations caused by fluid flow, sound waves, high intensity light rupturing and particle collision, respectively. The use of ultrasound to

induce cavitation in viscous and solid polymers dates back over half a century. Original investigations saw a decrease in the polymers viscosity, molecular weight and its distribution [157].

Early research on the effects of cavitation on fluids determined that it was due to viscous losses in the fluid, with cavitation not occurring in solutions with a viscosity greater than 2 Pa-s [158]. However, common theory also led to the idea that cavitation in polymer melts could occur when the acoustic pressure exceeds the triaxial tensile strength of the material. It was experimentally determined that the long term strength of a polymer such as polybutadiene (viscosity of 10^6 Pa-s) with a narrow molecular weight distribution in triaxial stretching is less than 1 MPa [157]. When considering the magnitude, it is comparable to materials of low viscosity, such as water. Therefore, theoretically, it can be expected to see cavitation in molten polymers; however, the effects of viscoelasticity have to be taken into account. This was first seen in the early 80's [159]. Work showed the formation of bubbles with ultrasonic treatment at a frequency of 17.8 kHz at amplitudes ranging from 0 to 15 microns [157]. In Figures 2.9 and 2.10 the ultrasonic scheme as well as the pictures taken of the cavitating fields are displayed, respectively. Other devices have also been used to verify the existence of cavitation by using a microphone to verify the sound given off from the collapse of the bubbles.

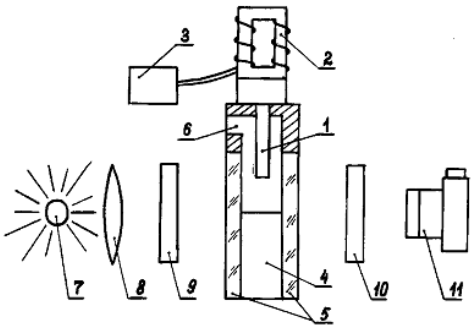

Figure 2.9: Schematic of the setup used to validate cavitation in viscous polymer melts (1:Ultrasonic wave guide, 2:Transducer, 3:Ultrasonic Generator, 4:Slotted Capillary, 5:Transparent walls of cavity, 6:Inlet, 7:Source of Light, 8:Condenser, 9:Polarizer, 10:Analyzer, 11:Camera) [157]

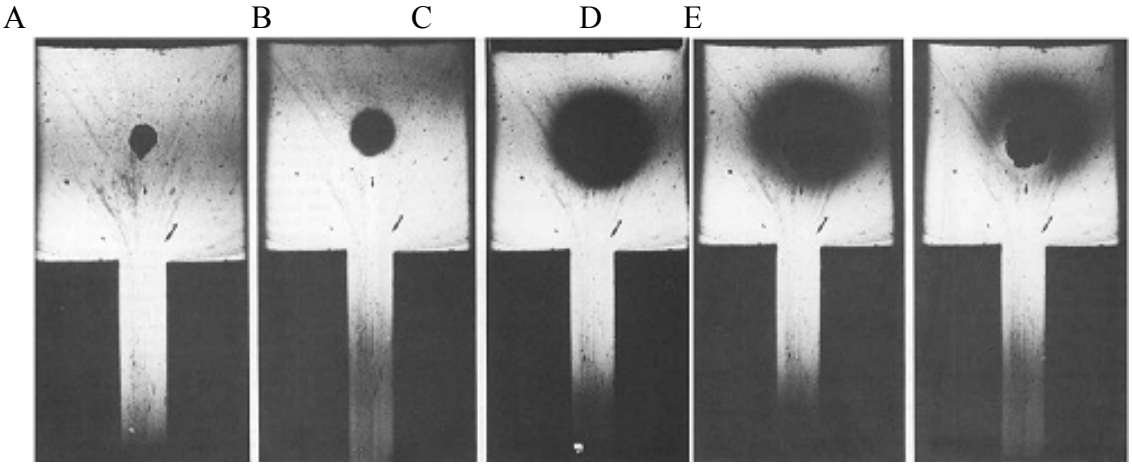

Figure 2.10: The formation and cavitation of bubbles around a piece of unvulcanized rubber (A, B, C) in an acoustic field and its disappearance (D, E) upon taking away the ultrasonic source [157]

2.6.1 Ultrasonic Studies on Composites

The effects of ultrasound on polymer solutions and composites have been widely studied. Most of the observed effects are those of degradation. The majority of work has

focused on low viscosity polymers, such as in chemical reactions, and the devulcanization of rubber, applied in the solid state. Sonochemical synthesis has been shown to initiate reactions and polymerizations [160], reduce agglomerations [161] and create more uniform molecular weight distributions [162] all in static conditions. Studies also showed that degradation proceeds faster at higher molecular weights [163, 164]. These changes were elucidated to be the breaking of the macromolecular chains. The cleavage of these chains has been shown to commonly occur near the center of the chain [165, 166] versus at random such as in thermal, photo or chemical degradation.

Ultrasound has been used to improve the compatibility and interfacial adhesion of immiscible blends [167]. The application of ultrasound can result in hemolytic chain cleavage and decreased molecular weight [162]. Hong and Isayev [168] used ultrasound on blends of HDPE and GRT. Their work showed that blends ultrasonically treated had enhanced tensile and impact properties compared to blends where only the GRT was treated and then blended with the HDPE. Oh *et al.* [169] used ultrasonically assisted process for the in situ compatibilization of PP/NR blends. The blends that were ultrasonically treated showed a significant improvement in mechanical properties compared to the untreated blends. Further investigation revealed that a decrease in domain size and better adhesion at the interface lead to the improvement in properties. Further work on PP/PA6 blends [170] showed up to a 100 percent increase in tensile toughness and impact strength for certain treated blend ratios. While there appears to be competition between compatibilization and degradation, a large net benefit can be obtained at certain processing conditions. A patent on this technology does exist [171].

The effect of ultrasound on the devulcanization of rubber during extrusion has been studied for over two decades with the majority of work done by Isayev and co-workers. During the devulcanization process sulfur and peroxide bonds are broken while minimal C-C bonds are broken, which is important for property retention in the revulcanized material. It is believed that the devulcanization process is due to cavitations in the vulcanized solid rubber particles. It has been experimentally verified that bubbles are created during static ultrasonic treatment [172, 173]. Cavitation can be initiated in voids, cavities, density fluctuations and at interfaces.

Isayev and co-workers have proven the usefulness of ultrasonic treatment as a fast and solvent free way of recycling tire rubber. Work on ground tire rubber and sulfur cured rubber [174-179], natural rubber [180], silicone rubber [181], ethylene propylene diene monomer (EPDM) rubbers [182] and blends of thermoplastics and rubber [183] have been carried out. Through these studies it was determined that ultrasound not only led to the breakup of the three dimensional networks that existed within the cured systems but also led to the cleavage of some C-C bonds as well. The properties of the revulcanized materials are dependent upon these two competing effects and optimized processing conditions are determined experimentally for the desired properties.

Ultrasound has also been applied to filled polymer systems. The complete dispersion of fillers and strong adhesion between the filler and the matrix are both required to enhance and not reduce the properties of the system. Fillers that are not adequately dispersed can become stress concentrators and fillers that have no adhesion to the system do not add anything for the space that they consume and therefore reduce the mechanical

properties. Ultrasonically assisted dispersion has been applied to both solution batch and continuous processes. Batch studies include polystyrene/nickel [184], polyaniline/silica [185] and. Koshio *et al.* [186] used ultrasound to disperse SWNTs in monochlorobenzene (MCB) and polymethylmethacrylate (PMMA). They noted that hot spots caused by cavitation resulted in the reaction between the SWNTs and the organic molecules but that the MCB and PMMA degraded while the SWNTs incurred defect sites with the use of ultrasound [186, 187]. Continuous processes on polypropylene/clay composites done by Lapshin and Isayev [188] and HDPE/clay composites by Swain and Isayev[189] have also been done. They showed that by applying ultrasound to a nano-clay polypropylene composite in the melt state that nano-clay gallery spacing can be increased by 40%. Swain and Isayev [189] verified the use of ultrasound on nano-clay composites by applying ultrasound to high density polyethylene/nano-clay composites. Treated samples showed enhanced mechanical properties in elongation at break and toughness. In EPDM/silica systems Isayev and co-workers used ultrasound to aid dispersion and saw over a 50% decrease in silica particle size [190].

2.6.2 Pressure Dependence

Studies have shown that pressure plays a significant role in the formation of voids and cavitation leading to the dispersion of agglomerates in a viscous fluid. Work by Yashin *et al.* [191] showed the variation in void radius that occurred under static ultrasonic treatment and related it to the observed power consumption during continuous processing conditions. As can be seen in Figure 2.11, it was observed that the relative radius of the voids decreased with increasing static pressure and that the power consumption increased

with increasing pressure during the continuous process. This is intuitive in that the ultrasonic wave can be more efficiently transferred into a denser material leading to increased power consumption and decreased relative radius.

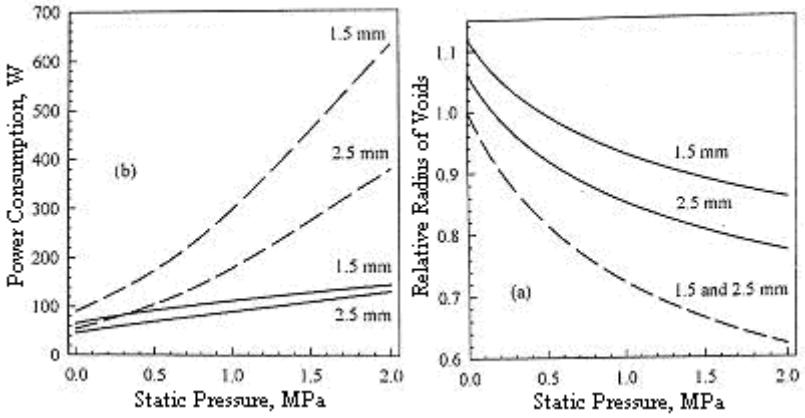

Figure 2.11: Approximation of void size showing the approximated non-linear effects (Dashed lines: linear approximation, Solid lines: second-order approximation) for relative void radius (a) and power consumption (b) versus static pressure for an amplitude of 10 μm for samples of 1.5 and 2 mm thick [191]

Suetsugu and Sato [192] did work on the dispersion of TiO_2 in polystyrene and polycarbonate showed that there exists a relationship between the pressure and viscosity at which dispersion and/or cavitation in the polymer exists. As can be seen in Figure 2.12, three very distinct regions exist. Region A represents conditions where cavitation and dispersion co-exist upon ultrasonic treatment, Region B the conditions where dispersion with no cavitation exists during treatment and Region C the conditions where no dispersion or cavitation exists with treatment. These areas relate to the required conditions for cavitation to occur. For bubble growth and energy transfer the medium that

is being treated has to be sufficiently viscous or under pressure but not to the extent that there exists so much force that the bubble growth is inhibited.

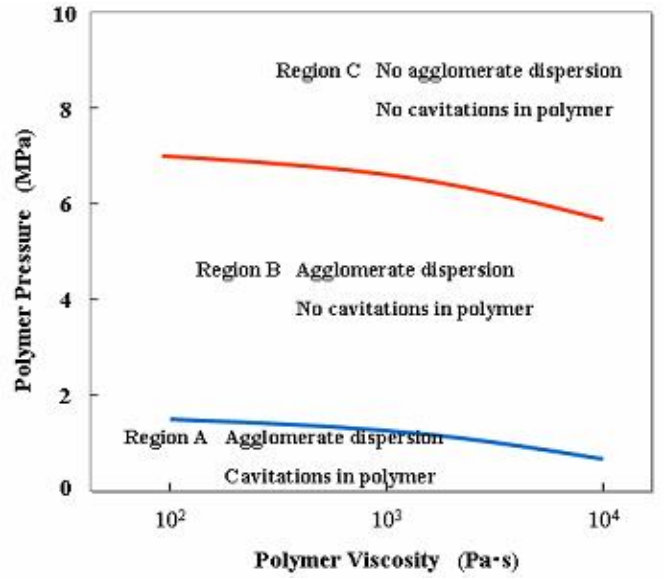

Figure 2.12: Experimental processing conditions for pressure and viscosity to induce cavitation in concentrated TiO_2 filled PS at 7 µm and 19 kHz [192]

In conclusion, to date there does not exist a process that is efficient in both the dispersion of CNT and CNF bundles and processing of composites, is environmentally friendly or that can be scaled up for commercial processing.

2.7 Resin Transfer Molding

Resin Transfer Molding (RTM) is a processing method commonly used in the manufacturing of thermoset composites in conjunction with a fiber preform and is under the broader category of liquid composite molding. It is adaptable, inexpensive and

commonly used in the aerospace industry. It is a highly flexible process and can accommodate virtually any shape or design. Most parts have a large aspect ratio or so called thin shell geometry referring to the part having a thickness that is very small compared to its other dimensions [193, 194].

RTM is a complex process that has to incorporate the rheological and cure behavior of the resin as well as the design of the anisotropic woven fiber preform into the design and layout of the part. The resin is infused into the fiber preform filled heated mold under relatively low pressures and velocity. Care is taken to ensure that merging flow fronts and curing do not leave trapped air or voids within the fiber preform or part. The heated mold initiates the curing of the resin which proceeds to completion. RTM is a highly nonisothermal process and has to account for conduction and convection from the mold and fiber preform to the resin as well as the exothermic reaction of curing. Since the filling is dependent upon viscosity and the viscosity is extremely sensitive to changes in temperature and degree of curing, modeling the process can be quite difficult. Control volume finite element methods have been developed but constant modifications have increased accuracy and decreased computational time. This section will discuss RTM and variations in the method, advantages and disadvantages in these processes and one current theory used for the simulation and optimization of these processes.

RTM has four basic steps [39, 195]. First, a fiber pre-form is placed into a heated mold and the mold is closed. Second, the pre-polymer or resin is then injected into the mold at a very low viscosity, less than 10 poise, and impregnates the fiber pre-form and fills the mold. The pre-polymer then goes through the third step of an optimized cure

cycle with predefined time-temperature periods. The last step is the removal of the part. Due to the complexities incurred in the impregnation of the fiber pre-form and the curing of the thermoset, optimizing the RTM cycle is very difficult. Flow into the fiber preform is difficult and trapped air as well as voids from curing are common problems. The large differences between RTM and conventional injection molding leave RTM in a category of its own and few similarities exist between RTM and other processing methods.

Fiber preforms can be directionally aligned to tailor the parts strength according to its application. Design of the preform is very extensive. Fibers have to be woven such that the 3D structure incorporates the desired finished part property requirements (strength, impact resistance, delamination resistance) while still allowing maximum processability (minimized resistance to flow, compressibility, minimized trapped air, flow during curing to minimize voids). Figure 2.13 shows the complexity of the weaves used in RTM [196].

The production of the preform can be the most costly part of the process. For small scale, non-production, and very large pieces the preform are often built by hand with layers of fibers being cut and stacked manually. It is a delicate art form that requires much experience and expertise in the field. Mechanical devices have been developed to produce both production preforms as well unique preform pieces.

To be able to impregnate the woven pre-form, injection times in RTM are on the order of minutes and comparatively low pressures are used to fill the mold. Vents are optimally placed in the areas of the mold that fill last. The heated mold and preform are often at a temperature differing from that of the polymer. This non-isothermal flow process

A B

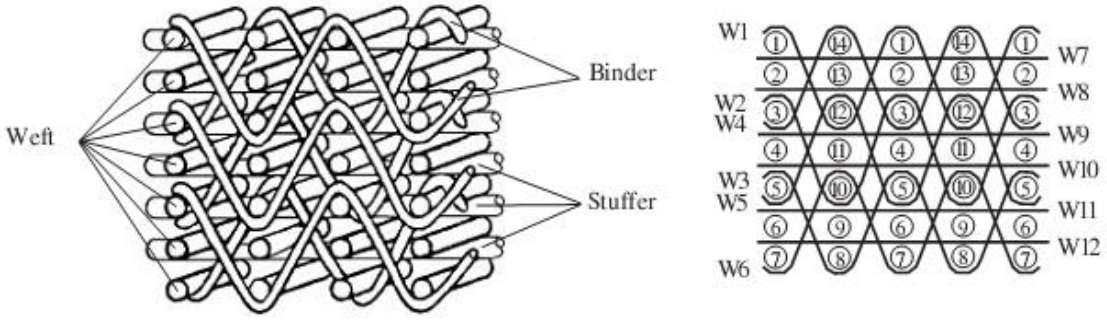

Figure 2.13: 3D (A) and 2D (B) images of a woven fiber preform [196]

temperature differing from that of the polymer. This non-isothermal flow process transfers heat from the mold and the preform to the polymer matrix. As the heat is transferred, curing begins and the resin's viscosity begins to increase. The curing or crosslinking of the matrix is highly exothermic and heat transfer changes dramatically. As the resin continues to cure the viscosity goes to that of a gel and then goes to infinity as it solidifies. An optimized curing cycle will often incorporate curing into the injection period to minimize the time of the complete cycle. However, care has to be taken to ensure that the curing polymer, with its increased viscosity, does not interfere with thoroughly impregnating the fiber preform and filling the mold, creating voids or dry spots.

RTM is a process that has been modified in many ways to try to enhance the properties of its products and to minimize the problems inherent in its design. Modified

methods include Vacuum Assisted Resin Transfer Molding (VARTM) and Flow Flooding Chamber Method (FFCM). These methods as well as many other methods are utilizing negative pressure and flow chambers to enhance the flow of the resin into the mold and preform while also promoting escape of the air to minimize dry spots. Some additional steps have also been tried to ease the complexity of the process. Pre-stamping of a fiber preform with a thermoplastic binder, which can be softened before stamping and then cooled again to retain its shape, has been implemented to save on the time intensive process of laying up the fiber preform by hand. More directional fiber layers can then be added to the stamped preform to directionally enhance the mechanical properties. Three dimensional fiber weaving is another advancement upon that of the stamped fiber preform. Tailored weaves can enhance mechanical properties as well as ease flow and processing problems. By using machines to do the weaving, repeatability increases while cost and time decrease.

There are many advantages to RTM. The mechanical properties of the part can be precisely controlled. Through fiber orientation during the preform weave and/or layup direction properties can be tailored for the specific application. The fiber orientation does not change during processing as in other processes, such as compression molding. The cycle time is less than other comparable processes. Due to the relatively low pressures, molds and tooling are made at minimal costs, lead times are minimal and for trials and/or small runs, epoxy can be used to create tooling. Inserts can easily be incorporated into the mold and since it is a non-abrasive process, tooling has a long life span.

Due to the complexity of the process there are difficulties in RTM. Mold filling depends on part geometry, where the injection gates are located, flow rate, injection pressure, vent location, how reactive the matrix is and what the weave of the fiber preform is. Multiple gates are often required to fill the mold in an appropriate time frame but care has to be taken so that air does not become trapped between the merging melt fronts. Questions arise such as should the flow be kept at a constant rate or should it be kept at a constant pressure? Other problems exist in monitoring the process while it is going on. How do you detect if the part is fully filled, how do you determine the overall temperature throughout the piece and accommodate rapidly for thermal changes? These issues can be very costly to determine using trial and error technique. Modeling of resin transfer molding is very important and almost necessary when optimizing the RTM processes if part to part reproducibility is to be achieved. However, there are numerous issues that have to be dealt with when modeling these systems. Since the matrix polymer has to flow through the woven fiber preform the tightness of the weave, trapped air, capillary effects and surface tension effects have to be taken into account along with the usually thin shell geometry of the overall part, curing rates and the effect of temperature changes during shearing and conduction through the mold walls and fiber preform.

The non-isothermal conditions in which the mold filling takes place is quite important. The injected resin is usually much cooler than the mold, to prevent premature curing prior to injection. Heat transfer from the mold to the resin, heat transfer from the fiber preform, which is assumed to be the same temperature as the mold, to the resin and the exothermic reaction that usually occurs as the resin cures has to be understood. Heat

transfer cannot be simplified using the standard one dimension approach of thin parts. The modeling of heat transfer in RTM parts has to incorporate the conduction in the thickness direction and convection in the flow direction as well as the heat generation from the curing. If a part cures unevenly then warpage can result. Understanding the complete heat transfer gives engineers and designers the ability to predict premature curing, appropriate amount of injection sites, rate of injection of the matrix and the temperature scheme needed to optimize the RTM process. Significant efforts in solving these problems have been made [197, 198].

2.8 Environmental Impact

While the quest for superior composites remains at the fore front of this research, the health and safety of the researcher and others in the vicinity of the research going on are of utmost importance. CNTs are inevitably released into the air during material handling, feeding and composite processing. Respirators are used to avoid inhalation of the nanostructures as research is beginning to suggest the adverse effects of these nanomaterials on living organisms. Therefore, it is important to investigate the effectiveness of different respirators at capturing and preventing the inhalation of these airborne nanostructures and a portion of this work investigated the ability of various respirators to prevent the permeation of CNTs during respirator use in a nanorich environment.

2.9 Summary of Literature Review and Objectives

No environmentally friendly, cost effective and readily scalable process for the homogenous dispersion of carbon nanotubes was found in literature. The main objective of this work is to develop a continuous, commercial and environmentally friendly process for the complete dispersion of CNTs into high temperature, high performance polymer matrices of PETI-330, a thermoset, and PEEK, a thermoplastic. The effects of ultrasonic amplitude and concentration on the dispersion of CNTs as well as the point of treatment have been investigated. Processed nanocomposites have been characterized for rheological mechanical, electrical, thermal and morphological properties.
PETI-330 is a new thermoset material and the curing parameters of resin transfer molded plaques is still under investigation. A non-isothermal cure kinetics model for PETI-330was developed that takes into account the entire time-temperature cure history. This model has been vetted experimentally to verify its accuracy.

A resin transfer molding system for manufacturing PETI/carbon fabric composite plaques was designed and manufactured in collaboration with NASA Langley. The manufactured panels were tested for void fraction and fiber content. The composite plaques were also tested for mechanical properties under various thermal conditions and compared against vacuum assisted resin transfer molded plaques.

While CNTs have been the topic of interest for several years in the academic environment, much is to be learned on their environmental containment and the practice of appropriate health and safety. A portion of this research was the investigation of the

effectiveness of commercially available respirators in a carbon nanotube rich environment. A testing machine was developed and various respirators were tested.

CHAPTER III

EXPERIMENTAL METHODS

3.1 Introduction

This chapter will detail the materials used and their characteristics, the experimental methods and characterizations used in the production and characterization of the nanocomposites, cure kinetics evaluation and environmental testing studies.

3.2 Materials

High temperature, high performance thermoplastic and thermoset resin matrices were studied in this research. Polyetheretherketone (PEEK) grades 450PF and 380P, thermoplastic resins in powder form produced by ICI under the tradename Victrex, and a phenylethynyl terminated imide (PETI) oligomer developed at NASA Langley Research

Table 3.1: Manufacture listed properties of PEEK [50] and PETI-330 [199]

Property	**PEEK**	**PETI-330**
Tensile Strength (MPa)	90	118
Tensile Modulus (GPa)	3.7	2.7
Elongation at Break (%)	30	8
Glass Transition (°C)	143	330
Specific Gravity	1.3	1.3
Volume Resistivity (Ohm-cm)	$>10^{16}$	$>10^{16}$

Center [27] and licensed to Ube Industries and produced under the trade name PETI-330, were used. The properties of PEEK and PETI-330 are listed in Tables 3.1 and 3.2, respectively.

Two different suppliers were used to obtain multi-wall carbon nanotubes (CNTs). A regularly entangled grade was obtained from Nanostructured and Amorphous Materials Inc., Houston, TX. These nanotubes have outside diameters of 10-20 nm, inside diameters of 5-10 nm and lengths of 0.5-200 μm. Multi-wall nanotubes have a specific surface area (SSA) >200 m^2/g and a bulk density of 0.04-0.05 g/cm^3 with an actual density of ~2.1 g/cm^3. A HRSEM micrograph taken of the obtained CNTs is shown in Figure 3.1. These materials were used for the PETI-330/CNT research work and have a C-purity of >95%. Additional CNTs were obtained from Bayer Scientific. Baytubes C150P are agglomerates of multi-walled CNTs with a C-purity of >95%, outside

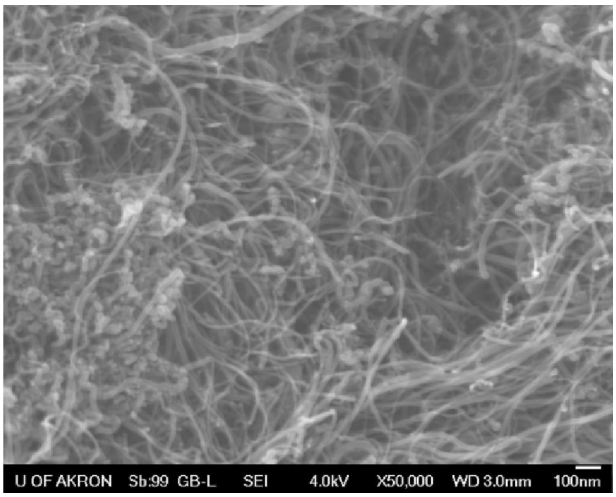

Figure 3.1: HRSEM of CNTs that were obtained from Nanostructured and Amorphous Materials.

diameters of 13-16 nm, inside diameters of 2-6 nm and lengths of 1-10 μm with a bulk density of 0.14-0.16 g/cm^3. Its BET surface area is 230 m^2/g. Manufacture supplied micrographs are shown in Figure 3.2.

For high temperature resin transfer molding experiments two different polymer matrices, three different carbon fabrics and 1 breather cloth were used. The two resins were used as received. PETI-330 resin was obtained from UBE Chemicals Ltd, Japan and PETI-8 resin was obtained from Imitec Inc., Schenectady, NY, USA. The resins came in a yellowish, powder form. Three different carbon fabrics were obtained from Textile

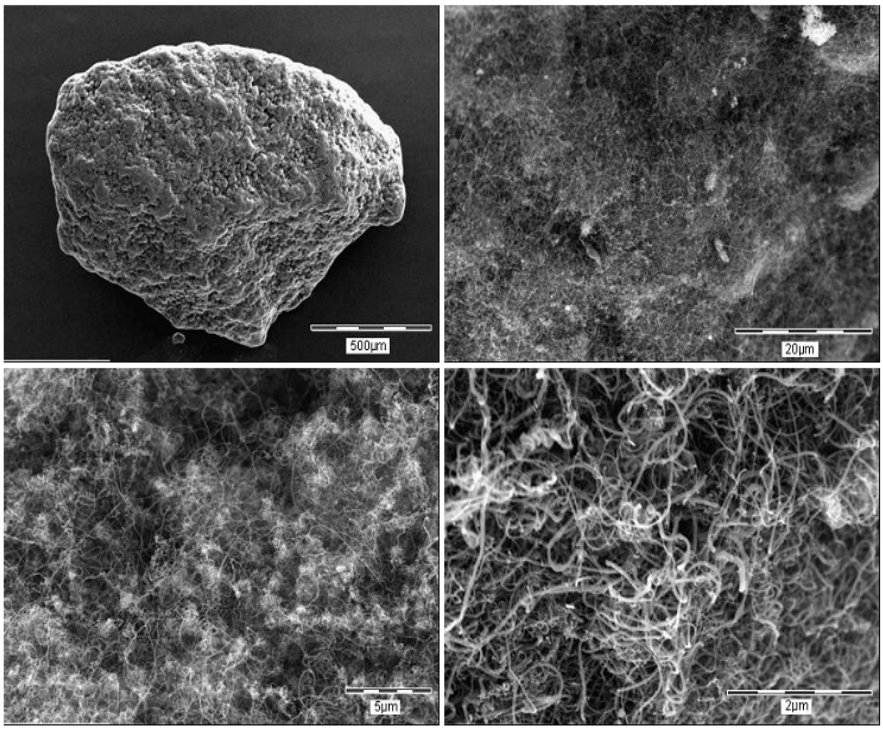

Figure 3.2: SEM of MWNTs C150P that were purchased from Bayer Scientific Materials [200]

Table 3.2: Properties of the Carbon Fabrics used in HT-RTM [201]

Carbon Fabric	Sizing	Areal Weight	Weave
IM7-6K	GP	280 g/m^2	5-harness Satin Weave
T650-35-3K	309	366 g/m^2	8-harness Satin Weave
IM7-6K	GP	160 g/m^2	Unidirectional Weave, Stick String 450 1/0 fill fiber

Products, Inc., Anaheim, CA. They are listed in Table 3.2. A breather fabric was used on the top and bottom of the plaque, ReleaseEase^{TM} fabric, to facilitate venting and flow. A sealant was used around the edges of the mold, General Sealant A-800-3G from Airtech Europe Sarl (Differdange, Luxembourg) through the thickness of the plaques to prevent jetting of the low viscosity PETI materials.

3.3 Experimental

The experimental methods of manufacturing and testing of the nanocomposites, resin transfer molding plaques, and respirators is detailed in the following sections.

3.3.1 Cure Kinetics Evaluation

Phenylethynyl terminated imide oligomer in powder form was obtained from Ube industries under the trade name PETI-330 and was used as received. This oligomer is based on 2,3,3',4' –biphenyltetracarboxylicdianhydride (a-BPDA), by Ube Industries.

A Carver 11 ton high temperature compression molding press (CARVER 4122, Wabsah, IN) was used to compression mold PETI-330 into 25mm diameter compacted discs at a temperature of 180^{o}C and force of 7 tons for ARES. The temperature trace of the press was measured. Compression molded slabs were also prepared with different

curing times. In order to halt curing, the slabs were quickly removed from the press and immediately quenched in ice water.

The rheological properties were measured using an ARES, TA Instruments, described in section 3.4.1. Two compacted discs were placed between the plates, melted and then squeezed to 1.5 mm. Excess material from around the plates was removed by a razor blade. Testing was conducted using 25 mm parallel plate geometry in oscillatory shear at a strain amplitude of 2% at fixed temperatures and over a temperature sweep of 4^{o}C/min.

Differential Scanning Calorimetry (DSC) was performed on a TA Instruments model Q2920, described in detail in section 3.4.2. Heating rates of 2.5, 5, 10 and 20^{o}C/min were used on samples of sizes of at most 10 mg sealed in aluminum pans with an empty pan for reference. A pure indium sample was used to calibrate both the temperature scale and enthalpy values before testing samples. Specimens were taken from the plaques to determine the degree of cure. Each specimen was carefully taken along the entire thickness of the molded samples.

3.3.2 Nanocomposite Preparation

An ultrasonically assisted, co-rotating, twin screw micro-compounder (PRISM USALAB 16, Thermo Electron Corp. UK) was used to compound all nanocomposites. The micro-compounder has a screw diameter of 16 mm and an L/D of 25. The matrix is fed into the throat of the extruder at feed port 1. To avoid the high stresses in the feeding zone, the CNT are fed separately downstream at a point where the matrix has already melted, between the first and second sets of kneading blocks shown in Figure 3.3 as feed

port 2. The composite material then passes through additional mixing and ultrasonic treatment zones for the dispersion of the CNTs.

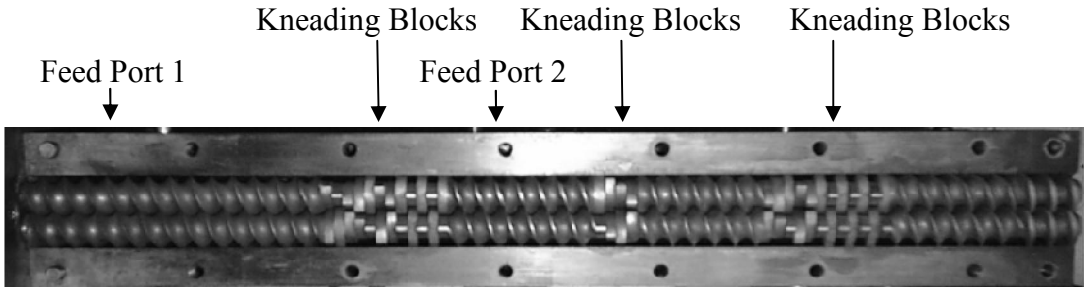

Figure 3.3: Photograph of extruder screw configuration showing points of feed for matrix and nanotubes and mixing zones.

Two different ultrasonically assisted extrusion configuration were developed and studied in this research. The first ultrasonically assisted extrusion design, design A, is depicted in Figure 3.4. In this design the composite material exits the extruder and enters a die. This die consists of two ultrasonic horns directly opposed to each other located on either side of the melt with a flow channel that has a cross-section of 4 mm thick by 19 mm wide that is 114 mm long (0.157 x 0.75 x 4.5 in^3). The ultrasonic systems (Branson Ultrasonic Corp., CT, USA) have a maximum power supply with a maximum output of 800 W and converter that operates at 40 kHz. The horns have a 19 mm x 19 mm (0.75 x 0.75 in^2) area that contacts the polymer melt and are situated in the middle of the die section directly in line with each other on opposing sides of the melt. On both sides of the top ultrasonic system a pressure transducer/thermocouple has been installed to measure pressure and temperature before and after ultrasonic treatment. The horns are internally cooled using a constant flow water bath set at 95°C. The screw stack up was as follows:

starting at the feed throat: 7 - 1 L/D forward conveying, 6 - 1/4 L/D forward conveying kneading blocks with each block rotated 30 degrees from the last, 6 - 1/4 L/D neutral conveying kneading blocks with each block rotated 90 degrees from the last,4 - 1 L/D forward conveying, 4 - 1/4 L/D forward conveying kneading blocks with each block rotated 30 degrees from the last,3 - 1 L/D forward conveying, 4 - 1/4 L/D forward conveying kneading blocks with each block rotated 30 degrees from the last, 6 - 1/4 L/D neutral conveying kneading blocks with each block rotated 90 degrees from the last,3 - 1 L/D forward conveying, 1 - 1.5 L/D forward pumping. This technology is covered under US patent application WO2007145918 A3.

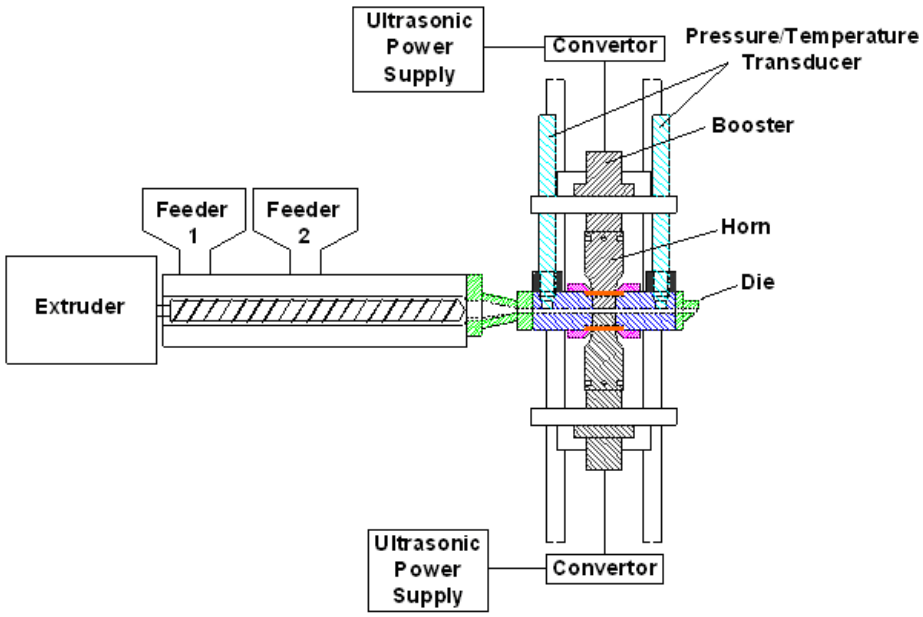

Figure 3.4: Micro-compounder with attached ultrasonic slit die - design A

The second ultrasonically assisted extrusion design, design B, was developed by modifying the extruder to incorporate the ultrasonic section within the extruder barrel as seen in Figure 3.5. In this design, after the nanotubes have been added to the molten polymer the composite material passes through one mixing zone and then is channeled to the top of the screws to pass through the ultrasonic treatment zone. Pressure transducers were incorporated before and after the ultrasonic treatment section. After treatment, the composite material passes through an additional mixing zone and then exits the extruder. This design provides many advantages over the initial design. First, the composite experiences ultrasonic treatment and shearing due to screw rotation simultaneously. This provides enhanced dispersion and distribution of the CNTs simultaneously for a more uniform composite. Also, by avoiding the added die section at the end of the extruder, less pressure is needed to pump the composite material and a shorter thermal history is experienced. The screw stack up was as follows starting at the feed throat: 7 - 1 L/D forward conveying, 5 - 1/4 L/D forward conveying kneading blocks with each block rotated 30 degrees from the last, 4 - 1/4 L/D neutral conveying kneading blocks with each block rotated 90 degrees from the last,3 - 1 L/D forward conveying, 5 - 1/4 L/D neutral conveying kneading blocks with each block rotated 90 degrees from the last,1 - 1 L/D forward conveying, 1 - 3 L/D smooth cylinder beneath ultrasonic zone, 4 - 1/4 L/D neutral conveying kneading blocks with each block rotated 90 degrees from the last, 4 - 1/4 L/D reverse conveying kneading blocks with each block rotated 30 degrees from the last,3 - 1 L/D forward conveying, 1 - 1.5 L/D forward pumping. This twin screw technology is covered under US patent application WO 2012142562 A1.

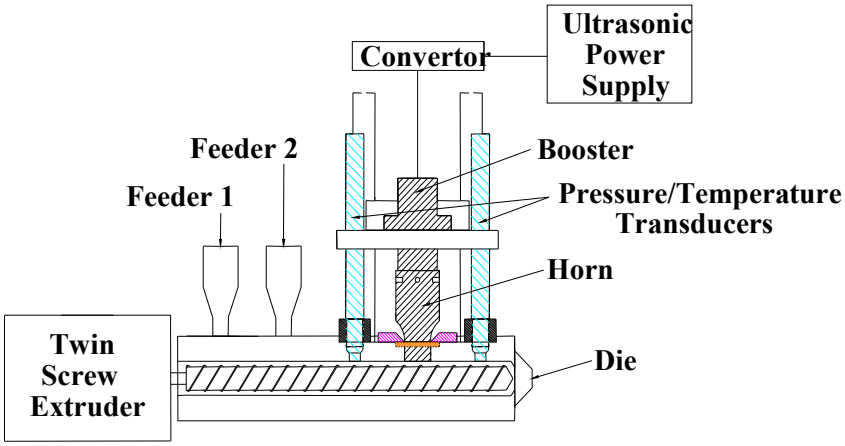

Figure 3.5: Micro-compounder with incorporated ultrasonic section - design B

3.3.3 Resin Transfer Molding

Resin transfer molded plaques were molded for a project conducted at NASA Langley Research Center, Hampton, VA. Two different matrix resins and three different carbon fiber fabrics were used. PETI-330 and PETI-8 resins were used as received from UBE Chemicals Ltd, Japan. The resins came in a yellowish powder form. The carbon fabric were produced by Textile Products, Inc., Anaheim, CA. They consisted of IM7-6K 5-harness satin woven fabric (GP sizing, 280 gsm), T650-35-3K 8 harness satin woven fabric (309 sizing, 366 gsm), and IM7-6K unidirectionally woven fabric (GP sizing, 160 gsm with Stick String 450 1/0 fill fiber). A fiber volume of 58% in the final plaque was required.

A resin transfer molding apparatus was designed and built internally for the process. This equipment is depicted in Figure 3.6. It consists of a mold and an injection system.

The mold consists of a top and bottom platens made of 4140 steel. Platens have dimensions of 34.29 x 34.29 cm^2 (13.5 x 13.5 $inches^2$) with thicknesses of 12.27 mm (0.5 inch) and were held to 0.002 inch parallelism. A frame of a specified thicknesses based on the laminate being prepared was inserted between platens to set the final thickness of the plaque. The frame thickness was calculated based on fabric densities provided by the manufacturer and the desired fiber volume fraction minimum of 58% by volume. The frame was made of 4140 steel. The carbon fiber lay-up consisting of carbon fabric plies, breather fabric was used for the outermost layers and high temperature sealant tape was placed along the periphery of the frame. The injection point is located at the center of one edge of the frame and has

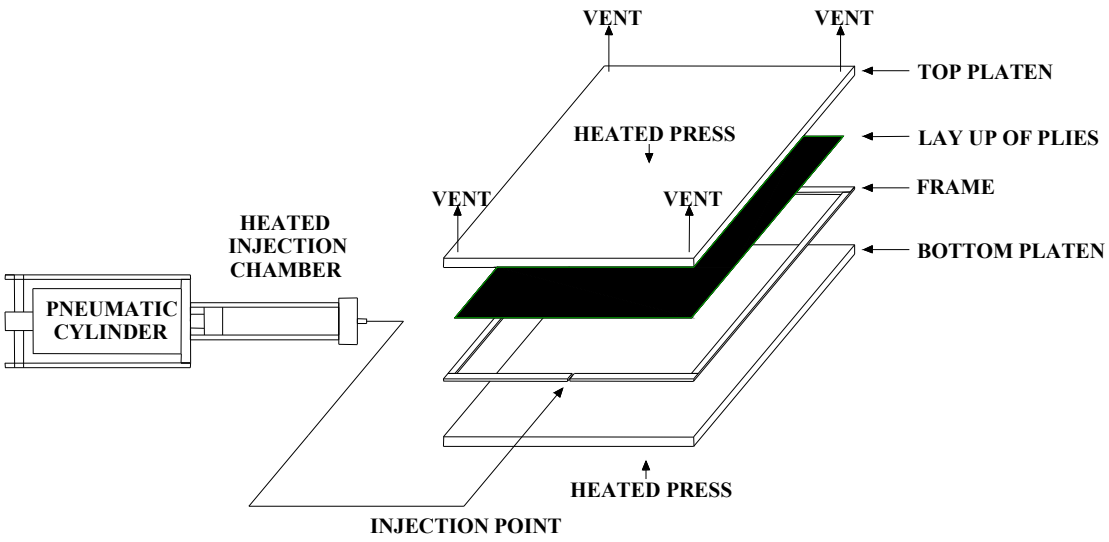

Figure 3.6: Schematic representation of RTM system used for the manufacturing of composite laminates

dimensions of 0.125 inch wide and has a thickness corresponding to the thickness of the frame being used. The top platen has a hole 3.175 mm (0.125 inch) in diameter at each corner for venting. The injection system consists of a 88.9 mm (3.5 inches) pneumatic cylinder with pressure control attached to a heated injection chamber of 3.81 cm (1.5 inches) in diameter for the infused resin. A pressure of 0.28 MPa (40 psi) was used on the cylinder to provide an injection pressure of approximately 1.52 MPa (220 psi) in the heated chamber. The mold was placed between 30.48 x 30.48 cm^2 (12 x 12 $inch^2$) platens of a high temperature compression molding press manufactured by Carver (CARVER 4122, Wabash, IN). The press has a maximum temperature of 400^oC and a clamping force of 24,000 lbf. The mold was heated by these temperature controlled platens. Insulation was used on all exposed areas for maximum temperature control.

Manufacturing of Laminates:

Four different laminates were manufactured. Laminate #1 was composed of PETI-8 resin and 10 plies of IM7-6K 5 Harness satin woven fabric (280 gsm, fiber density = 1.77 g/ml). A mold thickness of 2.727 mm was used based on calculations for a required fiber volume of 58%, as such:

$$Fabric\ \ Areal\ Weight = 280\frac{g}{m^2}$$

$$Area\ per\ ply = 31.75cm * 31.75cm = 1008.06cm^2$$

$$Total\ Area = 1008.06cm^2 * 10plies = 10080.62cm^2 = 1.008m^2$$

$$Weight = 280\frac{g}{m_2} * 1.008m^2 = 282.25g$$

$$FiberVolume = \frac{1cm^3}{1.77g} * 282.25g = 159.46cm^3$$

$$Total\ Volume = \frac{159.46cm^3}{0.58} = 274.94cm^3$$

$$Plaque\ Thickness = \frac{274.94cm^3}{(31.75cm)^2} = 0.27cm = 2.7mm$$

Plies were cut to 31.75 x 31.75 cm^2, using a cutting board, to fill out the mold as close as possible. Plies were stacked on top of each other in the mold with the same weave orientation. High temperature sealant tape was compressed to a thickness of 1.6 mm. Then it was cut into 3.1 mm strips and placed along the edges of the mold between the plies. This sealed area prevented racing of the infused resin during injection. The lay-up of the plies was as follows: 1 layer breather fabric, sealant tape, 2 layers carbon fabric and sealant tape repeated five times for a total of 10 plies and then another layer of breather fabric was placed on top. The sealant tape was placed a minimum of 3 cm away from all vents and the injection point to prevent blockage. After assembling the lay-up the mold was placed in the compression molding press and clamped using the maximum force. The vents were closed, a clamping force of 107 kN was applied, full vacuum was drawn and the temperature was raised to 400°C and held for two hours to remove the sizing on the carbon fabric. After this time the mold temperature was lowered to 316°C for injection.

A container with 240g of PETI-8 in powder form was placed into the vacuum oven, 30 inHg vacuum was drawn, and the polymer was degassed at 288^{o}C for 30 minutes. The material was then transferred to the injection chamber maintained at 316^{o}C and a pressure of 0.28 MPa (40 psi) was used at the cylinder to provide an injection pressure of approximately 1.52 MPa (220 psi). All exposed areas were insulated to maintain constant temperature. The vents were opened on the top platen and the resin was injected. As the resin reached each vent they were closed. After injection, the temperature was raised to 371^{o}C and cured for 1 hour with the injection pressure held to 1.52 MPa. After curing the heating was turned off and the laminate was left to cool to room temperature.

The remaining three laminates were manufactured in the same manner with the following differences, noting that the minimum fiber volume of 58% was used in the calculation above for each laminate described. Laminate #2 was composed of PETI-330 and 10 plies of IM7-6K 5 Harness satin woven fabric (280 gsm, fiber density = 1.77 g/ml). A mold thickness of 2.727 mm was used with the same lay-up configuration as in laminate #1. The PETI-330 resin was degassed for 40 min. Laminate #3 was composed of PETI-8 and 10 plies of T650-35-3K 8 Harness satin woven fabric (366 gsm, fiber density = 1.77 g/ml). A mold thickness of 3.28 mm was used with the same lay-up configuration as in laminate #1. Laminate #4 was composed of PETI-8 and 20 plies of IM7-6K unidirectionally woven fabric (160 gsm, fiber density = 1.77 g/ml) and a mold thickness of 3.07 mm was used. The lay-up was as follows: 1 layer of breather fabric, sealant tape, 2 layers carbon fabric, sealant tape, 3 layers carbon fabric, sealant tape, 5 layers carbon fabric, sealant tape, 5 layers carbon fabric, sealant tape, 3 layers carbon fabric, sealant

tape, 2 layers carbon fabric, sealant tape and 1 layer of breather fabric. The plies were all oriented perpendicular to the injection point.

3.3.4 Environmental Testing

A unique device has been designed and built in house to simulate the dynamic breathing process of an average sized male. In this completely hermetic system, air contaminated with carbon nanotubes was continuously cycled through a respirator for extended periods of time. Three different respirators of various filtration levels were used. These were all products commercially available through 3M® (Saint Paul, MN, USA) and are listed in Table 3.3. After the defined period of testing time the respirator was removed from the apparatus and Minwax (Upper Saddle River, NJ, USA) clear gloss urethane was used to solidify the CNTs in place for sectioning of the mask. The urethane was slowly infused into the mask to minimize the displacement of the contained nanotubes and allowed to dry for two days in a vented hood. The cured mask was then sectioned and optical micrographs were obtained. The penetration length of the CNTs was measured and used to evaluate the effectiveness of each mask.

Table 3.3: Respirators used for environmental testing

Manufacturer	**Rating**	**Model**	**Type**
3M®	N100	8233	Particulate Respirator
3M®	N95	8214	Particulate Respirator
3M®	Dust Mask	G1610	Nuisance Dust Mask

The designed system is shown in Figure 3.7. It consists of a 10 quart bell jar, a fan that continuously stirs the air to ensure that the nanomaterial remains suspended and does not

become stagnant along the walls, a mask, a pneumatic piston that forces air to be circulated and several check valves. The air is drawn through the mask and then recirculated back to the bottom jar to be cycled through the system again.

This system makes certain that unknown contaminants cannot enter the test environment, and also ensures that nanoparticles do not escape into the surroundings. If nanoparticles do in fact travel entirely though the mask. The system uses a pneumatically driven piston controlled by a timed solenoid and air under controlled pressure and flow rate. Each stroke of the piston cycles approximately 560 ml (34.2 in^3) of air. This amount is consistent with a typical tidal breath of a 154 lb male which is 500 ml. Typically, there are 12-20 breaths (inhale/exhale) per a minute and an average of 16 was chosen for this study. A time period of 24 hours was used for testing.

Many different respiration masks are currently available. All of the masks that were examined were mechanical filter respirators. These masks rely on the filter material to physically retain any particulate matter that may be contaminating the air. National Institute for Occupational Safety and Health (NIOSH) has released a rating system to assess a mask's ability to filter out air contaminants [202]. The masks range from filtering out 95% of all airborne particles up to 99.97% of all airborne particles being filtered out. The highest of the ratings, N100, relies strongly on the HEPA (High Efficiency Particulate Air) filter [203] and removes 99.97% of airborne particles 0.3 μm in diameter. This has been determined to be the most difficult size to filter

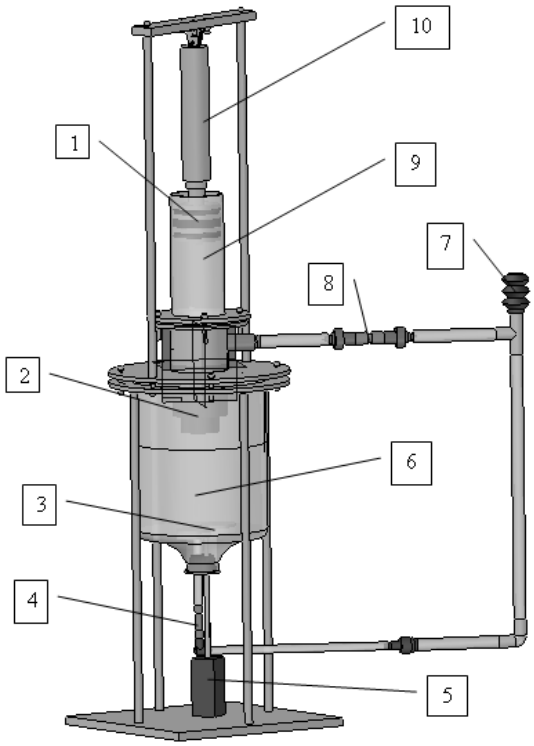

Figure 3.7: Machine Design Schematic. 1-Piston, 2-Mask, 3-Fan Blade, 4-Check Valve, 5-Fan Motor, 6-Glass Jar 7-Air Baffle, 8-Check Valve, 9-Cylinder, 10-Actuator

and therefore is the most penetrating particle size (MMPS). Particles larger and smaller than this (such as CNTs/CNFs) are filtered with higher efficiency. Particles that are larger than the MPPS tend to easily become embedded within the filter if they ever find a space large enough to penetrate into the mat of randomly arranged fibers. Particles smaller than 0.3 microns, such as nanotubes, adhere to the fibers due to electric charge and also embed into the fibers. Due to the small scales of these nanoparticles, diffusion into the filter media occurs once within the filter that enhances the entrapment of the particles from the previous two filtration methods.

3.4 Characterization

Nanocomposites were characterized for rheological, electrical, mechanical and morphological properties. The techniques for evaluation and methods used are detailed herein.

3.4.1 Rheological Properties

The rheology of polymer composite materials is an established method for the characterization dispersion and matrix filler interaction. The effects of the application of ultrasound on the interactions between the CNTs and the matrix, as well as that on the matrix chain structure were studied.

Compression molded PEEK discs of 25 mm in diameter and 2.0 mm thick were prepared using a compression molding press (Carver 4122, Wabash, IN, USA). Samples were dried for 24 hrs at 100^{o}C after processing then compression molded at 380^{o}C using high temperature mold release, Frekote HTM2 from Henkel AG & Co. KGaA, Dusseldorf, Germany, and Kapton film, Dupont, Wilmington, DE. PETI-330, UBE Chemicals Ltd, Japan, discs were injection molded using a mini-jet injection molding machine (HAAKE, Thermo Electron Corp. Germany). The material was dried for 24 hrs at 100^{o}C after processing, melted at 270^{o}C and then injected into a mold, coated with high temperature mold release, at 184^{o}C and demolded.

The rheological properties of the neat and nano-composite materials were studied to elucidate the effect of compounding and ultrasound on the matrix and the dispersion of CNTs. Rheological properties were measured using an Advanced Rheometric Expansion

System (Model ARES LS, TA Instruments). A parallel plate configuration, 25 mm in diameter, in oscillatory shear mode with frequency sweep over a range of 0.03 to 100 s^{-1} at a fixed strain amplitude of 2 % was used. Samples were placed in the machine, heated and allowed to reach the steady state temperature of the test, squeezed to 1.5 mm and then the excess material was removed with a razor to avoid edge effects. PETI-330 samples were measured at 200^{o}C and PEEK samples were measured at 360^{o}C. The complex viscosity, storage modulus, loss modulus and loss tangent as functions of frequency were measured.

3.4.2 Thermal Properties

Differential Scanning Calorimetry (DSC) was performed on all composites using a TA instruments calorimeter (Q200, TA instruments, New Castle, DE, USA). Samples of approximately 10 mg were sealed in hermetic pans and heated at 10°C per minute from 0°C to the desired temperature in a nitrogen atmosphere. Analysis of the DSC curves using TA Instruments Universal Analysis program was subsequently completed. From the analysis, T_g's, T_m's, heat evolution during curing for PETI-330, and heat evolution during melting for PEEK were attained. For PETI-330, the heat evolution of curing was used to calculate the percent of conversion and cure kinetics in PETI-330 samples using both isothermal an non-isothermal runs. The heat of fusion, T_g, and T_m were determined for all PEEK samples. Samples of approximately 10 mg were used for DSC measurements.

Thermogravimetric analysis was used to determine differences in composite thermal stability. A TGA (Q500, TA instruments, New Castle, DE, USA) was used for testing. Samples of approximately 10 mg were loaded into a clean and tared platinum pan and testing was conducted at a heating rate of 10^{o}C per a minute from 30°C to 900°C in a nitrogen environment. CNTs and are highly stable up to extremely high temperatures. The addition, dispersion and adhesion of CNTs into the matrix could give a synergistic effect to the polymer allowing greater stability at higher temperatures.

3.4.3 Mechanical Properties

Mechanical testing was performed on ASTM D638 tensile bars to determine the Young's modulus, ultimate strength, elongation at break and toughness on an Instron test machine (Model 5567, Instron Corp., Canton, MA, USA). An extensometer with a gauge length of 0.3 inches was used for accurate modulus measurements in the low strain portion of the test. Testing was carried out on a minimum of five samples according to ASTM D638 testing procedures at a cross head speed of 5 mm/min using a 10 kN load cell. A 7.62 mm (0.3 inch) strain gauge was used for all PETI-330 samples to be able to accurately record at the low strains during testing.

PEEK tensile bars, ASTM D638, were injection molded using a single cavity Mini-Jet injection molding machine (HAAKE, Thermo Electron Corp. Germany) at a barrel temperature of 370^{o}Cat a pressure of 100 MPa with a holding time of 10 seconds at a holding pressure of 60 MPa. All materials were dried in a vacuum oven at 100°C and -28 inHg prior to manufacturing tensile bars. PETI-330 and its nano-composites were placed

into a heated oven and degassed at 300°C for 2 hours under full, constant vacuum of -28 inHg. After degassing, samples are then placed into a heated compression molding press, 300°C, and compressed. The temperature was then ramped to 371°C and held for one hour to complete curing of un-oriented plaques 65 mm x 100 mm x 1 mm (2.5" x 4" x 0.04"). The ramp time to heat from 300°C to 371°C is 25 minutes. The cured plaques subsequently sectioned using a Buehler low speed saw (Model Isomet, Lake Bluff, Illinois) equipped with a diamond blade and oil bath. These sections were subsequently clamped into a metal tensile bar frame and machined using a Tensilkut high speed router (Model 10/21, Danbury, Connecticut) to machine the narrow and transition sections of the dog bone with a smooth finish. machined into ASTM D638 type F tensile bars for testing.

3.4.4 Electrical Properties

One of the attractive features of adding the carbon based fillers is their electrical conductivity. Many applications require the ability of parts to be able to leak charge away so that it does not build up and discharge with catastrophic consequences. Two different methods were used to measure conductivity.

For the first method, a Keithley Electrometer/High Resistance Meter (Model 6517 A, Keithley Instruments, Cleveland, OH, USA) equipped with a model 8009 test fixture was used to test the volume resistivity of molded plaques in accordance with ASTM D257 testing procedures. This apparatus is designed to measure volume resistivity from 10^{18} to 10^{3} Ohm-cm. Alternating polarity was used with a baseline of 0 volts and an alternating

voltage of +/- 1 volt. The method was set to take six reads for 10 seconds at each alternating voltage and then record the final read. The measurement was taken three different times for each sample and averaged. Standard deviation is reported.

The second method was designed and developed to test materials in the low resistivity region. A Keithley micro-ohmmeter (Model 580, Keithley Instruments, Cleveland, OH, USA) was used for both the output and input signals. The apparatus consisted of two cylindrical rubber blocks 64 mm in diameter that were coated on one side with Laird Technologies 3050-525 Nickel/Copper Ripstop Fabric (Laird Technologies, Saint Louis, Missouri, USA) that has a surface resistivity of < 0.07 Ω/square. The sample was placed between the two rubber blocks with the conductive side facing the sample. The blocks andsamples were squeezed and the electrodes for both the input and output signals were

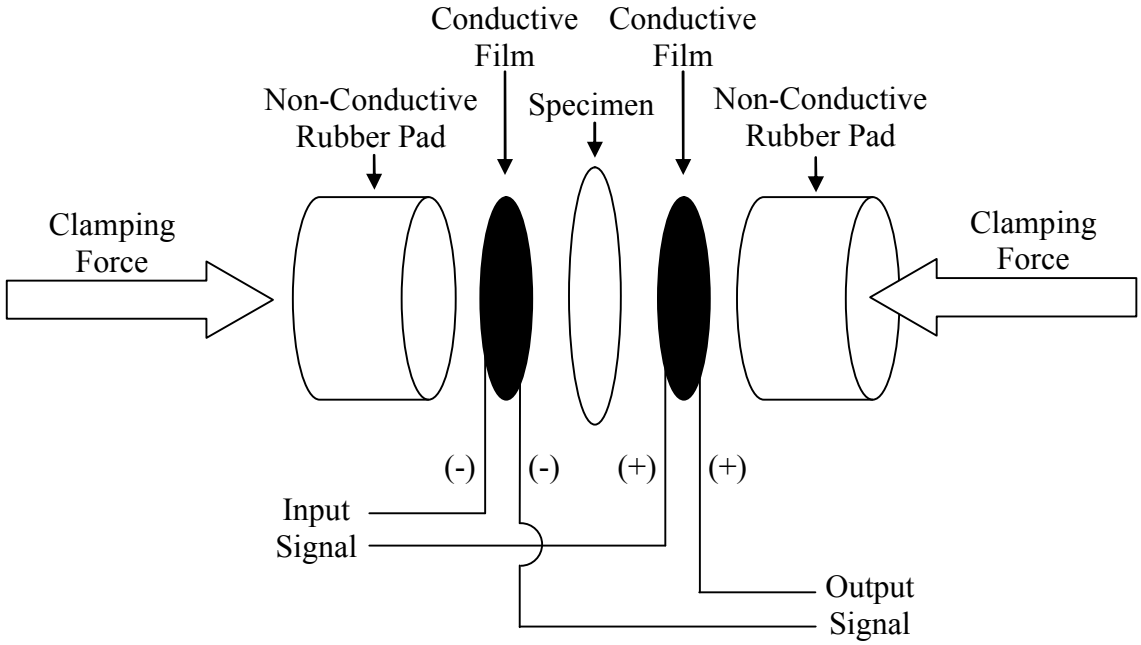

Figure 3.8: Resistivity measurement apparatus for low resistivity range - method 2

pressed against the conductive film and a measurement was taken. The measurement was taken three different times for each sample and averaged. Standard deviation is reported.

PEEK compression molded plaques 90 mm in diameter and 1 mm thick were molded using a compression molding machine at a temperature of 380^{o}C. For PETI-330 samples, cured compression molded samples 100 mm x 65 mm x 1mm were used for testing.

3.4.5 High Resolution Microscopy

High resolution topographical pictures were taken of fractured surfaces of the molded and cryogenically fractured specimens. A high resolution field emission scanning electron microscope (JOEL JSM-7401 F, JOEL, Peabody, MA) was used to look for bundles of CNTs and for adhesion of the matrix to the CNT. This method was used in conjunction with optical microscopy to verify the complete dispersion of the CNT bundles. Due to the small field of view, a local picture may not be truly representative of the entire sample. Care was taken to ensure that the micrographs reported are representative of the macroscopic scale and not just the microscopic scale.

High resolution topographical pictures were taken of cryogenically broken tensile bars, produced in the methods described above, in liquid nitrogen. A high resolution field emission scanning electron microscope (HRSEM) (JOEL JSM-7401 F, JOEL, Peabody, MA) was used to look for bundles of CNTs for dispersion. Due to the small field of view, a local picture may not be truly representative of the entire sample.

3.4.6 Optical Microscopy

In order to investigate the macroscopic morphological characteristics of the polymer nanocomposites, thin film analysis was used. The tensile testing samples were sectioned using a microtome(Leica Ultracut microtome, St. Louis, MO, USA) to obtain thin, translucent samples. The translucent film was then observed under a high power optical microscope, Olympus BX63 Microscope using 100X and 200X magnification. Large agglomerates of filler can be readily seen with this method that cannot be observed under electron microscopy.

3.4.7 Environmental Testing

Minwax low viscosity, quick set, clear urethane was used to solidify the respirator (mask) to keep all materials, respirator and CNTs, in place at the completion of testing for sectioning. The cured mask was sectioned using an Isomet (Buehler, Lake Bluff, Illinois) low speed saw with a diamond blade and oil bath. Sections were observed under optical microscopy, Olympus microscope (Model BX63, Shinjuku-ku, Japan). The distance the nanoparticles traveled through the respirators and/or their complete penetration was measured and recorded. The pressure profile on either side of the respirator was recorded during testing.

CHAPTER IV

A CURE KINETICS MODEL FOR THE NON-ISOTHERMAL CURING OF POLYIMIDE

4.1 Introduction

A series of thermoset imide oligomers have been synthesized in the search for resins with enhanced physical and mechanical properties at elevated temperatures at NASA Langley [21-24]. These thermoset materials cure under non-isothermal conditions and carry a complicated time dependent thermal history. Many curing models are based on isothermal rate equations and do not correctly account for heating ramps that are unavoidable in any actual processing condition. To be able to optimize the complicated cure cycle of these polymers an accurate model is needed to accounts for the entire time-temperature trace.

A cure kinetics model for curing PETI-330, a phenylethynyl terminated imide, has been proposed including induction and curing stages. Parameters for both stages were determined experimentally from non-isothermal DSC runs at various heating rates and corrected for temperature difference between the sample and the furnace. These parameters were used in conjunction with a model proposed by Isayev and Deng [36]to predict the state of cure. The model was verified experimentally using compression

molded slabs obtained at fixed temperatures while accounting for the curing that occurs during the transient temperature variation before reaching the set temperature.

4.2 Theoretical

In this study, the model developed by Isayev and Deng [36]for rubber and described in detail in Chapter 2.2was adapted to describe the cure kinetics of PETI-330. It is generally accepted that there exists three periods during curing; the induction period, the curing stage and the post curing stage. The induction period is the time during which no chemical reaction occurs, the curing stage is the period during which the majority of the reaction occurs, and the post curing stage is a heat treatment period. To accurately describe the degree of curing the induction time was combined with the nonisothermal kinetics to be able to predict the cure during any known time-temperature trace.

In 1970 an article by MacCullum and Tanner [35] started the discussion on what equation could be used to describe a non-isothermal system by questioning whether an isothermal kinetic rate equation, as shown in equation 4.1, could be used to describe non-isothermal behavior.

$$\left(\frac{\partial \alpha}{\partial t}\right)_T = K(T) f(\alpha) \tag{4.1}$$

where α is the fractional conversion, T is the temperature, t is the time, and K is the rate constant which is a function of temperature. Previous work had been based on the idea that the dynamic, nonisothermal, rate is equal to the isothermal rate but MacCallum and

Tanner proposed that in nonisothermal process the fractional conversion is a function of both time and temperature as seen in equation 4.2.

$$d\alpha = \left(\frac{\partial \alpha}{\partial t}\right)_T dt + \left(\frac{\partial \alpha}{\partial T}\right)_t dT \tag{4.2}$$

While many theories have been proposed to date there is still no consensus on the exact solution to this problem. Isayev and Deng proposed a model based on a reduced time approach to be able to predict the degree of cure in nonisothermal curing in rubber. This model was adopted and modified for the present research. Their model is described below for both isothermal and nonisothermal curing.

Isayev and Deng [37] used the following kinetics model to describe rubber vulcanization kinetics and the progression is directly from their work and is repeated below from Isayev, Chan, and Shyu [38] as the same theory was adapted for the current cure model. The isothermal model assumes that there is an induction period during which no reaction takes place. During isothermal conditions it is assumed that this induction period has an Arrhenius-type dependence on temperature as shown in equation 4.3.

$$t_i = t_0 \exp\left(\frac{T_b}{T}\right) \tag{4.3}$$

where T is the temperature, t_o and T_b are the material constants independent of temperature. Based on the work of Kamal and Sourour [39] a model for isothermal curing kinetics was used, as shown in Equation 4.4:

$$\alpha = \frac{kt^n}{1+kt^n} \tag{4.4}$$

where t is the actual time minus the induction time and k is the rate constant with an Arrhenius-type dependence on temperature as such:

$$k = k_o \exp\left(-\frac{E}{RT}\right) \tag{4.5}$$

where k_o is the pre-exponential factor, E is the activation energy and R is the universal gas constant. The derivative of equation 4.4 with respect to time yields:

$$\frac{d\alpha}{dt} = \frac{nkt^{n-1}}{\left(1+kt^n\right)^2} \tag{4.6}$$

By expressing t in terms of α and k in equation 4.4, equation 4.6 becomes:

$$\frac{d\alpha}{dt} = k_o e^{-E/RT} \alpha^{(n-1)/n} (1-\alpha)^{n+1/n} \tag{4.7}$$

where α, n, k, t, E, R and T are the degree of curing, order of reaction, a rate constant, time, activation energy, gas constant and temperature, respectively.

The nonisothermal induction time is derived from the isothermal induction time using the concept of induction time index.

$$\bar{t} = \int_0^{t_I} \frac{dt}{t_i(T)} = 1 \tag{4.8}$$

where t_I is the nonisothermal induction time, $t_i(T)$ is the isothermal induction time. As soon as the value of $\bar{t}$ attains unity, 1, the upper limit of the integral in Equation 4.6

becomes the induction time for the nonisothermal process. In this theory it is assumed that the nonisothermal induction time is made up of many minute isothermal steps. This non-isothermal time can be determined from DSC thermograms as a function of heating rate and is defined as the point at which the heat flow diverges from the base line.

4.3 Experimental

PETI-330 is a phenylethynyl terminated imide. It was used as supplied from UBE Chemicals Ltd, Japan, in a light yellow, powdered form. The oligomer was characterized by Differential Scanning Calorimetry (DSC) using a Q200 DSC (TA Instruments, New Castle, DE, USA). A sample of approximately 10 mg was sealed in a hermetic pan and heated from room temperature to 400°C at a heating rate of 2.5°C/min. The oligomeric material has a measured T_g of 145^{o}C. No significant reaction is seen during thermal

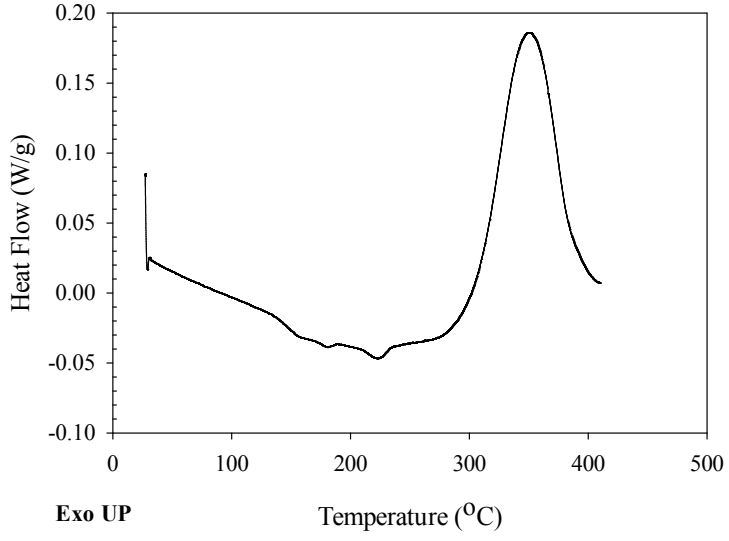

Figure 4.1: DSC trace of uncured PETI-330 at a heating rate of 2.5°C/min

analysis at temperatures below 290°C, as seen if Figure 4.1.

Rheological properties were measured on an ARES, TA instruments using parallel plate configuration. The material was dried for 24 hrs at 100°C after extrusion, melted at 280°C and then compression molded into samples 2.0 mm thick x 25 mm in diameter. The molded disc was placed between parallel plates, melted, and then compressed to 1.5 mm. Overflow material around the plates was removed after compression using a razor blade to minimize boundary effects. Testing was conducted using 25 mm parallel plate geometry in oscillatory shear mode with a frequency sweep test using a strain amplitude of 2% and a fixed temperature of 200°C. The complex viscosity, storage modulus, loss modulus and loss tangent were determined as a function of angular frequency. A

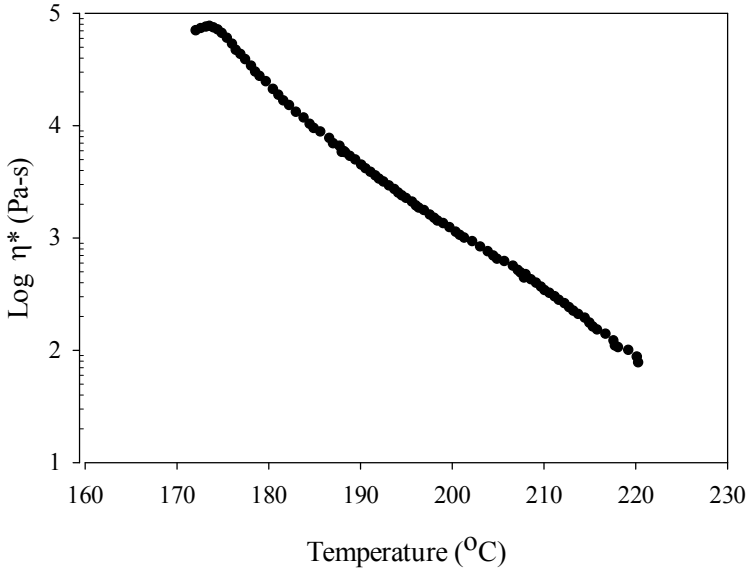

Figure 4.2: Complex viscosity of PETI-330 at a strain amplitude of 2% with a temperature ramp of 4°C/min at a frequency of 100 rad/s

relaxation time of 10 minutes after the samples were loaded and reached the testing temperature was used to allow the normal force to diminish from squeezing the sample.

PETI-330 displays the predictable characteristics of its oligomer form. The viscosity of the uncured neat material shows significant decrease with increasing temperature as shown in Figure 4.2. Figure 4.3 presents the complex viscosity of PETI-330 over a range of temperatures from 180°C to 230°C. Figure 4.4 presents the storage and loss modulus of PETI-330 over the temperature range from 180°C to 230°C. A continuous decrease in the viscosity and moduli is observed as expected. This is important for applications of infusion and resin transfer molding where this material is being utilized.

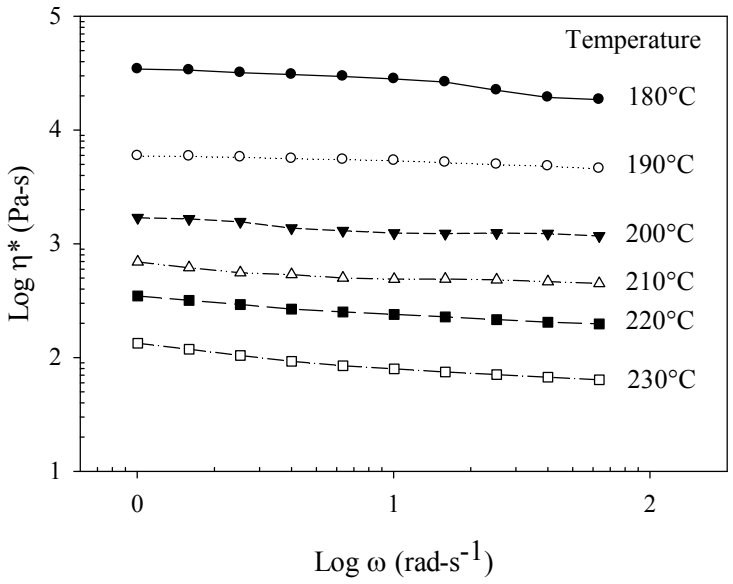

Figure 4.3: Complex viscosity of PETI-330 at a strain amplitude of 2% at various temperatures as a function of frequency

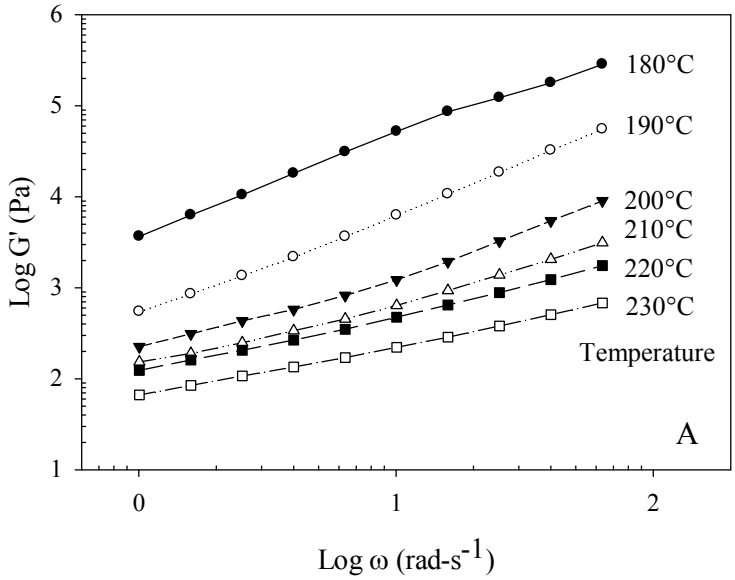

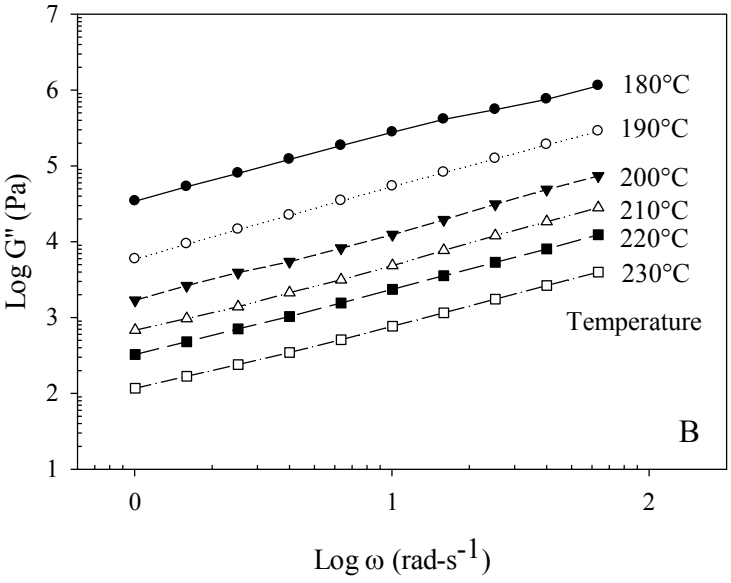

Figure 4.4: Storage modulus (A) and loss modulus (B) of PETI-330 at a strain amplitude of 2% at various temperatures as a function of frequency

Differential Scanning Calorimetry (DSC) was used to investigate the cure kinetics of this imide material under nonisothermal conditions. Prior to analyzing samples, indium calibration was performed to obtain data for temperature correction. Using the approach of Janeschitz-Krieg*et al.* [204], the heat transfer between the sample pan and the DSC furnace is not a function of the material in the pan but only between the pan and the furnace and can be obtained from the high temperature side of the indium calibration. Figure 4.5shows both the high temperature side exponential decay of heat flow during indium calibration and the best fit to the experimental data using linear regression.

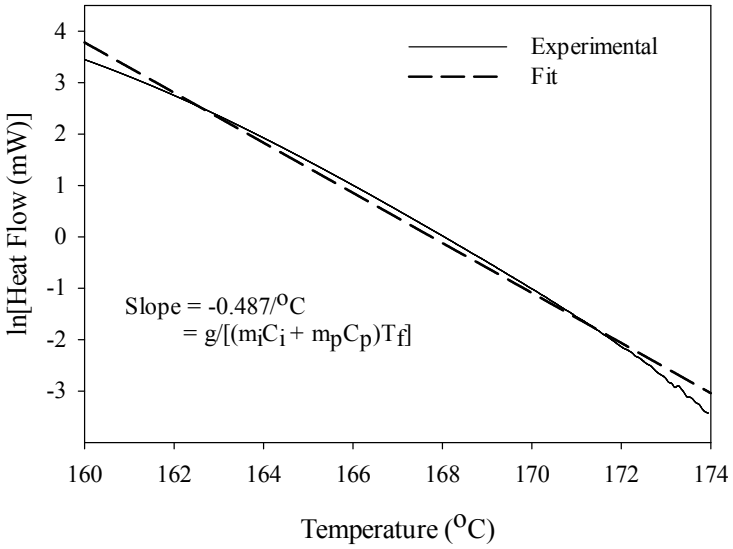

Figure 4.5: Natural logarithm of measured and fitted heat flow rate vs. furnace temperature on the high temperature side during DSC indium calibration at heating rate of 20°C/min to determine heat transfer coefficient.

It is important to account for differences between the actual and measured sample's temperature during the DSC runs. It is well known that the temperature of the sample in the DSC pan lags behind the temperature indicated by the DSC and that the difference increases with heating rate. Janeschitz-Kriegl *et al.* [204] proposed a heat balance equation for estimating the temperature lag between the sample and the furnace:

$$-\left(m_s C_s + m_p C_p\right)\frac{dT}{dt} + m_s Q_\infty \frac{d\alpha}{dt} = hA(T - T_f) \qquad 4.9$$

with the initial condition of $T(0) = T_{rf}$, where T_{rf} is a reference temperature, T is the sample temperature, Q_∞ is the total heat of reaction, m_s and c_s are the mass and specific

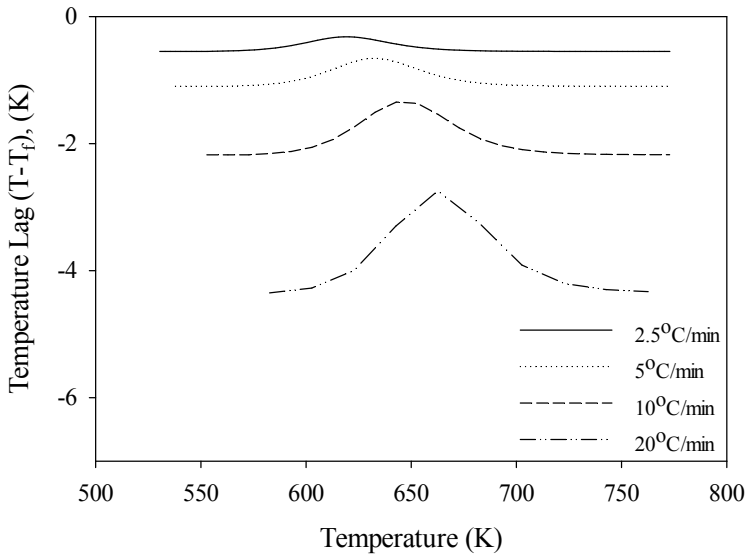

Figure 4.6: Temperature difference between sample and DSC furnace vs. furnace temperature for various heating rates

heat of the sample, *h* is the heat transfer coefficient between the furnance and the pan, *A* is the area of contact of the pan and dα/dt is described by Isayev and Deng [37] as:

$$\frac{d\alpha}{dt} = nk^{\frac{1}{n}}\alpha^{\frac{n-1}{n}}(1-\alpha)^{\frac{n+1}{n}} \qquad 4.10$$

Using Equation 4.9, calculated results for the temperature lag between the sample and the DSC furnace for different heating rates are shown in Figure4.6. It is readily observable that the temperature difference significantly increases with heating rate. At a heating rate of 2.5^{o}C this difference is minimal, around 0.5^{o}C, where at a heating rate of 20^{o}C there is a difference of more than 4^{o}C.

The high curing temperature and rapid rate of cure prohibited running isothermal cure evaluations in the DSC to determine model parameters. Therefore, all constants were determined under nonisothermal conditions. Samples of approximately 10mg were sealed in aluminum pans for thermal analysis. Constant heating rates of 5, 10, 15, and 20°C/min were used. The total heat of reaction was determined from the nonisothermal DSC data. The degree of curing can be determined by knowing the total heat of conversion and the heat of conversion from the start of the experiment to any time t of the measured sample. The residual heat of reaction from the samples obtained during curing was used to calculate the degree of cure, such that:

$$\frac{d\alpha}{dt} = \frac{Q_t}{Q_\infty} = \frac{Q_\infty - Q_{residual}}{Q_\infty} \qquad 4.11$$

where Q_t is the heat released from start to time t and Q_∞ is the total heat of reaction. The rate of heat generation was regarded as the rate of reaction. The parameters of the nonisothermal model were found by fitting the kinetic equations to the experimental data using the calculated degree of cure versus temperature curves from the four different nonisothermal runs. A computer program was used that had previously been developed to calculate these parameters [37]. The induction time was also obtained from the experimental data during the computational analysis. These parameters were subsequently used in the model built to predict the nonisothermal curing of any known time-temperature history.

The induction time is a material function that is dependent on the reaction temperature and can be predicted using Equation 4.8 and experimental values from DSC curing runs by fitting the induction time model. The calculated values for these parameters are listed in Table 4.1. Figure4.7 shows the ability of the nonisothermal induction time model to fit the start of curing as a function of heating rate in DSC runs for PETI-330. As can be seen, the fitted induction time is in good agreement with experimental results over the entire range of data.

Table 4.1: Parameters of cure by induction time model

Parametric Nonisothermal Model	
$\bar{t} = \int_0^t \frac{dt}{t_i(T)}$	$t_i = t_0 \exp\left(\frac{T_b}{T}\right)$
t_o(s)	T_b(K)
1.234 x 10^{-12}	18,288

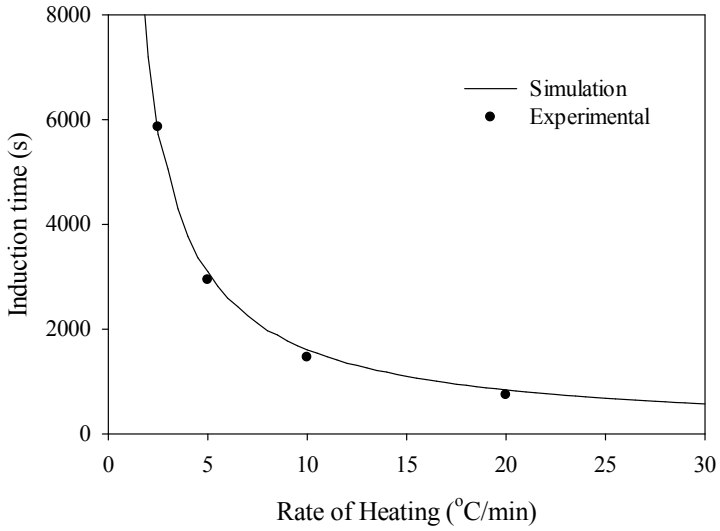

Figure 4.7: Measured and predicted non-isothermal induction time versus heating rate.

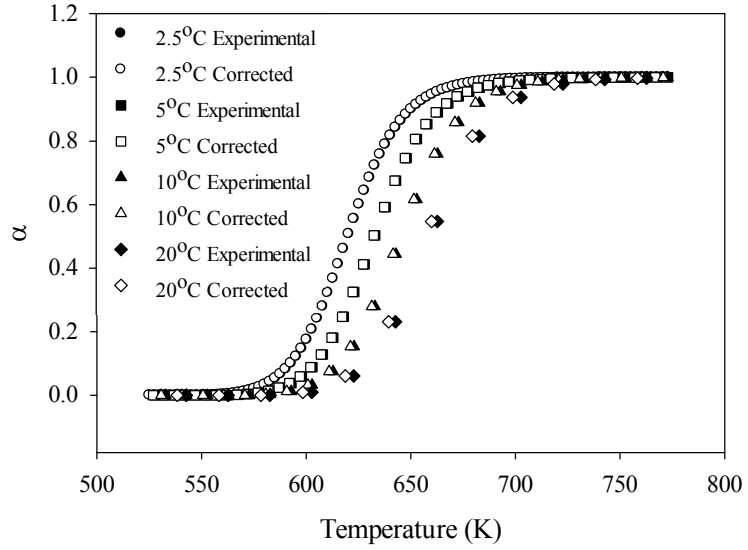

Figure 4.8: Measured and corrected degree of cure as a function of temperature at different heating rates.

All non-isothermal experimental results were first corrected for their corresponding temperature lag according to heating rate, shown in Figure 4.8. Figure4.8 depicts the degree of cure vs. measured temperature for uncorrected and temperature lag corrected DSC curing experiments at four different heating rates. Using the temperature lag corrected data for curing the computation program was used to iterate a best fit of Equation 4.10 for the non-isothermal curing kinetics discussed above. This fit provided the parameters for the kinetic model. Experimental results for the degree of curing are accurately predicted by the model over the entire range of data as shown in Figure 4.9.

The parametric values for the kinetic model, that were determined from the nonisothermal DSC runs, are listed in Table 4.2. These values were determined from the DSC thermograms for the nonisothermal runs at four different heating rates.

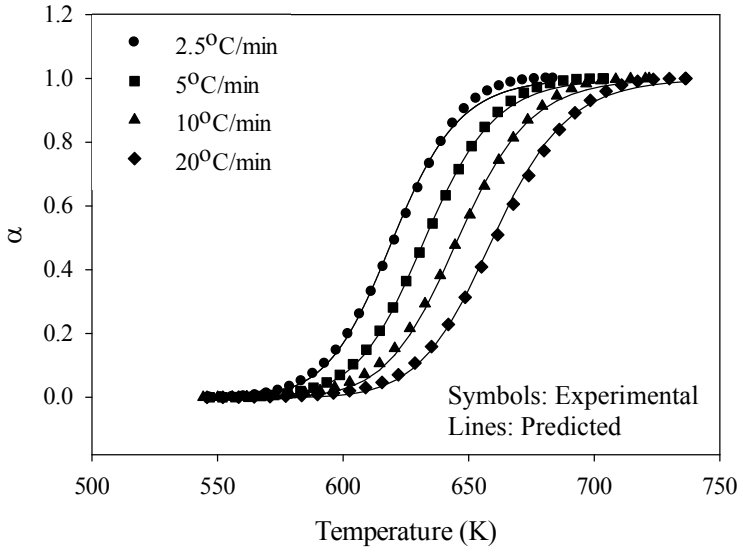

Figure 4.9: Measured and fitted degree of curing as a function of temperature for PETI-330 at different heating rates.

Table 4.2: Parameters of cure by kinetic model

Parametric Isothermal Model		
$\frac{d\alpha}{dt} = k_o e^{-E/RT} \alpha^{(n-1)/n} (1-\alpha)^{n+1/n}$		
n	$k_o(s^{-n})$	E/R (K)
1.384	4.193×10^{11}	20,161

Subsequently, these parameters were used to predict the degree of curing during isothermal DSC runs. However, it should be noted that at the high temperatures, such as 350^{o}C, curing starts very quickly and such a high temperature cannot be imposed instantaneously due to the transient response of the DSC. Therefore, the initial variation of temperature was included in the calculation of the induction time and degree of curing.

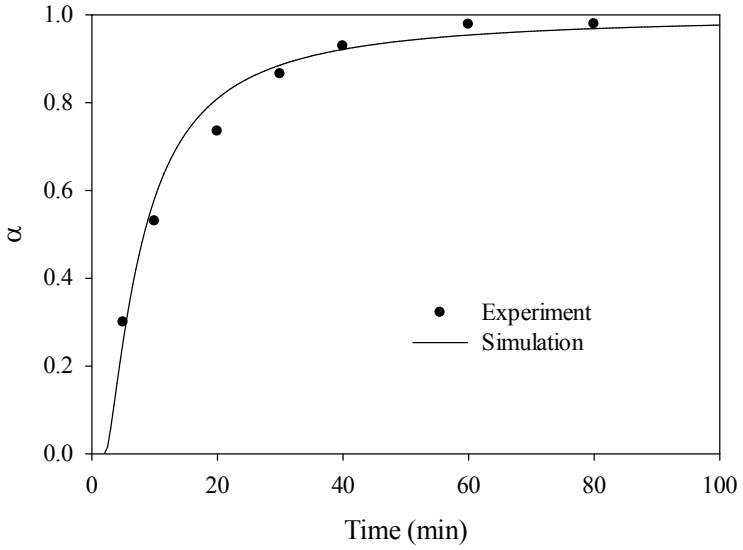

Figure 4.10: Measured and predicted degree of curing of PETI-330 as a function of time at 350^{o}C in DSC isothermal runs including transient response.

Figure 4.10 shows the predicted and experimental degree of curing vs. time during a DSC isothermal run at 350^{o}C. As can be seen, the predicted results are in good agreement with experimental data.

This model was further validated by testing its ability to predict the degree of cure in larger parts as a practical application. Compression molded slabs of 2 mm in thickness were cured for varying lengths of time at 350°C and immediately removed and quenched in ice water to stop the curing process. The slabs experience a temperature difference during curing through their thickness since heat is applied to the top and bottom of the slab by the compression molding press. Accordingly, this causes a deviation in cure between material at the outer edges and material at the center of the slab. Therefore, samples were obtained in the following manner. A specimen was taken through the entire thickness of the slab. The specimen was ground using a mortar and pestle and then an aliquot of the ground material was sampled for thermal analysis. Once again, as an instantaneous temperature could not be imposed, the temperature profile of the samples inserted into the press was measured. Figure 4.11 depicts the temperature ramp experienced by samples when heated from room temperature to 350°C. A polynomial was fit to the experimental data to acquire a complete time-temperature trace for the program.

Samples removed from the slabs cured at various lengths of time were then analyzed using DSC for the degree of cure. Figure 4.12 shows the experimental and predicted degree of cure along with the temperature trace of the experimental slabs. It can be seen

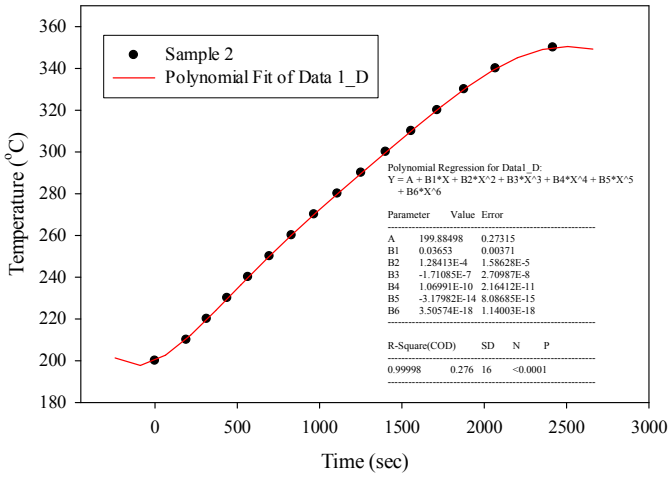

Figure 4.11: Experimental and fitted temperature profile in compression molding press

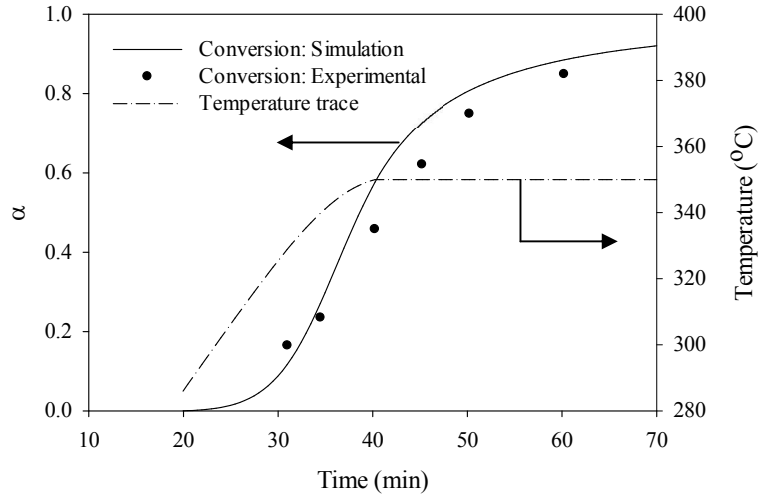

Figure 4.12: Temperature trace of slab during compression molding and measured and predicted degree of curing as a function of time for curing of 2 mm slab.

that during this nonisothermal run a long induction time of greater than20 min, where no curing takes place, occurs. It is also observed that the model is in good agreement with the measured degree of cure. Differences in the model versus experimental results are attributed to the difference in curing that is experienced through the thickness of the slab do to temperature variation in the compression molding press. The top and bottom layer of the plaque are at a higher temperature as they are in contact with the mold while the center of the plaque is heated through conduction from the material above and below.

4.4 Summary

A nonisothermal model for predicting the degree of cure in PETI-330 was proposed that accounts for the temperature dependent induction time, the duration of time at the start of the curing cycle where no curing occurs, and for the time-temperature dependent degree of curing. The material constants for PETI-330 were determined by using DSC and computational analysis according to the model proposed. The difference in temperatures between the sample and the DSC furnace at various heating rates were determined and corrected. The model was validated by compression molding plaques of PETI-330 with known time-temperature traces and halting the cure at various intervals. The degree of cure of the plaques was then determined experimentally. The predicted and experimental results for the degree of cure in the plaques is in good agreement. This model can be used for finding the optimal conditions of curing for products made from PETI-330.

CHAPTER V

CONTINUOUS HIGH POWER ULTRASONIC EXTRUSION OF PETI-330/CNT NANOCOMPOSITES

5.1 Introduction

Composite materials provide enhanced performance and functionality that pure materials cannot provide individually. In this chapter, the processing and characterization of PETI-330, a high temperature themoset material, and its CNT nanocomposites for enhanced mechanical and electrical properties are studied. While CNT composites have been studied with great scrutiny for their theoretical mechanical and electrical properties, an environmentally friendly, continuous and cost efficient method has not yet been developed for the dispersion of nanotubes in a polymer matrix to the author's knowledge. The nanocomposites for this study were processed using patented ultrasonically assisted twin screw extruder technology. Carbon nanotubes are known for their agglomeration during synthesis. This ultrasonic technology aids in the dispersion of CNTs and can be adapted to equipment that is currently used in industry aided by an ultrasonic energy. Prepared nanocomposites were characterized for processing, rheological, mechanical, thermal, electrical and morphological characteristics.

5.2 Experimental Procedures

A phenylethynyl terminated imide oligomer in a yellowish powder form was obtained from Ube Chemicals Ltd, Japan, under the trade name PETI-330, and was used as received. It has a T_g of 145°C and reacts at temperatures of 290°C and above. A regularly entangled grade of multiwalled carbon nanotubes was obtained from Nanostructured and Amorphous Materials Inc. (Houston, TX) and used as received. The CNTs have manufacture listed physical dimensions of outside diameters of 10-20 nm, inside diameters of 5-10 nm and lengths of 0.5-200 μm. These multi-walled nanotubes have a specific surface area of >200 m^2/g and a bulk density of 0.040-0.050 g/cm^3.

All materials were dried in a vacuum oven at 100°C for 24 hours prior to processing. A co-rotating twin screw micro-compounder (PRISM USALAB 16, Thermo Electron Corp.

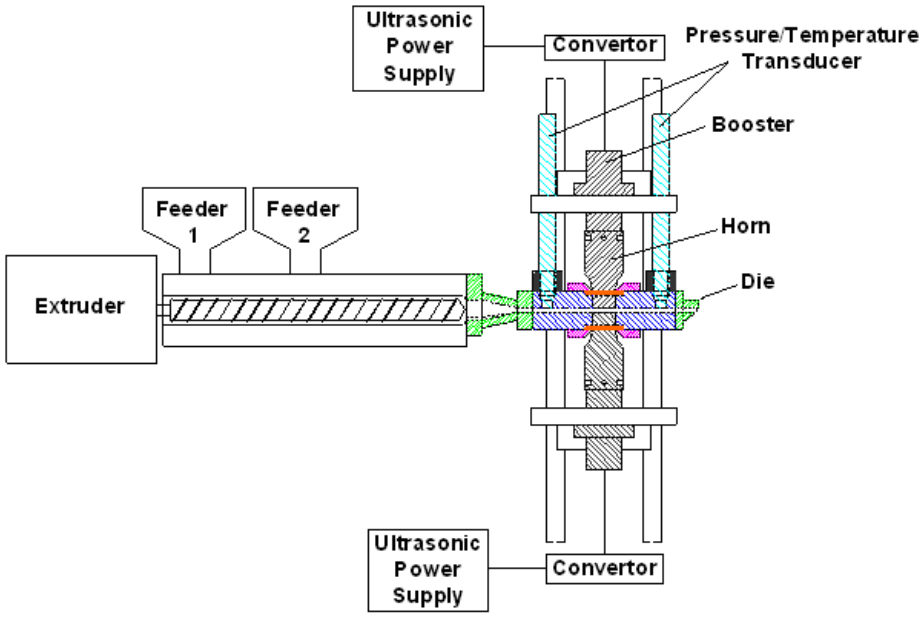

Figure 5.1: Micro-compounder with attached ultrasonic slit die - design A

UK) with an ultrasonic slit die attachment at the exit of the extruder was used to compound the material, as shown in the schematic Figure 5.1.

The micro-compounder has a screw diameter of 16 mm and an L/D of 25. The matrix is fed into the throat of the extruder at feed port 1. To avoid the high stresses in the feeding zone, the CNT are fed separately downstream at a point where the matrix has already melted, between the first and second sets of kneading blocks shown in Figure 5.1 as feed port 2. The composite material then passes through additional mixing and ultrasonic treatment zones for the dispersion of the CNTs. In this design, depicted in Figure 5.1, the composite material exits the extruder and enters a die. This die consists of two ultrasonic horns directly opposed to each other located on either side of the melt with a flow channel that has a cross-section of 4 mm thick by 19 mm wide that is 114 mm long (0.157 x 0.75 x 4.5 in^3). The ultrasonic systems (Branson Ultrasonic Corp., CT, USA) have a maximum power output of 800 W and operate at 40 kHz. The horns have a 19 mm x 19 mm (0.75 x 0.75 in^2) area that contacts the polymer melt and are situated in the middle of the die section directly in line with each other on opposing sides of the melt.

On both sides of the top ultrasonic system a pressure transducer/thermocouple has been installed to measure pressure and temperature before and after ultrasonic treatment. The horns are internally cooled using a constant flow water bath set at 95°C. The screw stack up was as follows starting at the feed throat: 7 - 1 L/D forward conveying, 6 - 1/4 L/D forward conveying kneading blocks with each block rotated 30 degrees from the last, 6 - 1/4 L/D neutral conveying kneading blocks with each block rotated 90 degrees from the last,4 - 1 L/D forward conveying, 4 - 1/4 L/D forward conveying kneading blocks

with each block rotated 30 degrees from the last,3 - 1 L/D forward conveying, 4 - 1/4 L/D forward conveying kneading blocks with each block rotated 30 degrees from the last, 6 - 1/4 L/D neutral conveying kneading blocks with each block rotated 90 degrees from the last,3 - 1 L/D forward conveying, 1 - 1.5 L/D forward pumping. This technology is covered under US patent application WO2007145918 A3.

The processing conditions used were as follows: a screw speed of 100 RPM, a feed rate of 454g/hr (1lb/hr) and an extrusion temperature profile of 180 and 200^{o}C for the first two zones and all remaining zones set to 225^{o}C. The residence time in the ultrasonic treatment zone is approximately 12 seconds for the flow rate of 454g/hr (1lb/hr).All treatment was done using a 40 kHz ultrasonic system at various amplitudes. Four different amplitudes and 5 different CNT concentrations were prepared. Table 5.1 is the testing matrix used for the PETI-330/CNT Nanocomposites.

Table 5.1:Testing Matrix for PETI-330/CNT Nanocomposites processed on Micro-compounder design A

CNT Concentration	RPM	Feed Rate (lb/hr)	Ultrasonic Amplitude (μm)
0	100	1	0, 2.5, 3.75, 5
0.5	100	1	0, 2.5, 3.75, 5
1	100	1	0, 2.5, 3.75, 5
2	100	1	0, 2.5, 3.75, 5
5	100	1	0, 2.5, 3.75, 5

5.3 Processing Characteristics

During extrusion the extruder torque as a % of max torque, pressure before and after the ultrasonic treatment zone and ultrasonic power consumption were recorded using a

online data acquisition system. As seen in Figure 5.2, the torque increased with increasing CNT concentration, as expected. At low concentrations of CNT no strong effect is seen with increasing ultrasonic treatment. However, as the concentration increased, there is a decrease in the torque with increasing ultrasonic treatment. This is readily seen in samples at 5 wt% CNT loading. The torque drops from 68 to 55% going from no treatment to a treatment at 3.75 μm. It should be noted that during the processing of the nanocomposite sample at 5 wt% CNT and the highest amplitude ultrasonic treatment, 5 μm, the ultrasonic power supply continuously overloaded and shut down.

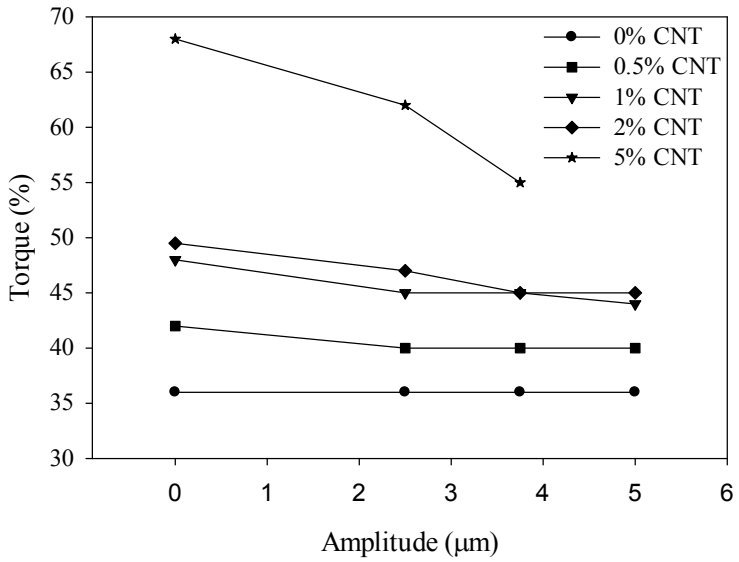

Figure 5.2: Extruder torque during compounding for PETI-330 nanocomposites for various wt% loadings

Therefore, a homogeneous sample could not be obtained. The die pressure was measured directly after the ultrasonic treatment section and is directly before the die, as depicted in Figure 5.1. An increase in die pressure was also observed with increasing CNT concentration, as expected, and a general decrease in pressure with increasing ultrasonic

amplitude as can be seen in Figure 5.3. This decrease in extruder torque and pressure with increasing ultrasonic treatment is attributed to both thermal and rheological effects. The vibration of the horn causes slip and decreased resistance to the flow of the polymer as well as a decrease in viscosity due to an increase in temperature from frictional heating at the surface of the horn and ultrasonic energy dissipation. This is also caused by recoverable thixotropic effects as the increase in ultrasonic treatment shows a decrease in die pressure but an increase in the viscosity [205], as shown in Figure 5.5. This decreased extruder torque and pressure would allow for increased throughput in industrial

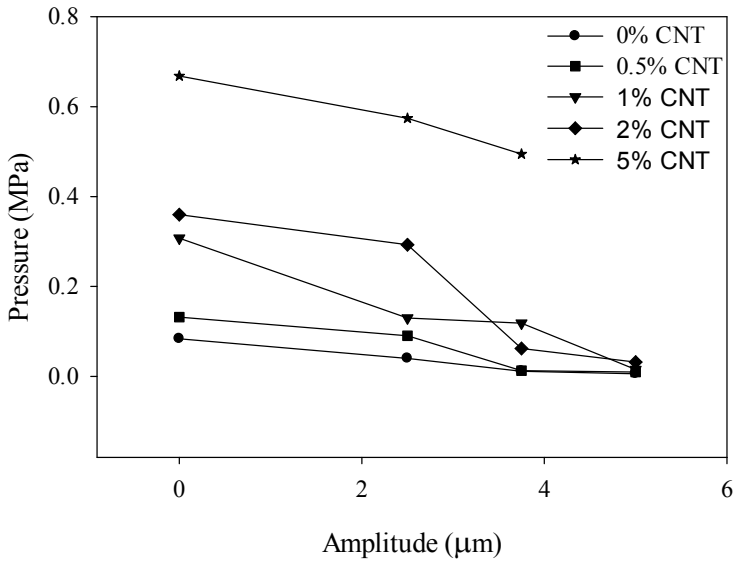

Figure 5.3: Die pressure versus ultrasonic amplitude for PETI-330/CNT nanocomposites applications.

Ultrasonic power consumption increased significantly with increasing ultrasonic amplitude at all concentrations, as seen in Figure 5.4, and generally increases with increasing concentration at higher amplitudes. As the amplitude increases there is more

interaction with the composite, due to the greater travel of the tip of the horn, and increased power consumption is expected. It should be noted that prior to all experiments the ultrasonic power consumption at all amplitudes was recorded as a baseline and subtracted from all processed material measurements.

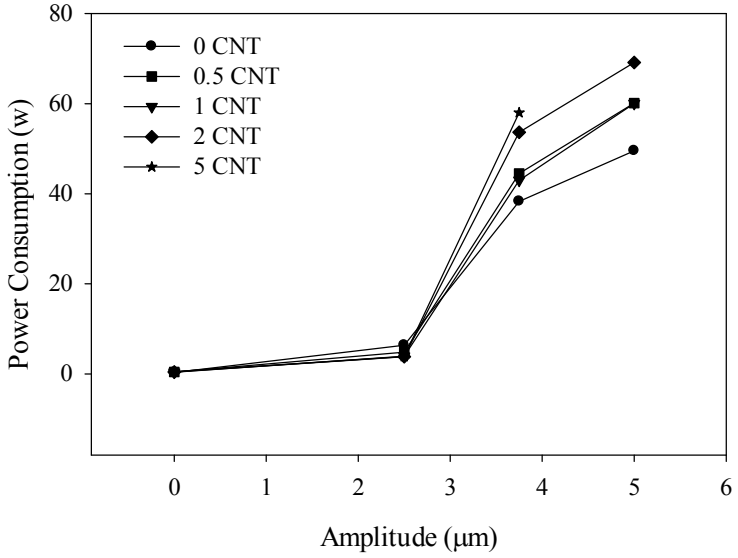

Figure 5.4: Power consumption versus amplitude of PETI-330/CNT composites for various concentrations

5.4 Rheology

Rheological properties were measured on an ARES, TA instruments using parallel plate configuration. The material was dried for 24 hrs at 100°C after processing, melted at 280°C and then compression molded into samples 2.0 mm thick x 25 mm in diameter. The molded disc was placed between parallel plates, melted, and then compressed to 1.5 mm. Overflow material around the plates was removed after compression using a razor

blade to minimize boundary effects. Testing was conducted using 25 mm parallel plate geometry in oscillatory shear mode with a frequency sweep test using a strain amplitude of 2% and a fixed temperature of 200°C. The complex viscosity, storage modulus, loss modulus and loss tangent were determined as a function of angular frequency. A

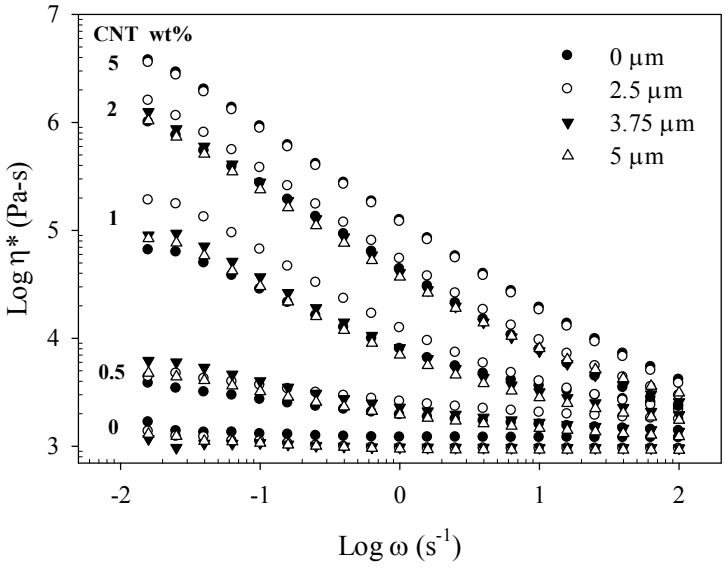

Figure 5.5: Complex viscosity of PETI-330/CNT nanocomposites measured at 200°C, 2% strain amplitude with and without ultrasonic treatment at various CNT concentrations as a function of frequency

relaxation time of 10 minutes after the samples were loaded and reached the testing temperature was used to minimize the normal force from squeezing the sample.

The complex viscosity of PETI-330/CNT nanocomposites untreated and treated are presented in Figure 5.5. Several things are observed in complex viscosity. An observable but very slight decrease in viscosity is seen in comparison of untreated and treated unfilled samples with all measured values being within 10% of each other. These unfilled samples show a nearly Newtonian behavior. However, filled samples show increasing

non-Newtonian behavior with increasing filler content. The effect of the CNT content is strongest at low frequencies and reduces with increasing frequency as the samples with greater than 1 wt% loading show a strong shear thinning effect. This is expected and has been previously observed in filled systems with high aspect ratio fillers [206, 207]. Filled samples progress from having nearly a Newtonian plateau at low frequencies for 0.5 and 1 wt% to complete non-Newtonian behavior at even low shear rates for concentrations of 2 and 5 wt%. The rheological percolation was found to be between 0.5 and 1 wt% CNT loading where an increase in viscosity of more than an order of magnitude is observed. An increase of 4 orders of magnitude in viscosity with the incorporation of up to 5 wt% CNT loading versus the neat matrix is observed. Ultrasonic treatment shows a significant effect on the rheological behavior at certain treatment levels. Notably, at a treatment amplitude of 2.5 μm a significant increase in viscosity is seen in samples containing 1 and 2 wt% CNT versus the untreated samples. This permanent increase in viscosity attributed to increased dispersion of the nanotubes and increased nanotube-matrix interaction at this loading. Treatment at higher ultrasonic amplitudes showed smaller changes in viscosity and resulted in values lower than that of 2.5 μm. This is believed to be caused by the breakage of the CNTs by the high power ultrasonic energy which shows a significant increase in power consumption at higher amplitudes and loadings as shown in Figure 5.4.

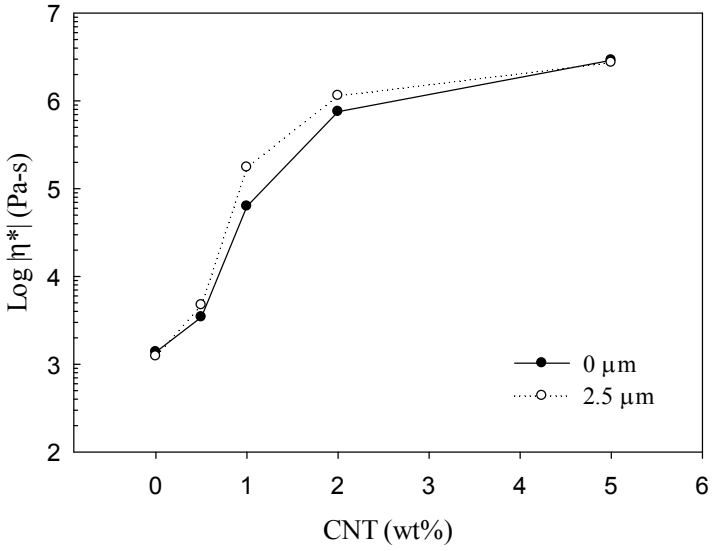

Figure 5.6: Complex viscosity of PETI-330/CNT nanocomposites measured at 200°C, 2% strain amplitude at a frequency of 0.0251 rad/s without and with 2.5µm ultrasonic treatment as a function of concentration

Figure 5.6 displays the complex viscosity of PETI-330/nanocomposites without and with 2.5 µm ultrasonic treatment at a frequency of 0.0251 rad/s. It is observed that there is a significant increase in the viscosity between the 0.5 and 1 CNT wt% loading. This is the observed rheological percolation of the system upon the incorporation of CNTs. This effect is greater in the sample treated at 2.5 µm versus the untreated sample.

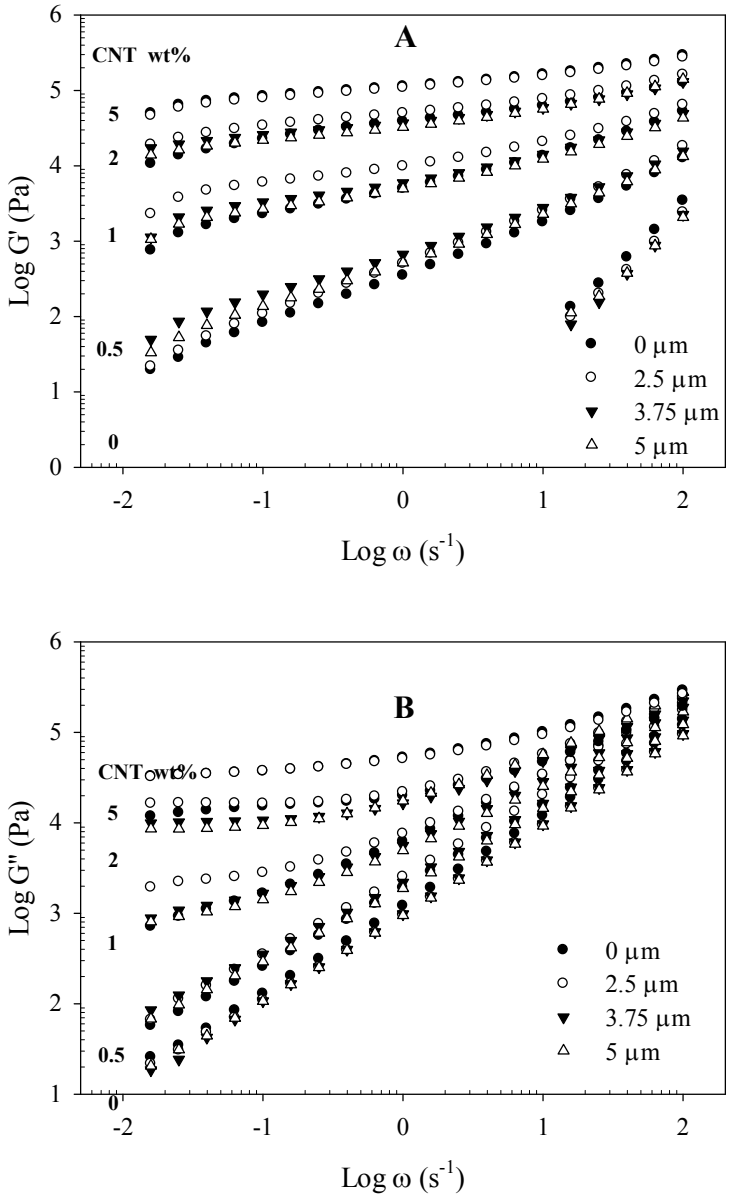

Figure 5.7: Storage (A) and loss (B) moduli of PETI-330/CNT nanocomposites measured at 200°C, 2% strain amplitude with and without ultrasonic treatment at various CNT concentrations as a function of frequency

The changes in the rheological properties is also observed in the storage and loss moduli presented in Figures 5.7 A and B, respectively. Corresponding to changes observed in the viscosity, it is observed that there is an increase in storage moduli at 2.5 μm at 1 and 2 wt%. A decrease in slope of both the storage and loss moduli with increasing filler content. This is indicative of interconnected structures within the matrix with large aspect ratios [208]. As the CNT concentration increases the interconnectivity increases, as shown by the increased plateau and increased values of G'. These results are in strong agreement with work by Schlea [209] who found the same trend and percolations for PETI-330/CNT nanocomposites processed using twin screw extrusion.

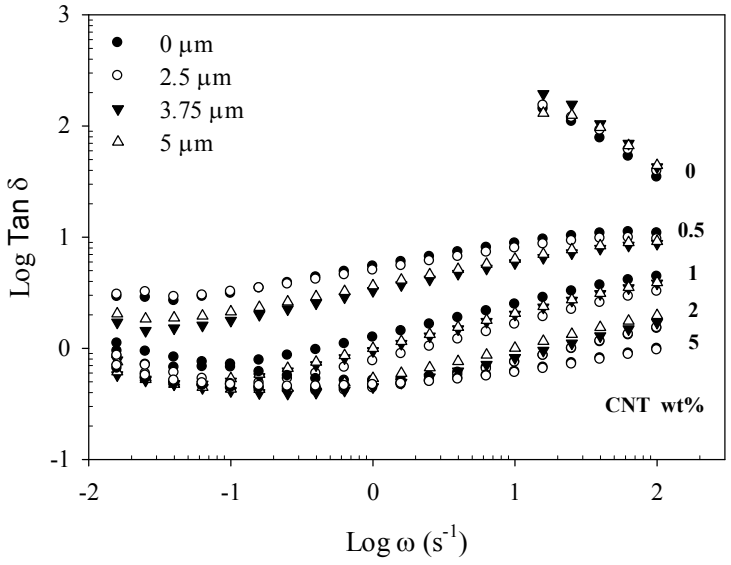

Figure 5.8: Tan δ of PETI-330/CNT nanocomposites measured at 200°C, 2% strain amplitude with and without ultrasonic treatment at various CNT concentrations as a function of frequency

Tan δ of both untreated and treated nanocomposites is presented in Figure 5.8. A strong decrease in Tan δ with increasing filler content is observed. This is attributed to increased interaction between the MWCNTs and the matrix. For 1 and 2 wt% loaded samples, treatment at 2.5 μm showed a decrease in Tan δ versus untreated sample.

The Cole-Cole plot for the treated and untreated PETI-330 nanocomposites is shown in Figure 5.9. Originally developed by Cole and Cole [210] in work on dielectrics, the so named Cole-Cole plot has been commonly used to study polymer rheology such as work by Harrell and Nakajima [211], Han [212] and others. The plot of log G' versus log G" provides useful insights into polymer systems. Harrell and Nakajima used a modified Cole-Cole plot to elucidate the effects of the molecular variations in the architecture of elastomers, specifically looking at the effects of branching and MWD. They showed that

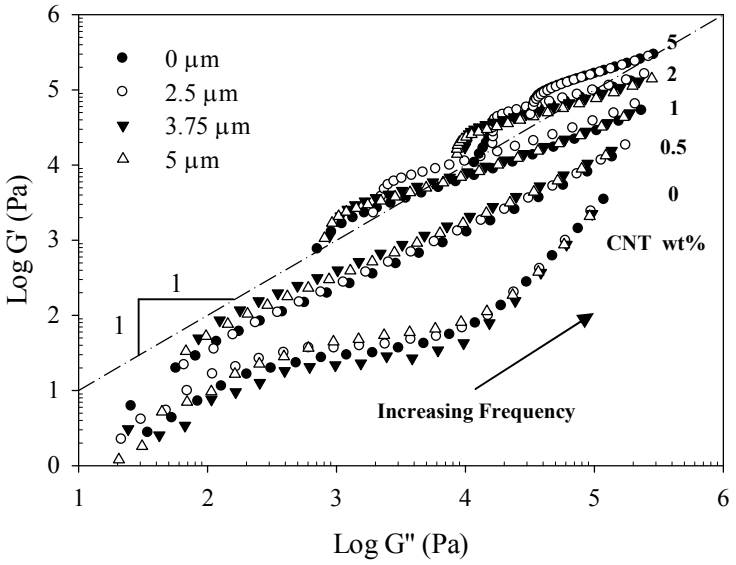

Figure 5.9: Cole-Cole plot of PETI-330/CNT nanocomposites measured at 200°C, 2% strain amplitude with and without ultrasonic treatment at various CNT concentrations.

a single plot, independent of molecular weight, can be used to distinguish changes in branching by shifts in the Cole-Cole plot to higher values of G' at constant values of G" at a constant temperature. Han used the Cole-Cole plot with binary blends to show that at molecular weights significantly greater than the entanglement molecular weight, the plots are independent of molecular weight and increase significantly when small amounts of a higher molecular weight material are added to a lower molecular weight material. As can be seen in Figure 5.9, the storage modulus increases substantially for a given loss modulus with increase in filler content. This increase in the storage modulus and deviation of the curve from the neat material points toward increasing changes in the microstructure of the composites.

5.5 Mechanical Analysis

PETI-330 and its nanocomposites were extruded and treated in their oligomeric form. Collected samples were then cured by the following process to obtain specimens for mechanical testing. Processed samples were first placed into a vacuum oven at 100°C and dried at -30 inHg vacuum. After drying, samples were placed into a pre-heated vacuum oven and degassed at 300^{o}C for 2 hours under full, constant vacuum of -30 inHg. Subsequently, the specimens were placed into a heated compression molding press, 300^{o}C, and compressed. The temperature was then ramped to 371^{o}C and held for one hour to complete curing. The ramp time from 300^{o}C to 371^{o}C was 25 minutes. Samples were removed from the press and placed between two steel plates, to remain flat, and allowed to cool to room temperature. An Isomet low speed saw (Buhler, Lake Bluff,

Illinois) equipped with a diamond blade and an oil bath was used to section the plaque into rectangles of constant widths specified under ASTM D638-02 Type V dog bones, 9.53 mm wide. These sections are subsequently clamped in a metal dog bone frame and machined using a Tensilkut high speed router (Model 10/21, Danbury, Connecticut) to obtain the neck section, 3.18 mm wide x 2 mm thick, and transitions of the dog bone with the smoothest finish possible, using a 1 inch diameter router bit.

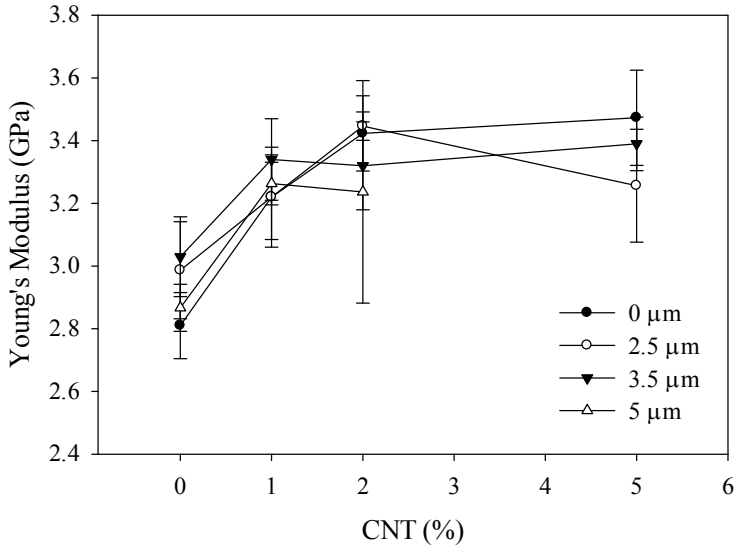

Figure 5.10: Young's modulus of PETI 330/CNT (wt%) nanocomposites treated at various ultrasonic amplitudes

The tensile properties were measured on an Instron test machine (Model 5567, Instron Corp., Canton, MA, USA). An extensometer with a gauge length of 0.3 inches was used for accurate modulus measurements in the low strain portion of the test. Testing was carried out on a minimum of five samples according to ASTM D638 testing procedures at a cross head speed of 5 mm/min using a 10 kN load cell. The Young's modulus, strength,

strain at break and toughness versus CNT concentration at various ultrasonic amplitudes are presented in Figures 5.10 to 5.13, respectively.

Figure 5.10 presents the measured Young's modulus of the nanocomposite samples. The manufacturer specification lists the material's modulus as 2.8 GPa [213]. The presented results for the neat, untreated material are in close agreement. It can be seen in Figure 5.10 that there is 20% increase in modulus with increasing concentration up to 2 wt% CNT for the untreated and treated samples. This is better than results on Triple A phenylethynyl terminated polyimide/MWNT by Ogasawara *et al.* [214] who found only a 7% increase in modulus up to a 3.3 wt% loading. Further loading to 5 wt% showed no further increase. This is also better than results on PETI-330/MWNT nanocomposites by Ghose*et al.* [147] who found injection molded plaques to have numerous defects due to voids that the data was rendered unusable. Ultrasonic treatment at 1 wt% showed a slight increase in modulus with treatment but all data falls within the range of error. While rheological data pointed to increased dispersion of the CNTs, strong adhesion between the CNTs and the PETI-330 matrix is required to obtain maximum performance due to the incorporation of the carbon filler. It is believed that adhesion between the matrix in the solid state and the filler was not achieved after curing and therefore the synergistic effect of the high L/D nanotubes is not realized.

Figure 5.11 displays the strength at break of the PETI-330/CNT nanocomposites. The manufacturer specification lists the material's strength of 118 MPa [213]. The presented results for the neat, untreated material are in close agreement. No change in the ultimate strength is observed between 0 and 1 wt% loadings. This is similar to results by

Ogasawara *et al.* [214] who reported a decrease of more than 10% with a loading of 3.3 wt% MWNT in a phenylethynyl terminated imide.

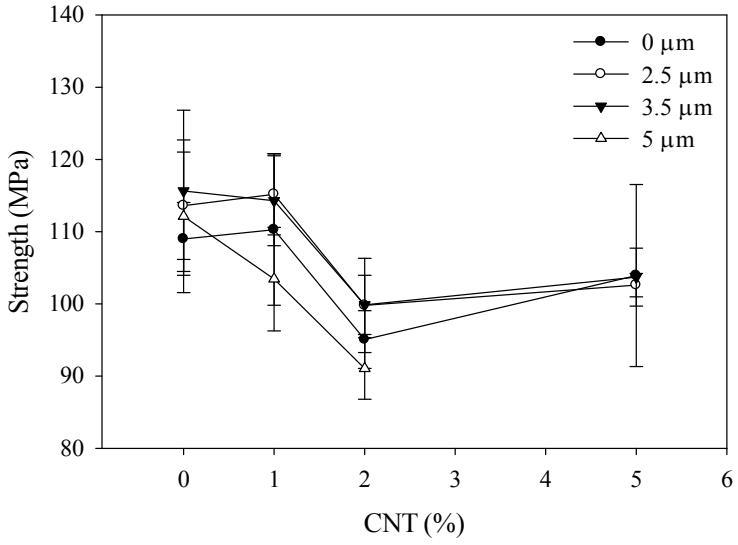

Figure 5.11: Ultimate strength of PETI-330/CNT nanocomposites treated at various ultrasonic amplitudes

However, upon increasing the loading to 2 and 5 wt% a decrease in the ultimate strength is observed. At the high treatment level of 5 µm, there is no difference in properties compared to the untreated sample at 0 wt% loading. However, upon the incorporation of nanotubes, a significant decrease in the ultimate strength is observed. During processing the ultrasonic energy consumption was very high at this treatment level, as seen in Figure 5. 4. The energy consumption was too high to obtain a sample at 5 wt%treated at 5 µm. This sample could not be obtained as the ultrasonic power supply continuously tripped, turned off, due to the high power consumption. It is believed that this high energy

consumption resulted in the breakage of the CNTs, creating stress concentrators, which caused the sample to break prematurely. It is suspected that stress concentrators introduced while routering the samples into the dog bone test shape increased the variability between samples giving rise to higher than expected error bars.

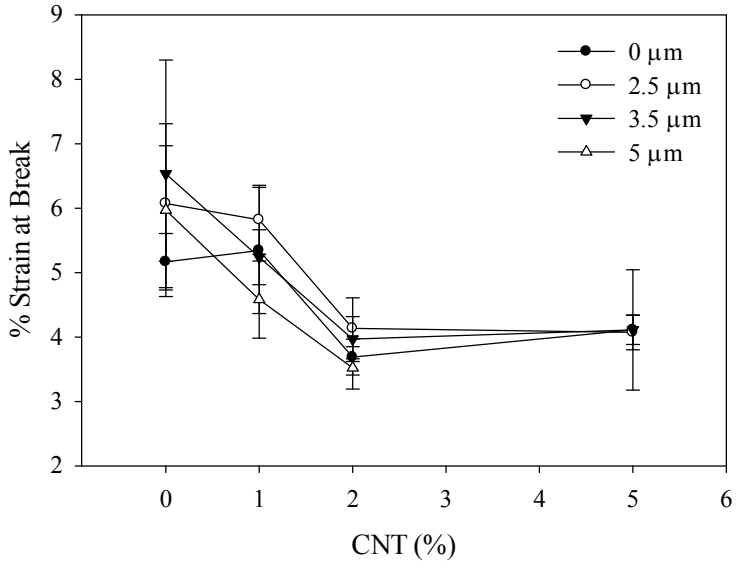

Figure 5.12: Strain at break of PETI 330/CNT nanocomposites treated at various ultrasonic amplitudes

The strain at break of the PETI-330/CNT nanocomposites is displayed in Figure 5.12. The manufacturer specification lists the material's strain at break as 8% elongation [213]. The presented results for the neat, untreated material is 6.1% and is lower than manufactures' data. It is believed that small cuts that are introduced into the dog bone sample through the router process acted as stress concentrators and caused premature failure in some samples, leading to the lower elongation at break and high sample

variability. These results are in agreement with work by Ogasawara *et al.* who found a decrease of nearly 50% at a loading of 3.3 wt% MWNT in a phenylethynyl terminated imide. The elongation at break continuously decreases with increasing filler concentration, as expected for filled materials.

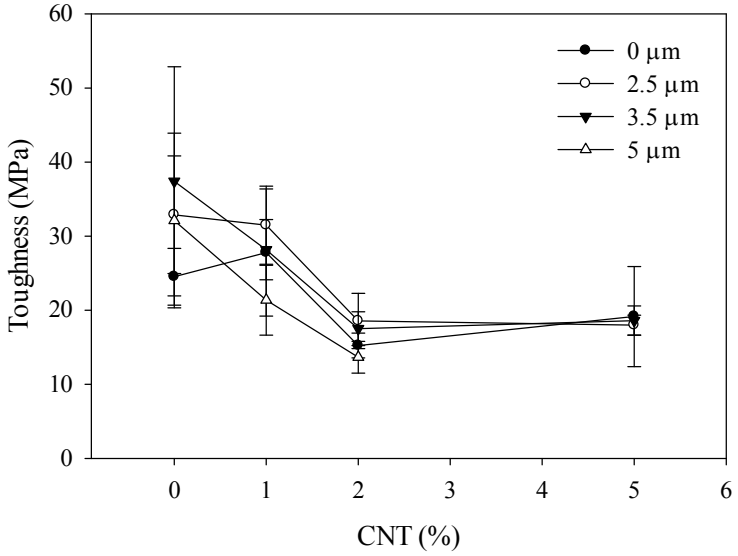

Figure 5.13: Toughness of PETI-330/CNT nanocomposites versus concentration for various ultrasonic amplitudes

The toughness of PETI-330/CNT nanocomposites is shown in Figure 5.13. The toughness decreases with increasing CNT concentration above 1 wt% loading, following the same trend as the elongation at break shown in Figure 5.16. As the carbon nanotubes increase the stiffness of the composite the rigid nature allows for less plastic deformation.

5.6 Thermal Analysis

Differential Scanning Calorimetry (DSC) was performed on all composites after curing using a TA instruments calorimeter (Q200, TA instruments, New Castle, DE, USA). Cured PETI-330 nanocomposite samples of approximately 10 mg were sealed in hermetic pans and heated at 10°C per minute from room temperature to 450°C in a nitrogen environment and analyzed for first and second order transitions using the TA Instruments Universal Analysis program. The tabulated data is an average of three tested samples. A typical DSC trace of neat PETI-330, post cure, is seen in Figure 5.14.

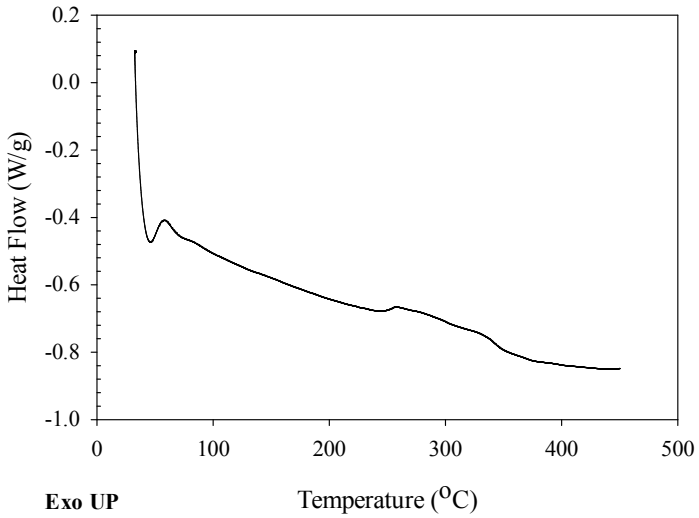

Figure 5.14: DSC scan of neat cured PETI-330 at a heating rate of 10°C/min from room temperature to 450°C as a function of temperature in air

The only transition observed in the cured plaques is the glass transition temperature occurring around 334°C. This is in agreement with literature on PETI-330[215]. Table

5.2 is the tabulated data of glass transitions for all of the produced samples. No variation was observed in the glass transition temperature due to either nanotube content or ultrasonic treatment. Since the material was treated in the oligomer form and temperatures remained well under the reaction temperature no changes in glass transition temperature were expected. The glass transition temperature is in agreement with Schlea*et al.* [215] who found the glass transition temperature to vary according to process temperature. A T_g of 334°C is in alignment with their reported results of 337°C for a processing temperature of 200°C.

Table 5.2: Tg of PETI-330/CNT filled nanocomposites at various loading and ultrasonic treatment levels

Amplitude (µm)	**CNT (%)**	**T_g (°C)**	**STDEV**
0	0	334.1	0.5
2.5	0	334.6	0.9
3.75	0	333.7	0.2
5	0	335.6	0.6
0	0.5	333.8	0.1
2.5	0.5	334.9	1.3
3.75	0.5	334.1	0.3
5	0.5	335.8	0.7
0	1	334.6	0.0
2.5	1	335.0	0.6
3.75	1	335.3	0.6
5	1	335.9	0.7
0	2	333.9	0.8
2.5	2	333.3	0.9
3.75	2	333.5	0.6
5	2	335.6	0.5
0	5	334.8	0.1
2.5	5	335.4	0.9
3.75	5	334.7	0.1

TGA analysis was carried out according to section 3.4.2. Samples of approximately 10 mg were loaded into the furnace and samples were equilibrated at 30°C and then subsequently heated at 20°C per/min to 900°C in an oxygen environment. Figure 5.15 depicts the TGA traces for extruded PETI-330 for untreated and ultrasonically treated samples. No distinguishable differences were observed between untreated and treated samples. Since the samples were processed with ultrasonic treatment while the polymer was in its oligomeric form and the processing temperature was kept well below the reaction temperature during processing, no differences were expected. Samples were tested in an oxygen environment and negligible residue remained at the final temperature of 900°C.

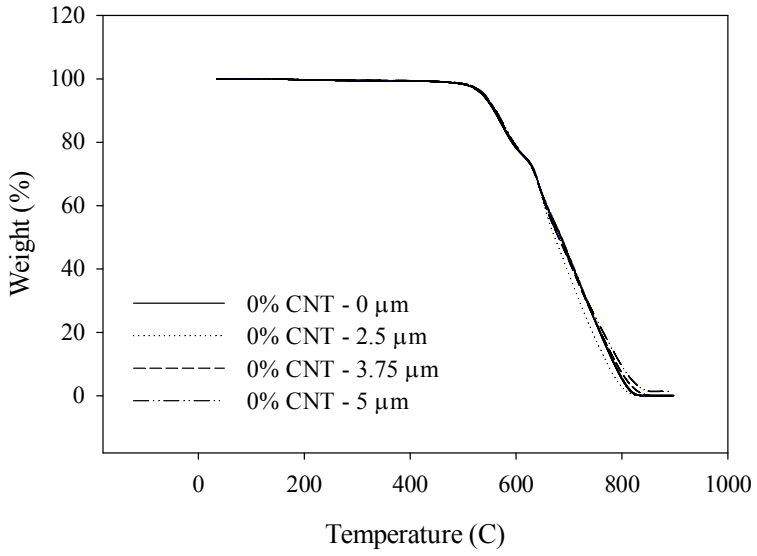

Figure 5.15: TGA weight loss analysis of neat PETI-330 extruded at different ultrasonic amplitudes in an oxygen environment as a function of temperature

Figure 5.16 shows the TGA traces for PETI-330/2% CNT nanocomposites with and without ultrasonic treatment as well as unfilled, untreated PETI-330 for comparison. Once again, no significant differences were observed due to ultrasonic treatment or CNT content for weight loss in an oxygen environment.

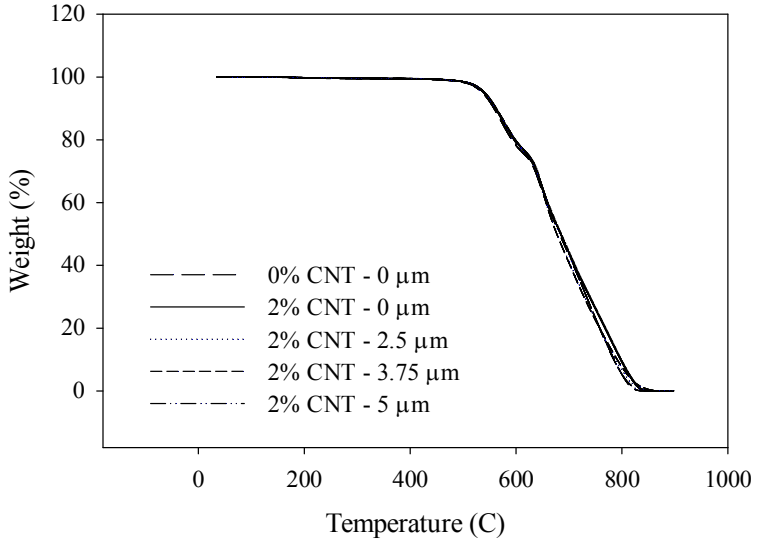

Figure 5.16: TGA analysis of 2% CNT filled PETI-330 nanocomposites in an oxygen environment as a function of temperature

5.7 Analysis of Electrical Properties

Two different methods were used to measure electrical conductivity and are described in detail in section 3.4.4. For the first method, a Keithley electrometer (Model 6517 A, Keithley Instruments, Cleveland, OH, USA) equipped with a model 8009 test fixture was used to test the volume resistivity of molded plaques in accordance with ASTM D257 testing procedures. This apparatus is designed to measure volume resistivity from 10^{18} to

10^3 ohm-cm. Alternating polarity was used with a baseline of 0 volts and an alternating voltage of +/- 1 volt. The method was set to take six reads for 10 seconds at each alternating voltage and then record the final read. The measurement was taken three different times for each sample and averaged. Standard deviation is reported.

The second method was designed and developed to test materials in the low resistivity region. A Keithley micro-ohmmeter (Model 580, Keithley Instruments, Cleveland, OH, USA) was used for both the output and input signals. The apparatus consisted of two cylindrical rubber blocks 64 mm in diameter that were coated on one side with 3M™ conductive film CN-3190 (3M, Saint Paul, MN, USA). The sample was placed between the two rubber blocks with the conductive side facing the sample. The blocks and samples were squeezed and the electrodes for both the input and output signals were pressed against the conductive film and a measurement was taken. The measurement was taken three different times for each sample and averaged. Standard deviation is reported.

The volume resistivity versus CNT concentration is shown in Figure 5.17 A and Bat various ultrasonic amplitudes for methods 1 and 2, respectively. As can be seen from the results, the electrical percolation lies between 0 and 0.5 wt% CNT loading. A further decrease was seen with increasing the loading up to 1 wt% loading but further decrease at loadings up to 5 wt% was not seen in method 1. However, a continuous decrease in resistivity with increasing concentration was observed using method 2. This points to the importance of verification of the limits of the method being used. For the present work method 1 was not able to distinguish differences at concentrations greater than 1% while

method 2 was not able to measure at resistivities higher than 10^8 ohm-cm. No significant difference is observed between treated and untreated samples.

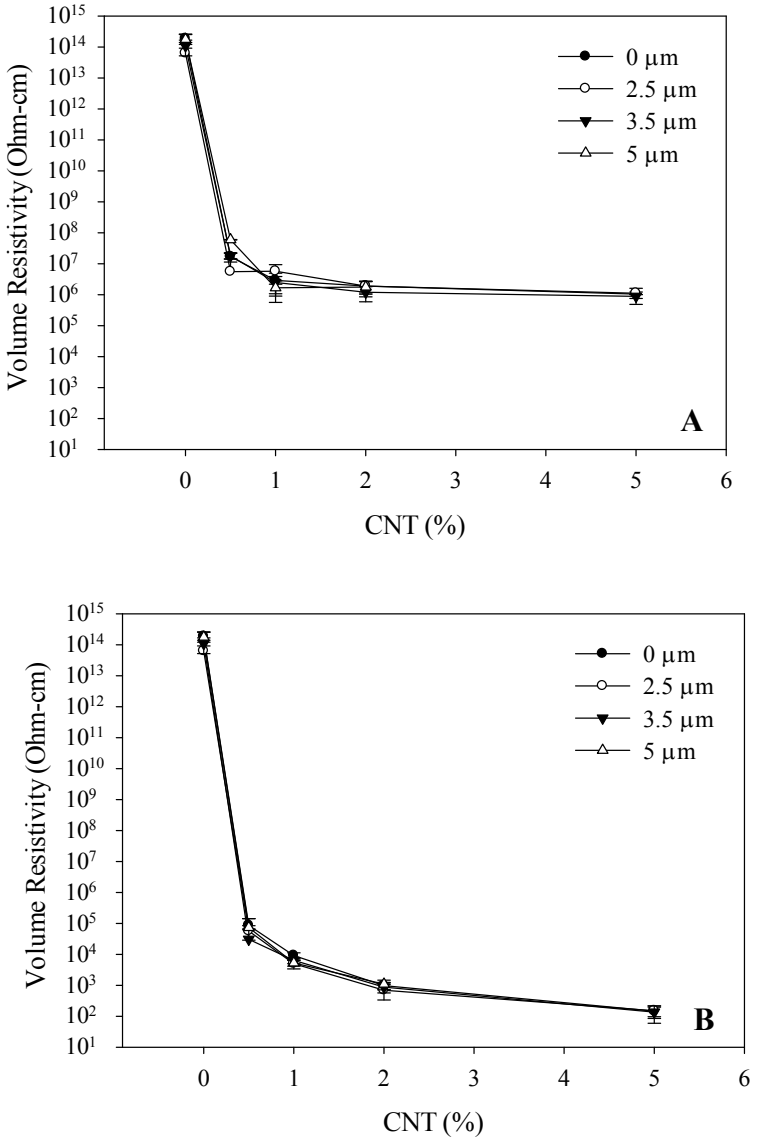

Figure 5.17: Volume resistivity of PETI-330\CNT (wt%) nanocomposites versus concentration for various ultrasonic amplitudes using method 1 (A) and method 2 (B)

5.8 Microscopy

Cryogenically fractured samples were evaluated using high resolution scanning electron microscopy (HRSEM). HRSEM micrographs of samples with 1 wt% CNT loading are shown in Figure 5.19 without (A) and with2.5 µm amplitude ultrasonic treatment (B). It is clearly seen in the micrographs that clusters of nanotubes exist in the untreated sample while the nanotubes in the sample treated at 2.5 µm show increased dispersion of the CNTs. These micrographs are characteristic of what was seen in several samples. To get a larger overview, optical micrographs of samples were also taken. As can be seen in Figure 5.20, samples without (A and B) and with 5 µm ultrasonic treatment (C and D) are observed to have remaining clusters of CNT. However, it can be seen that the clusters in the untreated samples are significantly larger than the clusters observed in the treated samples. While full dispersion of the CNT has not been achieved,

A B

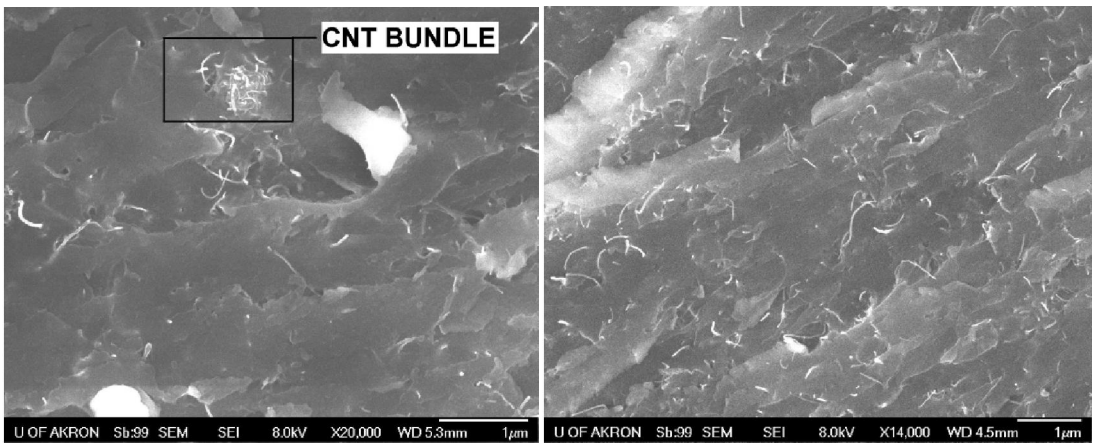

Figure 5.18: HRSEM micrograph of PETI-330\1 wt% CNT without (A) and with 2.5µm ultrasonic treatment (B)

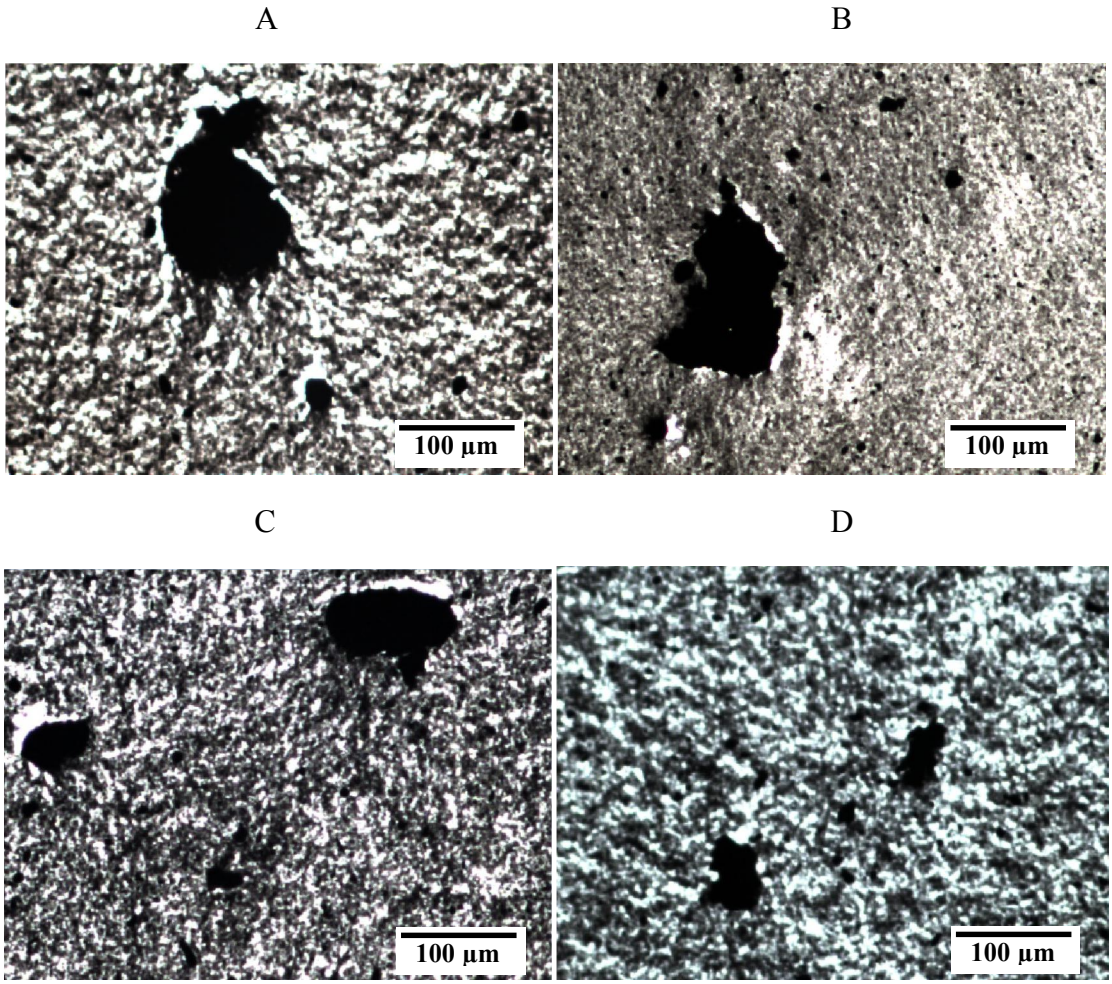

Figure 5.19: Optical Micrographs of PETI-330/2 wt% CNT nanocomposites without A,B and with 5 um ultrasonic treatment C,D at 100X magnification

there was a significant increase in the dispersion of the agglomerates in the ultrasonically treated samples.

5.9 Conclusions

Ultrasonically assisted extrusion has been used to processes PETI-330/CNT nanocomposites. Treated samples showed increased viscosity due to improved dispersion at certain amplitudes with an increase in viscosity of nearly 4 orders of magnitude upon the incorporation of 5 wt% CNT. The incorporation of CNTs into PETI-330 showed improvements in mechanical properties with a 20% increase in modulus with increasing loading concentration up to 2 wt% CNT for the untreated and treated samples. A rheological percolation level of 1 wt% was observed. Electrical percolation was achieved at a concentration 0.5 wt% CNT with drop in resistivity of more than 9 orders of magnitude. A further decrease in resistivity was seen with increasing filler concentration with a decrease in resistivity of almost 12 orders of magnitude at a 5 wt% CNT loading. Nanocomposites become electrically dissipative at 0.5 wt% CNT loading and were in the low conductivity range at 5 wt% CNT. Both HRSEM and optical micrographs of untreated and treated samples show increased dispersion of agglomerates in the treated samples. No change in thermal stability in TGA analysis was observed. While an increase in modulus is observed, it is believed that a lack of adhesion between the matrix in the solid state and the CNTs inhibits the full utilization of the CNTs for the enhancement of the mechanical properties after curing.

CHAPTER VI

HIGH TEMPERATURE RESIN TRANSFER MOLDING OF PETI-330/CARBON FIBER FABRICS

6.1 Introduction

High temperature resin transfer molding (HT-RTM) is an infusion process commonly used to produce composite parts with thermoset materials in conjunction with a fiber preform that is more affordable than conventional autoclave processes. In this method a mold with final part geometry is first filled with materials such as carbon or glass fabrics to provide enhanced properties or inserts that provide required functionality. The mold is thermally controlled to allow for differences in temperature during injection, curing, and/or post curing. The resin is heated and injected at a specified rate or pressure using a separate chamber where it can also be devolatilized. The process is very versatile for mold design and process variation. By controlling temperature, flow rate, and pressure composites can be manufactured to minimize voids, porosity, and part defects. For the following work, resin transfer molded plaques were molded for a project conducted with NASA Langley Research Center, Hampton, VA. Two different phenylethynyl imide matrix resins were used for their high glass transitions, high temperature and low oligomer viscosities and three different carbon fiber fabrics were used for mechanical property enhancement. Molded plaques were tested by NASA for physical and

mechanical properties under varying thermal conditions. The data reported here in is taken from their testing of the plaques manufactured in our laboratory.

6.2 Materials

Two resins were used as received. PETI-330 resin was obtained from UBE Chemicals Ltd, Japan and PETI-8 resin was obtained from Imitec Inc., Schenectady, NY, USA. The resins came in a yellowish, powder form. The glass transition temperature of cured resins are given in Table 6.1. Three different carbon fabrics were obtained from Textile Products, Inc., Anaheim, CA. They are listed in Table 6.2 with supplier provided information. A breather fabric, Release Ease^{TM} fabric, was used on the top and bottom of the plaque to facilitate venting and flow. A sealant tape, General Sealant A-800-3G from Airtech, was used around the edges of the mold through the thickness of the plaques to prevent jetting of the low viscosity PETI materials.

Table 6.1: Glass transition temperatures of phenylethynyl imides used [201]

Resin	Post Cured Tg
PETI-8	300°C
PETI-330	330°C

Table 6.2: Properties of the carbon fabrics used [201]

Carbon Fabric	Sizing	Areal Weight	Weave
IM7-6K	GP	280 g/m^2	5-harness Satin Weave
T650-35-3K	309	366 g/m^2	8-harness Satin Weave
IM7-6K	GP	160 g/m^2	Unidirectional Weave, Stick String 450 1/0 fill fiber

6.3 Experimental Procedures

This project was in collaboration with NASA Langley (LaRC). The guidelines for the fabrication of the plaques were are as follows:

- Panel dimensions shall be a minimum of 12" x 12" (30.48 cm x 30.48 cm)
- Void content shall be less than 2%, verified by acid digestion
- Fiber volume fraction shall be greater than 58%, verified by acid digestion
- The layups shall consist as specified in Table 6.3
- Resins shall be infused at 260°C (PETI-8) and 316°C (PETI-330)
- Panels shall be cured at 371°C for 1 hour

Table 6.3: Plaque configurations

Resin	Fabric	# of Plies	Plaque #
PETI-8	T650-3K	8	1
	IM7-6K	10	2
	IM7-Uni	10	3
	IM7-Uni	20	4
PETI-330	IM7-6K	10	5
	IM7-Uni	10	6

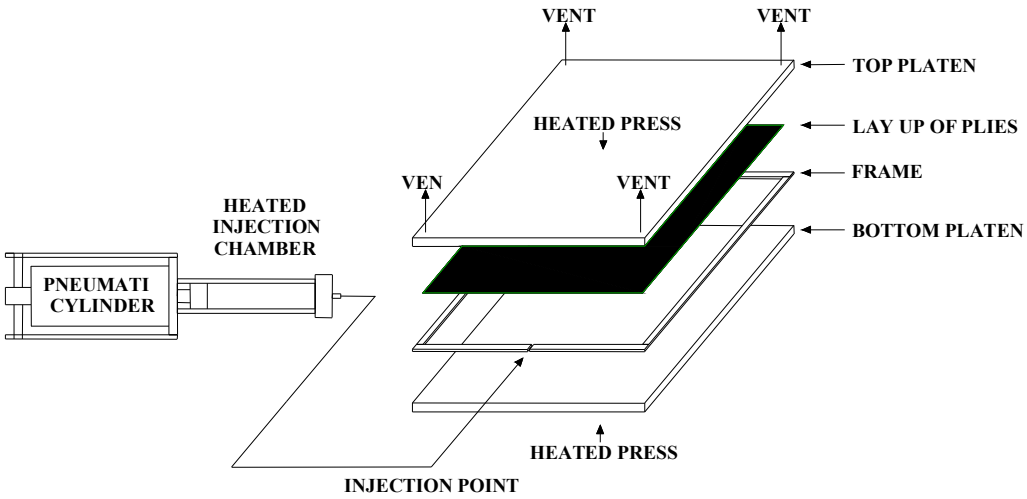

Figure 6.1: Schematic representation of RTM system used for the manufacturing of composite laminates

A mold was designed in house for the process and is depicted in Figure 6.1. It consisted of two plates, top and bottom, 34.3 cm x 34.3 cm x 1.3 cm in size and made of 4140 steel and 1/8" (3.175 mm) holes were drilled and tapped into each corner of the top plate to allow venting during fill and were closed during curing. In order to meet the minimum 58% fiber volume requirement the thickness of the mold was adjusted for each plaque. Using the number of specified plies and the specifications of the carbon fabric the required thickness for each plaque was calculated according to required fiber volume fraction of 58%. A sample calculation of the thickness of the mold is detailed for Plaque #2:

$$Fabric\ \ Areal\ Weight = 280\frac{g}{m^2}$$

$$Area\ per\ ply = 31.75cm * 31.75cm = 1008.06cm^2$$

$$Total\ Area = 1008.06cm^2 * 10plies = 10080.62cm^2 = 1.008m^2$$

$$Weight = 280\frac{g}{m_2} * 1.008m^2 = 282.25g$$

$$FiberVolume = \frac{1cm^3}{1.77g} * 282.25g = 159.46cm^3$$

$$Total\ Volume = \frac{159.46cm^3}{0.58} = 274.94cm^3$$

$$Plaque\ Thickness = \frac{274.94cm^3}{(31.75cm)^2} = 0.27cm = 2.7mm$$

Steel frames were made according to the calculated thickness, as demonstrated above, for each plaque and was secured to the bottom plate. Three layers of Teflon™ pipe thread tape was used above and below each frame to enhance sealing. The carbon fabric plies and breather cloth were cut on a 24 inch paper cutter to maintain the dimensions of the mold. Cloth and fabric plies were cut to 32.2 cm square. A sealant tape was used along the edge of the plies to prevent jetting of the matrix along the walls of the mold. The tape was squeezed into strips 0.5 mm in thickness between sheets of wax paper and subsequently cut into 3.1 mm strips. Numerous strips of the sealant tape were used and the layup of the plies and sealant strips are listed in Table 6.4 according to the number of plies required. All sealant tape was kept 1.5 cm away from the injection port and all vents. The injection point was located at the center of one edge of the frame and was 3 mm wide

with a thickness equivalent to the thickness of the frame. After filling the mold with the plies, breather cloth, and sealant tape it was placed in a high temperature Carver Compression Molding Press (CARVER 4122, Wabsah, IN) that was used to control the temperature of the mold. A photograph of the system use for HT-RTM is depicted in Figure 6.2. A clamping force of 107 kN was applied, full vacuum was drawn, and the temperature was raised to 400°C and held for two hours to remove the sizing on the carbon fabric. The vacuum was removed and the temperature was then lowered to the specified injection temperature, 316°C for PETI-330 composites or 260°C for PETI-8 composites. The injection system consisted of a 8.9 cm pneumatic cylinder with pressure control attached to a temperature controlled injection chamber 3.8 cm in diameter x 9 cm long. An aluminum plunger with Teflon® seals was attached to the piston shaft. A pressure of 0.28 MPa was used at the cylinder to provide an injection pressure of

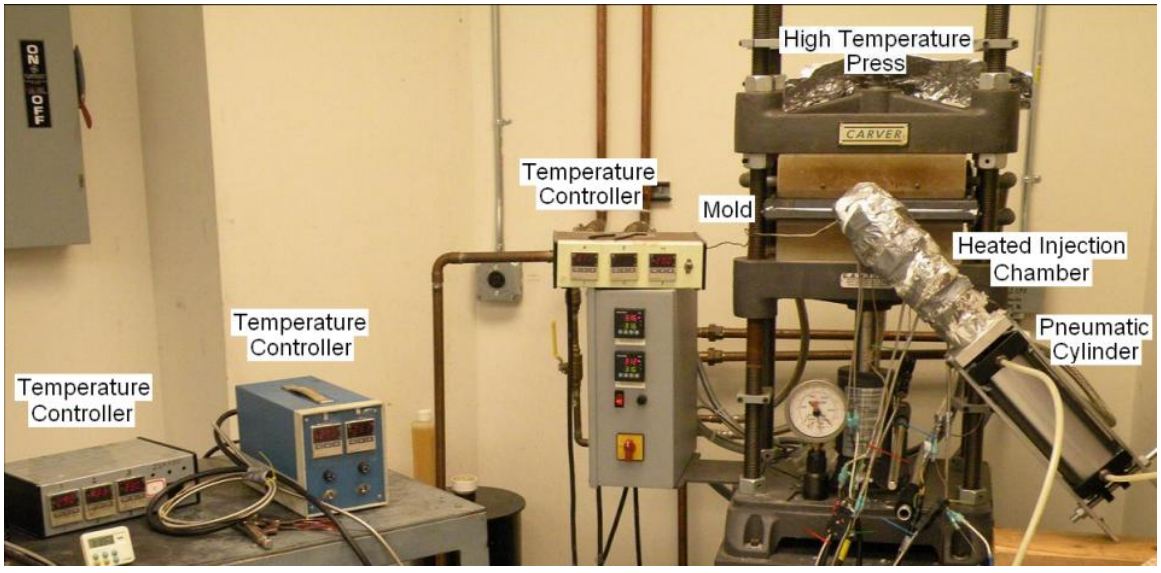

Figure 6.2: Photograph of RTM system used for the manufacturing of composite laminates

approximately 1.52 MPa. All exposed areas were insulated to maintain constant temperature.

The complex viscosity and temperature as a function of time are shown in Figures 6.3 and 6.4 for PETI-8 and PETI-330, respectively. From these graphs is can be seen that all measurements were at temperatures below the reaction temperature of the polymer. This is important for the degassing stage as any curing of the material would inhibit flow during the injection stage. As can be seen in Figure 6.3, PETI-8 is stable at a temperature of 260°C for more than 2 hours. Likewise, it can be seen from Figure 6.4 that PETI-330 is stable at temperatures up to 280°C for periods over 2 hours.

Table 6.4: Ply Stack Layup Configurations

8 Ply Configuration: Plaque # 1:	**10 Ply Configuration: Plaque 2, 3, 5, 6:**	**20 Ply Configuration: Plaque # 4:**
Breather Fabric	Breather Fabric	Breather Fabric
Sealant Tape	Sealant Tape	Sealant Tape
2 Plies	2 Plies	2 Plies
Sealant Tape	Sealant Tape	Sealant Tape
2 Plies	2 Plies	3 Plies
Sealant Tape	Sealant Tape	Sealant Tape
2 Plies	2 Plies	5 Plies
Sealant Tape	Sealant Tape	Sealant Tape
2 Plies	2 Plies	5 Plies
Sealant Tape	Sealant Tape	Sealant Tape
Breather Fabric	2 Plies	3 Plies
	Sealant Tape	Sealant Tape
	Breather Fabric	2 Plies
		Sealant Tape
		Breather Fabric

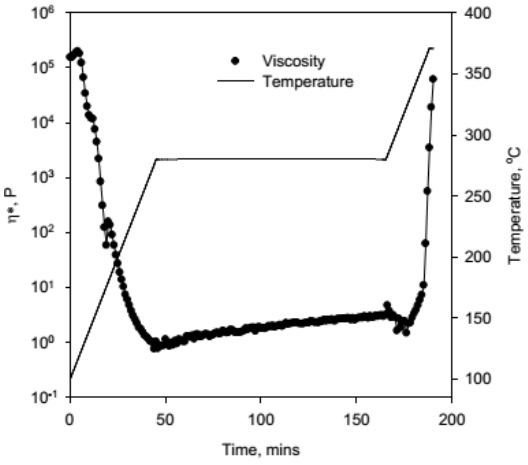

Figure 6.3: Complex viscosity and temperature as a function of time for PETI-8 held for 2 hours at 260°C [216]

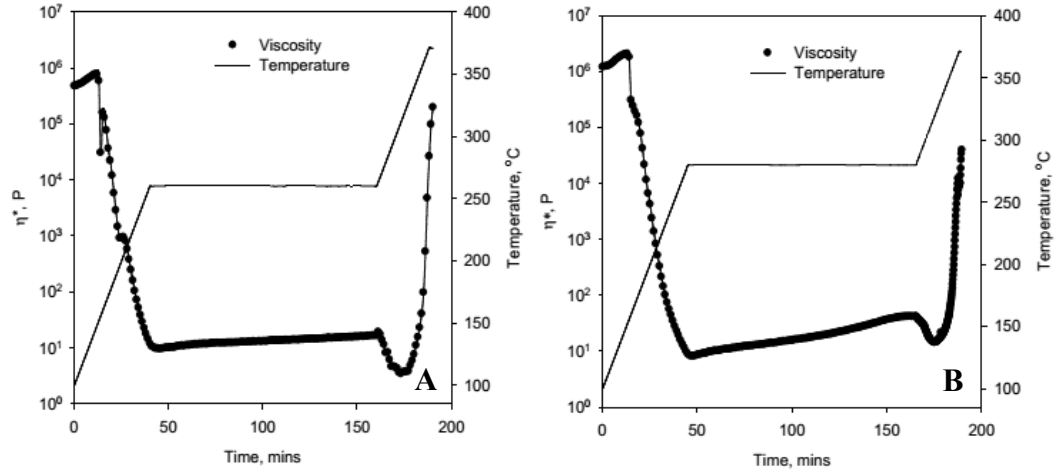

Figure 6.4: Complex viscosity and temperature as a function of time for PETI-330 held for 2 hours at 260°C (A) and 280°C (B) [216]

6.4 Physical Testing

All plaques produced were subsequently sent to NASA Langley for evaluation. The following testing and techniques were used to evaluate the physical properties of the produced plaques and is taken from the paper by Ghose*et al.*[201] of which I am a co-author. Acid digestion of the cured composites was done according to ASTM D3131. Specimens were weighed to the nearest 0.1mg and submerged in 30 ml of sulfuric acid. The mixture was heated on a hot plate under a fume hood until evolved gas was observed. After 5 hours of heating 30 ml of 30% hydrogen peroxide was added to oxidize the matrix and it was allowed to cool. The mixture was subsequently filtered into crucibles, washed with distilled water, washed with acetone, dried for 4 hours at 160°C, cooled in a desiccator, and subsequently weighed. If any matrix was still observed the oxidation process the procedure was repeated before washing. Volume fractions were calculated using 1.77 g/cm^3 fiber density and 1.31 g/cm^3 resin density.

The physical mechanical properties were tested for short beam shear strength (SBS) according to ASTM D2344. The testing was performed in a temperature controlled environment. A Sintech 2W testing machine with 454 kg load cell was used. A rate of 1.27 mm/min was used for all tests.

6.5 Results

Several problems were encountered during this work. At the high devolatilization and curing temperatures the mold warped in the center. The platens must be heat treated and stress relieved. The warpage created a thickness variation with a reduction of thickness

near the center of the platen. This led to high resistance to the flow during injection causing the resin to circumvent this area and entrap air. The high temperature sealant was found to be required to prevent racing of the resin along the wall (the vertical edges around the mold next to the cut edges of the fabric). Without the sealant tape, the infused resin ran along the wall and encapsulated air. Maintaining a constant pressure gradient throughout the mold is important for uniform flow of the resin during infusion.

The HT-RTM panels had dry spots, areas where the matrix material did not penetrate due to pressure differences. Samples were taken from areas where the matrix had wet out the carbon fabrics. Figures 6.5 and 6.6 are optical micrographs of PETI-330/IM7-6K and PETI-8/IM7-6K panels, respectively, made by high temperature resin transfer molding. As can be seen in the micrographs, the areas that were wet out during the HT-RTM process were completely wet out without any visible voids. Acid digestion verified that void volume content in the HT-RTM plaques was very low, 2.1% on one plaque and less than 1 % on the remaining plaques, as tabulated in Table 6.5. This is significantly lower than the same plaques made by vacuum assisted resin transfer molding (VARTM) by another research lab for the same project. The VARTM plaques ranged from 2.5 to 3.3 % void volume[201], however, the plaques were completely wet out. The void content is important for aerospace applications where a void fraction of less than 2% is required.

Table 6.5: Void and fiber volume content of HT-RTM plaques [201]

Resin	Fabric	Void Vol. %	Fiber VolumeWt. %
PETI-8	T650-3K	2.1	64.9
	IM7-6K	0.7	59.3
	IM7-Uni	0.6	61.3
PETI-330	IM7-6K	0.9	60.2

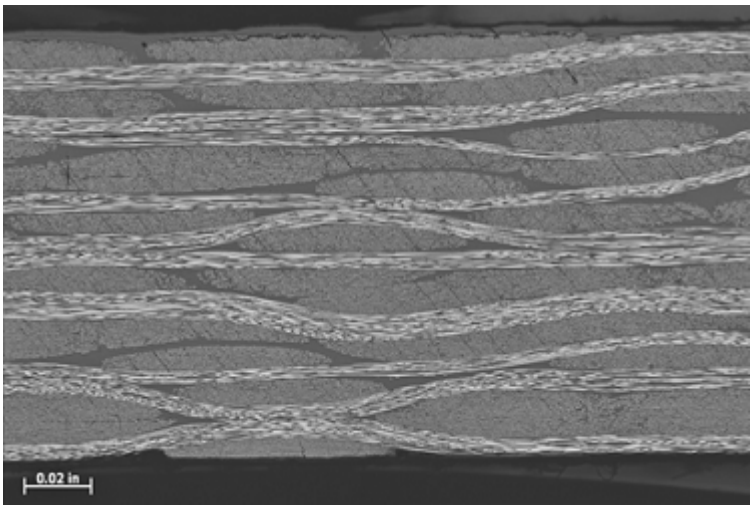

Figure 6.5: Laminate of PETI-330/IM7-6K made by HT-RTM [201]

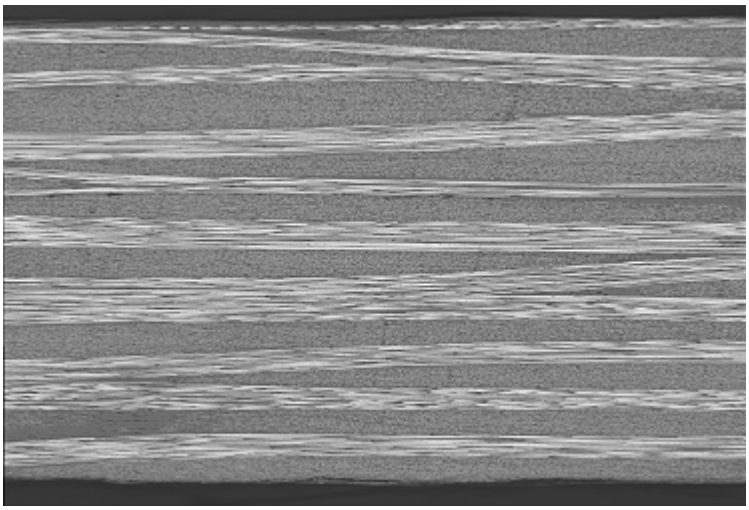

Figure 6.6: Laminate of PETI-8/IM7-6K made by HT-RTM [201]

Short beam shear testing on the HT-RTM plaques was promising. Figure 6.7 depicts the SBS results for PETI-8 plaques, both RTM and VARTM, over a range of temperatures. It is observed that the strength of the RTM plaques produced during this research tested significantly higher. The Uni-weave fabric tested the highest for all samples which is expected from the anisotropic layup of the carbon fibers. While the RTM plaques tested higher for Uni-weave and T650 layups at all temperatures and equal for IM7 layup at all temperatures compared to VARTM plaques, the retention of properties with the increase in temperature was slightly less. From room temperature (RT) to 177°C RTM plaques had retention of 62% and 76% for the Uni-weave and T650 plaques, respectively. Correspondingly, VARTM plaques had 68% and 89% for the Uni-weave and T650 plaques, respectively. Similar results were observed for PETI-330 RTM and VARTM plaques for SBS as shown in Figure 6.8. Testing at room temperature showed RTM plaques to have strengths higher than their VARTM counterparts. However, at 232°C the difference in values was negligible and at 288°C the strengths of the VARTM plaques were higher than the RTM counterparts.

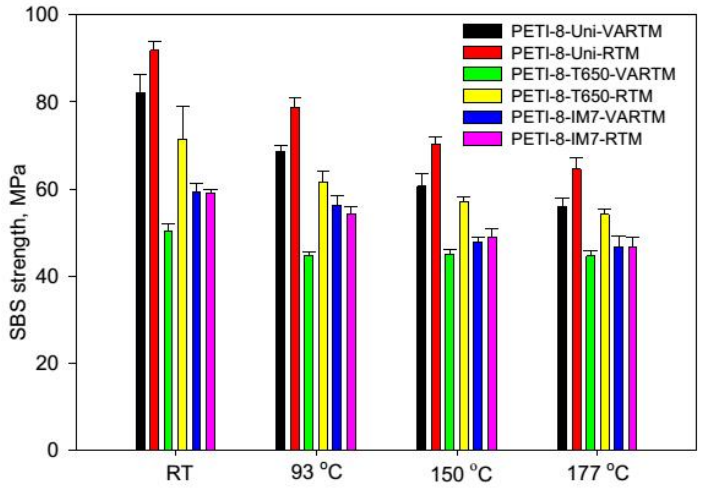

Figure 6.7: Short beam shear strength of PETI-8 plaques of various carbon fabrics [201]

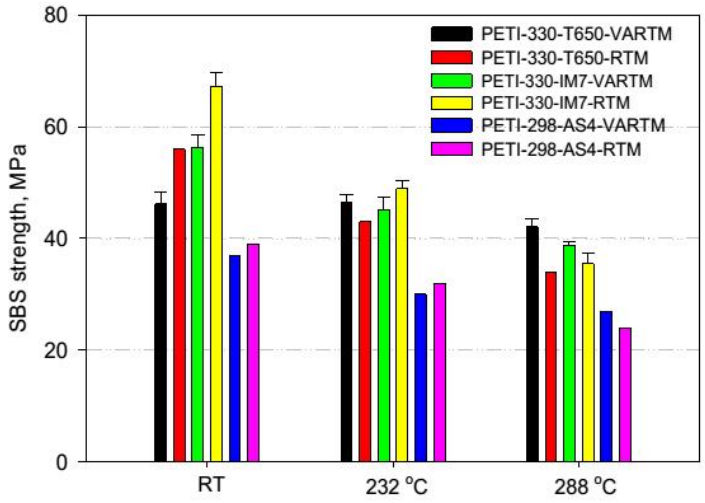

Figure 6.8: Short beam shear strength of PETI-330 with various carbon fabrics and PETI-298 with AS 4 fibers from a previous study [201, 217]

6.6 Conclusions

An apparatus for producing high temperature resin transfer molded plaques was designed and manufactured. While several plaques had dry spots, the areas that were infused had lower void fraction contents and superior short beam shear strength properties to those of the sample plaques made by VARTM at room temperature. However, plaques produced by HT-RTM did not have the retention of properties that the VARTM plaques had. It should be noted that while the RTM plaques had less retention than the VARTM plaques, RTM PETI-8 plaques had higher SBS values than VARTM PETI-8 plaques at all temperatures.

CHAPTER VII

CONTINUOUS HIGH POWER ULTRASONIC EXTRUSION OF PEEK 380P/CNT NANOCOMPOSITES

7.1 Introduction

PEEK is a semi-crystalline thermoplastic polymer with high mechanical performance and operating temperatures. In this chapter, the processing and characterization of PEEK 380P and its CNT nanocomposites for enhanced mechanical and electrical properties are studied. The nanocomposites for this study were processed using patented ultrasonically assisted twin screw extruder technology. Carbon nanotubes are known for their agglomeration during synthesis and this technology aids in the dispersion of CNTs by utilizing equipment that is currently used in industry aided by an ultrasonic energy. The focus of this chapter was the dispersion of CNTs in PEEK 380P for enhanced mechanical and electrical properties at loadings from 0-10 wt% CNT and in conjunction with a compatibilizer. Prepared nanocomposites were characterized for processing, rheological, mechanical, thermal, electrical and morphological characteristics.

7.2 Experimental Procedures

Polyetheretherketone in a white powder form was obtained from Victrex under the trade name PEEK 380P, and was used as received. It has a T_g of 145°C and a melting

temperature of 343°C. A regularly entangled grade of multiwalled carbon nanotubes was obtained from Nanostructured & Amorphous Materials and used as received. The CNTs have manufacture listed physical dimensions of outside diameters of 10-20 nm, inside diameters of 5-10 nm and lengths of 0.5-200 μm. These multi-walled nanotubes have a specific surface area of >200 m^2/g and a bulk density of 0.040-0.050 g/cm^3.

All materials were dried in a vacuum oven at 100°C for 24 hours prior to processing. A co-rotating twin screw micro-compounder (PRISM USALAB 16, Thermo Electron Corp. UK) with an ultrasonic slit die attachment at the exit of the extruder was used to compound the material, as described in Chapter 3.3.1 and depicted in Figure 7.1.

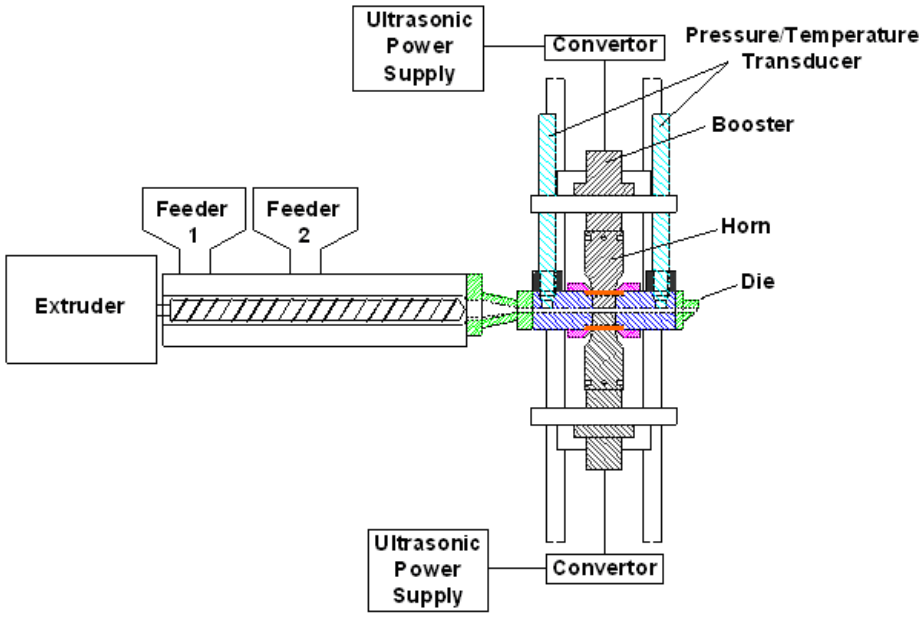

Figure 7.1: Micro-compounder with attached ultrasonic slit die - design A

The micro-compounder has a screw diameter of 16 mm and an L/D of 25. The matrix is fed into the throat of the extruder at feed port 1. To avoid the high stresses in the feeding zone, the CNT are fed separately downstream at a point where the matrix has already melted, between the first and second sets of kneading blocks shown in Figure 7.1 as feed port 2. The composite material then passes through additional mixing and ultrasonic treatment zones for the dispersion of the CNTs. In this design, depicted in Figure 5.1, the composite material exits the extruder and enters a die. This die consists of two ultrasonic horns directly opposed to each other located on either side of the melt with a flow channel that has a cross-section of 4 mm thick by 19 mm wide that is 114 mm long (0.157 x 0.75 x 4.5 in^3). The ultrasonic systems (Branson Ultrasonic Corp., CT, USA) have a maximum power output of 800 W and operate at 40 kHz. The horns have a 19 mm x 19 mm (0.75 x 0.75 in^2) area that contacts the polymer melt and are situated in the middle of the die section directly in line with each other on opposing sides of the melt.

On both sides of the top ultrasonic system a pressure transducer/thermocouple has been installed to measure pressure and temperature before and after ultrasonic treatment. The horns are internally cooled using a constant flow water bath set at 95°C. The screw stack up was as follows starting at the feed throat: 7 - 1 L/D forward conveying, 6 - 1/4 L/D forward conveying kneading blocks with each block rotated 30 degrees from the last, 6 - 1/4 L/D neutral conveying kneading blocks with each block rotated 90 degrees from the last,4 - 1 L/D forward conveying, 4 - 1/4 L/D forward conveying kneading blocks with each block rotated 30 degrees from the last, 3 - 1 L/D forward conveying, 4 - 1/4 L/D forward conveying kneading blocks with each block rotated 30 degrees from the last,

6 - 1/4 L/D neutral conveying kneading blocks with each block rotated 90 degrees from the last,3 - 1 L/D forward conveying, 1 - 1.5 L/D forward pumping. This technology is covered under US patent application WO2007145918 A3.

The processing conditions used were as follows: a screw speed of 100 RPM, a feed rate of 454 g (1lb)/hr and an extrusion temperature profile of 350^{o}C for the feed throat and 390^{o}C for the remaining extruder zones. All die zones were set to 380^{o}C. The residence time in the ultrasonic treatment zone is approximately 12 seconds for the flow rate of 454g (1lb)/hr. All treatment was done using a Branson Ultrasonic System operating at 40 kHz and various amplitudes. Four different amplitudes and 5 different CNT concentrations were prepared. Table 7.1 is the testing matrix used for the PEEK 380P/CNT Nanocomposites. In addition to the effects of ultrasound, one compatibilizer was also evaluated for its affect on PEEK 380P/CNT nanocomposites.

Table 7.1: Testing matrix for PEEK/CNT nanocomposites processed on micro-compounder design A

CNT Concentration	RPM	Feed Rate (lb/hr)	Ultrasonic Amplitude (μm)
0	100	1	0, 2.5, 3.75, 5
1	100	1	0, 2.5, 3.75, 5
2	100	1	0, 2.5, 3.75, 5
5	100	1	0, 2.5, 3.75, 5
10	100	1	0, 2.5, 3.75, 5
5 (NZ 2%)	100	1	0, 2.5, 3.75, 5

The additive, Ken-React® CAPOW® NZ® by Kenrich Petrochemicals, New Zealand, was used at loading of 2 wt% at a concentration of 5 wt% CNT. The additive was added at the second feed throat with the CNTs.

7.3 Processing Characteristics

During extrusion the extruder torque as a % of max torque and ultrasonic power consumption were recorded using an online data acquisition system. As seen in Figure 7.2, the torque increased with increasing CNT concentration, as expected due to the increase in viscosity of the system. Also observed is a constant decrease in torque with increasing ultrasonic amplitude. The torque decreased by 26% going from 50% torque with no treatment to 37% at a treatment at 5 μm for the neat material. This effect was consistent with increasing CNT loading, showing a decrease from 83% to 59%, a 29% decrease at 10 wt% CNT, the highest loading studied. This decrease in extruder torque was accompanied by a decrease in die pressure with increasing ultrasonic treatment as

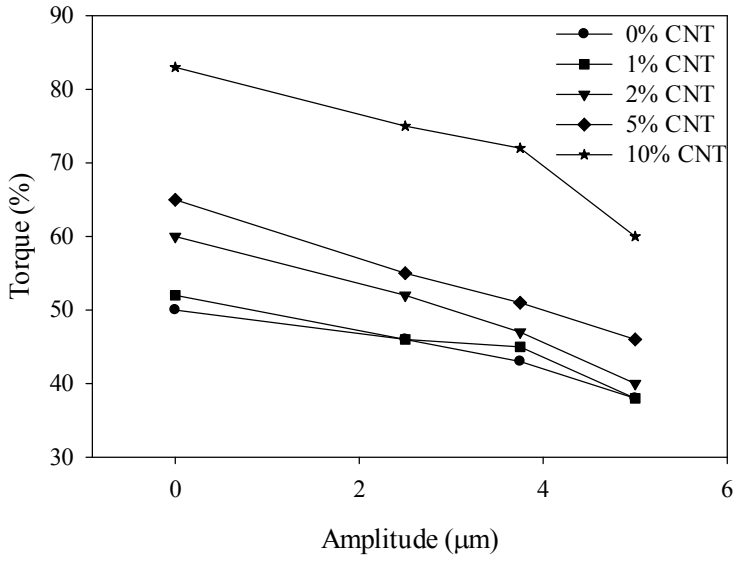

Figure 7.2: Extruder torque versus amplitude for various PEEK 380P/CNT nanocomposites

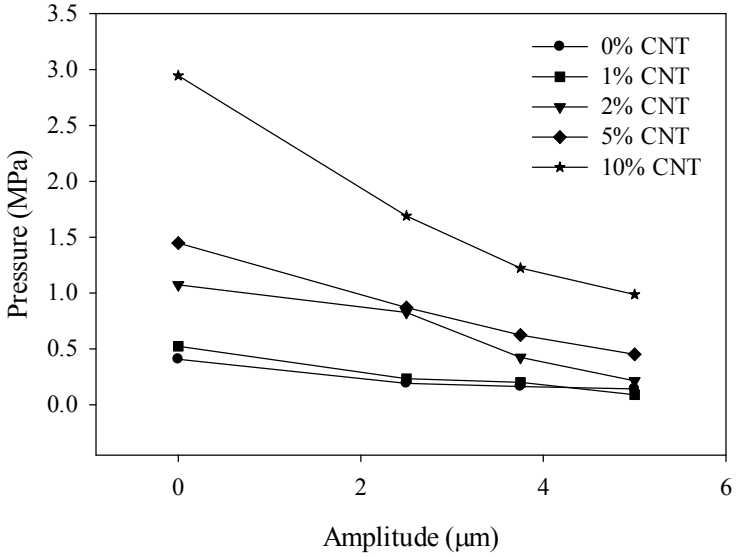

Figure 7.3: Die pressure versus ultrasonic amplitude for various PEEK 380P/CNT nanocomposites

displayed in Figure 7.3. The die pressure was measured after ultrasonic treatment just before the die. The decrease in torque and die pressure is attributed to both thermal and rheological effects. The vibration of the horn causes slip and decreased resistance to the flow of the polymer as well as a decrease in viscosity due to an increase in temperature from frictional heating at the surface of the horn and ultrasonic energy dissipation. These decreases are also due to a permanent decrease in viscosity of the filled nanocomposites with increasing ultrasonic amplitude seen in Figure 7.5. While no significant change in viscosity was observed in the neat, treated samples a decrease in viscosity is observed in filled samples. A general increase in power consumption with increasing concentration is also observed in the ultrasonic power consumption displayed in Figure 7.4. The ultrasonic power consumption increased significantly with increasing ultrasonic

amplitude at all concentrations, as seen in Figure 7.4. As the amplitude increases there is more interaction with the composite and increased power consumption is expected. It should be noted that prior to all experiments the ultrasonic power consumption at all amplitudes was recorded as a baseline and subtracted from all processed material measurements. It can also be seen that power consumption increases with ultrasonic amplitude. This is more prominent as filler loading increases which causes a corresponding increase in the viscosity. The power consumption at 5 μm is almost 30% higher for samples at 10% loading than that of the unfilled material.

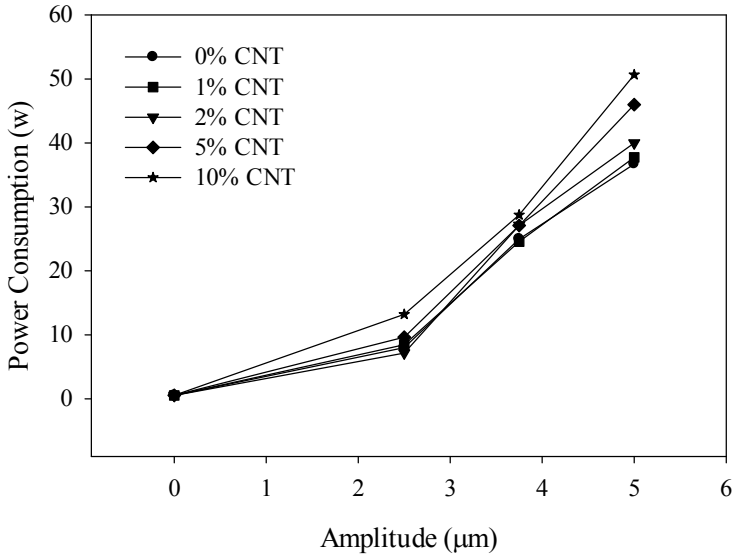

Figure 7.4: Ultrasonic power consumption versus amplitude for various PEEK 380P/CNT nanocomposites

7.4 Rheology

Rheology has been established as a method for elucidating difference in nanocomposite structures [126, 218-220]. Rheological properties were measured on an ARES, TA instruments using parallel plate configuration. The material was dried for 24 hrs at 100°C after processing, melted at 380°C and then compression molded into samples 2.0 mm thick. The molded disc was placed between parallel plates, melted, and then compressed to 1.5 mm. Overflow material around the plates was removed after compression using a razor blade to minimize boundary effects. Testing was conducted using 25 mm parallel plate geometry in oscillatory shear mode with a frequency sweep test using a strain amplitude of 2% and a fixed temperature of 360°C. The complex viscosity, storage modulus, loss modulus and loss tangent were determined as a function

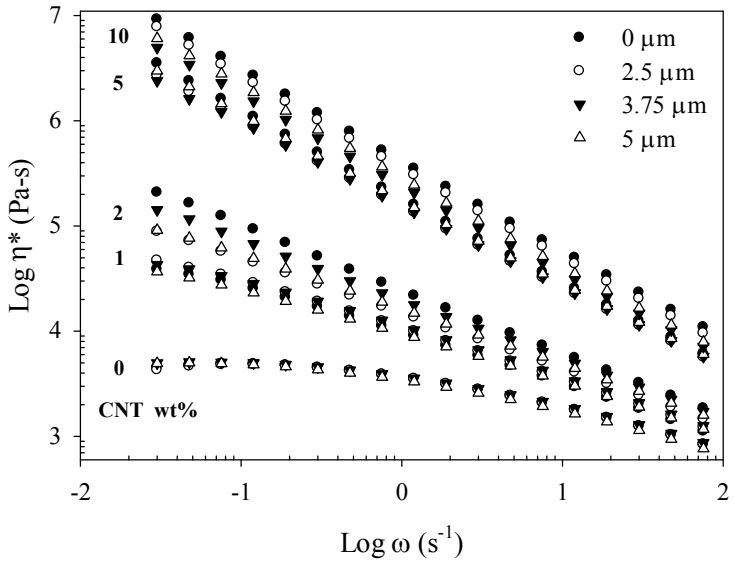

Figure 7.5: Complex viscosity versus shear rate for treated and untreated PEEK 380P/CNT nanocomposites as a function of frequency

reached the testing temperature was used to allow the normal force to diminish from squeezing the sample.

The complex viscosity of PEEK 380P/CNT nanocomposites untreated and treated are presented in Figure 7.5. The viscosity of the neat material is unchanged with ultrasonic treatment as shown by the overlapping curves. A Newtonian plateau is observed in the low frequency range of the neat material and becomes non-Newtonian with increasing frequency. As CNTs are incorporated into the composite a distinct trend is observed. First, at even the lowest concentration there is no Newtonian plateau observed. Secondly, all filled materials show a strong shear thinning behavior, as commonly observed for high

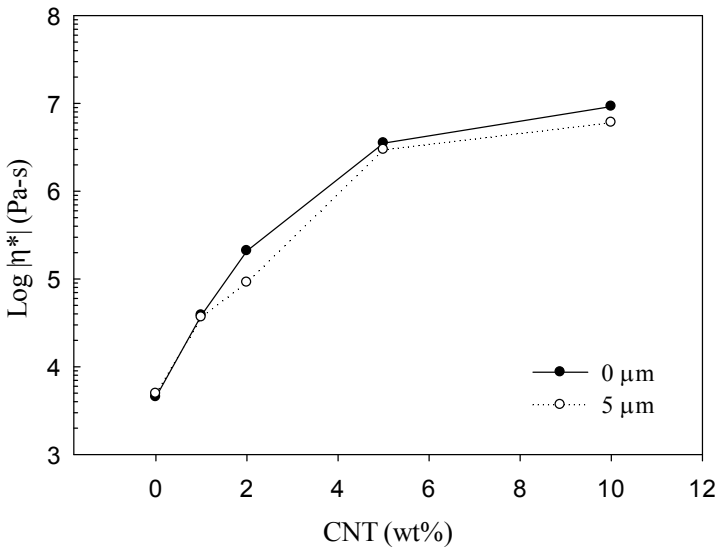

Figure 7.6: Complex viscosity of PEEK 380P/CNT nanocomposites measured at 360°C, 2% strain amplitude at a frequency of 0.0300 rad/s without and with 5μm ultrasonic treatment as a function of concentration

of angular frequency. A rest time of 10 minutes after the samples were loaded and L/D filler composites [206, 207].As expected, the viscosity increases with increasing filler content. An increase of more than an order of magnitude is observed between 0 and 1 wt% loadings and 2 and 5 wt% loadings. From this data, the rheological percolation lies between the 0 and 1wt% loadings. Most intriguing is the trend of decreasing viscosity with increasing ultrasonic amplitude. While the differences are less at high frequencies versus at low frequencies, they are still seen at higher frequencies. This decrease in viscosity with increasing ultrasonic treatment is believed to be caused by the breaking of nanotubes and polymer chains due to high power ultrasonic treatment. The power consumption during processing, displayed in Figure 7.4, increased significantly with both increasing ultrasonic amplitude and increasing filler content. The viscosity of untreated and treated samples increases with filler content. In addition, viscosity of treated samples decreases with ultrasonic amplitude with the effect being higher at higher loadings. Due to the physical design of the ultrasonic treatment section the flow in the ultrasonic section consists of only pressure driven flow. Due to this design, the material at the interface of the horn receives the greatest amount of treatment. At the high amplitude and high treatment times due to the limited flow rate of the extruder, some degradation of the composite was expected and is shown in the decrease in viscosity of the material.

Figure 7.6 displays the complex viscosity of PEEK 380P/nanocomposites without and with 5 μm ultrasonic treatment at a frequency of 0.0300 rad/s. It is observed that there is a significant increase in the viscosity between the 0 and 1 CNT wt% loading. This is the observed rheological percolation of the system upon the incorporation of CNTs.

Similar trends in the storage and loss moduli, Figure 7.7 A and B, were observed. The storage modulus increases dramatically with increasing filler content with an increase of

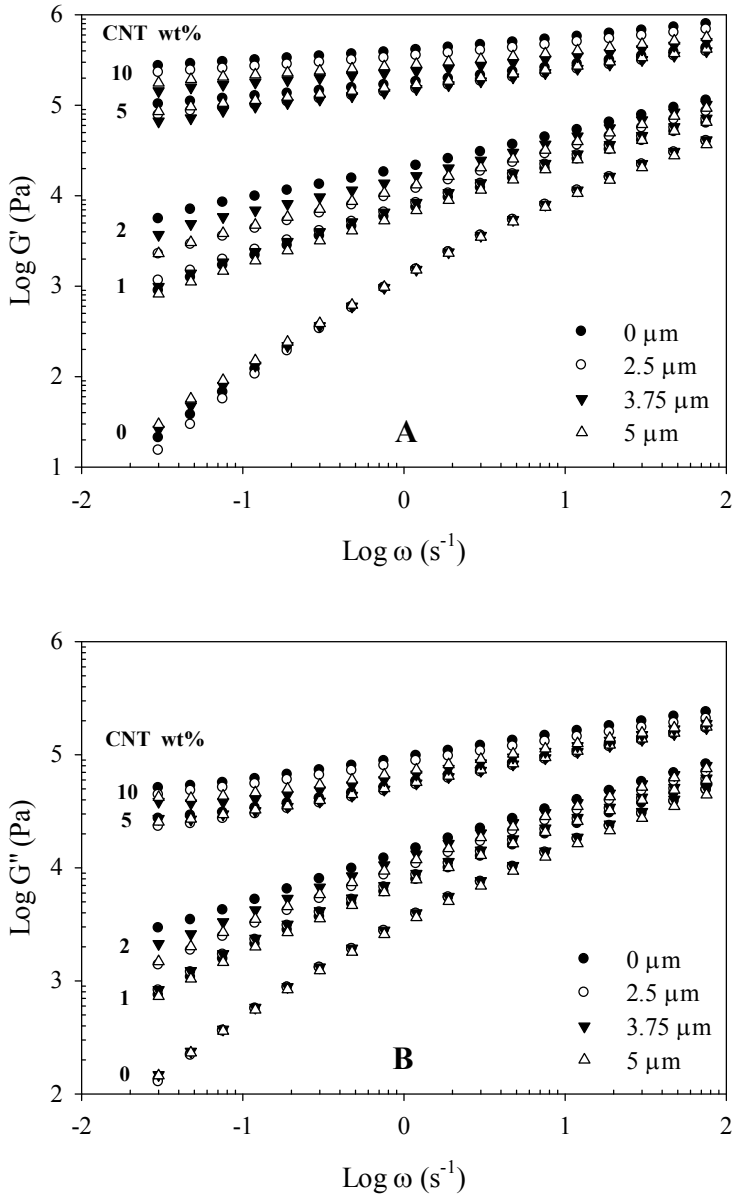

Figure 7.7: Storage (A) and loss moduli (B) versus shear rate for untreated and treated PEEK 380P/CNT nanocomposites as a function of frequency

over four orders of magnitude with the incorporation of 10 wt% CNT. The slope of the storage modulus significantly decreases with increasing filler content. It has been proposed that this behavior is indicative of interconnected structures of anisometric fillers leading to an apparent yield stress that is evident by the plateau [208, 218, 221]. While minimal differences are observed in the neat material due to ultrasonic treatment, the effect of ultrasound is observed in all of the filled samples. A strong decrease in the storage modulus with increasing ultrasonic treatment is seen, pointing to degradation of the nanocomposites. The change in the loss modulus is of a lesser magnitude as that of the storage modulus but follows the same trend. There is an increase in the loss modulus of almost two orders of magnitude, approaching the plateau that is described above for the storage modulus.

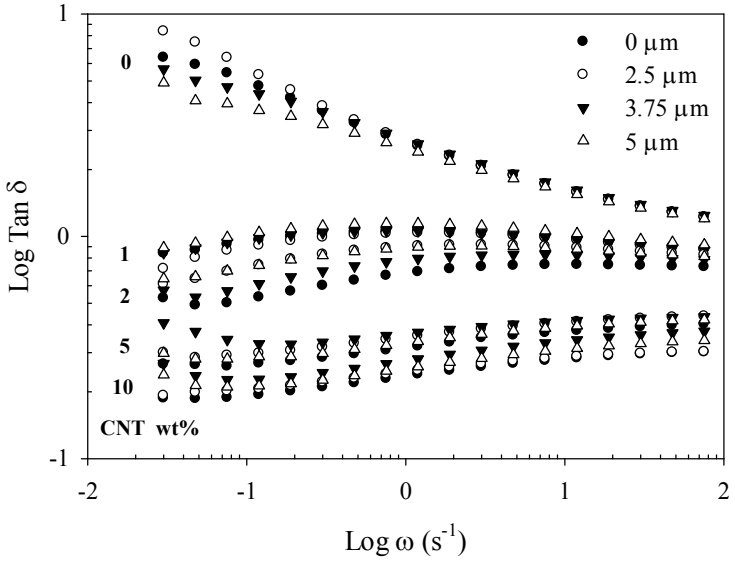

Figure 7.8: Tan delta versus shear rate for untreated and treated PEEK 380P/CNT nanocomposites as a function of frequency

PEEK and its nanocomposites were also evaluated for their damping characteristics. Tan δ of the untreated and treated nanocomposites is shown in Figure 7.8. A dramatic decrease in Tan δ is seen with the incorporation of 1 wt% CNTs. It continuously decreases with increasing filler content. At low frequencies nearly an order of magnitude drop is seen between filled samples at 1 wt% and filled samples of 10 wt%. This is consistent for CNT nanocomposites reported in literature [221] as seen in PE/MWNT nanocomposites. This is attributed to the increased interfacial interactions between the matrix and the CNTs causing decreased energy dissipation and hindered chain relaxation.

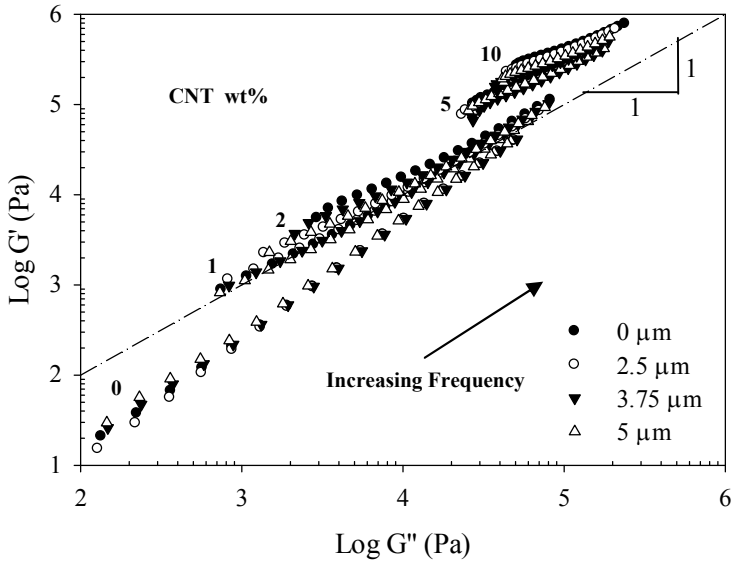

Figure 7.9: Cole-Cole for untreated and treated PEEK 380P/CNT nanocomposites

The Cole-Cole plot is displayed in Figure 7.9 to see how the storage and loss moduli change relative to each other. There is no distinguishable difference between treated and

untreated samples. It is noted that the slope of the curve decreases with increasing CNT content.

7.5 Thermal Analysis

PEEK 380P/CNT nanocomposites were evaluated using DSC and TGA analysis. For DSC, samples of approximately 10 mg were loaded into a sealed hermetic pan for testing. Each sample went through a heat-cool-heat cycle to erase any thermal history so that the second heat could be used for comparison purposes in a nitrogen environment. The complete cycle consisted of an equilibration at 50°C, heating ramp of 20°C/min to 380°C, hold for 5 min, cooling ramp of 10°C/min to 40°C and then a heating ramp of 10°C/min to 380°C. The values of the T_g, T_m and heat of fusion, ΔH_f, for the second heat were used for comparison purposes. Figure 7.10 displays the cooling and second heat DSC traces

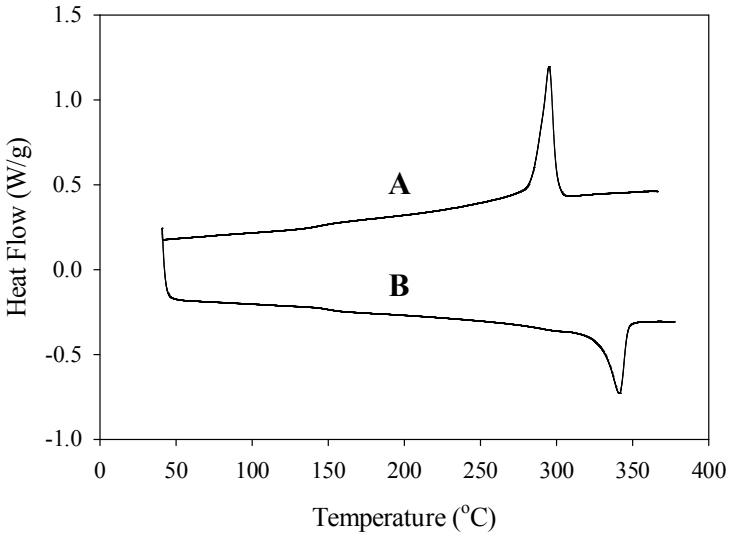

Figure 7.10: Cooling (A) and second heat (B) DSC traces of as received PEEK 380P at a heating and cooling rate of 10°C/min

for as received PEEK 380P. All curves were similar in nature. Data from the DSC traces was analyzed using the TA Instruments Universal Analysis program and the data is reported in Table 7.2.

The degree of crystallinity was studied for the prepared nanocomposites. The degree of crystallinity was calculated by comparing the heat flux at melting of the tested specimen to the theoretical maximum heat flux of 100% crystalline PEEK. This 100% crystalline value was taken from literature to be 130 J/g [222]. The following equation was used:

$$\varphi_c = \frac{\Delta H_{m,PEEK}}{\Delta H^0_{PEEK}} \times 100$$

where $\Delta H_{m,PEEK}$ is the heat flux at melting of the sample, ΔH^0_{PEEK} is the heat flux of melting of a 100% crystalline sample. It should be noted that the heat flux of melting and the corresponding degree of crystallinity have been corrected for CNT concentration by dividing by the weight fraction of polymer in the tested sample using the following equation:

$$\Delta H_{m,PEEK} = \frac{\Delta H_{m,PEEK}\ (measured)}{Weight\ fraction\ of\ polymer\ in\ sample}$$

All results are an average of two runs using the second heat for comparison purposes. Table 7.2 displays the thermal analysis data for all PEEK 380P nanocomposites. From the data in Table 7.2 it is observed that there is no significant change in the glass transition, melting temperature or degree of crystallinity. Nanotubes traditionally act as

nucleating agents and a change in thermal behavior of the nanocomposites was expected. Work by Ryan *et al.*[223] on PVA/MWNT composites and Bhattacharyya *et al.*[224] on PP/SWNT composites showed increased crystallinity with the incorporation of CNTs.Diez-Pascual *et al.*[225] and Sandler *et al.*[131] found the crystallinity, glass transition and melting temperature to be uneffected with the incorporation of up to 1.0 wt%. SWCNT. It has been suggested that the CNT confines the polymer chain inhibiting

Table 7.2: Thermal characteristics of PEEK 380P/CNT nanocomposites

Amplitude (μm)	**CNT (%)**	**T_g (°C)**	**T_m (°C)**	**ΔH_m (J/g)**	**Φ_c (%)**
Neat	0	151.3	341.6	39.1	30.1
0	0	150.6	341.5	39.5	30.4
2.5	0	150.4	341.8	41.4	31.8
3.75	0	150.9	341.7	40	30.8
5	0	150.7	341.8	39.9	30.7
0	1	149.6	342.3	40.8	31.4
2.5	1	150.2	342.4	41.3	31.8
3.75	1	150	342.4	39.8	30.6
5	1	148.1	341.7	41	31.5
0	2	149.3	342.1	40.7	31.3
2.5	2	148	342.3	41.8	32.2
3.75	2	150.5	342.9	41.1	31.6
5	2	148.7	342.5	39.2	30.2
0	5	148.4	342.4	42.4	32.6
2.5	5	148.6	342.4	40.5	31.2
3.75	5	149	342.3	39.9	30.7
5	5	148.4	342.2	42.2	32.5
0	10	148.9	341.9	40.5	31.2
2.5	10	148.6	342.2	39.7	30.5
3.75	10	149.4	342.2	40.6	31.2
5	10	149.1	342	40.4	31.1

diffusion and crystal growth which minimizes the changes due to the incorporation of the CNTs.

For TGA analysis approximately 10 mg of sample was loaded into a previously cleaned and tared platinum pan. Samples were equilibrated at 40°C and heated at 20°C/min to 900°C in a nitrogen atmosphere. Figure 7.11 are the TGA traces of unfilled PEEK 380P both untreated and ultrasonically treated. From the traces it is seen that there is no significant distinguishable difference in weight loss between treated and untreated samples of the neat polymer.

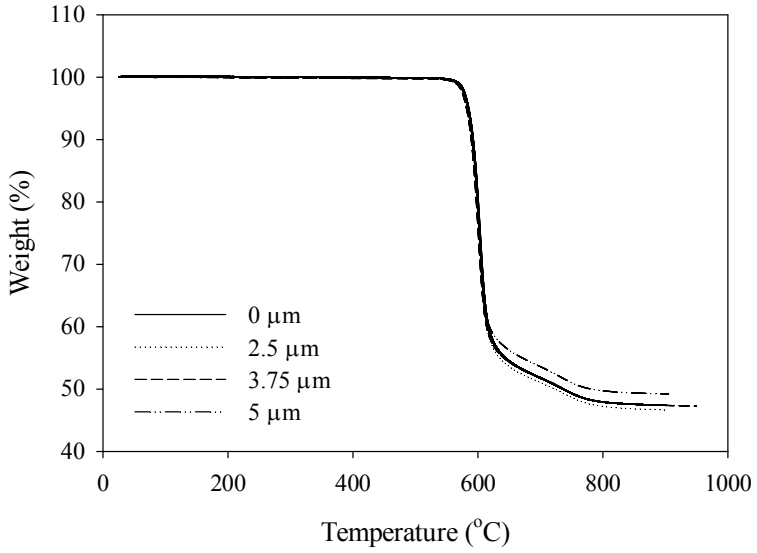

Figure 7.11: Weight loss for untreated and treated PEEK 380P in nitrogen

Figure 7.12 depicts the weight loss of PEEK 380P/10% CNT nanocomposites untreated and treated at 5 µm. From the curves it is shown that there is also no

distinguishable difference between untreated and ultrasonically treated samples at the highest loading and highest ultrasonic amplitude tested. This is in agreement with literature where the incorporation of CNTs into PEEK showed less than 5°C increase in initial degradation as seen by comparison of the temperatures for each material upon reaching a weight loss of 10%[225]. CNTs have been shown toenhance the thermal stability of nanocomposites. From these two figures it can be determined that the ultrasonic treatment of this process has no negative effects on the weight loss with temperature of unaged PEEK nanocomposites. The Ken-React CAPOW NZ 37/H

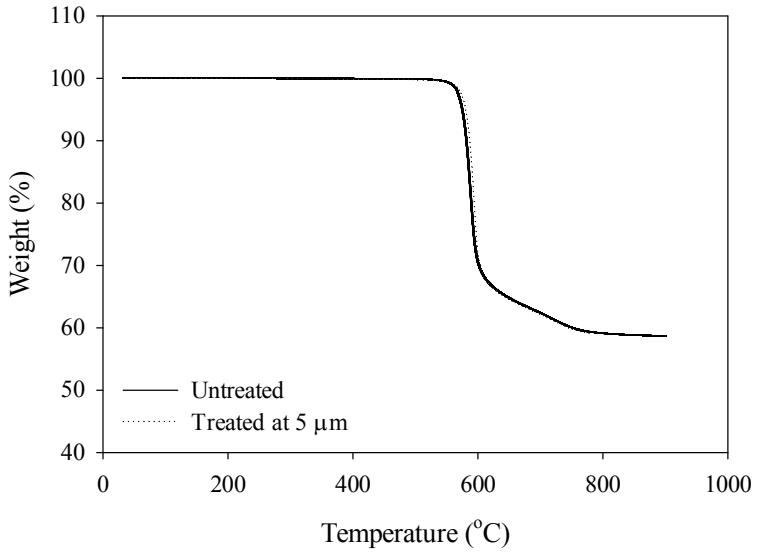

Figure 7.12: Weight loss for untreated (solid) and treated at 5 µm (dashed) PEEK 380P/ 10% CNT nanocomposites

additive for increased compatibility was analyzed using TGA in its as received form. Figure 7.13 shows that the NZ additive does not sustain even moderate temperatures

without significant weight loss. Over 50% loss in weight is observed before reaching a temperature of 200°C. Due to the high processing temperatures required for PEEK, it is believed that the majority of this additive is lost during processing. Samples that had the additive incorporated into the formulation showed no difference in thermal performance.

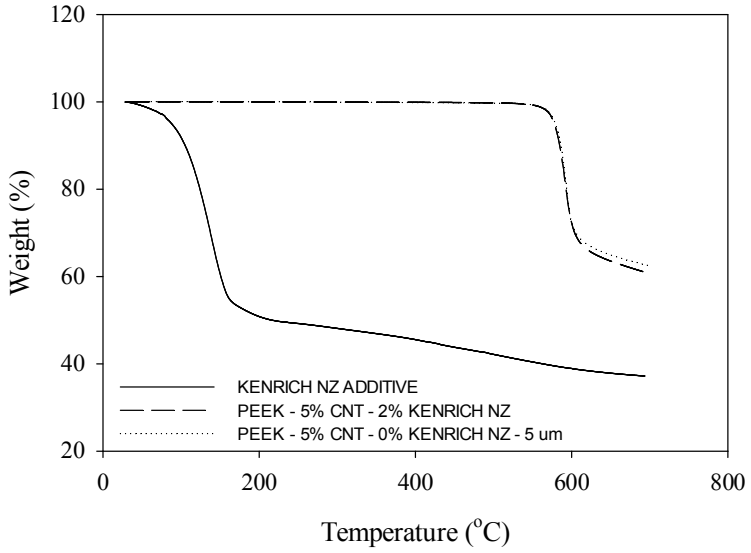

Figure 7.13: Weight loss for pure Ken-React® CAPOW® NZ® 37/H additive and composites untreated and treated PEEK 380P/CNT

7.6 Mechanical Analysis

The PEEK nanocomposites were extruded through a strand die, quenched in a room temperature water bath and subsequently pelletized. After pelletizing, samples were dried in a vacuum oven at 100°C for 24 hours and then tensile bars, ASTM D638, were injection molded using a single cavity MiniJet injection molding machine (HAAKE, Thermo Electron Corp. Germany) at a barrel temperature of 370°C**,** a pressure of 100

MPa, with a holding time of 10 seconds, a holding pressure of 60 MPa and a mold temperature of 160°C. Mechanical testing was performed on the tensile bars to evaluate the Young's modulus, ultimate strength, elongation at break and toughness using an Instron test machine (Model 5567, Instron Corp., Canton, MA, USA). Testing was carried out on a minimum of five samples according to ASTM D638 testing procedures at a cross head speed of 5 mm/min using a 10 kN load cell. No extensiometer was used.

Figure 7.14 shows the Young's modulus of PEEK 380P/CNT nanocomposites at various CNT loadings with and without ultrasonic treatment. It should be noted that the reported values are less than manufacture specifications of 3.7 GPa [50]. This is due to

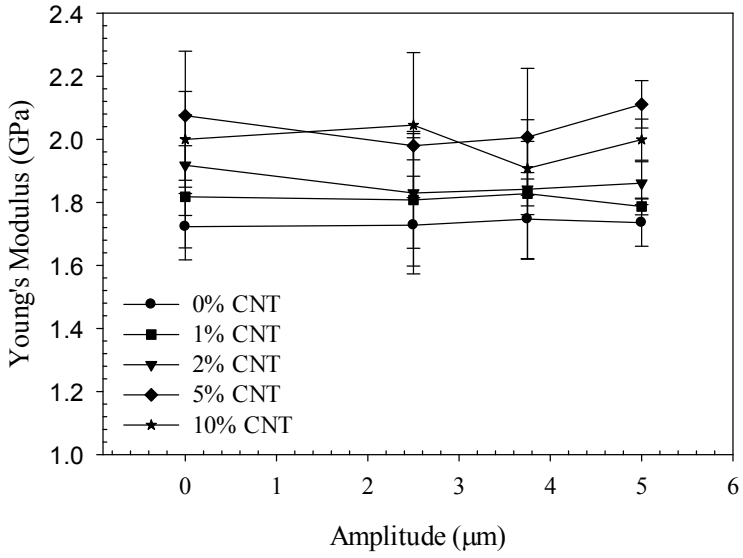

Figure 7.14: Young's modulus versus ultrasonic amplitude of PEEK 380P/CNT nanocomposites

the fact that no extensiometer was used during testing. A consistent trend of increasing modulus with increasing CNT concentration is seen up to 5 wt%. There is an increase of

more than 20% in the Young's modulus with the incorporation of 5 wt% CNT. There was no additional increase in modulus observed for samples containing 10 wt% CNT.

Sandler *et al.* [131] reported an increase in the Young's modulus of PEEK/CNF nanocomposites of 25% with a 10 wt% loading. This is also similar to results by Rong *et al.* [226] who found a 20% increase in modulus with the addition of 5 wt% MWNTs after twin screw extrusion. This is better than results published by Chen [227] who found an 8% decrease in modulus with the incorporation of 5 wt% super critical CO_2 expanded MWNTs after melt mixing. This is less than results reported by Ogasawara *et al.* [228]who reported an increase of 50% in the Young's modulus with the incorporation of 9 wt% MWNT by twin screw extrusion or results by Bangarusampath *et al.* [229] who found a 30% increase in modulus with the incorporation of 10 wt% of CNTs using twin screw extrusion and testing of annealed samples. Samples were injection molded and annealed for 5 hours at 230°C prior to testing at 1 mm/min strain rate. No significant trend was observed with ultrasonic treatment on the modulus of the nanocomposites. There is neither an increase or decrease in the modulus with ultrasonic treatment for nanocomposites up to 5 wt% loading. Samples containing the NZ additive were also tested for mechanical performance. As seen in Figure 7.15, samples containing the NZ additive produced results that were of no significant difference compared to samples not containing the additive. This continues to point to the previously held conclusion that the additive did not survive the extrusion process.

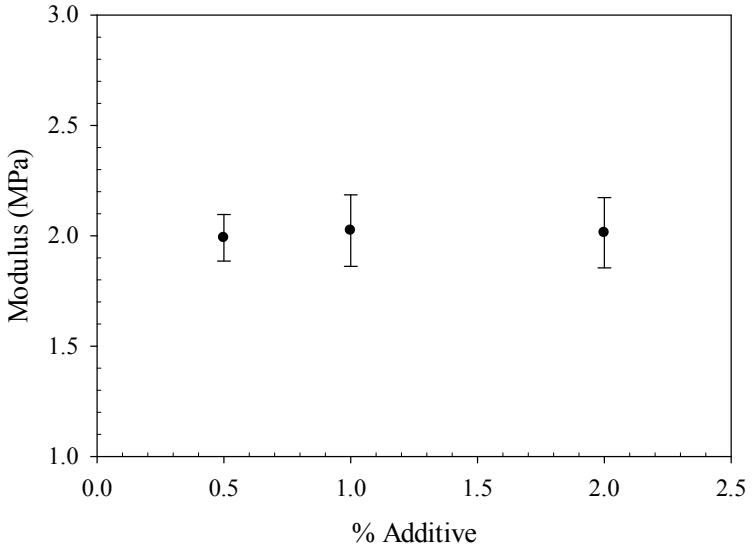

Figure 7.15: Young's modulus versus % Ken-React® CAPOW® NZ® Additive of PEEK 380P/5wt% CNT nanocomposites

The tensile strength for the PEEK 380P/CNT nanocomposites is shown in Figure 7.16. A continuous increase in strength with increasing CNT concentration is seen for all loading levels. An increase of 12% in strength is observed with the incorporation of 10 wt% CNT over the neat material. This is better than reported results by Rong *et al.* [226] who found a 3% and 6% increase in tensile strength with loadings of 5 wt% un-functionalized and functionalized MWNTs in twin screw extruded nanocomposites, respectively. This is slightly better than the findings by Diez-Pascual *et al.* [230] who found a 8 and 10% increase in strength at break with a 1 wt% loading of arc grown and laser grown SWNTs, respectively, while using MWNTs. This is significantly better than the findings by Chen [227] who found a decrease of 5% in the tensile strength with the incorporation of 5 wt% of Nanocyl-7000 multi-walled nanotubes using a super critical CO_2 expansion of the

nanotubes prior to melt compounding. These results are also better than Ogasawara *et al.* [228] who found a 7.5% increase in ultimate strength with the incorporation of 9 wt% MWNT after melt mixing. No significant effect due to ultrasonic treatment is observed up to 3.75 μm. However, a significant effect is seen at the 5 μm treatment level. A strong decrease is seen at the higher loading levels is observed with a 7% decrease in strength at the 2 wt% filler loading and a 45% and 50% decrease at 5 and 10 wt% loadings, respectively. This is believed to be due to the degradation of the CNTs and matrix at the high ultrasonic amplitude. Consistent with the previous data, the ultimate strength of the nanocomposites containing the Kenrich NZ additive, Figure 7.17, showed no increase or decrease in strength compared to samples without the additive.

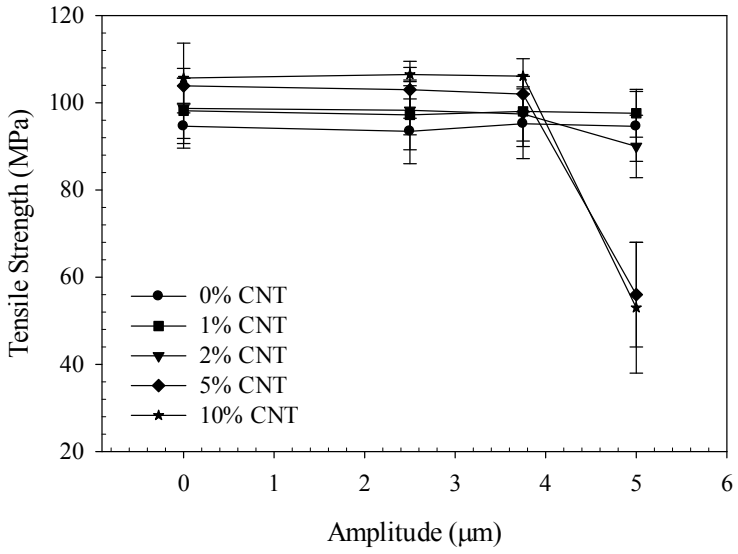

Figure 7.16: Tensile strength at yield versus ultrasonic amplitude of PEEK 380P/CNT nanocomposites

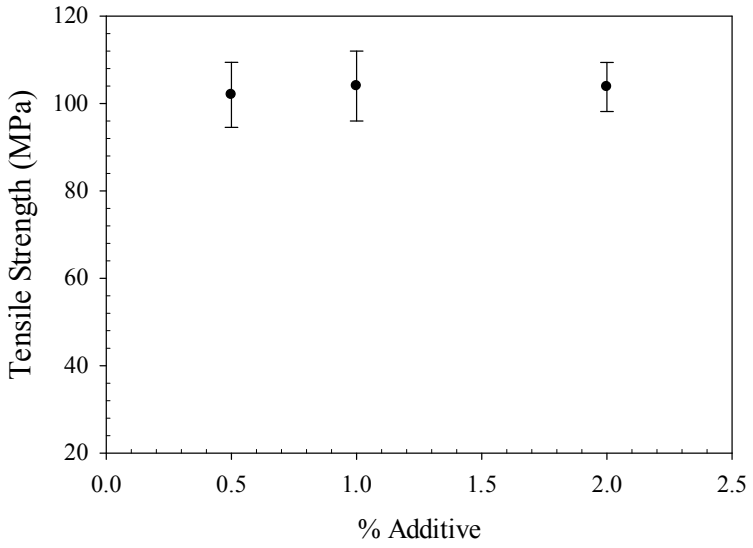

Figure 7.17: Tensile strength at yield versus % Ken-React® CAPOW® NZ® additive of PEEK 380P/5wt% CNT nanocomposites

The strain at break of the PEEK 380P/CNT composites is shown in Figure 7.18. No difference is observed between PEEK without filler and PEEK containing 1 wt% CNTs. A continuous decrease in strain at break is observed with increasing CNT concentration after a loading level of 1 wt%. This is contrary to work by Diez-Pascual *et al.* [230] who found a decrease of almost 50% in the strain at break at a loading of only 1 wt% SWNTs in PEEK. Sandler *et al.*[131] found no significant decrease in strain at break in CNF/PEEK nanocomposites up to 10 wt%. However, upon increasing the loading to 15 wt% CNF the sample failed in a brittle manner with a decrease in elongation of 80%. No effect of ultrasonic treatment is observed below the treatment level at 5 μm. While no difference is observed for the unfilled sample, a significant decrease in the strain at break is observed for all samples containing CNTs. A 10% decrease in strain at break is

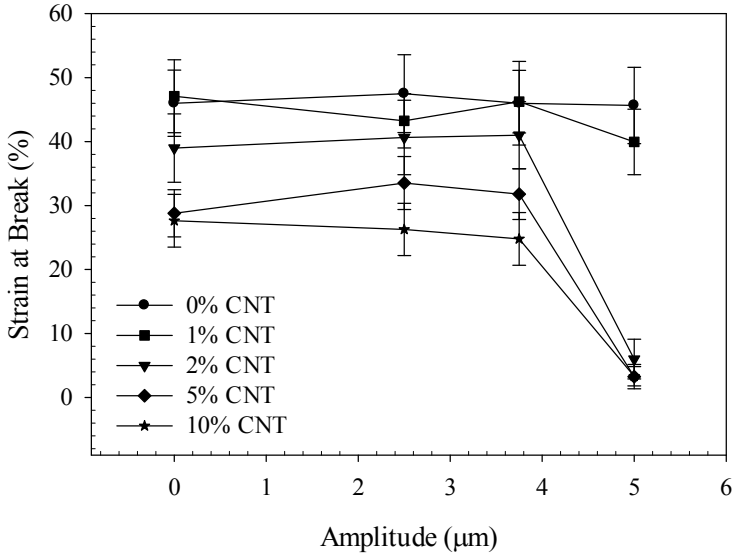

Figure 7.18: Strain at break versus ultrasonic amplitude of PEEK 380P/CNT nanocomposites

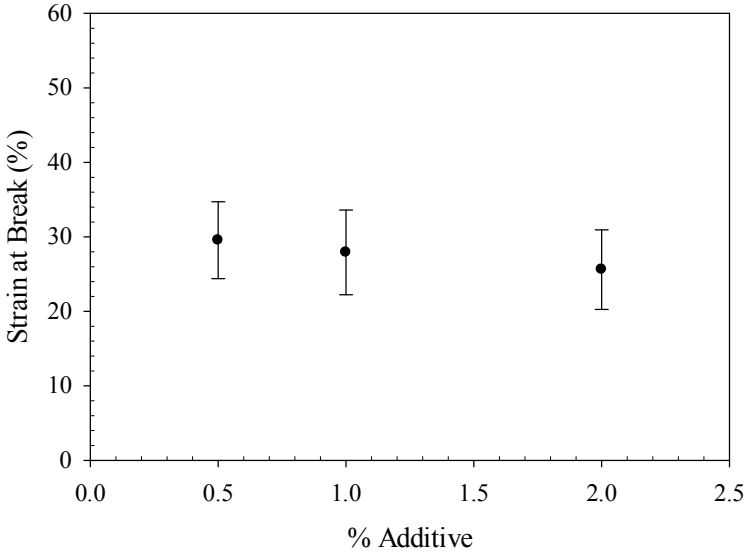

Figure 7.19: Strain at break versus ultrasonic amplitude of PEEK 380P/ 5% CNT nanocomposites containing Ken-React® CAPOW® NZ® additive at various levels

observed for samples with 2wt% filler loading and a severe decrease is observed for samples with higher filler loadings. This believed to be due to the effect of high power ultrasound on the matrix on CNTs. In agreement with all previous results there was no observable difference between samples with Kenrich NZ additive, Figure 7.19, and samples without the additive.

7.7 Analysis of Electrical Properties

Two different methods were used to test compression molded plaques 90 mm in diameter and 1 mm thick. All samples were molded after drying at 100°C for 24 hrs under a vacuum of -30 in Hg. All plaques were compression molded at 380^{o}C in a Carver (CARVER 4122, Wabsah, IN) compression molding press and subsequently removed and allowed to cool to room temperature between two metal plates to maintain flatness.

For the first method, a Keithley electrometer (Model 6517 A, Keithley Instruments, Cleveland, OH, USA) equipped with a model 8009 test fixture was used to test the volume resistivity of molded plaques in accordance with ASTM D257 testing procedures. This apparatus is designed to measure volume resistivity from 10^{18} to 10^{3} ohm-cm. Alternating polarity was used with a baseline of 0 volts and an alternating voltage of +/- 1 volt. The method was set to take six reads for 10 seconds at each alternating voltage and then record the final read. The measurement was taken three different times for each sample and averaged. Standard deviation is reported.

The second method was designed and developed to test materials in the low resistivity region. A Keithley micro-ohmmeter (Model 580, Keithley Instruments, Cleveland, OH,

USA) was used for both the output and input signals. The apparatus consisted of two cylindrical rubber blocks 64 mm in diameter that were coated on one side with 3M™ conductive film CN-3190 (3M, Saint Paul, MN, USA). The sample was placed between the two rubber blocks with the conductive side facing the sample. The blocks and samples were squeezed and the electrodes for both the input and output signals were pressed against the conductive film and a measurement was taken. The measurement was taken three different times for each sample and averaged. Standard deviation is reported.

Resistivity results, Figure 7.20, showed a percolation between 0 and 1 wt% CNT loading. A drop of more than 7 orders of magnitude was observed. The percolation is in agreement with literature where studies done on PC/MWNT [126, 143] composites show the percolation from 1-2 wt% while studies on PC/SWNT [124]showed a percolation of less than 1 wt%. This is in agreement with PEEK/SWNT work done by Diez-Pascual *et al.* [230] who showed a strong increase in electrical conductivity at a 1 wt% loading of SWNTs as well as with data reported by Nanocyl Inc. [231] on PEEK/NC7000 MWNTs that showed a percolation between 0.5 and 1 wt%. The current work shows a much lower percolation than work by Mohiuddin [232] that showed a percolation at 3.6 wt% MWNT or work by Socher *et al.* [233]who showed almost no change in resistivity up to a loading of 1.5 wt% Baytubes C150P MWNTs in PEEK after conical twin screw extrusion. After the current percolation only a minor decrease in resistivity was observed with further filler loading was observed using method 1. However, method 2 showed a continuous decrease in resistivity with increasing CNT concentration with a decrease of almost 9 orders of magnitude at the 10 wt% loading. This strong difference in data shows the

importance of verifying testing equipment. While the equipment of method 1 is rated to work in the volume resistivity range of 10^3 to 10^{18} ohm-cm, in house testing

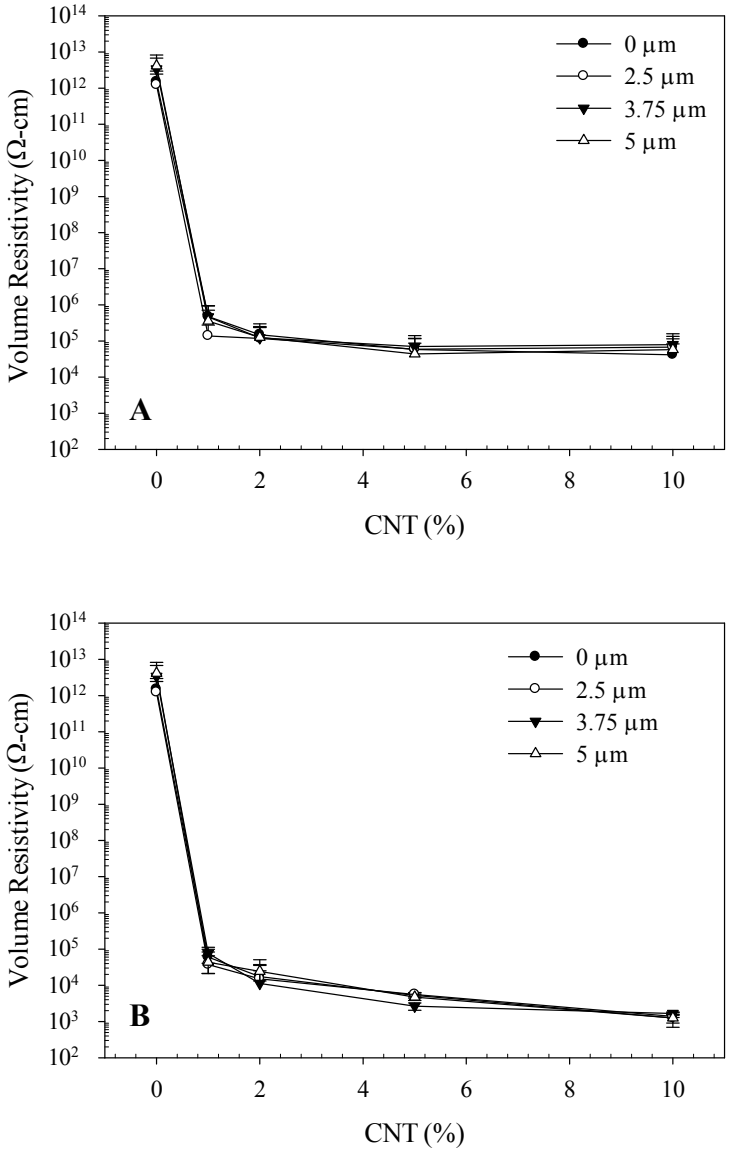

Figure 7.20: Volume resistivity versus ultrasonic amplitude of PEEK 380P/CNT nanocomposites tested using method 1 (A) and method 2 (B)

using the equipment showed this not to be the case for the alternating polarity method used in method 1 or any other method tried. Method 2was verified using a series of resistors (1, 10 and 100 ohms) to verify the measurement range.

7.8 Microscopy

Samples of PEEK injection molded tensile bars were microtomed and observed under optical microscope. An Olympus microscope was used to collect images at a magnification of 200X. A Leica Ultracut microtome was used to prepare the microtome samples. Several images were collected and representative micrographs are depicted. Optical micrographs of samples with 2 wt% CNT loading without and with ultrasonic treatment at 5 µm amplitude are shown in Figure 7.21. From the micrographs it is observed that in the untreated samples the CNT agglomerates are regularly shaped,

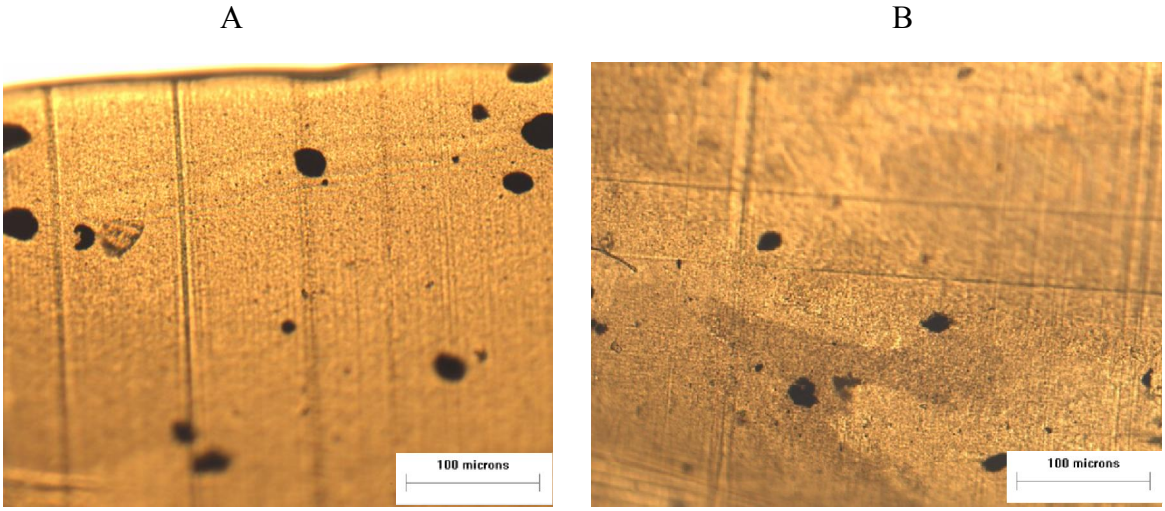

Figure 7.21: Micrographs taken at 200X of PEEK 380P/2wt%CNT nanocomposites without (A) and with 5 µm amplitude treatment (B)

smooth and larger than those in the sample treated at 5 μm. There are fewer agglomerates and they appear more irregular in shape. These micrographs are characteristic of what was seen in several samples but further statistical analysis and more micrographs need to be collected. However, both micrographs still show a significant number of agglomerates. AFM imaging was used to look at the edge of the agglomerates but CNTs could not be distinguished from the matrix in microtomed samples.

7.9 Conclusions

PEEK/CNT nanocomposites were prepared using a novel twin screw extruder utilizing an ultrasound assisted slit die attachment that was designed and manufactured for this work. CNTs at concentrations of 0-10 wt.% were fed downstream into the melt state to avoid the high shear area at the feed throat of the extruder. Die pressure and ultrasonic power consumption were recorded. It was observed that the die pressure increased with increasing concentration of CNT loading and decreased with ultrasonic amplitude. Both of these observations were anticipated. Complex viscosity data showed a significant increase between loadings of 0 and 1 wt% and 2 and 5 wt% with the rheological percolation falling between 0 and 1wt% with tan delta showed corresponding decreases. An increase in viscosity of more than three orders of magnitude was observed upon the incorporation of 10 wt% CNT loading. The viscosity data explains the decrease in die pressure with increasing ultrasonic amplitude due to permanent changes in the viscosity. Mechanical testing showed increases in modulus and strength of more than 20 % and 10 %, respectively, and a decrease in strain at break of 35 % with the addition of up to 5 wt.% CNT. Electrical resistivity showed a percolation with a drop of more than

seven orders of magnitude with a loading of 1 wt% CNT. Further filler loading resulted in a continuous decrease in resistivity with a drop of 9 orders of magnitude achieved at the 10 wt% CNT loading. An increase in mechanical properties was observed and microscopy showed an increase in dispersion, however, it is believed that lack of adhesion between the nanotubes and the solid matrix prohibits the full synergistic enhancement of the CNT filled nanocomposites.

CHAPTER VIII

CONTINUOUS HIGH POWER ULTRASONIC EXTRUSION OF PEEK 450PF / CNT NANOCOMPOSITES - NEW ULTRASONIC DESIGN

8.1 Introduction

In this chapter, the processing and characterization of PEEK 450PF, a high temperature thermoplastic, and its CNT nanocomposites for enhanced mechanical and electrical properties is studied. The nanocomposites for this study were processed using a patented, ultrasonically assisted twin screw extruder technology that was designed for this research. In comparison with the previous chapter, the ultrasonic system was redesigned and manufactured. The ultrasonic system was moved out of the die area and into the extruder. Carbon nanotubes are known for their agglomeration during synthesis and this technology aids in the dispersion of CNTs by utilizing equipment that is currently used in industry aided by an ultrasonic energy. The effects of compounding with and without ultrasound on die pressure, power consumption, rheological, morphological, mechanical and electrical properties in polyetheretherketone (PEEK) filled with 0-5 wt% CNTs were evaluated.

The focus of the following work was to improve the dispersion of CNTs in PEEK 450PF matrix using a modified micro-compounder with ultrasonic assisted technology. PEEK 450PF was chosen because of its excellent mechanical strength, dimensional

stability, high temperature performance, wear resistance and chemical resistance. It is also processable by conventional methods such as injection molding allow it to be used in numerous applications. The effects of ultrasound on die pressure, electrical conductivity, rheological, morphological and mechanical properties were studied.

8.2 Experimental Procedures

After the previous study on the processing PEEK 380P/CNT nanocomposites using an ultrasonic slit die attachment, the system was redesigned. The new system was designed and manufactured as discussed below. In the previous design, Figure 8.1, the ultrasonic treatment was applied at the end of the extrusion process using two opposing horns encasing the processed material that was advanced by only pressure driven flow.

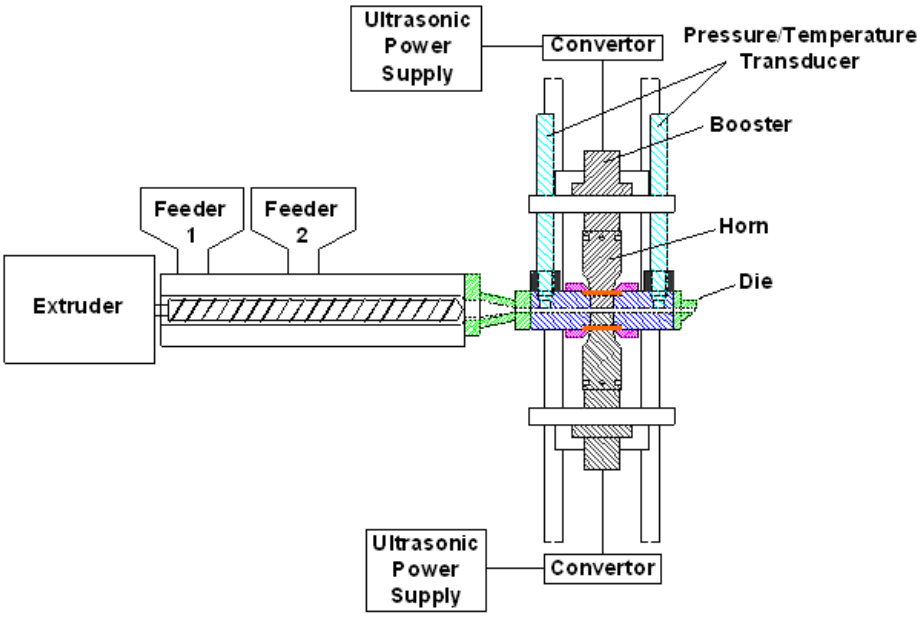

Figure 8.1: Micro-compounder with attached ultrasonic slit die - design A

The new enhanced design, Figure 8.2, moved the ultrasonic treatment into the extruder to take advantage of the shearing and mixing of the screws while simultaneously applying the ultrasonic treatment. To maintain dispersion, after cavitation breaks the bundles apart due to ultrasound the matrix material needs to flow in-between the nanotubes in order to prevent their re-agglomeration. The addition of the rotation of the screws along with pressure driven flow in the treatment section provides increased transverse direction shearing along with increased material mixing so that all of the material receives a more homogenous treatment.

Prior to extrusion all materials were dried in a vacuum oven at 100°C for 24 hours to ensure low moisture content. A co-rotating twin screw micro-compounder, (PRISM USALAB 16, Thermo Electron Corp. UK) with an ultrasonic treatment zone contained within the extruder, as seen in Figure 8.2, was used for all PEEK 450PF/CNT nanocomposite experiments. The micro-compounder has a screw diameter of 16 mm and an L/D of 25. A screw speed of 100 RPM, a feed rate of 227g/hr (1/2 lb/hr), and a temperature of 380^{o}C in all zones were the set processing conditions. Two separate feeders were used to feed the PEEK 450PF matrix and the CNTs. The matrix was fed into the extruder at the throat, feeder 1 in Figure 8.2. To avoid the high shear zone and impact on the CNTs at feeder 1, the nanotubes were fed separately downstream at a point where the matrix was already melted. After the CNTs were fed into the second feed port the composite material continues downstream through a mixing section before it enters the treatment zone and is exposed to ultrasonic waves. The ultrasonic modification consists of a flow channel 2.54 mm deep x 28 mm wide x 28 mm long with the horn acting as the

top part of the channel. All of the material being processed is forced to pass through this channel.

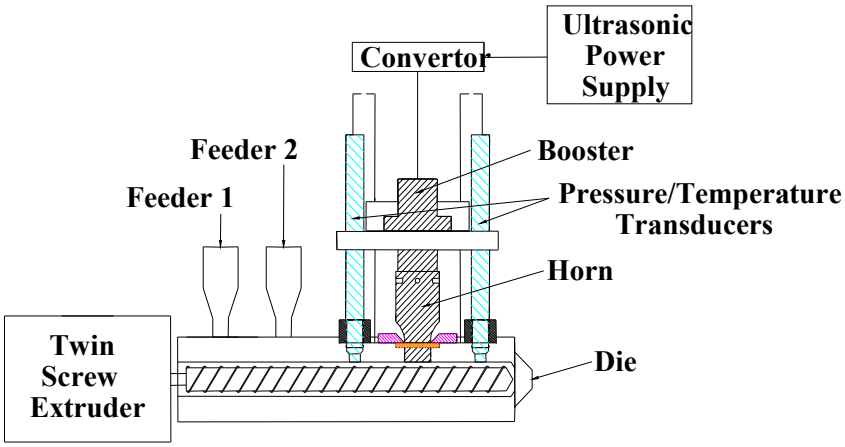

Figure 8.2: Micro-compounder with incorporated ultrasonic section - design B

The ultrasonic system (Branson Ultrasonic Corp., CT, USA) has a maximum power output of 800 W and operates at 40 kHz. After exiting the ultrasonic section the composite passes through an additional mixing section to homogenize the melt before exiting through a strand die where the strand is subsequently water quenched and pelletized. Power consumption was measured using a Dataq data acquisition system connected directly to the power supply. The horn has a surface area of 28 mm x 28 mm that contacts the polymer. The gap underneath the ultrasound was set at 2.54 mm. The mean residence time in the ultrasonic treatment zone is approximately 28 seconds for a flow rate of 227g/hr (1/2 lb/hr).

Polyetheretherketone in a white powder form was obtained from Victrex under the trade name PEEK 450PF, and was used as received. It has a T_g of 145°C and a melting temperature of 343°C. A regularly entangled grade of multiwalled carbon nanotubes was obtained from Bayer Scientific Materials and used as received. The Baytubes C150P are agglomerates of multi-walled CNTs with a C-purity of >95%, with a manufactures outside diameters of 13-16 nm, inside diameters of 2-6 nm and lengths of 1-10 um with a bulk density of 140-160 kg/m^3[200]. Table 8.1 is the testing matrix used for the PEEK 450PF/CNT Nanocomposites.

Table 8.1**:** Testing Matrix for PEEK/CNT Nanocomposites processed on Micro-compounder design B

CNT Concentration	RPM	Feed Rate (lb/hr)	Ultrasonic Amplitude (μm)
0	100	0.5	0, 2.5, 5, 10
1	100	0.5	0, 2.5, 5, 10
2	100	0.5	0, 2.5, 5, 10
5	100	0.5	0, 2.5, 5, 10

8.3 Processing Characteristics

During extrusion the extruder torque as a % of max torque and ultrasonic power consumption were recorded using an online data acquisition system. Extruder torque as a function of CNT concentration and ultrasonic amplitude is depicted in Figure 8.3. Extrusion of the nanocomposites showed a trend of increasing extruder torque with increasing CNT concentration and a decrease with increasing ultrasonic amplitude. The increase in torque was minimal at CNT concentrations up to 2 wt% but had a significant increase at a concentration at 5 wt%. This decrease in extruder torque is attributed to

recoverable thixotropic effects as the viscosity of treated samples is shown to remain constant or increase with ultrasonic treatment, as shown in Figure8.6.

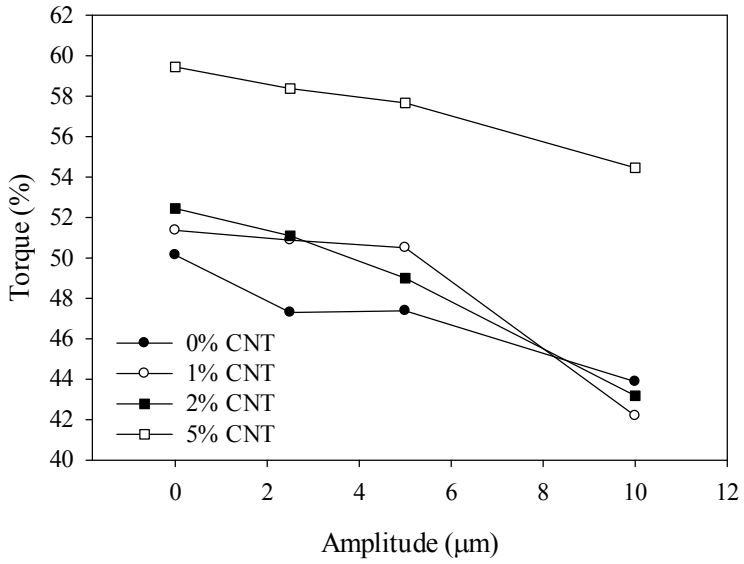

Figure 8.3: Extruder percent torque versus ultrasonic amplitude for PEEK 450PF/CNT nanocomposites at various loadings

The melt temperature of the composite after passing through the ultrasonic treatment section is presented in Figure 8.4. There was an increase in the melt temperature for all composites with increasing ultrasonic amplitude. This is due to increased energy absorption from the ultrasonic horn. As can be seen, the temperature of the PEEK/CNT nanocomposite at 5% CNT had the highest temperature at all amplitudes. This is attributed to increased viscous heating due to the higher viscosity of the material at the high loading of CNTs.

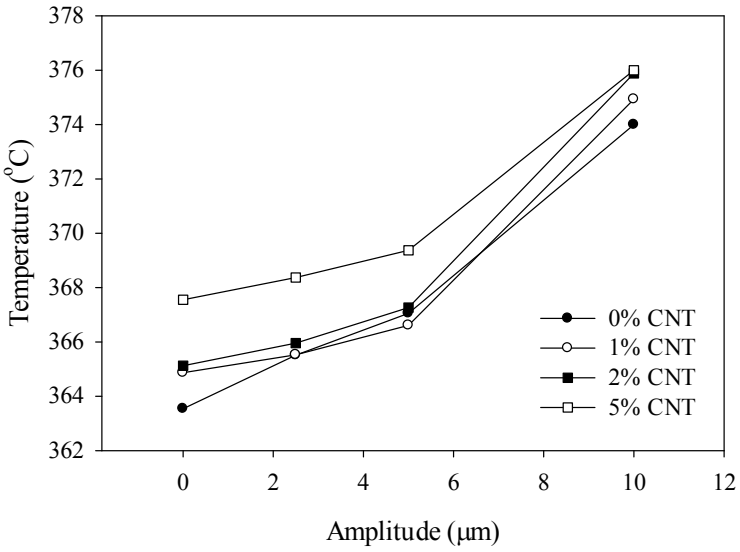

Figure 8.4: Melt temperature after ultrasonic treatment versus ultrasonic amplitude for PEEK 450PF/CNT nanocomposites at various CNT loadings

The decrease in extruder torque with increasing ultrasonic treatment is attributed to both thermal and rheological effects. The vibration of the horn causes slip and decreased resistance to the flow of the polymer as well as a decrease in viscosity due to an increase in temperature from frictional heating at the surface of the horn and ultrasonic energy dissipation. This is also caused by recoverable thixotropic effects as the increase in ultrasonic treatment shows a decrease in die pressure with no change or an increase in the viscosity, as shown in Figure 8.7. This decreased extrudertorque would allow for increased throughput in industrial applications.

The pressure measured directly after the ultrasonic treatment zone is depicted in Figure 8.4. While there was minimal increases in pressure for concentrations of 1 and 2

wt% at low ultrasonic amplitude there was a significant increase in pressure at the 5 wt% loading level. There is also a trend of increasing pressure difference with ultrasonic treatment, with a significant increase in pressure at the 10μm amplitude treatment. This is

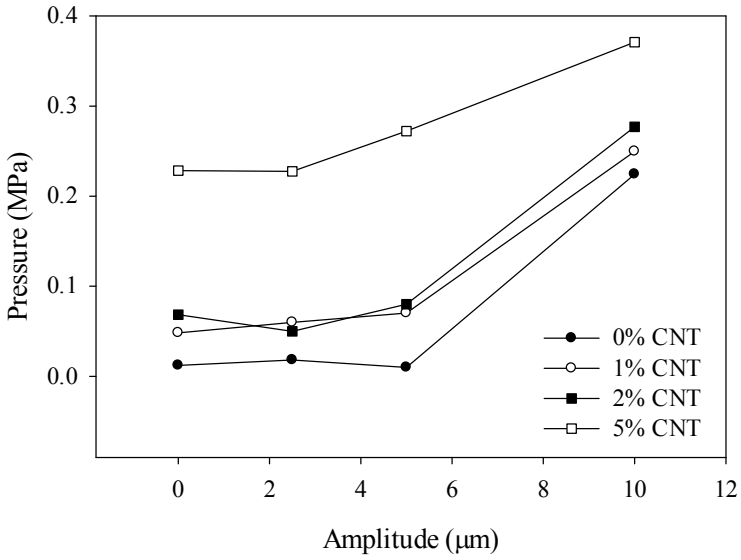

Figure 8.5: Pressure after ultrasonic treatment versus ultrasonic amplitude for PEEK 450PF/CNT nanocomposites at various CNT loadings

most observable in the 5 wt% loading. This increase in pressure is attributed to the increase in dispersion of the CNTs at the high amplitude ultrasonic treatment. This is corroborated in the complex viscosity of the nanocomposites in Figure 8.7 where filled samples treated at the highest amplitude had the highest viscosity.

Ultrasonic power consumption versus ultrasonic amplitude for various CNT loadings of the processed nanocomposites is shown in Figure 8.6. The ultrasonic power consumption increased with increasing ultrasonic amplitude, as expected for increased

ultrasonic amplitude. Negligible differences are seen between the power consumption at the same ultrasonic treatment for the various CNT loadings. The throughput of the system is limited by the maximum torque of the extruder which minimized the allowable

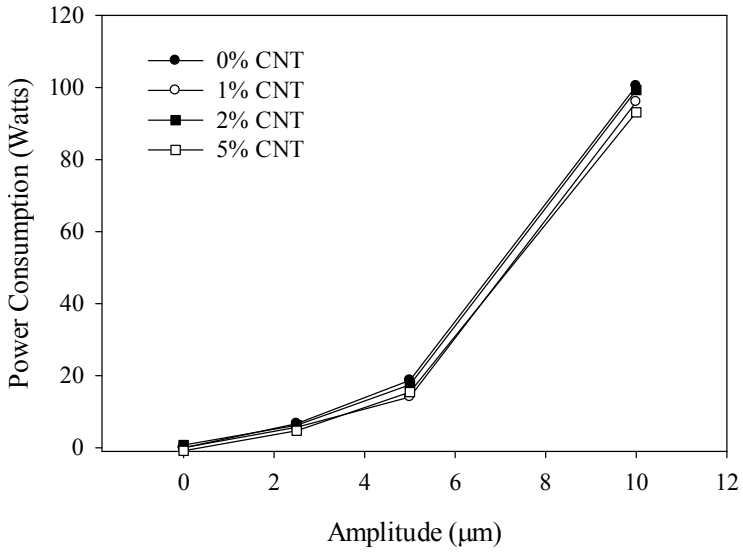

Figure 8.6: Power Consumption versus ultrasonic amplitude for PEEK 450PF/CNT nanocomposites at various CNT loadings

pressure that was able to be attained. The power consumption therefore varied mainly due to the increase in amplitude during ultrasonic treatment. It should be noted that there was a visual difference in color in the unfilled samples between samples at 0, 2.5 and 5 μm and the sample processed at 10 μm. The sample processed at 10μm had a distinguishably darker color. This eludes to the possibility of degradation.

8.4 Rheology

Rheological properties were measured on an ARES, TA instruments using parallel plate configuration. The material was dried for 24 hrs at 100°C after processing, melted at 380°C and then compression molded into samples 2.0 mm thick x 25 mm in diameter. The molded disc was placed between parallel plates, melted, and then compressed to 1.5 mm. Overflow material around the plates was removed after compression using a razor blade to minimize boundary effects. Testing was conducted using 25 mm parallel plate geometry in oscillatory shear mode with a frequency sweep test using a strain amplitude of 2% and a fixed temperature of 360°C. The complex viscosity, storage modulus, loss modulus and loss tangent were determined as a function of angular frequency. A

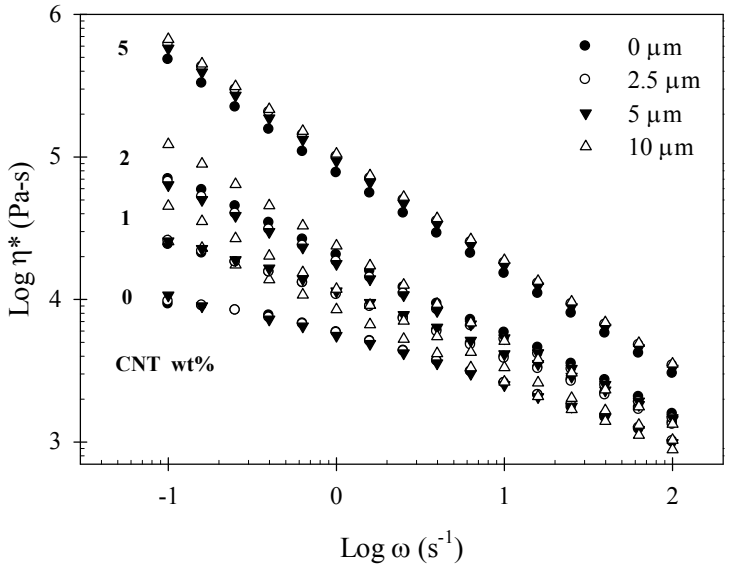

Figure 8.7: Viscosity versus frequency of PEEK 450PF/CNT nanocomposites at various loadings and ultrasonic treatments

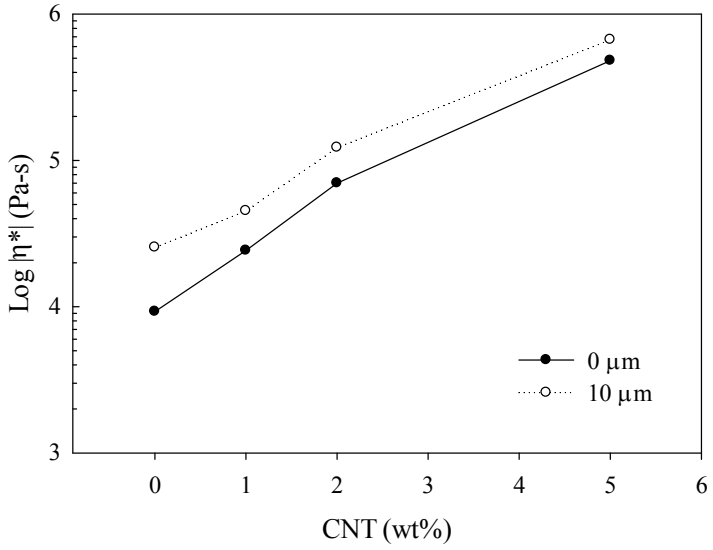

Figure 8.8: Complex viscosity of PEEK 450PF/CNT nanocomposites measured at 360°C, 2% strain amplitude at a frequency of 0.1 rad/s without and with 10μm ultrasonic treatment as a function of concentration

rest time of 10 minutes after the samples were loaded and reached the testing temperature was used to minimize the normal force from squeezing the sample.

The complex viscosity of PEEK/CNT nanocomposites untreated and treated at 2.5, 5 and 10 μm are presented in Figure 8.7. From the figure it is observed that there is no distinguishable difference for the unfilled samples without and with ultrasonic treatment, until an amplitude of 10 μm is reached. At 10 μm an increase in the complex viscosity is observed. This is attributed to cross-linking due to degradation as also observed by Galloway *et al.* [234]. Figure 8.8 displays the complex viscosity of PEEK 450/nanocomposites without and with 10 μm ultrasonic treatment at a frequency of 0.1000 rad/s. It is observed that there is a significant increase in the viscosity between the

1 and 2 CNT wt% loading. This is the observed rheological percolation of the system upon the incorporation of CNTs.

A visual color change in the neat material was observed with ultrasonic treatment. Figure 8.9 displays photographs of compression molded plaques of untreated and treated neat PEEK 450PF. The change of color goes from a gray for the untreated gradually changing to a dark brown for the sample treated at 10 μm, the highest treatment level of this study. This color change is supportive of the viscosity data in that it suggests degradation. Filled samples were all black in color and no color difference was observed. A greater increase in viscosity is was observed for filled samples at the highest treatment level. A continuous increase in viscosity is observed with increasing CNT concentration. A increase of almost two orders of magnitude is observed with the incorporation of 5 wt% CNT versus the neat material. This increase in viscosity is contrary to the work using the original ultrasonic die design used to process PEEK 380P/CNT nanocomposites.

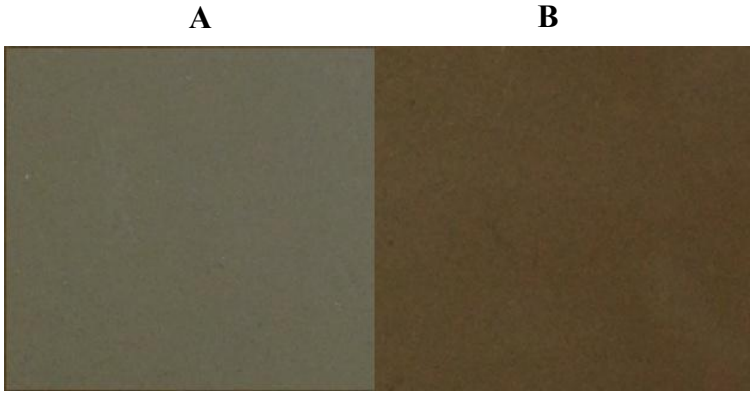

Figure 8.9: Photograph of neat PEEK 450PF without (A) and with 10 μm amplitude ultrasonic treatment (B)

PEEK 380P nanocomposites showed no change in color and a decrease in viscosity with treatment. The rheological percolation of the PEEK 450PF/CNT nanocomposites was observed to be between 1 and 2wt% loading and is comparable to that seen in the previous study on PEEK 380P where there was an increase of approximately 2.5 orders in magnitude in viscosity upon the incorporation of 5 wt% CNT. It is believed that the high bulk density of the Baytubes CNTs used in the current study made the final degree of dispersion less than that of the Nanostructured & Amorphous Materials CNTs which have a lower bulk density, 1.5 g/cm^3 compared to less than 1 g/cm^3.

All nanocomposites showed a strong shear thinning behavior. This is in accordance with literature for high L/D filler composites [206, 207]. None of the samples show significant changes in viscosity at low ultrasonic treatments of 0, 2.5 and 5 μm amplitudes. However, a significant increase in viscosity is seen for all samples with an ultrasonic treatment of 10 μm. This increase in the neat material is attributed to cross-linking and is attributed to cross-linking and increased dispersion of the CNT agglomerates leading to increased interaction between the CNTs and the matrix for the filled samples. This is supported by the increased power consumption, Figure 8.5,observed at the highest level of ultrasonic treatment.

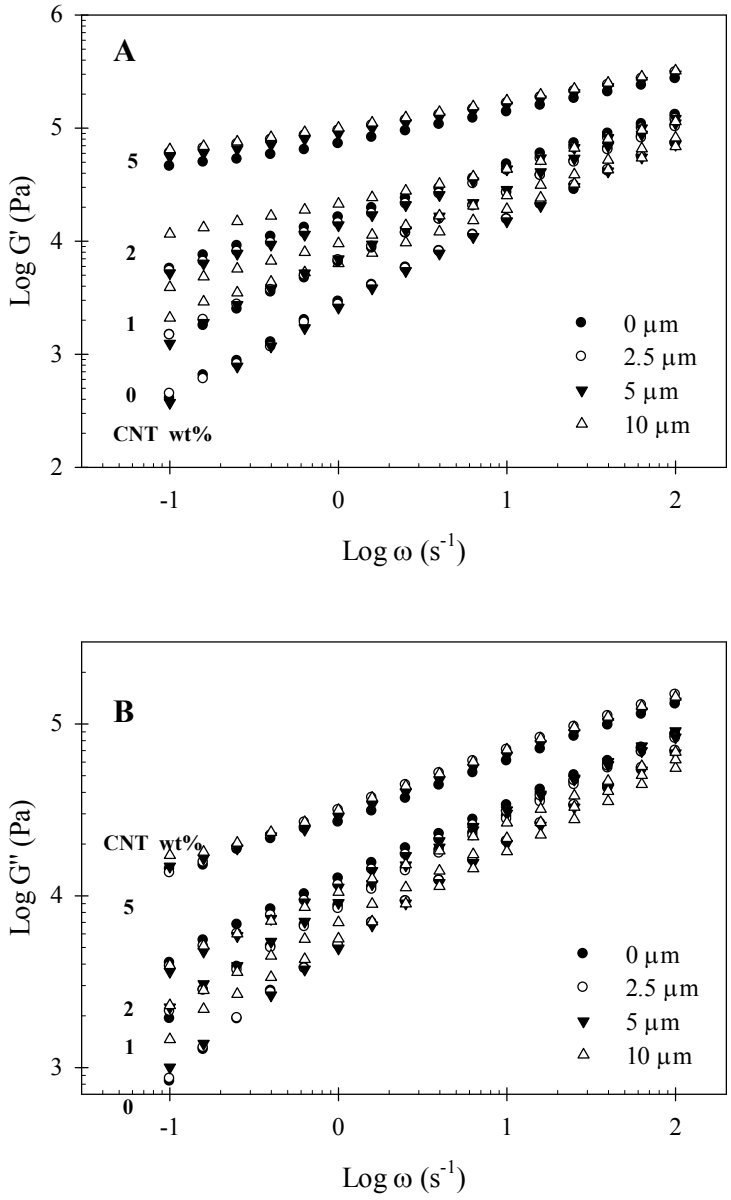

Figure 8.10: Storage (A) and loss (B) moduli of PEEK 450PF/CNT nanocomposites at various loadings and ultrasonic treatments as a function of frequency

Figure 8.10 shows the storage (A) and loss (B) moduli of the PEEK 450PF/CNT nanocomposites, respectively. A strong increase in the storage modulus is observed with

increasing CNT content. An increase of almost 2.5 orders of magnitude in storage modulus is observed with the incorporation of 5 wt%. This is comparable to the results obtained in the work on PEEK 380P/CNT nanocomposites. The largest increase is observed between 2 and 5 wt%. The slope of the curve decreases with increasing concentration. This has been proposed to be indicative of interconnected structures of anisomertric fillers leading to an apparent yield stress that is evident when a plateau is observed[208, 218, 221]. While little difference is observed at low amplitude ultrasonic treatment, treatment at 10 μm showed significant increases in the storage modulus of PEEK at loadings of 0, 1 and 2 wt% at low frequencies. This is contrary to the work on PEEK 380P nanocomposites where a strong decrease in the storage modulus was observed at high ultrasonic amplitude. This is attributed to cross-linking and increased dispersion in the filled samples.

The loss modulus is depicted in Figure 8.10 B. The loss modulus continuously increased with increasing filler concentration. The effect of ultrasound is most significant in the unfilled sample. A significant increase in the loss modulus was observed in the neat material at a treatment of 10 μm at low frequencies and lower than that of the untreated sample at high frequency. For samples containing 1 and 2 wt% CNT, the loss modulus for the 10 μm sample is the same as that of the untreated sample at low frequencies but is significantly lower than that of the untreated sample at high frequencies. This suggests that the matrix material is affected by ultrasonic treatment as its properties dominate the changes observed at higher frequencies, as supported by the change in color observed in the unfilled, treated samples.

The damping characteristics of the polymer and its nanocomposites were also evaluated. Tan δ of the untreated and treated nanocomposites is shown in Figure 8.11. A constant decrease is seen with the incorporation of CNTs. It continuously decreases with increasing filler content and the slope decreases from negative to positive. At low frequencies nearly an order of magnitude drop is seen between unfilled and 5 wt% filled samples. This is consistent for CNT nanocomposites reported in literature [221] as seen in PE/MWNT nanocomposites. This is attributed to the increased interfacial interactions between the matrix and the CNTs causing increased energy dissipation and hindered chain relaxation.

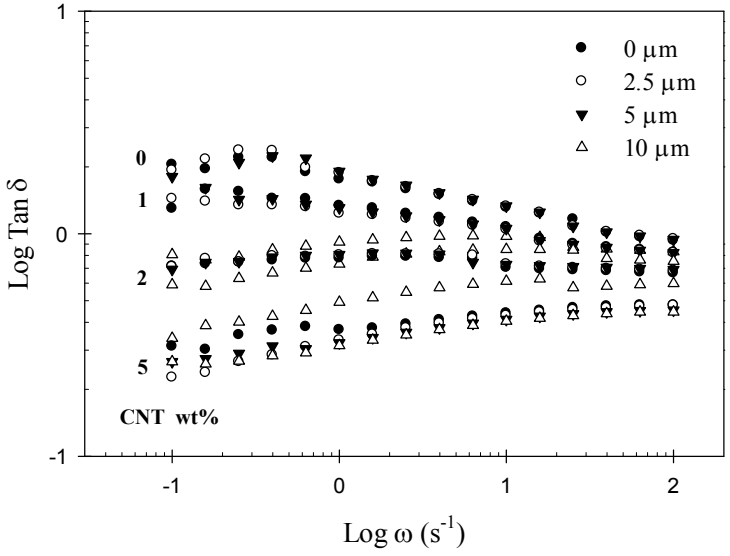

Figure 8.11: Tan δ of PEEK 450PF/CNT nanocomposites at various loadings and ultrasonic treatments as a function of frequency

The Cole-Cole plot is displayed in Figure 8.12 to see how the storage and loss moduli change relative to each other. It can be seen that upon the incorporation of CNTs there is much greater increase in G' than there is in G". There is no distinguishable difference between treated and untreated samples at low ultrasonic amplitudes of 2.5 and 5 μm. However, there is a strong change at 10 μm observed at 0, 1 and 2 wt% loadings. It is noted that the slope of the curve decreases with increasing CNT content. A strong decrease in Tan δ at 10 μm amplitude treatment is observed in 0, 1 and 2 wt% loadings and is attributed to degradation by cross-linking in the matrix.

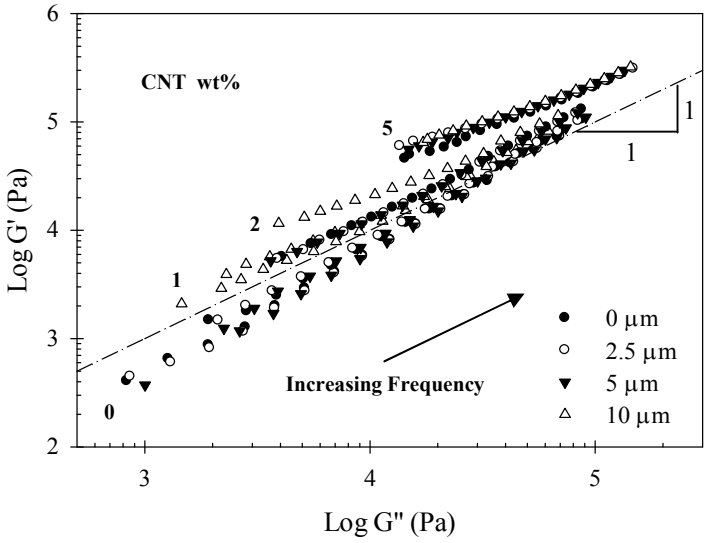

Figure 8.12: Cole-Cole plot of PEEK of PEEK 450PF/CNT nanocomposites at various loadings and ultrasonic treatments

8.5 Thermal Analysis

PEEK 450PF/CNT nanocomposites were evaluated using DSC and TGA analysis. For DSC, samples of approximately 10 mg were loaded into a sealed hermetic pan for testing. Each sample went through a heat-cool-heat cycle to erase any thermal history so that the second heat could be used for comparison purposes in a nitrogen environment. Samples were equilibrated at 0°C, heated at 20°C/min to 380°C, held for 5 min, cooled at 10°C/min to 0°C and then heated at 10°C/min to 380°C. The values of the T_g, T_m and heat of fusion, ΔH_f, for the second heat were reported. Figure 8.13 displays the cooling and second heat DSC traces for as received PEEK 450PF. All curves were similar in nature. Data from the DSC traces was analyzed using the TA Instruments Universal Analysis program and the data is reported in Table 8.2.

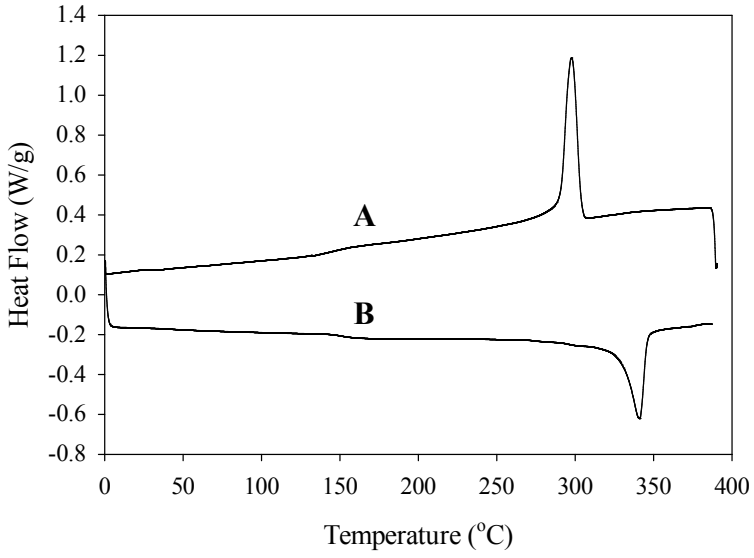

Figure 8.13: Cooling (A) and second heat (B) DSC traces of as received PEEK 450PF at a heating and cooling rate of 10°C/min

The degree of crystallinity was studied for the prepared nanocomposites. The degree of crystallinity was calculated by comparing the heat flux at melting of the tested specimen to the theoretical maximum heat flux of 100% crystalline PEEK. This 100% crystalline value was taken from literature to be 130 J/g [222]. The following equation was used:

$$\varphi_c = \frac{\Delta H_{m,PEEK}}{\Delta H^0_{PEEK}} \times 100$$

where$\Delta H_{m,PEEK}$ is the heat flux at melting of the sample, $\Delta H^0_{PEEK}$is the heat flux of melting of a 100% crystalline sample. It should be noted that the heat flux of melting and the corresponding degree of crystallinity have been corrected for CNT concentration by correcting the weight fraction of polymer in the tested sample using the following equation:

$$\Delta H_{m,PEEK} = \frac{\Delta H_{m,PEEK}\ (measured)}{Weight\ fraction\ of\ polymer\ in\ sample}$$

All results are an average of two runs using the second heat for comparison purposes.

Table 8.2 displays the thermal analysis data for all PEEK 450PF nanocomposites. From the data it is observed that there is no significant change in the glass transition or melting temperature. This differs from the work on PEEK380P/CNT nanocompositesas a slight decrease in the degree of crystallinity was observed at the highest nanotube loading. Nanotubes traditionally act as nucleating agents and a change in thermal behavior of the nanocomposites was expected. Work by Ryan *et al.*[223] on PVA/MWNT composites

and Bhattacharyya *et al.*[224] on PP/SWNT composites showed increased crystallinity with the incorporation of CNTs. However, this is consistent with work by Diez-Pascual*et al.*[225] and Sandler *et al.*[131] also found the crystallinity, glass transition and melting temperature to be unaffected with the incorporation of SWNTs. It has been suggested that the CNT confines the polymer chain inhibiting diffusion and crystal growth which minimizes the changes due to the incorporation of the CNTs.

Table 8.2: Thermal properties of PEEK 450PF/CNT nanocomposites evaluated by DSC

Amplitude (µm)	**CNT (%)**	**T_g (°C)**	**T_m (°C)**	**ΔH_f (J/g)**	**Φ_c (%)**
Neat	0	149.2	341.2	40.6	31.2
0	0	148.8	340.8	40.3	31.0
2.5	0	149.9	340.1	41.0	31.5
5	0	149.8	341.1	40.0	30.8
10	0	150.9	338.4	40.1	30.9
0	1	150.9	340.7	41.0	31.6
2.5	1	149.9	341.3	41.6	32.0
5	1	148.8	340.8	39.8	30.6
10	1	150.1	339.1	40.1	30.8
0	2	148.7	340.6	39.0	30.0
2.5	2	149.6	340.4	39.9	30.7
5	2	150.8	340.9	41.8	32.1
10	2	149.7	340.1	42.3	32.5
0	5	149.4	339.8	38.1	29.3
2.5	5	149.5	339.8	38.6	29.7
5	5	149.0	339.7	36.9	28.4
10	5	149.0	339.7	37.8	29.1

For TGA analysis approximately 10 mg of sample was loaded into a previously cleaned and tared platinum pan. Samples were equilibrated at 0°C and heated at

20°C/min to 900°C in a nitrogen atmosphere. Figure 8.14 depicts the TGA traces of unfilled PEEK 450PF both untreated and ultrasonically treated. From the traces it is seen that there is no significant distinguishable difference in weight loss between treated and untreated samples of the neat polymer.

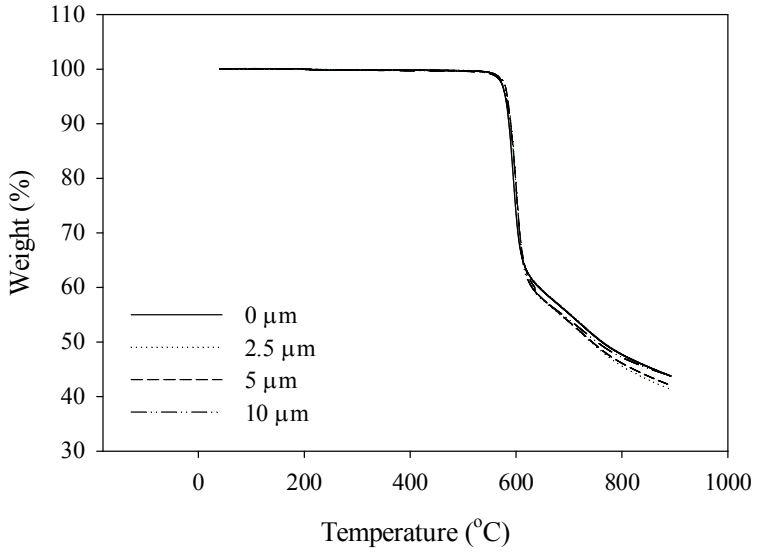

Figure 8.14: Weight loss for untreated and treated PEEK 450PF in a nitrogen environment

Figure 8.15 depicts the weight loss of PEEK 450PF/5wt%CNT nanocomposites untreated and treated at 10 µm. From the curves it is shown that there is also no distinguishable difference between untreated and ultrasonically treated samples at the highest loading and highest ultrasonic amplitude tested. This is in agreement with literature where the incorporation of CNTs into PEEK showed less than 5°C increase in initial degradation and 10% weight loss temperatures [225]. From these two figures it can be determined

that the ultrasonic treatment of this process has no negative effects on the weight loss with temperature of unaged PEEK nanocomposites.

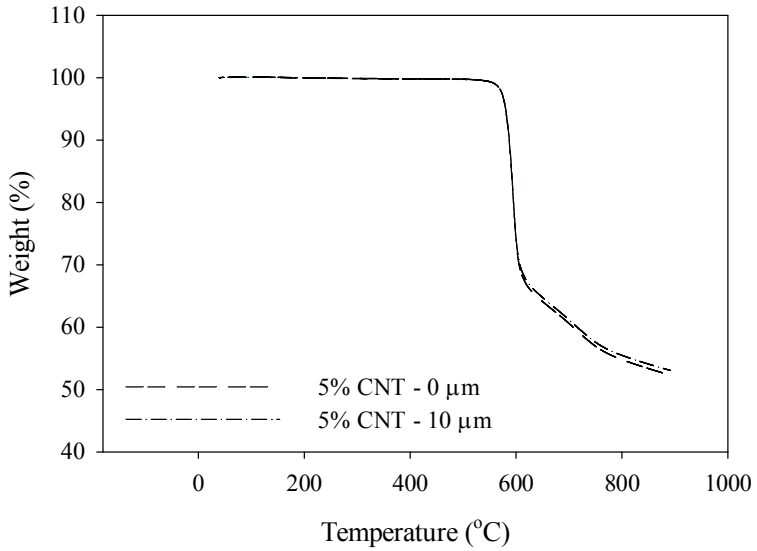

Figure 8.15: Weight loss for untreated (dotted) and treated at 10 µm (dashed) PEEK 450PF/5% CNT nanocomposites in a nitrogen environment

8.6 Mechanical Properties

The PEEK nanocomposites were extruded through a strand die, cooled in room temperature water bath and subsequently pelletized. After pelletizing, samples were dried in a vacuum oven at 100°C for 24 hours and then tensile bars, ASTM D638, were injection molded using a single cavity MiniJet injection molding machine (HAAKE, Thermo Electron Corp. Germany) at a barrel temperature of 370°C**,** a pressure of 100 MPa, with a holding time of 10 seconds and at a holding pressure of 60 MPa, and a mold temperature of 160°C. Mechanical testing was performed on the tensile bars to evaluate

the Young's modulus, ultimate strength, elongation at break and toughness on an Instron test machine (Model 5567, Instron Corp., Canton, MA, USA). Testing was carried out on a minimum of five samples according to ASTM D638 testing procedures at a cross head speed of 5 mm/min using a 10 kN load cell. The Young's modulus, ultimate strength, elongation at break and toughness were measured. No extensometer was used due to the large elongation of the PEEK nanocomposites.

The Young's modulus of PEEK 450PF nanocomposites is shown in Figure 8.16. It can be seen that there is a continuous improvement in modulus with increasing CNT loading. A 15% increase in tensile strength is observed with the incorporation of 5 wt% CNTs. This result is in line with increases in the Young's modulus for PEEK/CNT literature

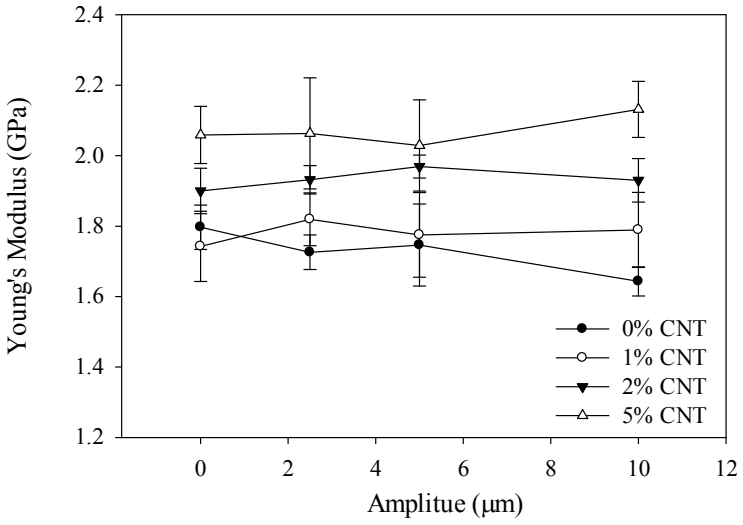

Figure 8.16: Young's modulus versus ultrasonic amplitude of PEEK 450PF/CNT nanocomposites at various loadings and ultrasonic treatment

related to the incorporation of CNFs and CNTs into PEEK. Sandler *et al.*[131] reported an increase in the Young's modulus of PEEK/CNF nanocomposites of 20% with a 7.5 wt% loading of carbon nano-fibers. This is also similar to results by Rong *et al.* [226]who found a 20% increase in modulus with the addition of 5 wt% MWNTs after twin screw extrusion and to results by Bangarusampath *et al.* [229] who found a 20% increase in modulus with the incorporation of 5 wt% of CNTs using twin screw extrusion and testing of annealed samples. This is also in line with results by Deng *et al.* [235] who found a 32% increase in modulus in PEEK/MWNT composites at a loading of 6.5 wt% after twin screw extrusion. This is better than results published by Chen [227] who found an 8% decrease in modulus with the incorporation of 5 wt% super critical CO_2 expanded MWNTs after melt mixing. This is less than results reported by Ogasawara *et al.* [228] who reported an increase of 50% in the Young's modulus with the incorporation of 9 wt% MWNT by twin screw extrusion but did not report data for lower concentrations. No significant trend was observed with ultrasonic treatment on the modulus of the nanocomposites. While the viscosity data points to increased dispersion at an ultrasonic treatment at 10 μm amplitude in all samples, only a slight observable difference is seen at a loadings of 5 wt% is only observed at the 10 μm treatment level. It is believed that due to limited interaction between the CNT surfaces and the solid matrix the synergistic effect of the incorporation of CNTs is not obtained.

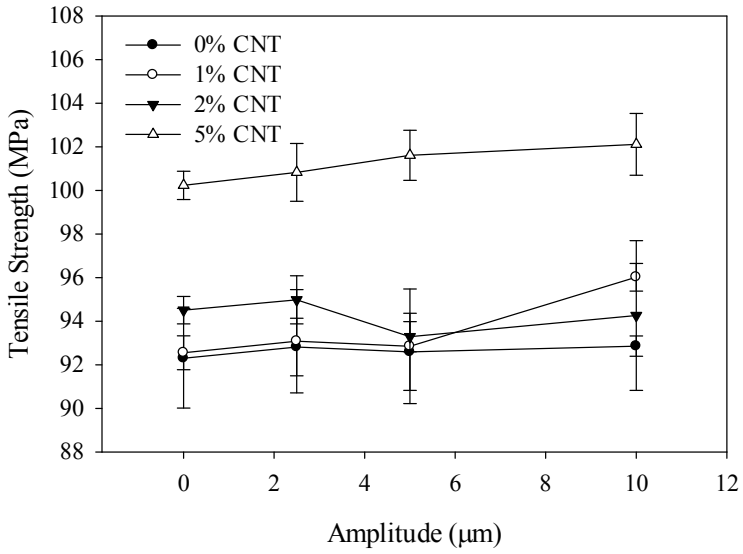

Figure 8.17: Tensile strength at yield versus ultrasonic amplitude of PEEK 450PF/CNT nanocomposites at various loadings and ultrasonic treatment

Figure 8.17 shows the tensile strength of PEEK 380P/CNT nanocomposites at various CNT loadings with and without ultrasonic treatment. The tensile strength increased with increasing CNT concentration. An increase of 10% is seen in samples at 5 wt% versus the neat material. This is similar to findings by Diez-Pascual*et al.* [230] who found a 8 and 10% increase in the strength at break with a 1 wt% loading of arc grown and laser grown SWNTs, respectively. This is significantly better than the findings by Chen [227] who found a decrease of 5% in the tensile strength with the incorporation of 5 wt% of Nanocyl-7000 multi-walled nanotubes using a super critical CO_2 expansion of the nanotubes prior to melt compounding. These results are also better than Ogasawara *et al.* [228] who found a 7.5% increase in ultimate strength with the incorporation of 9 wt% MWNT after melt mixing. No defined trend with ultrasonic treatment is observed but a

slight improvement with ultrasonic treatment is observed for samples at the 5 wt% loading. It is believed that the change in viscosity of the molten polymer has limited interaction between the CNT surfaces and the solid matrix and therefore the synergistic effect of the incorporation of CNTs is not obtained in the solid state.

The strain at break of the PEEK 450PF/CNT composites is shown in Figure 8.18. A strong and continuous difference is observed at all loading levels compared to the neat sample. A loading level of 1 wt% CNTs showed a decrease of more than 30% in elongation and a further increase to 5 wt% of CNT content yielded a decrease of nearly 50% in elongation versus the neat material. This is in agreement with the previous work on PEEK 380P/5 wt% CNT nanocomposites which showed a 50% decrease in

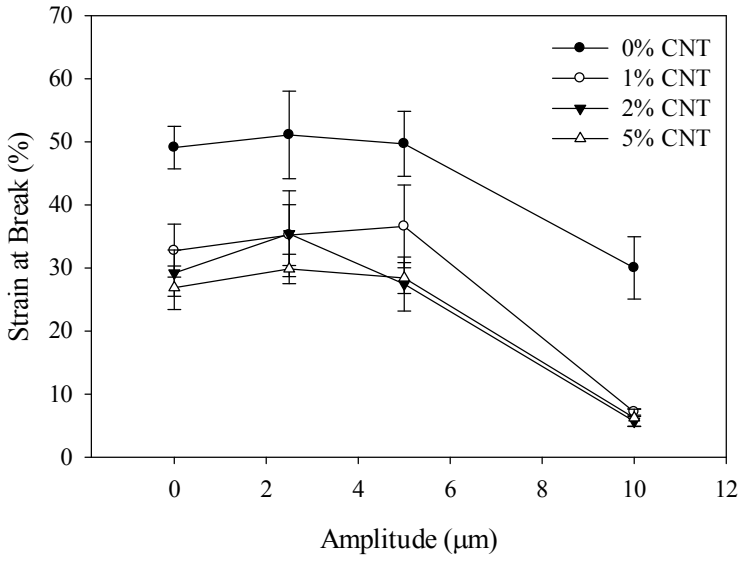

Figure 8.18: Elongation at break versus ultrasonic amplitude of PEEK 450PF/CNT nanocomposites at various loadings and ultrasonic treatment

strain at break. This is better than work by Diez-Pascual *et al.* [230] who found a decrease of almost 50% in the strain at break at a loading of only 1 wt% SWNTs in PEEK but similar to Sandler *et al.* [131] found no significant decrease in strain at break in CNF/PEEK nanocomposites up to 10 wt%. However, upon increasing the loading to 15 wt% CNF the sample failed in a brittle manner with a decrease in elongation of 80%. This is also in agreement with work by Deng *et al.*[235] who showed a decrease of 40% in the strain at break with a 6.5 wt% loading in twin screw extruded PEEK/CNT nanocomposites. There is no observable effect of ultrasound up to 5 μm amplitude. However, at 10 μm a significant effect is observed in all samples. The neat material elongation decreased by more than 30% and the filled materials decreased by more than 70%. As this trend is observed in the neat material as well as in the filled materials, it is attributed to degradation of the matrix due to the effect of high power ultrasound.

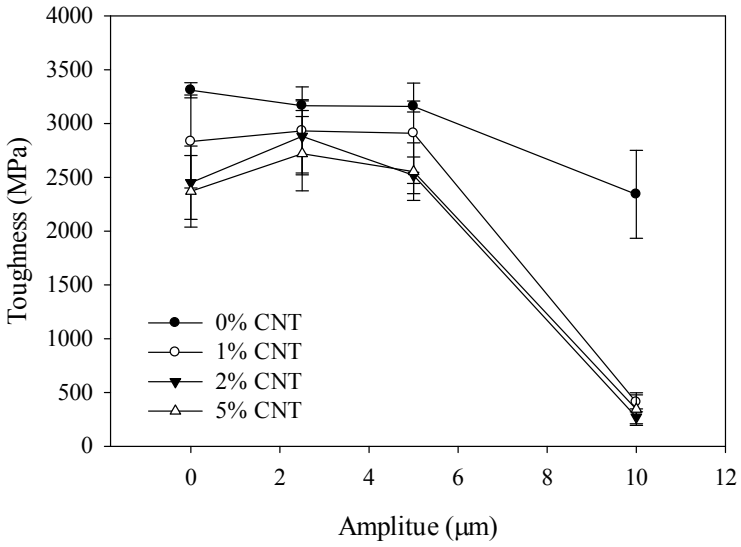

Figure 8.19: Toughness versus ultrasonic amplitude of PEEK 450PF/CNT nanocomposites at various loadings and ultrasonic treatment

The toughness, Figure 8.19, of the PEEK 450PF nanocomposites followed the same trends as the strain at break. The toughness decreased with increased filler loading. No difference was observed due to ultrasonic treatment except the strong decrease observed at the highest ultrasonic treatment level. At the highest ultrasonic treatment level a decrease of 25% in the toughness of the unfilled material and a complete loss of toughness for all filled materials. This decrease is attributed to the degradation of the backbone due to high power ultrasonic treatment. This is agreement with PEEK/SWNT work done by Diez-Pascual *et al.* [230] who showed a strong decrease in impact properties at a loading of 1 wt% SWNT.

8.7 Analysis of Electrical Properties

Compression molded plaques 90 mm in diameter and 1 mm thick of all samples, after drying at 100°C for 24 hrs under a vacuum of 30 in-Hg, were made for resistivity testing. All plaques were compression molded at 380^{o}C in a Carver (CARVER 4122, Wabash, IN) compression molding press and subsequently removed and allowed to cool to room temperature between two metal plates to maintain flatness. Two different methods were used to measure conductivity.

For the first method, a Keithley electrometer (Model 6517 A, Keithley Instruments, Cleveland, OH, USA) equipped with a model 8009 test fixture was used to test the volume resistivity of molded plaques in accordance with ASTM D257 testing procedures. This apparatus is designed to measure volume resistivity from 10^{18} to 10^{3} ohm-cm. Alternating polarity was used with a baseline of 0 volts and an alternating voltage of +/- 1

volt. The method was set to take six reads for 10 seconds at each alternating voltage and then record the final read. The measurement was taken three different times for each sample and averaged. Standard deviation is reported.

The second method was designed and developed to test materials in the low resistivity region. A Keithley micro-ohmmeter (Model 580, Keithley Instruments, Cleveland, OH, USA) was used for both the output and input signals. The apparatus consisted of two cylindrical rubber blocks 64 mm in diameter that were coated on one side with 3M^{TM} conductive film CN-3190 (3M, Saint Paul, MN, USA). The sample was placed between the two rubber blocks with the conductive side facing the sample. The blocks and samples were squeezed and the electrodes for both the input and output signals were pressed against the conductive film and a measurement was taken. The measurement was taken three different times for each sample and averaged. Standard deviation is reported.

The volume resistivity versus CNT concentration is shown in Figure 8.20 A and B at various ultrasonic amplitudes for method 1 and 2, respectively. As can be seen from the results, the electrical percolation lies between 0 and 1 wt% CNT loading. Both methods showed a drop of more than 4 orders of magnitude with percolation. This is in agreement with PEEK/SWNT work done by Diez-Pascual *et al.* [230] who showed a strong increase in electrical conductivity at a 1 wt% loading of SWNTs. This is also in agreement with data reported by Nanocyl Inc. [231] on PEEK/NC7000 MWNTs that showed a percolation between 0.5 and 1 wt%. This work shows a much lower percolation than work by Mohiuddin [232] that showed a percolation at 3.6 wt% MWNT or work by Socher *et al.* [233] who showed almost no change in resistivity up to a loading of 1.5

wt% Baytubes C150P MWNTs in PEEK after conical twin screw extrusion. However, method 1 showed no further decrease in resistivity while method 2 showed a continuous

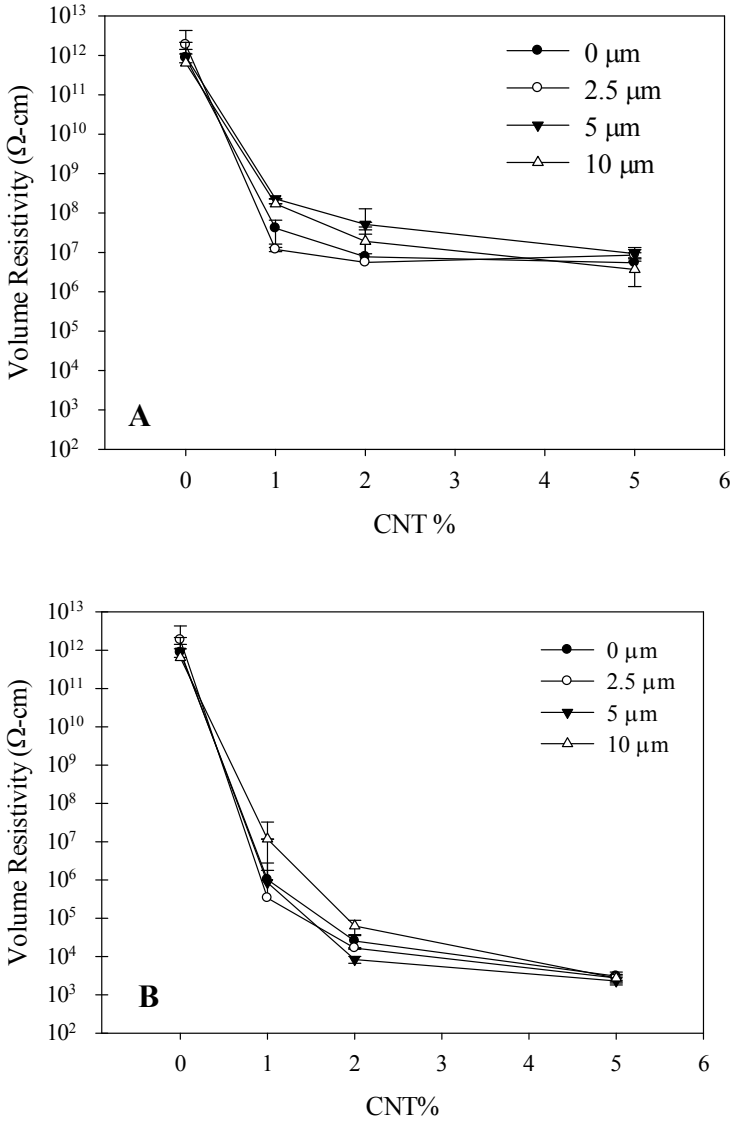

Figure 8.20: Volume resistivity versus CNT loading of PEEK 450PF/CNT nanocomposites at various ultrasonic treatments using method 1 (A) and method 2 (B)

decrease in resistivity with increasing filler loading with the resistivity decreasing almost 9 orders of magnitude at the 5 wt% loading. Method 2 was verified using a series of resistors (1, 10 and 100 ohms) to verify the measurement range.

8.8 Microscopy

Samples of PEEK injection molded tensile bars were microtomed and observed under optical microscope. An Olympus microscope with a 20X lens and 10X eye piece was used to collect images. A Leica Ultracut microtome was used to prepare the microtome samples. Several images were collected and representative micrographs are depicted. Optical micrographs of samples with 2 wt% CNT loading without and with ultrasonic treatment at 10 μm amplitude are shown in Figure 8.21. From the micrographs it is observed that in the untreated samples the CNT agglomerates are regularly shaped and smooth while in the sample treated at 10 μm the agglomerates appear more irregular in shape and there also appears to be a greater number of smaller particles. These micrographs are characteristic of what was seen in several samples but further statistical analysis and more micrographs need to be collected. However, both micrographs still show a significant number of agglomerates. AFM imaging was used to look at the edge of the agglomerates but CNTs could not be distinguished from the matrix in microtomed samples.

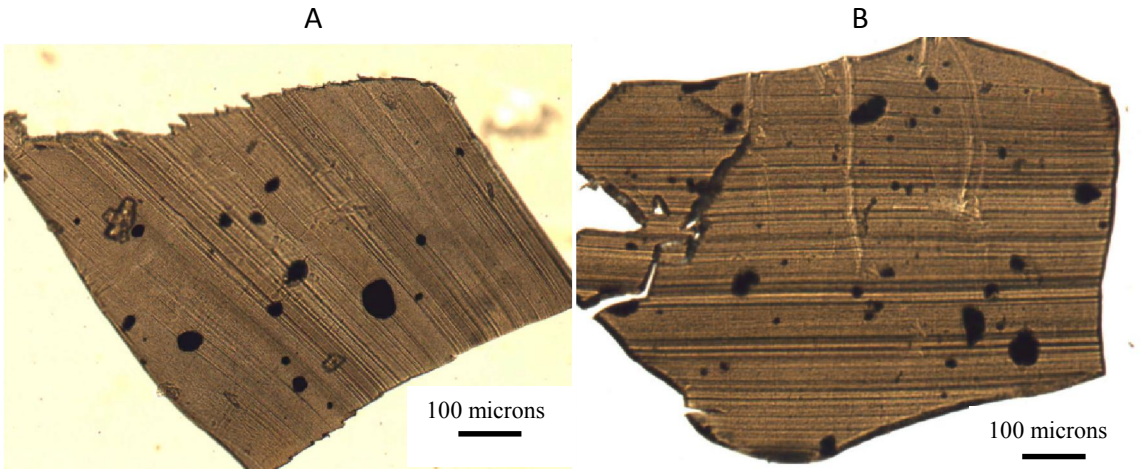

Figure 8.21: Optical micrograph of a PEEK/2wt% CNT nanocomposites untreated (A) and treated at 10 µm (B) at 200X magnification

8.9 Conclusions

A modified extrusion process was designed and manufactured for this work that incorporates ultrasound assisted dispersion into the extruder. This novel design for the dispersion of nanocomposites was used to process PEEK 450PF/CNT nanocomposites. CNTs were fed downstream to avoid the high shear zone at the feed throat. The pressure after ultrasonic treatment, melt temperature and ultrasonic power consumption were recorded. Pressure at the treatment zone was observed to increase with increasing nanotube concentration and with increasing ultrasonic power. This change is a permanent effect that is observed in the viscosity and is attributed to the increased dispersion of CNTs. A decrease in extruder torque was observed with increasing ultrasonic amplitude and is attributed to recoverable thixotropic effects. This decrease in extruder torque is beneficial for industrial applications where torque limits throughput. An increase in complex viscosity of nearly two orders of magnitude was observed with the addition of 5 wt% of CNT. Samples ultrasonically treated at 10 µm showed a significant increase in

viscosity over untreated samples and is attributed to improved dispersion. The rheological percolation is observed to be between 1 and 2%. Mechanical properties showed an increase of 20% in the Young's modulus and a 10% increase in strength with the addition of 5 wt% CNT. A continuous decrease in the strain at break increasing filler was observed. A significant decrease in electrical resistivity of more than 5 orders of magnitude at CNT loading of 1 wt% was observed with the electrical percolation below the 1 wt% loading. A further decrease in resistivity was observed with increasing filler concentration with a drop of more than 8 orders of magnitude at a loading of 5 wt%. Optical microscopy of ultrasonically treated samples showed enhanced dispersion of the CNT bundles.

CHAPTER IX

A METHOD FOR THE EVALUATION OF RESPIRATORS IN A NANORICH ENVIRONMENT

9.1 Introduction

The excitement and hysteria over the possible properties of carbon nanotube filled matrices for enhanced mechanical, electrical and thermal properties has proliferated their use in labs. Since these nano-scaled fillers are being encountered in the unincorporated form, it is important to prevent the inhalation of these nanostructures and understand the effectiveness of common, commercially available personal protective equipment (PPE) for the respiratory system. The field of nanotoxicology was introduced to deal specifically with the potentially toxicological interaction between nano-structured materials and living matter [236]. Nanotoxicology was developed from the understanding that the small size and large surface area of nanostructures brings unique characteristics to these materials as compared to their larger counterparts. Although this study does not deal with the actual effects that nanostructures have on the human body during inhalation, it was concerned with determining the current ability to prevent inhalation of the carbon nanostructures. The airborne release of materials, such as carbon nanotubes (CNTs), carbon nanofibers (CNFs) and nanoclays, into the air during compounding is inevitable. In conventional polymer processing these fillers pose a

potential threat until they are encapsulated in a polymer matrix. This occurs while transporting or feeding nanostructures into the process. Typically, the operator uses a respirator to avoid inhaling nanostructures into the body that escape engineering controls and it is therefore important to investigate how efficient these respirators are at capturing these airborne materials. The purpose of this research was to design and build a device to artificially simulate human breathing and to test the ability of commercially available masks to filter out nanostructures from the air during their use. In particular, this study focused on the effectiveness of a mask's ability to stop the inhalation of CNTs when the nanostructures are suspended in the air.

Many different respiration masks are currently available on the market. All of the masks that were evaluated are mechanical filter respirators. These masks rely on the filter material to physically retain any particulate matter that may be contaminating the air. NIOSH (National Institute for Occupational Safety and Health) has released a rating system to assess a mask's ability to filter out air contaminants [202]. The masks range from filtering out 95% of all airborne particles up to 99.97% of all airborne particles being filtered out. The highest of the ratings, N100, relies strongly on the HEPA (High Efficiency Particulate Air) filter which was developed during the Manhattan Project in the 1940s [203]. HEPA filters claim to remove 99.97% of airborne particles 0.3 micrometers in diameter, which has been determined to be the most difficult to filter and therefore is the most penetrating particle size (MPPS). Particles larger and smaller than this are filtered with higher efficiency. Particles that are larger than the MPPS tend to easily become embedded within the filter if they ever find a space large enough to

penetrate into the mat of randomly arranged fibers. On the other hand, particles smaller than 0.3 micrometers tend to adhere to the fibers due to electric charge and also have a chance of embedding into the fibers. In the case of this study, due to the nanostructure of the particles (10-100 nm diameter and L/D ranges from 100 to 1000), most of the filtration occurs due to both interception (particles adhere to small fibers when coming within one radius of the fiber because of electric charge) and by impaction (particles are physically embedded into larger fibers). Due to the scale of these nanoparticles, diffusion occurs once they are within the filter. Diffusion occurs as a result to the collision of the contaminants with gas molecules, thereby changing their path through the filter. In order to truly determine which mask works most effectively for this specific purpose, masks of different ratings was compared to find the optimal choice and degree of protection.

9.2 Experimental Procedures

Three different respirators of various ratings were evaluated in this study. Disposable mechanical filter respirators produced by 3M with N100 and N95 filter ratings along with a common dust nuisance mask were evaluated. While it was understood that the nuisance mask would not be effective it was deemed worthy as it is common in the work place environment for individuals to use whatever respirator is most readily available. Carbon nanotubes produced by Bayer Scientific, Baytubes C150P were used in the evaluations of these respirators and are depicted in Figure 9.1. These nanotubes have diameters in the range of 10-100 nm and lengths in the range of 1,000- 100,000 nm.

To determine the resistance of respiratory masks to the permeation of nanostructures required a controlled environment for quantitative conclusions to be reached. In order to test the ability of mechanical particulate filter respirators to prevent this permeation, an

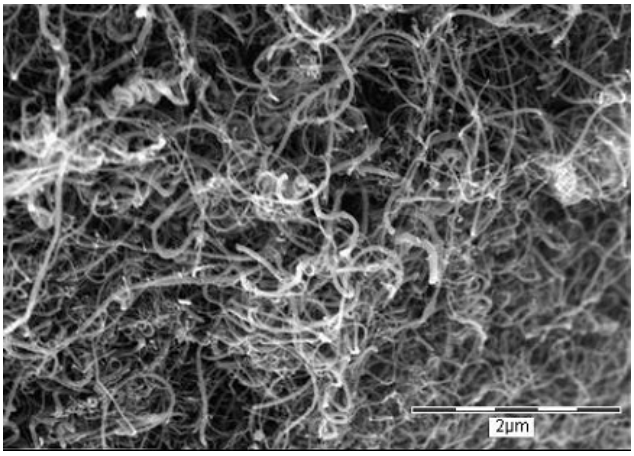

Figure 9.1: SEM of Baytubes C150P by Bayer [200]

artificial respiration device was developed to contain the nanorich environment. The designed device consists of a closed loop system where air is consistently being pulled out of a nanorich environment through a respiratory mask. A schematic of the developed device is depicted in Figure 9.2.

The inhalation device uses a piston apparatus, parts 1 and 9, to simulate the breathing process in which the volume of air and air flow time simulates an actual human breath and is pneumatically driven. The piston in the upper jar cycles over a specified stroke length. Approximately 34.2 in^3 (560 ml) of air is passed through the mask with each stroke. This amount is consistent with a typical tidal breath of a 154 lb male (30.5 in^3 per a breath (500 ml)). The cycle of the artificial inhale/exhale provides 16 breaths per a

minute. This amount is also consistent with the typical respiratory rate of a healthy adult of 12-20 breaths/minute. If desired, the respiratory rate can be altered. The air is pulled

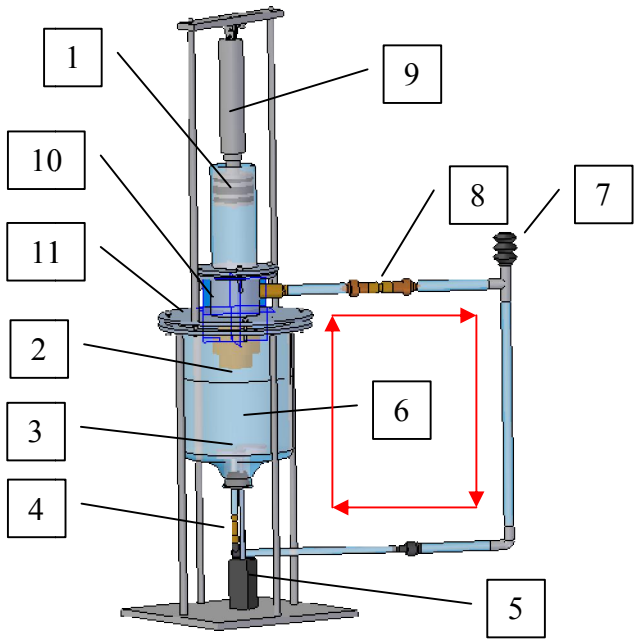

Figure 9.2: Schematic of simulated inhalation device. 1-Piston, 2-Mask, 3-Fan Blade, 4-Check Valve, 5- Fan Motor, 6-Glass Jar 7-Air Baffle, 8-Check Valve, 9-Actuator, 10 and 11 - Pressure transducers

from a 10 quart bell jar of contaminated air. The jar contains the respirator being tested and a mixing device (fan). Two grams of CNTs is charged into the jar at the beginning of each experiment. The air within the large bell jar is constantly being circulated by a variable speed fan to ensure that the nanostructures are always suspended in the air. Two baffles were attached vertically along the inside of the chamber opposite of each other to ensure turbulence in the air flow for random distribution. The fan was fixed 100 RPM at a speed in which it created turbulent flow to disperse the filler into the air but did not

cause the filler to agglomerate in a tornado type pattern along the outside walls and was positioned such that it did not force air through the mask. A mask is placed at the opposite end of the fan and is attached to a check valve. Once the air has been drawn through the mask the check valve closes and the air is then re-circulated back to the opposite side of the bell jar to be cycled through the mask again. This was done as the majority of respirators that have a N95 value and greater have outlet for exhalation. The closed system ensures that nanostructures do not escape into the surrounding areas. The entire unit is disassembled and cleaned after each experiment.

The mask was evaluated using optical microscopy. An Olympus BX63 microscope with transmission and reflection capability was used to carry out the microscopy studies of the mask at 50, 100 and 200 magnifications. A Minwax clear gloss urethane was used to solidify the CNTs in place for sectioning of the mask. The urethane was slowly infused into the mask to minimize the displacement of the contained nanotubes and allowed to dry for two days in a vented hood. The cured mask was then sectioned using a Buehler low speed saw (Model Isomet, Lake Bluff, Illinois) equipped with a diamond blade and oil bathand optical micrographs were obtained. The penetration length of the CNTs was measured and used to evaluate the effectiveness of each mask.

Ports into both the bell jar and the upper cylinder allowed for pressure measurements to be taken to ensure replication of actual conditions. The pressure inside the bell jar remained near zero that simulates the breathing environment in a large room as well as to ensure that no nanotubes were forced through the mask due to positive pressure. Traces

of the pressure profiles in both the testing chamber and the piston are displayed in Figure 9.3.

Initial testing used a continuous testing time of 24 hours to evaluate each of the respirators. While it is understood that most individuals do not work for 24 hours in a

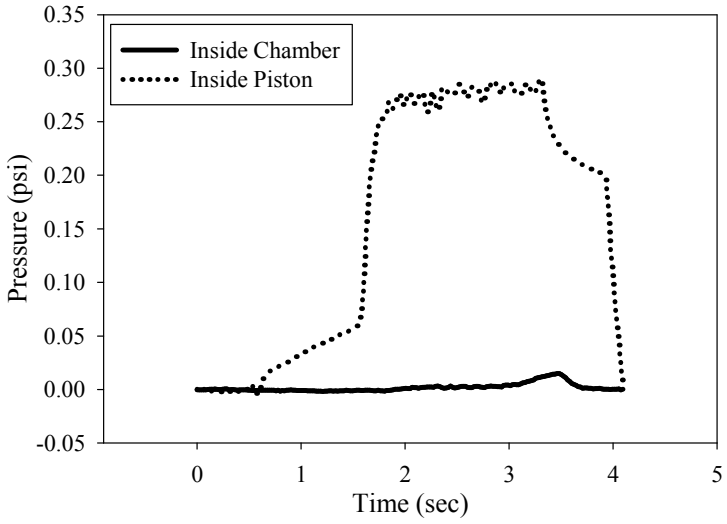

Figure 9.3: Pressure profiles inside testing chamber (jar) and piston

row it is also understood that the majority of individuals use a mask multiple times before disposal. After each testing cycle the mask was carefully removed to ensure that there was no contamination of the tested mask. Immediately after removed the mask inner portion of the mask was covered until it was solidified in urethane.

9.3 Results

Several difficulties arose in this study. Consistency of the breathing apparatus was found to make a tremendous difference on the penetration distance of the CNTs. During initial experiments on the N95 respirators it was noticed that the piston was binding against the glass wall causing a palpation in the inhalation process. This stick slip of the seals on the piston along the cylinder wall caused small quick increases in the drawing of air through the respirators. At the end of these experiments the CNTs had completely penetrated the N95 mask. However, under normal breathing conditions the N95 respirator appears to be sufficient at capturing the airborne CNTs. This does lead to the speculation that under heavy breathing conditions that the CNTs would likely completely permeate the N95 respirator.

Figure 9.4 is a micrograph of the nuisance dust mask at 100X magnification. It can be seen that that the CNTs completely permeate the mask. This was also observed upon taking the mask out of the device. The inside of the mask had areas that were completely black and visible to the eye.

Inside of respirator Outside of respirator

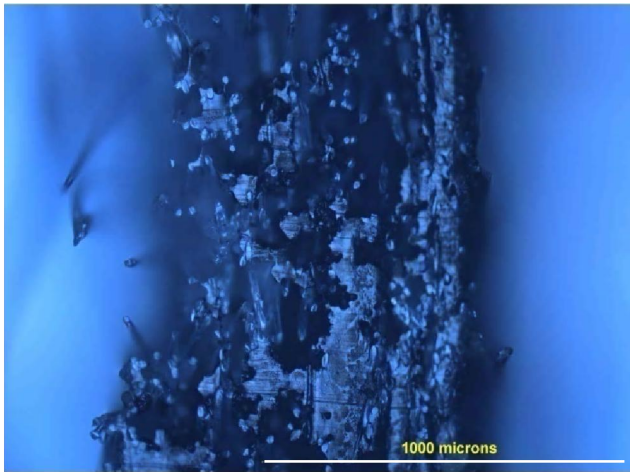

Figure 9.4: Micrograph of tested dust nuisance mask at 100X magnification showing complete penetration after 24 hours of testing

Inside of respirator Outside of respirator

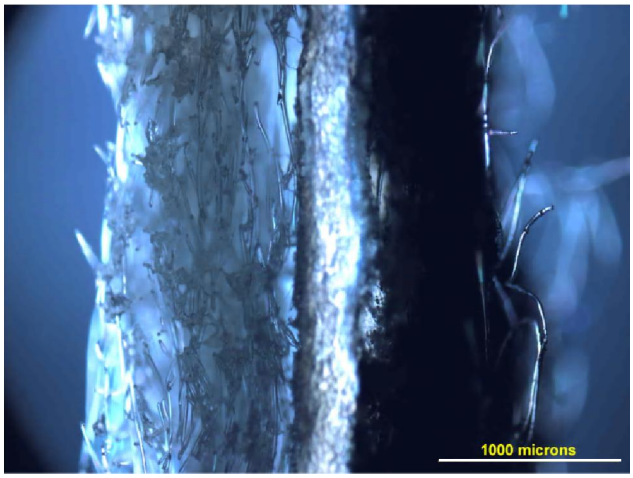

Figure 9.5: Micrograph of tested N95 respirator at 50X magnification after testing for 24 hours

Inside of respirator Outside of respirator

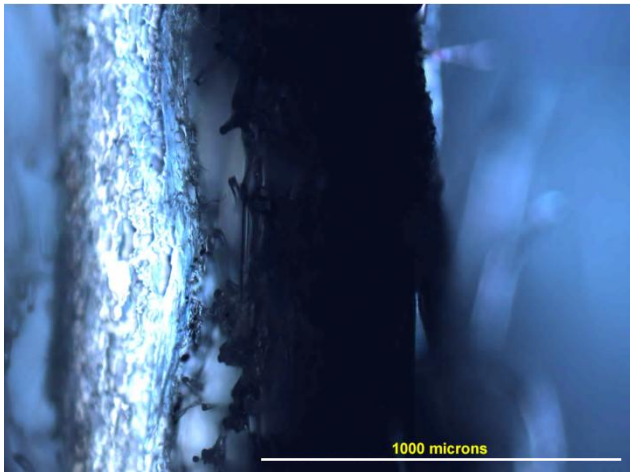

Figure 9.6: Micrograph of tested N95 respirator at 100X magnification after testing for 24 hours

Figures 9.5 and 9.6 are micrographs of the N95 respirator at a 50X and 100X magnifications. The N95 mask had no visual permeation on the inside of the mask. As can be seen in Figure 9.5, the CNTs penetrated more than 1000 microns into the mask. As per the mechanism of confinement, the outer 1000 micron layer was completely filled with CNTs. Figure 9.6 was taken to show the adhesion of the CNT bundles to the fibrous material of the respirator. The individual bundles of the CNTs are stuck to the fiber.

Figures 9.7 and 9.8 are micrographs of the N100 respirator at 50X and 100X magnifications. None of the N100 masks had any visual penetration of the CNTs on the inside of the mask. From Figure 9.7 it is seen that the CNTs penetrate approximately 1000 microns into the outer surface of the mask.

Inside of respirator Outside of respirator

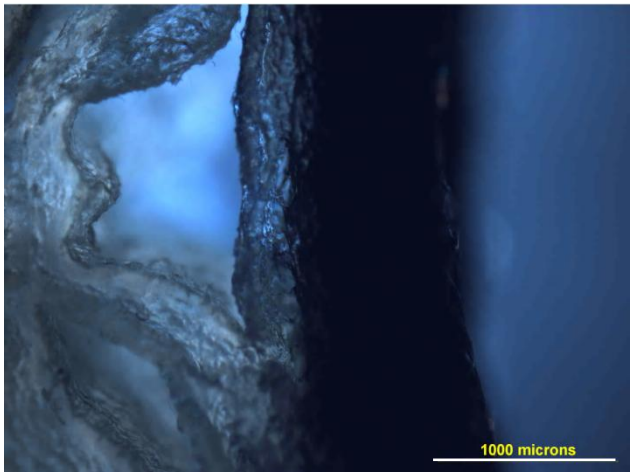

Figure 9.7: Micrograph of tested N100 respirator at 50X magnification after testing for 24 hours showing penetration of the exterior portion of the mask

Inside of respirator Outside of respirator

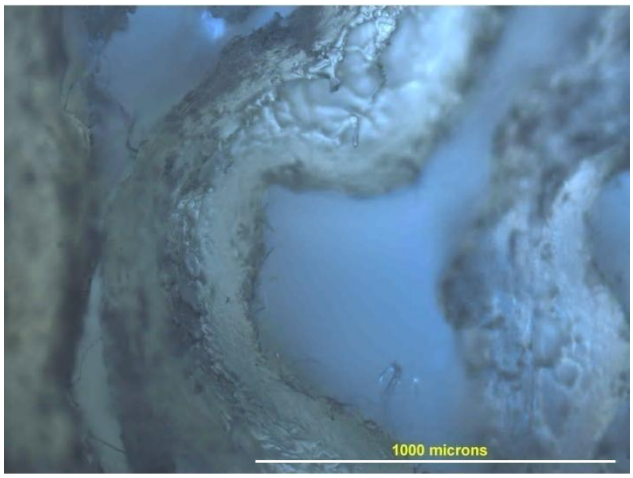

Figure 9.8: Micrograph of tested N100 respirator at 100X magnification after testing for 24 hours showing no CNT penetration to the interior of the mask

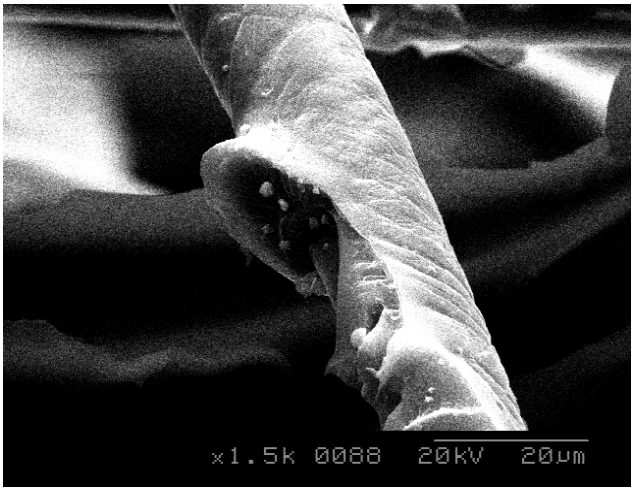

Figure 9.9: SEM image of an untested N95 respirator fiber

Figure 9.10: SEM image of an untested N100 respirator fibers

It can also be observed from the micrographs that the N100 respirator is a much denser mask and that the fibrous materials making up the structure are finer than the lower rated respirators. All masks were evaluated at 100X optical magnification for

comparison purposes and the N95 and N100 respirators were also evaluated using SEM, Figures 9.9 and 9.10, to show the differences in fibrous material. It was seen that in all respirators, Figures 9.4 - 9.7, that the CNTs penetrated approximately 1000 microns. This was the entire thickness of the nuisance mask, approximately half the thickness of the N95 filter and approximately a quarter of the thickness of the N100 mask.

9.4 Conclusions

Based on the results of this work the following are the opinions of the authors based on optical evaluation of the tested respirators. Typical dust masks are not sufficient to prevent the inhalation of nanostructures and should not be used. In less than 24 hours in a nanorich environment there was complete penetration of the CNTs. Both the N95 and N100 respirators showed the ability to prevent penetration of the CNTs under normal breathing conditions. The CNTs only penetrated half of the thickness of the N95 respirator and only a quarter of the thickness of the N100 respirator. However, as stated previously, under duress or abnormal breathing conditions, the palpations of the stick slip, it was seen that there was complete penetration of the N95 mask in less than 18 hours.

CHAPTER X

CONCLUSION AND RECOMMENDATIONS

Two novel methods for the manufacturing of high performance nanocomposites were developed. The first method utilized an ultrasonic slit die attachment as the die for the twin screw extruder. The second method was an enhancement of the first design by incorporating the ultrasonic treatment into the extruder to utilize the shearing of the polymer by the screws while simultaneously applying treatment. Both methods are environmentally friendly, can be adapted to utilize current manufacturing equipment and are readily scalable. Two different high performance materials were studied. A phenylethynyl imide thermoset material, PETI-330, and polyetherether ketone, PEEK, thermoplastic were evaluated for enhanced mechanical and electrical properties with the incorporation of multiwalled carbon nanotubes . Ultrasonic treatment was observed to show distinct changes in the rheological, morphological and mechanical properties, showing enhanced dispersion of the CNT bundles at certain amplitudes and loadings.

PETI-330/CNT nanocomposites at concentrations up to 5 wt% CNT were processed using an ultrasonically assisted slit die attachment. An increase in viscosity of nearly 4 orders of magnitude upon the incorporation of 5 wt% CNT was observed and treated samples showed increased viscosity due to improved dispersion at certain amplitudes.

The incorporation of CNTs into PETI-330 showed improvements in mechanical properties with a 20% increase in modulus with increasing concentration up to 2 wt% CNT for the untreated and treated samples. Electrical percolation was achieved at a concentration 0.5 wt% CNT with drop in resistivity of more than 9 orders of magnitude. A further decrease in resistivity was seen with increasing filler concentration with a total drop in resistivity of almost 12 orders of magnitude at a 5 wt% CNT loading. Micrographs of untreated and treated samples show increased dispersion of agglomerates in the treated samples. No change in thermal stability of nanocomposites.

PEEK/CNT nanocomposites at concentrations up to 10 wt% CNT were also prepared using the twin screw extruder utilizing an ultrasound assisted slit die attachment. It was observed that the die pressure increased with increasing concentration of CNT loading and decreased with ultrasonic amplitude. This allows for enhanced throughput in industrial applications. An increase in viscosity of more than three orders of magnitude was observed upon the incorporation of 10 wt% CNT loading. Mechanical testing showed increases in modulus and strength of more than 20 % and 10 %, respectively, with the addition of up to 5 wt.% CNT. Electrical resistivity showed a percolation with a drop of more than seven orders of magnitude at a loading of 1 wt% CNT. Further filler loading resulted in a continuous decrease in resistivity with a drop of 9 orders of magnitude achieved at the 10 wt% CNT loading

A second modified extrusion process was designed and manufactured for this work that incorporated ultrasound assisted dispersion into the extruder. This novel design for the dispersion of nanocomposites was used to process PEEK 450PF/CNT

nanocomposites at up to 5 wt% loadings. A decrease in extruder torque was observed with increasing ultrasonic amplitude and is attributed to recoverable thixotropic effects.

This decrease in extruder torque is beneficial for industrial applications where torque limits throughput. An increase in complex viscosity of nearly two orders of magnitude was observed with the addition of 5 wt% of CNT. Samples ultrasonically treated at 10 μm showed a significant increase in viscosity over untreated samples and is attributed to improved dispersion. Mechanical properties showed an increase of 20% in the Young's modulus and a 10% increase in strength with the addition of 5 wt% CNT. A significant decrease in electrical resistivity of more than 5 orders of magnitude at CNT loading of 1 wt% was observed indicating the electrical percolation is below the 1 wt% loading. A further decrease in resistivity was observed with increasing filler concentration with a drop of more than 8 orders of magnitude at a loading of 5 wt%. Optical microscopy of ultrasonically treated samples showed enhanced dispersion of the CNT bundles.

A curing model for PETI-330 was proposed, developed and evaluated during this research. The goal of this model was to predict the degree of cure of PETI-330 under non-isothermal curing conditions. The curing conditions are crucial for resin transfer molding applications and understanding the time-temperature curing cycle is critical to being able to develop high performance industrial components. The proposed model was developed using an induction time approach with computationally derived constants based on differential thermal scanning calorimetry (DSC) data. The model was validated experimentally by comparing predicted values with experimental measurements of a

compression molded plaque at various degrees of cure. The predicted and experimentally measured degrees of cure were in good agreement.

An apparatus for producing high temperature resin transfer molded plaques was designed and manufactured. While several plaques had dry spots, the areas that were infused had lower void fraction contents and superior short beam shear strength properties to those of the sample plaques made by vacuum assisted resin transfer molding at room temperature. It should be noted that while the RTM plaques had less retention than the VARTM plaques, RTM PETI-8 plaques had higher SBS values than VARTM PETI-8 plaques at all temperatures.

The environmental aspect of nanomaterials in a processing environment was researched, focusing on the prevention of inhalation of nanofillers. A method was developed and equipment was designed and manufactured for the testing of commercially available respirators in an environment that is contaminated with nanofillers. Three respirators were tested and evaluated including a common dust nuisance respirator and N95 and N100 NIOSH rated respirators. Results showed distinct differences in respirators according to their specified rating. Based on the results of this work the following are the opinions of the authors based on optical evaluation of the tested respirators. Typical nuisance dust masks are not sufficient to prevent the inhalation of nanostructures and should not be used. In less than 24 hours in a nanorich environment there was complete penetration of the CNTs. Both the N95 and N100 respirators showed the ability to prevent penetration of the CNTs under normal breathing conditions. The CNTs only penetrated half of the thickness of the N95 respirator and only a quarter of the

thickness of the N100 respirator. However, under duress or abnormal breathing conditions it was seen that there was complete penetration of the N95 mask in less than 18 hours.

REFERENCES

1. Iijima, S., Helical microtubules of graphitic carbon. *Nature (London, United Kingdom)*, 1991. **354**(6348): p. 56-8.

2. Hergenrother, P., ed. *Advances in Polymer Science: High Performance Polymers*. 1994, Springer-Verlag: New York. 337.

3. Kroschwitz, J., ed. *High Performance Polymers and Composites*. Encyclopedia Reprint Series. Vol. 1. 1991, John Wiley & Sons: New York. 992.

4. Rabilloud, G., ed. *High-Performance Polymers: Chemistry and Applications (Polyquinoxalines and Polyimides)*. Editions Technip. 1997, Institut Francais du Petrole Publications: Paris.

5. Wilson, D., Stenzenberger, H., and Hergenrother, P., eds. *Polyimides*. 1990, Chapman and Hill: New York. 297.

6. Seymour, R. and Kirshenbaum, G., eds. *High Performance Polymers: Their Origin and Development*. 1986, Elsevier: New York. 461.

7. Lin, S. and Pearce, E., eds. *High-Performance Thermosets*. 1993, Hanser: New York.

8. Hergenrother, P., The use, design, synthesis, and properties of high performance/high temperature polymers: An overview. *High Performance Polymers*, 2003. **15**(1): p. 3-45.

9. Sroog, C., Polyimides. *Journal of Polymer Science: Macromolecular Review* 1976. **11**(1): p. 161-208.

10. Hergenrother, P., Watson, K., Smith, J., Connell, J., and Yokota, R., Polyimides from 2,3,3',4'-biphenyltetracarboxylic dianhydride and aromatic diamines. *Polymer*, 2002. **43**(19): p. 5077-5093.

11. Connell, J., Smith, J., and Hergenrother, P., Oligomers and Polymers Containing Phenylethynyl Groups. *Journal of Macromolecular Science: Reviews in Macromolecular Chemistry & Physics*, 2000. **40**(2/3): p. 207-30.

12. Lee, Y., Huang, J., Kuo, S., and Chang, F., Low-dielectric, nanoporous polyimide films prepared from PEO-POSS nanoparticles. *Polymer*, 2005. **46**(23): p. 10056-65.

13. Jiang, X., Bin, Y., and Matsuo, M., Electrical and Mechanical properties of polyimide-carbon nanotubes composites fabricated by in situ polymerization. *Polymer*, 2005. **46**(18): p. 7418-23.

14. Yang, C. and Su, Y., Colorless polyimides from 2,3,3',4'-biphenyltetracarboxylic dianhydride (a-BPDA) and various aromatic bis (ether amine)s bearing pendent trifluoromethyl groups. *Polymer*, 2005. **46**(15): p. 5797-5807.

15. Hergenrother, P., Watson, K., Smith, J., Connell, J., and Yokota, R., Copolyimides from 2,3,3',4'-biphenyltetracarboxylic dianhydride and pyromellitic dianhydride with 4,4'-oxydianiline. *Polymer*, 2004. **45**(16): p. 5441-49.

16. Watson, K., Ghose, S., Delozier, D., Smith, J., and Connell, J., Transparent, flexible, conductive carbon nanotube coatings for electrostatic charge mitigation. *Polymer*, 2005. **46**(7): p. 2076-85.

17. Fang, X., Xang, Z., Zhang, S., Gao, L., and Ding, M., Snythesis and properties of polyimides derived from cis- and trans- 1,2,3,4-cyclohexanetetracarboxylic dianhydrides. *Polymer*, 2004. **45** (8): p. 2539-49.

18. Smith, J., Connell, J., Delozier, D., Lillehei, P., Watson, K., Lin, Y., Zhou, B., and Sun, Y., Space durable polymer/carbon nanotube films for electrostatic charge mitigation. *Polymer*, 2004. **45**(3): p. 825-36.

19. Southcott, M., Amone, M., Senger, J., Wang, A., Polio, A., and Sheppards, C., The development of processable, fully imidized, polyimides for high-temperature applications. *High Performance Polymers*, 1994. **6**(1): p. 1-12.

20. Hay, J.N., Boyle, J.D., Parker, S.F., and Wilson, D., Polymerization of N-phenylnadimide: a model for the crosslinking of PMR-15 polyimide. *Polymer*, 1989. **30**(6): p. 1032-1040.

21. Bryant, R., Jensen, B., and Hergenrother, P., Chemistry and properties of a phenylethynyl-terminated polyimide. *Journal of Applied Polymer Science*, 1996. **59**(8): p. 1249-54.

22. Meyer, G., Glass, T., Grubbs, H., and McGrath, J., Synthesis and characterization of polyimides endcapped with phenylethynylphthalic anhydride. *Journal of Polymer Science, Part A: Polymer Chemistry*, 1995. **33**(13): p. 2141-9.

23. Smith, J., Connell, J., Hergenrother, P., Ford, L., and Criss, J., Transfer molding imide resins based on 2,3,3',4'-biphenyltetracarboxylic dianhydride. *Macromolecular Symposia*, 2003. **199**(Polycondensation 2002): p. 401-418.

24. Harris, F., Pamidimukkala, A., Gupta, R., Das, S., Wu, T., and Mock, G., Synthesis and characterization of reactive end-capped polyimide oligomers. *Journal of Macromolecular Science, Chemistry*, 1984. **A21**(8-9): p. 1117-35.

25. Paul, C.W.M., NJ), Schultz, Rose A. (Princeton, NJ), Fenelli, Steven P. (Hillsborough, NJ), Polyimides end-capped with diaryl substituted acetylene. 1992, National Starch and Chemical Investment Holding Corporation (Wilmington, DE): United States.^

26. Fang, X., Rogers, D., Scola, D., and Stevens, M., A study of the thermal cure of a phenylethynyl-terminated imide model compound and a phenylethynyl-terminated imide oligomer (PETI-5). *Journal of Polymer Science, Part A: Polymer Chemistry*, 1998. **36**(3): p. 461-470.

27. Connell, J.W.Y., VA), Smith, Joseph G. (Smithfield, VA), Hergenrother, Paul M. (Yorktown, VA), Composition of and method for making high performance resins for infusion and transfer molding processes. 2002, The United States of America as represented by the Administrator, National Aeronautics and Space Administration (Washington, DC): United States.^

28. Wang, K., Ogasawara, T., and Ishida, Y., Optimization of liquid molding cycle for a phenylethynyl terminated polyimide composite. *Journal of Reinforced Plastics and Composites*, 2006. **25**(4): p. 361-377.

29. Connell, J., Smith, J., Hergenrother, P., and Criss, J., High temperature transfer molding resins: Laminate properties of PETI-298 and PETI-330. *High Performance Polymers*, 2003. **15**(4): p. 375-394.

30. Bain, S., Ozawa, H., and Criss, J., Development of a cure/postcure cycle for PETI-330 laminates fabricated by resin transfer molding. *High Performance Polymers*, 2006. **18**(6): p. 991-1001.

31. Connell, J., Smith, J., Hergenrother, P., and Criss, J., High temperature transfer molding resins: status of PETI-298 and PETI-330. *International SAMPE Technical Conference*, 2003. **35**: p. 281-295.

32. Ghose, S., Watson, K., Working, D., Siochi, E., Connell, J., and Criss, J., Fabrication and characterization of high temperature resin/carbon nanofiber composites. *High Performance Polymers*, 2006. **18**(4): p. 527-544.

33. Fang, X., Hutcheon, R., and Scola, D., A study of the kinetics of the microwave cure of a phenylethynyl-terminated imide model compound and imide oligomer (PETI-5). *Journal of Polymer Science, Part A: Polymer Chemistry*, 2000. **38**(14): p. 2526-2535.

34. Fang, X. and Scola, D., Investigation of microwave energy to cure carbon fiber reinforced phenylethynyl-terminated polyimide composites, PETI-5/IM7. *Journal of Polymer Science, Part A: Polymer Chemistry*, 1999. **37**(24): p. 4616-4628.

35. MacCullum, J.R., Tanner, J., Derivation of Rate Equations used in Thermogravimetry. *Nature*, 1970. **225**(12): p. 2.

36. Deng, J. and Isayev, A., Nonisothermal Vulcanization of Rubber Compounds. *Rubber Chemistry and Technology*, 1988. **61**(2): p. 340-61.

37. Deng, J. and Isayev, A., Injection Molding of Rubber Compounds: Experimentation and Simulation. *Rubber Chemistry and Technology*, 1991. **64**(2): p. 296-324.

38. Chan, T.W., Shyu, G.D., and Isayev, A.I., Reduced Time Approach to Curing Kinetics, Part I: Dynamic Rate and Master Curve from Isothermal Data. *Rubber Chemistry and Technology*, 1993. **66**(5): p. 849-864.

39. Kamal, M.R. and Sourour, S., Kinetics and thermal characterization of thermoset cure. *Polymer Engineering & Science*, 1973. **13**(1): p. 59-64.

40. Johnson, R., Farnham, A., Clendinning, R., Hale, W., and Merriam, C., Poly(aryl ethers) by nucleophilic aromatic substitution. I. Synthesis and properties. *Journal of Polymer Science, Part A-1: Polymer Chemistry*, 1967. **5**(9): p. 2375-98.

41. Vogel, H., Polyarylsulfones, synthesis and properties. *Journal of Polymer Science, Part A-1: Polymer Chemistry*, 1970. **8**(8): p. 2035-47.

42. Ueda, M. and Sato, M., Synthesis of aromatic poly(ether ketones). *Macromolecules*, 1987. **20**(11): p. 2675-8.

43. Hay, A., Blanchard, H., Endres, G., and Eustance, J., Polymerization by oxidative coupling. *Journal of the American Chemical Society*, 1959. **81**: p. 6335-6.

44. Percec, V. and Nava, H., Synthesis of aromatic polyethers by Scholl reaction. I. Poly(1,1'-dinaphthyl ether phenyl sulfone)s and poly(1,1'-dinaphthyl ether phenyl ketone)s. *Journal of Polymer Science, Part A: Polymer Chemistry*, 1988. **26**(3): p. 783-805.

45. Colon, I. and Kwiatkowski, G., High-molecular-weight aromatic polymers by nickel coupling of aryl polychlorides. *Journal of Polymer Science, Part A: Polymer Chemistry*, 1990. **28**(2): p. 367-83.

46. Colquhoun, H., Dudman, C., Thomas, M., O'Mahoney, C., and Williams, D., Synthesis, structure, and ring-opening polymerization of strained macrocyclic biaryls: a new route to high-performance materials. *Journal of the Chemical Society, Chemical Communications*, 1990(4): p. 336-9.

47. Ozden, S., Charayev, A., and Shaov, A., The synthesis of polyetheretherketones and investigations of their properties. *Journal of Materials Science*, 1999. **34**(11): p. 2741-2744.

48. Blundella, D. and Osborna, B., The morphology of poly(aryl-ether-ether-ketone). *Polymer*, 1983. **24**(8): p. 953-58.

49. Nguyen, H. and Ishida, H., Molecular analysis of the melting behaviour of poly(aryl-ether-ether-ketone). *Polymer*, 1986. **27**(9): p. 1400-05.

50. Victrex. 2008 [cited 2008 10/10/2008]; Victrex Peek]. Available from: http://www.victrex.com/en/peek_poly/properties.php, http://www.victrex.com/docs/literature-docs/Victrex_Material%20Properties%20Guide%20%20%203_7_US.pdf.^

51. Anderson, D.P., Kumar, S., and Adams, W.W., Wide angle x-ray diffraction as a tool to examine the morphology of semicrystalline thermoplastic matrix composites. *Polymer Preprints (American Chemical Society, Division of Polymer Chemistry)*, 1985. **26**(1): p. 275-6.

52. Chalmers, J., Gaskin, W., and Mackenzie, M., Crystallinity in poly(aryl ether ketone) plaques studied by multiple internal reflection spectroscopy. *Polymer Bulletin (Berlin, Germany)*, 1984. **11**(5): p. 433-5.

53. Dawson, P. and Blundell, D., X-ray data for poly(aryl ether ketones). *Polymer*, 1980. **21**(5): p. 577-8.

54. Hay, J., Kemmish, D., Langford, J., and Rae, A., The structure of crystalline PEEK[poly(aryl-ether-ether ketone)]. *Polymer Communications*, 1984. **25**(6): p. 175-8.

55. Rueda, D., Ania, F., Richardson, A., Ward, I., and Balta Calleja, F., X-ray diffraction study of die-drawn poly(aryl ether ketone) (PEEK). *Polymer Communications*, 1983. **24**(9): p. 258-60.

56. Nguyen, H. and Ishida, H., Poly(aryl-ether-ether-ketone) and its advanced composites: a review. *Polymer Composites*, 1987. **8**(2): p. 57-73.

57. Cogswell, F., *Thermoplastic aromatic polymer composites: a study of the structure, processing and properties of carbon fibre reinforced polyetheretherketone and related materials*. 1992, Oxford: Butterworth-Heinemann.^

58. Gao, S. and Kim, J., Correlation among crystalline morphology of PEEK, interface bond strength, and in-plane mechanical properties of carbon/PEEK composites. *Journal of Applied Polymer Science*, 2002. **84**(6): p. 1155-1167.

59. Nuriel, H., Klein, N., and Marom, G., The effect of transcrystalline layer on the mechanical properties of composite materials in the fibre direction. *Composites Science and Technology*, 1999. **59**(11): p. 1685-1690.

60. Stern, T., Marom, G., and Wachtel, E., Origin, morphology and crystallography of transcrystallinity in polyethylene-based single-polymer composites. *Composites, Part A: Applied Science and Manufacturing*, 1997. **28A**(5): p. 437-444.

61. Cantwell, W., Davies, P., Bourban, P., Jar, P., and Kausch, H., Joining and repair of carbon fiber/PEEK. *Swiss Materials*, 1990. **2**(1): p. 25-9.

62. Cebe, P., Chung, S., and Hong, S., Effect of thermal history on mechanical properties of poly(ether ether ketone) below the glass transition temperature. *Journal of Applied Polymer Science*, 1987. **33**(2): p. 487-503.

63. Davies, P., Cantwell, W., Jar, P.Y., Richard, H., Neville, D., and Kausch, H., Cooling rate effects in carbon fiber/PEEK composites. *ASTM Special Technical Publication*, 1991. **STP 1110**(Compos. Mater.: Fatigue Fract. (3rd Vol.)): p. 70-88.

64. Lustiger, A., Uralil, F., and Newaz, G., Processing and structural optimization of PEEK composites. *Polymer Composites*, 1990. **11**(1): p. 65-75.

65. Russell, J. and Curliss, D., Effects of different thermal histories on the mechanical properties and fracture toughness of APC-2. *International SAMPE Technical Conference*, 1991. **23**(Adv. Mater./Affordable Processes): p. 91-103.

66. Saiello, S., Kenny, J., and Nicolais, L., Interface morphology of carbon fiber PEEK composites. *Journal of Materials Science*, 1990. **25**(8): p. 3493-6.

67. Seferis, J., Poly(ether ether ketone) (PEEK): processing-structure and properties studies for a matrix in high performance composites. *Polymer Composites*, 1986. **7**(3): p. 158-69.

68. Talbott, M., Springer, G., and Berglund, L., The effects of crystallinity on the mechanical properties of PEEK polymer and graphite fiber-reinforced PEEK. *Journal of Composite Materials*, 1987. **21**(11): p. 1056-81.

69. Unger, W. and Hansen, J., The effect of cooling rate and annealing on residual stress development in graphite fiber-reinforced PEEK laminates. *Journal of Composite Materials*, 1993. **27**(2): p. 108-37.

70. Vu-Khanh, T. and Denault, J., Effect of molding parameters on the interfacial strength in PEEK/carbon composites. *Journal of Reinforced Plastics and Composites*, 1993. **12**(8): p. 916-31.

71. Kroto, H., Heath, J., O'Brien, S., Curl, R., and Smalley, R., C60: buckminsterfullerene. *Nature (London, United Kingdom)*, 1985. **318**(6042): p. 162-3.

72. Xie, X., Mai, Y., and Zhou, X., Dispersion and alignment of carbon nanotubes in polymer matrix: A review. *Materials Science & Engineering, R: Reports*, 2005. **R49**(4): p. 89-112.

73. Ajayan, P.M., Ebbesen, T.W., Ichihashi, T., Iijima, S., Tanigaki, K., and Hiura, H., Opening carbon nanotubes with oxygen and implications for filling. *Nature (London, United Kingdom)*, 1993. **362**(6420): p. 522-25.

74. Tsang, S., Harris, P., and Green, M., Thinning and opening of carbon nanotubes by oxidation using carbon dioxide. *Nature (London, United Kingdom)*, 1993. **362**(6420): p. 520-2.

75. Nalwa, H., *Handbook of Nanostructured Materials and Nanotechnology*. Vol. 5. 2000, New York: Academic Press.^

76. Baddour, C. and Briens, C., Carbon Nanotube Synthesis: A Review. *International Journal of Chemical Reactor Engineering*, 2005. **3**(1): p. 1279.

77. Journet, C. and Bernier, P., Production of carbon nanotubes. *Applied Physics A Materials Science & Processing*, 1998. **67**(1): p. 1-9.

78. Ajayan, P.M., Nanotubes from Carbon. *Chemical Reviews (Washington, D. C.)*, 1999. **99**(7): p. 1787-1799.

79. Guo, T., Nikolaev, P., Thess, A., Colbert, D., and Smalley, R., Catalytic growth of single-walled nanotubes by laser vaporization. *Chemical Physics Letters*, 1995. **243**(1-2): p. 49-54.

80. Popov, V., Carbon nanotubes: properties and application. *Materials Science and Engineering: R: Reports*, 2004. **43**(3): p. 61-102.

81. Satishkumar, B., Govindaraj, A., Sen, R., and Rao, C., Single-walled nanotubes by the pyrolysis of acetylene-organometallic mixtures. *Chemical Physics Letters*, 1998. **293**(1-2): p. 47-52.

82. Marangoni, R., Serp, P., Feurer, R., Kihn, Y., Kalck, P., and Vahlas, C., Carbon nanotubes produced by substrate free metalorganic chemical vapor deposition of iron catalysts and ethylene. *Carbon*, 2001. **39**(3): p. 443-449.

83. Li, J., Ma, P., Chow, W., To, C., Tang, B., and Kim, J., Correlations between percolation threshold, dispersion state, and aspect ratio of carbon nanotubes. *Advanced Functional Materials*, 2007. **17**(16): p. 3207-3215.

84. Yakobson, B., Brabec, C., and Bernholc, J., Nanomechanics of carbon tubes: instabilities beyond linear response. *Physical Review Letters*, 1996. **76**(14): p. 2511-14.

85. Ruoff, R. and Lorents, D., Mechanical and thermal properties of carbon nanotubes. *Carbon*, 1995. **33**(7): p. 925-30.

86. Treacy, M., Ebbesen, T., and Gibson, J., Exceptionally high Young's modulus observed for individual carbon nanotubes. *Nature (London)*, 1996. **381**(6584): p. 678-680.

87. Yu, M., Lourie, O., Dyer, M., Moloni, K., Kelly, T., and Ruoff, R., Strength and breaking mechanism of multiwalled carbon nanotubes under tensile load. *Science (Washington, D. C.)*, 2000. **287**(5453): p. 637-640.

88. Bower, C., Kleinhammes, A., Wu, Y., and Zhou, O., Intercalation and partial exfoliation of single-walled carbon nanotubes by nitric acid. *Chemical Physics Lettters*, 1998. **288**(2-4): p. 6.

89. Rudhardt, D., Bechinger, C., and Leiderer, P., Repulsive depletion interactions in colloid-polymer mixtures. *Journal of Physics: Condensed Matter*, 1999. **11**(50): p. 10073-78.

90. Bechinger, C., Rudhardt, D., Leiderer , P., Roth, R., and Dietrich, S., Understanding Depletion Forces beyond Entropy. *Physical Review Letters*, 1999. **83**(19): p. 3960-63.

91. Tjong, S., Structural and mechanical properties of polymer nanocomposites. *Materials Science & Engineering, R: Reports*, 2006. **R53**(3-4): p. 73-197.

92. Tibbetts, G.G., Lake, M.L., Strong, K.L., and Rice, B.P., A review of the fabrication and properties of vapor-grown carbon nanofiber/polymer composites. *Composites Science and Technology*, 2007. **67**(7-8): p. 1709-1718.

93. Boul, P., Liu, J., Mickelson, E., Huffman, C., Ericson, L., Chiang, I., Smith, K., Colbert, D., Hauge, R., Margrave, J., and Smalley, R., Reversible sidewall functionalization of buckytubes. *Chemical Physics Letters*, 1999. **310**(3-4): p. 367-72.

94. Liu, J., Casavant, M., Cox, M., Walters, D., Boul, P., Lu, W., Rimberg, A., Smith, K., Colbert, D., and Smalley, R., Controlled deposition of individual single-walled carbon nanotubes on chemically functionalized templates. *Chemical Physics Letters*, 1999. **33**(1-2): p. 125-129.

95. Ausman, K., Piner, R., Lourie, O., Ruoff, R., and Korobov, M., Organic Solvent Dispersions of Sing le-Walled Carbon Nanotubes: Toward Solutions of Pristine Nanotubes. *The Journal of Physical Chemistry B*, 2000. **104**(38): p. 8911-14.

96. Duesberg, G., Muster, J., Krstic, V., Burghard, M., and Roth, S., Chromatographic size separation of single-wall carbon nanotubes. *Applied Physics A Materials Science & Processing*, 1998. **67**(1): p. 117-19.

97. Krstic, V., Duesberg, G., Muster, J., Burghard, M., and Roth, S., Langmuir−Blodgett Films of Matrix-Diluted Single-Walled Carbon Nanotubes. *Chemistry of Materials*, 1998. **10**(9): p. 2338-40.

98. Liu, J., Rinzler, A., Dai, H., Hafner, J., Bradley, R., Boul, P., Lu, A., T., I., Shelimov, K., Huffman, C., RodriguezMacias, R., Shon, Y., Lee, T., Colbert, D., and Smalley, R., Fullerene Pipes. *Science (Washington D.C.)*, 1998. **280**(5367): p. 1253-1256.

99. Jin, Z., Huang, L., Goh, S., Xu, G., and Ji, W., Characterization and nonlinear optical properties of a poly(acrylic acid)–surfactant–multi-walled carbon nanotube complex. *Chemical Physics Letters*, 2000. **332**(5-6): p. 461-66.

100. Gong, X., Liu, J., Baskaran, S., Voise, R.D., and Young, J.S., Surfactant-Assisted Processing of Carbon Nanotube/Polymer Composites. *Chemistry of Materials*, 2000. **12**(4): p. 4.

101. Bower, C., Kleinhammes, A., Wu, Y., and Zhou, O., Intercalation and partial exfoliation of single-walled carbon nanotubes by nitric acid. *Chemical Physics Letters*, 1998. **288**(2-4): p. 481-85.

102. Lu, J., Elastic properties of single and multilayered nanotubes. *Journal of Physics and Chemistry of Solids*, 1997. **58**(11): p. 1649-1652.

103. Shaffer, M., Fan, X., and Windle, A., Dispersion and packing of carbon nanotubes. *Carbon*, 1998. **36**(11): p. 1603-12.

104. Chen, J.H., M.A.; Hu, H.; Chen, Y.; Rao, A.M.; Eklund, P.C.; Haddon, R.C.;, Solution Properties of Single-Walled Carbon Nanotubes. *Science*, 1998. **282**(5386): p. 95-99.

105. Wong, S.S.J., Ernesto; Woolley, Adam T. ; Cheung, Chin Li; Lieber, Charles M. , Covalently functionalized nanotubes as nanometre- sized probes in chemistry and biology. *Nature*, 1998. **394**: p. 4.

106. Riggs, J., Guo, Z., Carroll, D., and Sun, Y., Strong Luminescence of Solubilized Carbon Nanotubes. *Journal of the American Chemical Society*, 2000. **24**: p. 5879-5881.

107. Riggs, J., Walker, D., Carroll, D., and Sun, Y., Optical Limiting Properties of Susp ended and Solubilized Carbon Nanotubes. *The Journal of Physical Chemistry B*, 2000. **30**: p. 7071-76.

108. Jia, Z., Wang, Z., Xu, C., Liang, J., Wei, B., Wu, D., and Zhu, S., Study on poly(methyl methacrylate)/carbon nanotube composites. *Materials Science and Engineering: A*, 1999. **271**(1-2): p. 395-400.

109. Tang, B. and Xu, H., Preparation, Alignment, and Optical Properties of Soluble Poly(phenylacetylene)-Wrapped Carbon Nanotubes. *Macromolecules*, 1999. **32**(8): p. 2569-77.

110. Glasgow, D.G., Tibbetts, G.G., Matuszewski, M.J., Walters, K.R., and Lake, M.L., Suface treatment of carbon nanofibers for improved composite mechanical properties, in *SAMPE 2004*. 2004: Long Beach, CA.^

111. Lakshminarayanan, P.V., Toghiani, H., and Pittman Jr, C.U., Nitric acid oxidation of vapor grown carbon nanofibers. *Carbon*, 2004. **42**(12-13): p. 2433-42.

112. Lafdi, K. and Matzek, M., Carbon nanofibers as a nano-reinforcement for polymeric nanocomposites, in *35th ISTC*. 2003: Dayton,OH.^

113. Baek, J.-B., Lyons, C.B., and Tan, L.S., Grafting of Vapor-Grown Carbon Nanofibers via in-Situ Polycondensation of 3-Phenoxybenzoic Acid in Poly(phosphoric acid). *Macromolecules*, 2004. **37**(22): p. 8278-85.

114. Lordi, V. and Yao, N., Molecular mechanics of binding in carbon-nanotube-polymer composites. *Journal of Material Research*, 2000. **15**(12): p. 2770-79.

115. Park, C., Ounaies, Z., Watson, K., Pawlowski, K., Lowther, S., Connell, J., Siochi, E., Harrison, J., and St. Claire, T., Polymer-Single wall carbon nanotube composites for potential spacecraft applications. , in *Mat. Res. Soc. Symp.* . 2002.^

116. Wise, K., Park, C., Siochi, E., and Harrison, J., Stable dispersion of single wall carbon nanotubes in polyimide: the role of noncovalent interactions. *Chem. Phys. Lett.*, 2004(391): p. 207.

117. Cochet, M., Maser, W., Benito, A., Callejas, M., Martínez, M., Benoit, J., Schreiber, J., and Chauvet, O., Synthesis of a new polyaniline/nanotube composite: "in-situ" polymerisation and charge transfer through site-selective interaction. *Chemical Communications*, 2001. **2001**(16): p. 1450-51.

118. Park, C., Ounaies, Z., Watson, K., Crooks, R., J., S., Lowther, S., Connell, J., Siochi, E., Harrison, J., and St. Clair, T., Dispersion of single wall carbon nanotubes by in situ polymerization under sonication. *Chemical Physics Letters*, 2002. **364**(3-4): p. 303-308.

119. Velasco-Santos, C., Martínez-Hernández, A., Fisher, F., Ruoff, R., and Castaño, V., Improvement of Thermal and Mechanical Properties of Carbon Nanotube Composites through Chemical Functionalization. *Chemistry of Materials*, 2003. **15**(23): p. 4470-75.

120. Jang, J., Bae, J., and Yoon, S., A study on the effect of surface treatment of carbon nanotubes for liquid crystalline epoxide–carbon nanotube composites. *Journal of Materials Chemistry*, 2003. **13**(4): p. 676-81.

121. Uchida, T., Dang, T., Min, B., Zhang, X., and Kumar, S., Composties Part B. *Processing, structure, and properties of carbon nano fiber filled PBZT composite fiber*, 2005. **36**(3): p. 183-7.

122. Ajayan, P.M., Stephan, O., Colliex, C., and Trauth, D., Aligned Carbon Nanotube Arrays Formed by Cutting a Polymer Resin-Nanotube Composite. *Science*, 1994. **265**(5176): p. 1212-1214.

123. Sandler, J., Shaffer, M., Prasse, T., Bauhofer, W., Schulte, K., and Windle, A., Development of a dispersion process for carbon nanotubes in an epoxy matrix and the resulting electrical properties. *Polymer*, 1999. **40**(21): p. 5967-71.

124. Hornbostel, B., Poetschke, P., Kotz, J., and Roth, S., Single-walled carbon nanotubes/polycarbonate composites. Basic electrical and mechanical properties. *Physica Status Solidi B: Basic Solid State Physics*, 2006. **243**(13): p. 3445-3451.

125. Takase, H., Mikata, Y., Matsuda, S., and Murakami, A., Dispersion of carbon-nanotubes in a polymer matrix by a twin-screw extruder. *Seikei Kako*, 2002. **14**(2): p. 126-131.

126. Potschke, P., Fornes, T., and Paul, D., Rheological behavior of multiwalled carbon nanotube/polycarbonate composites. *Polymer*, 2002. **43**(11): p. 3247-3255.

127. Covas, J., Bernardo, C., Carneiro, O., Maia, J., van Hattum, F., Gaspar-Cunha, A., Biro, L., Horvath, Z., Kiricsi, I., Konya, Z., and Niesz, K., Continuous production of polycarbonate-carbon nanotube composites. *Journal of Polymer Engineering*, 2005. **25**(1): p. 39-57.

128. Sennett, M., Welsh, E., and Wright, J., Dispersion and alignment of carbon nanotubes in polycarbonate. *Materials Research Society Symposium Proceedings*, 2002. **706**(Making Functional Materials with Nanotubes): p. 97-102.

129. Bronikowski, M., Willis, P., Colbert, D., Smith, K., and Smalley, R., Gas-phase production of carbon single-walled nanotubes from carbon monoxide via the HiPco process: A parametric study. *Journal of Vacuum Science & Technology A: Vacuum, Surfaces, and Films*, 2001. **19**(4): p. 1800-1805.

130. Zeng, J., Saltysiak, B., Johnson, W., Schiraldi, D.A., and Kumar, S., Processing and properties of poly(methyl methacrylate)/carbon nano fiber composites. *Composites Part B: Engineering*, 2004. **35**(2): p. 173-8.

131. Sandler, J., Werner, P., Shaffer, M., Demchuk, V., Altstaedt, V., and Windle, A., Carbon nanofiber-reinforced poly(ether ether ketone) composites. *Composites, Part A: Applied Science and Manufacturing*, 2002. **33A**(8): p. 1033-1039.

132. Zhang, Q., Rastogi, S., Chen, D., Lippits, D., and Lemstra, P., Low percolation threshold in single-walled carbon nanotube/high density polyethylene composites prepared by melt processing technique. *Carbon*, 2006. **44**(4): p. 778-785.

133. Kim, J., Park, H., and Kim, S., Multiwall-carbon-nanotube-reinforced poly(ethylene terephthalate) nanocomposites by melt compounding. *Journal of Applied Polymer Science*, 2007. **103**(3): p. 1450-1457.

134. Liu, T., Phang, I., Shen, L., Chow, S., and Zhang, W., Morphology and mechanical properties of multiwalled carbon nanotubes reinforced nylon-6 composites. *Macromolecules*, 2004. **37**(19): p. 7214-7222.

135. Zhang, W., Shen, L., Phang, I., and Liu, T., Carbon Nanotubes Reinforced Nylon-6 Composite Prepared by Simple Melt-Compounding. *Macromolecules*, 2004. **37**(2): p. 256-259.

136. Qian, D., Dickey, E., Andrews, R., and Rantell, T., Load transfer and deformation mechanisms in carbon nanotube-polystyrene composites. *Applied Physics Letters*, 2000. **76**(20): p. 2868-2870.

137. Cadek, M., Coleman, J., Barron, V., Hedicke, K., and Blau, W., Morphological and mechanical properties of carbon-nanotube-reinforced semicrystalline and amorphous polymer composites. *Applied Physics Letters*, 2002. **81**(27): p. 5123-25.

138. Kruiger, R., Alam, K., and Anderson, D., Strength prediction of partially aligned discontinuous fiber-reinforced composties. *Journal of Materials Research*, 2001. **16**(1): p. 226-32.

139. Melechko, A.V., Klein, K.L., Fowlkes, J.D., Hensley, D.K., McKnight, T.E., Rack, P.D., Horton, J.A., and Simpson, M.L., Control of carbon nanostructure: From nanofiber toward nanotube and back. *Journal of Applied Physics*, 2007. **102**(074314): p. 1-7.

140. Bokobza, L., Multiwall carbon nanotube elastomeric composites: A review. *Polymer*, 2007. **48**(17): p. 4907-20.

141. Smith, J., Delozier, D., Connell, J., and Watson, K., Carbon nanotube-conductive additive-space durable polymer nanocomposite films for electrostatic charge dissipation. *Polymer*, 2004. **45**(18): p. 6133-6142.

142. Ramasubramaniam, R., Chen, J., and Liu, H., Homogeneous carbon nanotube/polymer composites for electrical applications. *Applied Physics Letters*, 2003. **83**(14): p. 2928-2930.

143. Potschke, P., Bhattacharyya, A., and Janke, A., Melt mixing of polycarbonate with multiwalled carbon nanotubes: microscopic studies on the state of dispersion. *European Polymer Journal*, 2003. **40**(1): p. 137-148.

144. Sung, Y., Han, M., Song, K., Jung, J., Lee, H., Kum, C., Joo, J., and Kim, W., Rheological and electrical properties of polycarbonate/multi-walled carbon nanotube composites. *Polymer*, 2006. **47**(12): p. 4434-4439.

145. R., K. and Vaia, R.A., *Polymer Nanocomposites: Synthesis, Characterization and Modeling*. American Chemical Society Symposium Series. Vol. 804. 2001, Washington DC: American Chemical Society.^

146. Coleman, J., Curran, S., Dalton, A., Davey, A., McCarthy, B., Blau, W., and Barklie , R., Percolation-dominated conductivity in a conjugated-polymer-carbon-nanotube composite. *Physical Review B*, 1998. **58**(12): p. 7492-95.

147. Ghose, S., Watson, K., Sun, K., Criss, J., Siochi, E., and Connell, J., High temperature resin/carbon nanotube composite fabrication. *Composites Science and Technology*, 2006. **66**(13): p. 1995-2002.

148. Choi, E., Brooks, J., Eaton, D., Al-Haik, M., Hussaini, M., Garmestani, H., Li, D., and Dahmen, K., Enhancement of thermal and electrical properties of carbon nanotube polymer composites by magnetic field processing. *Journal of Applied Physics*, 2003. **94**(9): p. 6034-39.

149. Sandler, J., Kirk, J., Kinloch, I., Shaffer, M., and Windle, A., Ultra-low electrical percolation threshold in carbon-nanotube-epoxy composites. *Polymer*, 2003. **44**(19): p. 5893-99.

150. Kashiwagi, T., Grulke, E., Hilding, J., Harris, R., Awad, W., and Douglas, J., Thermal Degradation and Flammability Properties of Poly(propylene)/Carbon Nanotube Composites. *Macromolecular Rapid Communications*, 2002. **23**(13): p. 761-765.

151. Biercuk, M., Llaguno, M., Radosavljevic, M., Hyun, J., Johnson, A., and Fischer, J., Carbon nanotube composites for thermal management. *Applied Physics Letters*, 2002. **80**(15): p. 2767-69.

152. Goyal, R., Tiwari, A., Mulik, U., and Negi, Y., Effect of aluminum nitride on thermomechanical properties of high performance PEEK. *Composites, Part A: Applied Science and Manufacturing*, 2006. **38A**(2): p. 516-524.

153. Ahir, S. and Terentjev, E., eds. *Polymeric Nanostructures and Their Application*. ed. H.S. Nalwa. 2005, American Scientific: New York.

154. Huang, Y., Ahir, S., and Terentjev, E., Dispersion rheology of carbon nanotubes in a polymer matrix. *Physical Review B*, 2006. **73**(12): p. 125422-30.

155. Mason, T., *Sonochemistry: the use of ultrasound in chemistry*. 1990, Cambridge, England: Royal Society of Chemistry.^

156. Young, R., *Cavitation*. Vol. 1. 1989, Great Britain: The Alden Press, Oxford. 418.^

157. Peshkovskii, S.L., Friedman, M.L., Tukachinskii, A.I., Vinogradov, G.V., and Enikolopian, N.S., Acoustic cavitation and its effect on flow in polymers and filled systems. *Polymer Composites*, 1983. **4**(2): p. 126-34.

158. Knapp, R., Daily, J., and Hammitt, F., *Cavitation*. 1970, New York: McGraw-Hill Book Company. 578.^

159. Peshkovskii, S., Friedman, M., and Brizitskii, G., Effect of Acoustic Cavitation on High Polymer Flow. *Dokl. AN SSSR*, 1981. **258**: p. 706.

160. Ebdon, J. and Eastmond, G., *New Methods of Polymer Synthesis*. Vol. 2. 1995, New York: Chapman and Hall.^

161. Harris, B., Hamielec, A., and Marten, L., Emulsion polymerization kinetics. Chain entanglements and glassy-state transition. *ACS Symposium Series*, 1981. **165**(Emulsion Polym. Emulsion Polym.): p. 315-26.

162. Suslick, K. and Price, P., Applications of ultrasound to materials chemistry. *Annual Review of Materials Science*, 1999. **29**: p. 295-326.

163. Thomas, J., Sonic degradation of high polymers in solution. *Journal of Physical Chemistry*, 1959. **63**: p. 1725-9.

164. Ovenall, D., Ultrasonic degradation of polymer molecules in solution. Some comments on recent papers. *Journal of Polymer Science*, 1960. **42**: p. 455-61.

165. Van der Hoff, B. and Glynn, P., Rate of degradation by ultrasonation of polystyrene in solution. *Journal of Macromolecular Science, Chemistry*, 1974. **8**(2): p. 429-49.

166. Smith, W. and Temple, H., Polymer studies by gel permeation chromatography. IV. Degradation of polystyrene by ultrasonics and by benzoyl peroxide. *Journal of Physical Chemistry*, 1968. **72**(13): p. 4613-19.

167. Bucknall, C. and Paul, D., *Polymer Blends*. 2000, New York: Wiley.^

168. Hong, C. and Isayev, A., Plastic/Rubber Blends of Ultrasonically Devulcanized GRT with HDPE. *Journal of Elastomers and Plastics*, 2001. **33**(1): p. 47-72.

169. Oh, J., Isayev, A., and Rogunova, M., Continuous ultrasonic process for in situ compatibilization of polypropylene/natural rubber blends. *Polymer*, 2003. **44**(8): p. 2337-2349.

170. Lin, H. and Isayev, A., Ultrasonic treatment of polypropylene, polyamide 6, and their blends. *Journal of Applied Polymer Science*, 2006. **102**(3): p. 2643-53.

171. Isayev, A., Hong, C., and Kim, K., Continuous mixing and compounding of polymer/filler and polymer/polymer mixtures with the aid of ultrasound. *Rubber Chemistry and Technology*, 2003. **76**(4): p. 923-947.

172. Isayev, A., Yushanov, S., and Chen, J., Ultrasonic devulcanization of rubber vulcanizates. I. Process model. *Journal of Applied Polymer Science*, 1996. **59**(5): p. 803-13.

173. Hong, C. and Isayev, A., Ultrasonic devulcanization of unfilled SBR under static and continuous conditions. *Rubber Chemistry and Technology*, 2002. **75**(1): p. 133-142.

174. Isayev, A., Chen, J., and Tukachinsky, A., Novel ultrasonic technology for devulcanization of waste rubbers. *Rubber Chemistry and Technology*, 1995. **68**(2): p. 267-80.

175. Isayev, A., Kim, S., and Levin, V., Superior mechanical properties of reclaimed SBR with bimodal network. *Rubber Chemistry and Technology*, 1997. **70**(2): p. 194-201.

176. Johnston, S., Massey, J., von Meerwall, E., Kim, S., Levin, V., and Isayev, A., Ultrasound devulcanization of SBR: molecular mobility of gel and sol. *Rubber Chemistry and Technology*, 1997. **70**(2): p. 183-193.

177. Levin, V., Kim, S., and Isayev, A., Vulcanization of ultrasonically devulcanized SBR elastomers. *Rubber Chemistry and Technology*, 1997. **70**(1): p. 120-128.

178. Levin, V., Kim, S., Isayev, A., Massey, J., and von Meerwall, E., Ultrasound devulcanization of sulfur vulcanized SBR: crosslink density and molecular mobility. *Rubber Chemistry and Technology*, 1996. **69**(1): p. 104-14.

179. Tukachinsky, A., Schworm, D., and Isayev, A.I., Devulcanization of waste tire rubber by powerful ultrasound. *Rubber Chemistry and Technology*, 1996. **69**(1): p. 92-103.

180. Tapale, M. and Isayev, A., Continuous ultrasonic devulcanization of unfilled NR vulcanizates. *Journal of Applied Polymer Science*, 1998. **70**(10): p. 2007-2019.

181. Diao, B., Isayev, A., and Levin, V., Basic study of continuous ultrasonic devulcanization of unfilled silicone rubber. *Rubber Chemistry and Technology*, 1999. **72**(1): p. 152-164.

182. Yun, J., Yashin, V., and Isayev, A., Ultrasonic devulcanization of carbon black-filled ethylene propylene diene monomer rubber. *Journal of Applied Polymer Science*, 2004. **91**(3): p. 1646-1656.

183. Luo, T. and Isayev, A., Rubber/plastic blends based on devulcanized ground tire rubber. *Journal of Elastomers and Plastics*, 1998. **30**(2): p. 133-160.

184. Kumar, R., Koltypin, Y., Palchik, O., and Gedanken, A., Preparation and characterization of nickel-polystyrene nanocomposite by ultrasound irradiation. *Journal of Applied Polymer Science*, 2002. **86**(1): p. 160-165.

185. Xia, H. and Wang, Q., Preparation of conductive polyaniline/nanosilica particle composites through ultrasonic irradiation. *Journal of Applied Polymer Science*, 2003. **87**(11): p. 1811-1817.

186. Koshio, A., Yudasaka, M., Zhang, M., and Iijima, S., A Simple Way to Chemically React Single-Wall Carbon Nanotubes with Organic Materials Using Ultrasonication. *Nano Letters*, 2001. **1**(7): p. 361-63.

187. Yudasaka, M., Zhang, M., Jabs, C., and Iijima, S., Effect of an organic polymer in purification and cutting of single-wall carbon nanotubes. *Applied Physics A Materials Science & Processing*, 2000. **71**(4): p. 449-451.

188. Lapshin, S. and Isayev, A., Continuous process for melt intercalation of PP-clay nanocomposites with aid of power ultrasound. *Journal of Vinyl & Additive Technology*, 2006. **12**(2): p. 78-82.

189. Swain, S. and Isayev, A., Effect of ultrasound on HDPE/clay nanocomposites: Rheology, structure and properties. *Polymer*, 2007. **48**(1): p. 281-289.

190. Tan, H. and Isayev, A.I., Comparative Study of Silica-, Nanoclay- and Carbon Black-Filled Ethylene Propylene Diene Monomer (EPDM) Rubbers Treated by Ultrasound. *Rubber Chemistry and Technology*, 2008. **81**(1): p. 138-155.

191. Yashin, V., Hong, C., and Isayev, A., Thermomechanical degradation of sbr during ultrasonic treatment under the static conditions. *Rubber Chemistry and Technology*, 2004. **77**(1): p. 50-77.

192. Suetsugu, Y. and Sato, A., Novel Dispersion Technique for Nano-Particles by Ultrasonic Wave. *Proceedings of Polymer Processing Society 24th Annual Meeting*, 2008.

193. Advani, S.G., *Flow and Rheology in Polymer Composite Manufacturing*. 1994, New York, New York: Elsevier.^

194. Bickerton, S., Stadtfel, H., Steiner, K., Advani, S., Design and application of actively controlled injection schemes for resin-transfer molding. *Composites Science and Technology*, 2001. **61**: p. 12.

195. Harper, C., *Handbook of Plastic Process*. 2006, Hoboken, NJ: Wiley-Interscience.^

196. Yiand, H., Ding, X., Convential Approach on Manufacturing 3D Woven reforms used for Composites. *Journal of Industrial Textiles*, 2004. **34**(1): p. 11.

197. Advani, S. and Hsiao, K.T., *Manufacturing Techniques for Polymer Matrix Composites (PMCs)*. 2012: Elsevier Science.^

198. Rudd, C.D., Long, A.C., and Kendall, K.N., *Liquid Moulding Technologies: Resin Transfer Moulding, Structural Reaction Injection Moulding and Related Processing Techniques*. 1997: Society of Automotive Engineers.^

199. UBE. UPILEX DATA SHEET PETI-330. 2008 [cited 2011; H:[PETI-330 Data Sheet]. Available from: https://ssl.alpha-prm.jp/upilex.jp/data_sheet/DS_PETI-330_Rev_H.pdf.^

200. Materials, B.S. Baytubes C150P. Datasheet 2011 [cited 2011; Available from: http://www.baytubes.com/downloads/datasheet_baytubes_c_150_p.pdf.^

201. Ghose, S., Lewis, T. M., Cano, R. J., Watson, K. A., Isayev, A. I. Infusion processing of phenylethynyl terminated imides by high temperature RTM and VARTM. in *SAMPE US FALL PROCEEDINGS*. 2011. Fort Worth, TX: SAMPE.

202. Charney, W., *Handbook of Modern Hospital Safety*. 1999, Boca Raton, Florida: CRC Press.^

203. Lewis, E., *Decontamination of HEPA Filters*. 1977, Springfield, Virgina: National Technical Information Service.^

204. Janeschitz-Kriegl, H., Wippel, H., Paulik, Ch., Eder, G., Polymer crystallization dynamics, as reflected by differential scanning calorimetry. Part 1: On the calibration of the apparatus. *Colloid Polymer Science*, 1993. **271**: p. 8.

205. Isayev, A.I., Wong, C.M., and Zeng, X., Effect of oscillations during extrusion on rheology and mechanical properties of polymers. *Advances in Polymer Technology*, 1990. **10**(1): p. 31-45.

206. Kitano, T. and Kataoka, T., The effect of the mixing methods on viscous properties of polyethylene melts filled with fibers. *Rheologica Acta*, 1980. **19**(6): p. 753-763.

207. Kitano, T., Kataoka, T., and Nagatsuka, Y., Shear flow rheological properties of vinylon- and glass-fiber reinforced polyethylene melts. *Rheologica Acta*, 1984. **23**(1): p. 20-30.

208. Utracki, L.A., Flow and flow orientation of composites containing anisometric particles. *Polymer Composites*, 1986. **7**(5): p. 274-282.

209. Schlea, M.R., Processing and Characterization of High Performance Polyimide Nanocomposites, in *Materials Science and Engineering*. 2011, Georgia Institue of Technology: Atlanta, GA, USA. p. 215.^

210. Cole, K.S., Cole, Robert H. , Dispersion and Absorption in Dielectrics I. Alternating Current Characteristics. *Journal of Chemical Physics*, 1941. **9**: p. 341.

211. Harrell, E.R. and Nakajima, N., Modified Cole–Cole plot based on viscoelastic properties for characterizing molecular architecture of elastomers. *Journal of Applied Polymer Science*, 1984. **29**(3): p. 995-1010.

212. Han, C.D., Influence of molecular weight distribution on the linear viscoelastic properties of polymer blends. *Journal of Applied Polymer Science*, 1988. **35**(1): p. 167-213.

213. High Temp Composites - PETI-330. 2008; Available from: http://www.upilex.jp/e_composites.html.^

214. Ogasawara, T., Ishida, Y., Ishikawa, T., and Yokota, R., Characterization of multi-walled carbon nanotube/phenylethynyl terminated polyimide composites. *Composites Part A: Applied Science and Manufacturing (Incorporating Composites and Composites Manufacturing)*, 2004. **35**(1): p. 67-74.

215. Schlea, M.R., Renee Brown, T., Bush, J.R., Criss, J.M., Mintz, E.A., and Shofner, M.L., Dispersion control and characterization in multiwalled carbon nanotube and phenylethynyl-terminated imide composites. *Composites Science and Technology*, 2010. **70**(5): p. 822-828.

216. Ghose, S., Cano, R. J., Watson, K. A., Britton, S. M., Jensen, B. J., Connell, J. W., Herring, H. M., Linberry, Q. J. , High temperature VARTM of phenylethynyl terminated imides. *High Performance Polymers*, 2009. **21**(5): p. 20.

217. Criss, J.M., Koon, R. W., Hergenrother, P.M., Connell, J. W., Smith Jr., J. G., High temperature VARTM of phenylethynyl terminated imide composites, in *Science of Advanced Materials Process Engineering Technical Conference*. 2001, SAMPE: Seattle, WA. p. 1009-1021.^

218. Pötschke, P., Abdel-Goad, M., Alig, I., Dudkin, S., and Lellinger, D., Rheological and dielectrical characterization of melt mixed polycarbonate-multiwalled carbon nanotube composites. *Polymer*, 2004. **45**(26): p. 8863-8870.

219. Bhattacharyya, A.R., ouml, tschke, P., Abdel-Goad, M., and Fischer, D., Effect of encapsulated SWNT on the mechanical properties of melt mixed PA12/SWNT composites. *Chemical Physics Letters*, 2004. **392**(1-3): p. 28-33.

220. Mitchell, C.A., Bahr, J.L., Arepalli, S., Tour, J.M., and Krishnamoorti, R., Dispersion of Functionalized Carbon Nanotubes in Polystyrene. *Macromolecules*, 2002. **35**(23): p. 8825-8830.

221. McNally, T., Pötschke, P., Halley, P., Murphy, M., Martin, D., Bell, S.E.J., Brennan, G.P., Bein, D., Lemoine, P., and Quinn, J.P., Polyethylene multiwalled carbon nanotube composites. *Polymer*, 2005. **46**(19): p. 8222-8232.

222. Blundell, D.J. and Osborn, B.N., The morphology of poly(aryl-ether-ether-ketone). *Polymer*, 1983. **24**(8): p. 953-958.

223. Ryan, K.P., Cadek, M., Nicolosi, V., Walker, S., Ruether, M., Fonseca, A., Nagy, J.B., Blau, W.J., and Coleman, J.N., Multiwalled carbon nanotube nucleated

crystallization and reinforcement in poly (vinyl alcohol) composites. *Synthetic Metals*, 2006. **156**(2-4): p. 332-335.

224. Bhattacharyya, A.R., Sreekumar, T. V., Liu, T., Kumar, S., Ericson, L. M., Hauge, R. H., Smalley, R. E. , Crystallization and orientation studies in polypropylene/single wall carbon nanotube composites. *Polymer*, 2003. **44**: p. 4.

225. Diez-Pascual, A.M., Mohammed, N., Gomez, M.A., Marco, C., Ellis, G., Martinez, M.T., Anson, A., Gonzalez-Dominguez, J.M., Martinez-Rubi, Y., and Simard, B., Development and characterization of PEEK/carbon nanotube composites. *Carbon*, 2009. **47**(13): p. 3079-3090.

226. Rong, C., Ma, G., Zhang, S., Song, L., Chen, Z., Wang, G., and Ajayan, P.M., Effect of carbon nanotubes on the mechanical properties and crystallization behavior of poly(ether ether ketone). *Composites Science and Technology*, 2010. **70**(2): p. 380-386.

227. Chen, C., The Manufacture of Polymer Nanocomposite Materials Using Supercritical Carbon Dioxide, in *Chemical Engineering*. 2011, Virginia Polytechnic Institute and State University: Blacksburg, VA.^

228. Ogasawara, T., Tsuda, T., and Takeda, N., Stress–strain behavior of multi-walled carbon nanotube/PEEK composites. *Composites Science and Technology*, 2011. **71**(2): p. 73-78.

229. Bangarusampath, D.S., Ruckd, auml, schel, H., Altst, auml, dt, V., Sandler, J.K.W., Garray, D., and Shaffer, M.S.P., Rheology and properties of melt-processed poly(ether ether ketone)/multi-wall carbon nanotube composites. *Polymer*, 2009. **50**(24): p. 5803-5811.

230. Diez-Pascual, A.M., Mohammed, N., Gonzalez-Dominguez, J.M., Anson, A., Martinez-Rubi, Y., Martinez, M.T., Simard, B., and Gomez, M.A., High performance PEEK/carbon nanotube composites compatibilized with polysulfones-II. Mechanical and electrical properties. *Carbon*, 2010. **48**(12): p. 3500-3511.

231. Inc., N. Plasticyl PEEK1001 Technical Data Sheet. 2010 June 23, 2010 [cited 2011 August 8]; 2:[Conductivity of PEEK/MWNT composites].^

232. Mohiuddin, M., Effect of Pressure and Temperature on Electrical Conductivity of CNT-PEEK Composites, in *Mechanical and Industrial Engineering*. 2012, Concordia University: Montreal, Quebec, Canada. p. 206.^

233. Socher, R., Krause, B., Muller, M.T., Boldt, R., and Potschke, P., The influence of matrix viscosity on MWCNT dispersion and electrical properties in different thermoplastic nanocomposites. *Polymer*, 2012. **53**(2): p. 495-504.

234. Galloway, J., Hoffman, R., and Sanjiv, B., Effect of multiple shear histories on rheological behavior and devolatilization of poly(ether ether ketone), in *ANTEC*, SPE, Editor. 2007, Curran Associates: Cincinnati, OH. p. 5.^

235. Deng, F., Ogasawara, T., and Takeda, N., Tensile properties at different temperature and observation of micro deformation of carbon nanotubes–poly(ether ether ketone) composites. *Composites Science and Technology*, 2007. **67**(14): p. 2959-2964.

236. Loiseau, A., Launois-Bernede, P., Petit, P., Roche, S., and Salvetat, J.P., *Understanding Carbon Nanotubes: From Basics to Applications*. 2006: Springer.^